ST. LOUIS PUBLIC LIBRARY
AUG 13 1956

JOURNAL OF THE AERONAUTICAL SCIENCES

VOLUME 23 AUGUST, 1956 NUMBER 8

CONTENTS

Exact and Approximate Solutions for the Supersonic Delta Wing ..... L. R. FOWELL 709

The Integrated Use of Analog and Digital Computing Machines for Aircraft Dynamic Load Problems ..... BERNARD MAZELSKY AND ROBERT F. O'CONNELL 721

An Analysis of the Performance of an Axial-Flow Compressor at Low Reynolds Number ..... ROBERT L. SOHN 741

The Oscillations of a Supersonic Gas Jet Embedded in a Supersonic Stream ..... D. C. PACK 747

Effect of Wind-Tunnel Contraction on Free-Stream Turbulence ..... MAHINDER S. UBEROI 754

The Human Pilot and the High-Speed Airplane ..... JAMES L. DECKER 765

On the Aerodynamic Instability of Thin Panels ..... JOHN W. MILES 771

Dynamic Behavior During Accelerated Flight with Particular Application to Missile Launching ..... TELFORD W. OSWALD 781

Readers' Forum 792–804

Published by
INSTITUTE OF THE AERONAUTICAL SCIENCES, INC.

JOURNAL OF THE AERONAUTICAL SCIENCES

Editor: W. R. SEARS
Director, Graduate School of Aeronautical Engineering, Cornell University

Associate Editor: ROBERT R. DEXTER *Managing Editor:* RITA J. TURINO
Editorial Assistant: CAROLINE TAYLOR

Editorial Committee

Aerodynamics and Fluid Mechanics
Holt Ashley
H. Julian Allen
Dean R. Chapman
Francis H. Clauser
Hugh L. Dryden
John C. Evvard
Antonio Ferri
Alexander Flax
Wallace D. Hayes
R. T. Jones
Carl Kaplan
H. W. Liepmann
C. C. Lin
H. F. Ludloff
Harold Luskin
Clark B. Millikan
C. D. Perkins
H. J. E. Reid
George S. Schairer
G. B. Schubauer
John Stack
Theodore Theodorsen
Arthur N. Tifford
Th. von Kármán

Flight Testing
R. R. Gilruth
Melvin N. Gough
W. L. Howland
W. F. Milliken, Jr.

Rotating Wing Aircraft
F. B. Gustafson
K. H. Hohenemser
Bartram Kelley
R. B. Maloy
Ralph McClarren
R. H. Miller
R. H. Prewitt
Igor I. Sikorsky

Structures
John E. Duberg
N. J. Hoff
Samuel Levy
J. F. McBrearty
W. Ramberg
E. E. Sechler
F. R. Shanley
C. R. Strang
S. Timoshenko

Meteorology
C. F. Brooks
D. M. Little
F. W. Reichelderfer
K. C. Spengler

Vibration and Flutter
Lee Arnold
M. A. Biot
R. L. Bisplinghoff
Harold A. Cheilek
I. E. Garrick
Martin Goland

Aircraft Design
W. E. Beall
E. H. Heinemann
Hall L. Hibbard
Richard Hutton
C. L. Johnson
A. A. Kartveli
E. G. Stout
F. K. Teichmann
Robert J. Woods

Electronics
Welcome W. Bender
K. C. Black
M. V. Kiebert, Jr.
David S. Little
S. B. Rogers
Paul Rosenberg
L. M. Sherer

Physiologic Problems
H. G. Armstrong
Louis H. Bauer
Robert J. Benford
W. Randolph Lovelace, II
Ross A. MacFarland

Flight Propulsion
William Bollay
George W. Brady
R. P. Kroon
Frank E. Marble
Abe Silverstein
Martin Summerfield
E. S. Taylor

Instruments
Alan G. Binnie
Charles H. Colvin
Frank R. Cook
C. S. Draper
S. G. Eskin
C. F. Savage
R. C. Sylvander

SUBSCRIPTION RATES

JOURNAL OF THE AERONAUTICAL SCIENCES, Published Monthly.—United States and Possessions: 1 Year, $15.00; Single Copies, $1.50. Foreign Countries Including Canada (American Currency Rates): 1 Year, $16.00; Single Copies, $1.50.

AERONAUTICAL ENGINEERING REVIEW, Published Monthly.—United States and Possessions: 1 Year, $3.00; Single Copies, $0.50. Foreign Countries Including Canada (American Currency Rates): 1 Year, $3.50; Single Copies, $0.50.

Notices of change of address should be sent to the Institute at least 30 days prior to actual change of address.

Manuscripts for publication, proofs, and all correspondence should be addressed to the Editorial Office of the JOURNAL.

Correspondence regarding subscriptions may be addressed to the Editorial Office of the JOURNAL OF THE AERONAUTICAL SCIENCES, 2 East 64th Street, New York 21, N.Y., or to the Publication Office, 20th and Northampton Sts., Easton, Pa.

© *Copyright, 1956, by the Institute of the Aeronautical Sciences, Inc.*

Entered as Second Class Matter at the Post Office, Easton, Pa., May 1, 1937. Acceptance for mailing at a special rate of Postage provided for in the Act of August 24, 1912. Authorized April 29, 1937.

JOURNAL OF THE AERONAUTICAL SCIENCES

VOLUME 23 AUGUST, 1956 NUMBER 8

Exact and Approximate Solutions for the Supersonic Delta Wing

L. R. FOWELL†

University of Toronto

SUMMARY

For a plane delta wing with supersonic leading edges, an exact analysis based upon the equations for inviscid flow with constant stagnation enthalpy showed the existence of two cases in the solution of the flow over the expansion surface; below a critical angle of attack a continuous solution can exist while above this angle the solution must be discontinuous.

Exact solutions were found for the flow over the compression surface and for that over the expansion surface in the continuous case. Analytically, the boundaries of the domain (or region of influence) of the wing apex (excepting the shock segment on the compression side) and the solutions outboard of the boundaries were obtained. The solutions within the apex domain were found by relaxation processes—that on the compression side involving an iteration procedure for location of the curved shock portion of the domain boundary. On the compression side, the region of non-zero entropy gradients was determined and the rotationality effect was calculated. A singularity in the entropy along the wing centerline was established.

A method was proposed to yield a close approximation to such exact solutions by means of an adjustment of the linearized solution, based upon a matching of the linearized and exact solutions at the boundary of the apex domain. This method was of considerable help in obtaining the numerical exact solutions and may in its own right serve as an approximate solution of considerably increased accuracy.

For the discontinuous case of the flow over the expansion surface, an approximate method of solution was suggested in which the discontinuity takes the form of a conical shock. This case was investigated experimentally and the results found support the mechanism proposed.

While the linearized theory was found to err considerably in determining perturbation velocity potentials and the analogous rotational flow velocity functions—as much as 34 per cent for a wing having an angle of sweepback of 45° in a flow possessing a free-stream Mach Number of 3 at an angle of attack of 4°—the errors are of opposite sense on the two wing surfaces and are of such a distribution that the integrated effect is of a smaller order (in the case cited the linearized theory underestimated the lift by 2 per cent).

Received May 16, 1955.

† Research Assistant, Institute of Aerophysics.

The author wishes to express his gratitude to A. Robinson and G. N. Patterson for their guidance and counsel during the course of this project. The stimulation and encouragement of discussions with all the staff members of the Institute of Aerophysics and the Department of Applied Mathematics are sincerely appreciated.

The research was supported by the Canadian Defence Research Board.

SYMBOLS

a_0	=	free-stream speed of sound
a	=	local nondimensional speed of sound, Eq. (2.2.1)
$f(X_2X_3)$	=	the perturbation velocity potential, Eq. (2.4.5)
f^*	=	a velocity function, Eq. (4.3.6)
c^*	=	the limiting velocity for the flow in the (r, θ) plane, Eq. (2.3.1)
L, r, θ	=	cylindrical polar coordinates, Fig. 1
M_0	=	free-stream Mach Number
$\bar{M}_2$	=	nondimensional velocity, (flow velocity)/a_0, where a_0 is the free-stream speed of sound
q	=	local total nondimensional velocity, Eq. (2.2.1)
s	=	dependent variable representing entropy, Eq. (4.3.3)
u, v, w	=	nondimensional velocity components along the x_1, x_2, x_3 axes, respectively, Eq. (2.2.1)
x_1, x_2, x_3	=	right-handed Cartesian coordinate system, Fig. 1
X_2, X_3	=	dimensionless conical coordinates, Section (2.2)
α	=	the angle of attack in the (r, θ) plane, Section (2.3)
$\bar{\alpha}$	=	the angle of attack of the free-stream relative to the wing centerline, Eq. (2.4.1)
β	=	angle between M_0 and the leading edge, Section (2.3)
γ	=	ratio of the specific heats of the gas, $\equiv c_p/c_v$
$\bar{\gamma}$	=	semiapex angle, Fig. 1
θ^*	=	angle measured from the normal to a velocity with $M = 1$, Fig. 2
λ	=	ratio, $(\gamma - 1)^{1/2}(\gamma + 1)^{-1/2}$
$\bar{\mu}$	=	Mach angle appropriate to the free stream, Section (2.4)
τ	=	a function of velocity and position, Eq. (4.3.5)
Φ	=	total velocity potential

The subscript notation for differentiation is used such that the partial derivative $(\partial/\partial x)\Phi$ is written $\Phi_{\partial x}$ while the total derivative $(d/dX_2)X_3$ is written X_{3dX_2}.

(1) INTRODUCTION

IN THIS PAPER the principal results are reported of an investigation performed at the Institute of Aero-

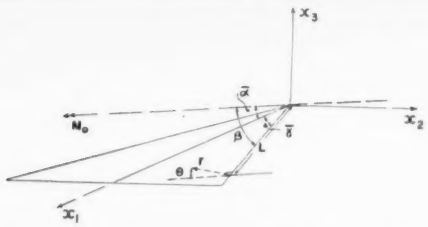

FIG. 1. Coordinate systems and wing geometry.

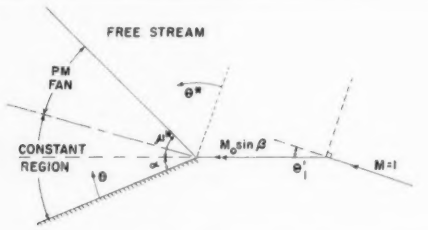

FIG. 2. Flow structure in section perpendicular to leading edge, expansion surface.

physics, and the methods used are indicated. A complete description of the research, including details of the analysis, methods of solution, and experimental procedure, is available as Report #30 of the Institute.[6]

The primary aim of the investigation was to obtain an exact solution of the equations governing steady inviscid supersonic flow with constant stagnation enthalpy about an infinitely thin flat delta wing with supersonic leading edges at a finite angle of attack and zero angle of yaw—a problem in exact cone field theory. In doing so it was hoped that understanding of the nature of more general conical flows would be improved and that methods of general applicability would be developed.

Cone fields[1] are those for which the functions under consideration—velocities, pressure, density, entropy—are homogeneous. In the case under consideration the degree of homogeneity is zero, such that the functions are constant along half lines issuing from the origin of the field.

For such problems the only known exact solution in closed form is that of Taylor and Maccoll under restricted boundary conditions.[2] A numerical method for solving the exact equations in more general cases has been proposed by Maslen.[4]

In exact cone field theory the complete inviscid flow equations are used with no terms neglected, and the actual physical geometry of the problem is retained. The wave systems must be attached at the leading edges in order that the flow be supersonic everywhere and that the boundary conditions be conical.

An exact theory is desirable to define the limits of usefulness of the simpler linearized theories within the tolerable errors and, beyond these limits, to yield the desired information not otherwise obtainable. The elimination of the errors caused by neglect of nonlinearity will permit better understanding of the effects of the remaining factors which have been neglected, such as viscosity, enabling the extraction of more information from a comparison of theory with experiments.

(2) Expansion Surface—Exact Theory

(2.1) *General Flow Structure*

The expansion and compression surfaces may be considered independently because of the supersonic velocity component normal to the leading edge. The flow on the expansion surface was assumed to be continuous and irrotational such that the equation to be solved was the three-dimensional equation in the total velocity potential, Φ,

$$\sum_{i\,j} \Phi_{\partial x_i \partial x_j} \left[\Phi_{\partial x_i}\, \Phi_{\partial x_j} - \delta_{ij} \times \left\{1 + (\gamma - 1)2^{-1}(M_0^2 - \Phi_{\partial x_k}\, \Phi_{\partial x_k})\right\}\right] = 0 \quad (2.1.1)$$

where $i, j, k = 1, 2, 3$. Here δ_{ij} is the Kronecker delta, equal to 1 for $i = j$, equal to zero for $i \neq j$. All velocities are nondimensional, being written as multiples of the free-stream velocity of sound.

Eq. (2.1.1) is of hyperbolic type throughout the region of interest such that the space influenced by any field point is that contained within the characteristic conoid[4, 5] appropriate to Eq. (2.1.1) and issuing from the point. It was seen that the characteristic conoid emanating from the wing apex divided the flow field into two fundamentally different regions. The regions outboard of the conoid are effectively two-dimensional, being free of the influence of the apex, and the flow solution may be obtained as for a yawed infinite wing. The inboard region, contained within the conoid, may be considered as the interaction region for the flows from the leading edges.

(2.2) *The Boundary of the Inboard Region*

The characteristic conoid of a quasilinear second-order partial differential equation, such as Eq. (2.1.1), is in general curvilinear, but reduces to an extension of

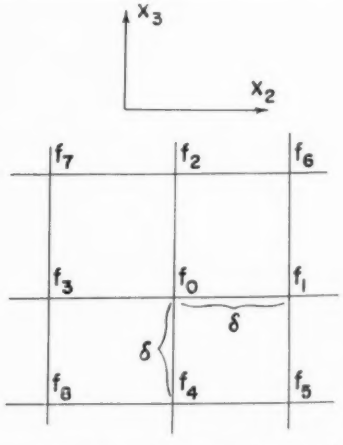

FIG. 3. Numbering of values on finite difference grid, relative to the point f_0 under consideration.

the characteristic (or Monge) cone for the point of its origin[4] when the coefficients of the terms $\Phi_{\partial x_i \partial x_j}$ are constants. In the case of the conoid emanating from the apex of a delta wing, the coefficients are constant along straight lines from the apex since they are functions of the velocities. Hence the characteristic conoid, which originates as an infinitesimal straight line cone from the apex, reduces to the extended Monge cone in this case.

Since the flow properties are independent of distance from the apex in a cone field, the flow is a function only of the ratios $X_2 = x_2/x_1$, $X_3 = x_3/x_1$ where x_1, x_2, x_3 designate a Cartesian coordinate system with x_1 directed in the same general sense as the free-stream velocity. Hence, one may consider the problem in two-dimensional cone-field space, using the conical coordinates X_2, X_3.

It was shown in Reference 6, Appendix I, that, if one considers Eq. (2.1.1) in a cone field of zero degree, the parabolic line (separating the region for which the equation is hyperbolic from that for which it is elliptic) of the equation transformed into conical coordinates is identical with the intersection by a plane of the extended Monge cone from the cone field origin and appropriate to Eq. (2.1.1).

Therefore, the boundary of the inboard region in the X_2, X_3-plane was obtained as the parabolic line of Eq. (2.1.1) thus transformed, and, in this plane, the outboard region is hyperbolic and the inboard region elliptic.

The equation for this boundary is

$$(1 + X_2^2 + X_3^2)(q^2 - a^2) = (u + vX_2 + wX_3)^2 \tag{2.2.1}$$

Here a is the local nondimensional velocity of sound: u, v, w are the nondimensional velocity components appropriate to x_1, x_2, x_3 respectively, and $q = (u^2 + v^2 + w^2)^{1/2}$.

(2.3) *Solution for the Outboard Region*

The flow may be completely described in this region by obtaining the solution in a section perpendicular to the leading edge, the region being effectively a yawed two-dimensional wing. A cylindrical polar coordinate system (L, r, θ) based upon the leading edge was used (Fig. 1), and the velocity component $M_0 \cos \beta$ parallel to the leading edge was superimposed upon a Prandtl-Meyer expansion of the component $M_0 \sin \beta$ through the angle α (see Fig. 2) in a section normal to the leading edge. Here β is the angle between the free-stream velocity and the wing leading edge, while α is the angle between $M_0 \sin \beta$ and the wing trace in the (r, θ) plane.

The limiting velocity c^* for the flow normal to the leading edge was given by

$$(M_0 \sin \beta)^2 + 2(\gamma - 1)^{-1} = c^{*2} \tag{2.3.1}$$

The usual analysis[7] then yielded the velocities in the region of expanding flow

$$\left.\begin{aligned} \Phi_{\partial r} &= c^* \sin(\lambda\theta^*) \\ -r^{-1}\Phi_{\partial\theta} &= c^*\lambda \cos(\lambda\theta^*) \\ \Phi_{\partial L} &= M_0 \cos\beta \end{aligned}\right\} \tag{2.3.2}$$

Here $\lambda = (\gamma - 1)^{1/2}(\gamma + 1)^{-1/2}$ and $\theta^* = (\alpha + (\pi/2) + \theta_1') - \theta$ where θ_1' is the expansion angle required to achieve the velocity $M_0 \sin \beta$ from an initial velocity with $M = 1$. The corresponding velocities u, v, w were then given by

$$\left.\begin{aligned} u &= \Phi_{\partial L}\cos\bar{\gamma} + (c^* \sin\bar{\gamma})[(\tan\bar{\gamma} - X_2)^2 + X_3^2 \sec^2\bar{\gamma}]^{-(1/2)}[(\tan\bar{\gamma} - X_2)\sin(\lambda\theta^*) + X_3\lambda\cos(\lambda\theta^*)\sec\bar{\gamma}] \\ v &= \Phi_{\partial L}\sin\bar{\gamma} + c^*\cos\bar{\gamma}[(\tan\bar{\gamma} - X_2)^2 + X_3^2\sec^2\bar{\gamma}]^{-(1/2)}[(X_2 - \tan\bar{\gamma})\sin(\lambda\theta^*) - X_3\lambda\cos(\lambda\theta^*)\sec\bar{\gamma}] \\ w &= c^*[(\tan\bar{\gamma} - X_2)^2 + X_3^2\sec^2\bar{\gamma}]^{-(1/2)}[X_3\sin(\lambda\theta^*)\sec\bar{\gamma} - (\tan\bar{\gamma} - X_2)\lambda\cos(\lambda\theta^*)] \end{aligned}\right\} \tag{2.3.3}$$

In the constant velocity region below the expansion fan

$$\left.\begin{aligned} u &= \bar{M}_2 \sin\bar{\gamma} + \Phi_{\partial L}\cos\bar{\gamma} \\ v &= -\bar{M}_2\cos\bar{\gamma} + \Phi_{\partial L}\sin\bar{\gamma} \\ w &= 0 \end{aligned}\right\} \tag{2.3.4}$$

where

$$\bar{M}_2 = c^*(\sin^2[\lambda\theta_2^*] + \lambda^2\cos^2[\lambda\theta_2^*])^{1/2}$$

$$\theta_2^* = \alpha + \theta_1' + \tan^{-1}[\lambda^{-1}\tan(\lambda\theta_2^*)]$$

corresponding to the last characteristic of the expansion fan.

(2.4) *The Solution of the Inboard Region*

For the case of a continuous field, the solution for the outboard region applies up to and including the points of the boundary of the inboard region. The velocities given by this outboard solution may therefore be used in the equation specifying the boundary itself and to specify the conditions that must be satisfied there by the inboard solution.

The equation for the boundary [Eq. (2.2.1)] takes three particular forms according to the velocity region of the outboard solution that determines it. The free-stream velocities

$$u = M_0 \cos\bar{\alpha}, \qquad v = 0, \qquad w = M_0 \sin\bar{\alpha}$$

transform Eq. (2.2.1) into

$$(1 + X_2^2 + X_3^2)(1 - M_0^{-2}) = (\cos \bar{\alpha} + X_3 \sin \bar{\alpha})^2 \tag{2.4.1}$$

The velocities of the expansion fan give

$$X_2^2(\Phi_{\partial r}^2 \tan^2 \bar{\gamma} - \Phi_{\partial L}^2) - X_3^2(\Phi_{\partial L}^2 \sec^2 \bar{\gamma}) + 2X_2(\tan \bar{\gamma})(\Phi_{\partial r}^2 + \Phi_{\partial L}^2) + (\Phi_{\partial r}^2 - \Phi_{\partial L}^2 \tan^2 \bar{\gamma}) = 0 \tag{2.4.2}$$

as the boundary equation in that region, while, for the constant velocity region adjacent to the wing, Eq. (2.2.1) becomes

$$[(\bar{M}_2 \tan \bar{\gamma} + \Phi_{\partial L}) + X_2(\Phi_{\partial L} \tan \bar{\gamma} - \bar{M}_2)]^2 = (1 + X_2^2 + X_3^2)(\sec^2 \bar{\gamma})(\Phi_{\partial L}^2 + c^{*2} \sin^2 \{\lambda \theta_2^*\}) \tag{2.4.3}$$

The first and last characteristic lines of the expansion fan are given by $\theta = \alpha + \sin^{-1}(\sin \bar{\mu} \csc \beta)$ and θ_2 (corresponding to θ_2^*), respectively, substituted into

$$\sin \bar{\gamma} - X_2 \cos \bar{\gamma} = X_3 \cot \theta \tag{2.4.4}$$

thus defining the regions of applicability of Eqs. (2.4.1), (2.4.2), and (2.4.3).

Eq. (2.1.1) was written in terms of the conical coordinates and was transformed by the introduction of a perturbation velocity potential

$$f(X_2, X_3) = (\Phi - x_3 M_0 \sin \bar{\alpha})(x_1 M_0 \cos \bar{\alpha})^{-1} - 1 \tag{2.4.5}$$

The differential equation thus obtained was written in finite difference form using the first finite difference approximation with equal increments (δ) in X_2 and X_3, resulting in

$$(f_1 + f_3)[1 - (B^2A^{-1} - X_2^2)] + (f_2 + f_4)[1 - (C^2A^{-1} - X_3^2)] - 2f_0[1 - (B^2A^{-1} - X_2^2) + 1 - (C^2A^{-1} - X_3^2)] + 2^{-1}(f_5 + f_7 - f_6 - f_8)(BCA^{-1} - X_2X_3) = 0 \tag{2.4.6}$$

which holds for the point corresponding to f_0. Here

$$A = \frac{2 + (\gamma - 1)M_0^2}{2M_0^2 \cos^2 \bar{\alpha}} - \frac{\gamma - 1}{2}[f_{\partial X_2}^2 + (\tan \bar{\alpha} + f_{\partial X_2})^2 + (1 + f - X_2 f_{\partial X_2} - X_3 f_{\partial X_3})^2]$$

$$B = X_2(1 + f - X_2 f_{\partial X_2} - X_3 f_{\partial X_3}) - f_{\partial X_2}$$

$$C = X_3(1 + f - X_2 f_{\partial X_2} - X_3 f_{\partial X_3}) - (\tan \bar{\alpha} + f_{\partial X_3})$$

and the subscripts on the function values (f) indicate their relative positions on the finite difference grid (see Fig. 3). The inboard region has been shown to be elliptic [see Section (2.2)] and hence amenable to solution by the relaxation method.[8-12] The point relaxation operator based on the first finite difference approximation was used

$$\begin{array}{ccc} & 1 - (C^2A^{-1} - X_3^2) & \\ & | & \\ 1 - (B^2A^{-1} - X_2^2) & -2\{1 - (B^2A^{-1} - X_2^2) + 1 - (C^2A^{-1} - X_3^2)\} & 1 - (B^2A^{-1} - X_2^2) \\ & | & \\ & 1 - (C^2A^{-1} - X_3^2) & \end{array} \tag{2.4.7}$$

Boundary values for f in the inboard region were provided by the velocity distribution of the outboard solution together with the relationship

$$f = [u - M_0 \cos \bar{\alpha} + X_2 v + X_3(w - M_0 \sin \bar{\alpha})][M_0 \cos \bar{\alpha}]^{-1} \tag{2.4.8}$$

At the wing surface, the condition of zero velocity normal to the wing completed the specification of boundary conditions, yielding $f_{\partial X_3} = -\tan \bar{\alpha}$.

The relaxation method was found to converge quite satisfactorily.

(2.5) *An Example*

The particular case was considered for which $M_0 = 3$, $\gamma = 1.402$, $\bar{\gamma} = 45°$, $\bar{\alpha} = 4°$. The exact boundary of the inboard region as given by Eq. (2.2.1) is shown in Fig. 4, compared with the linearized boundary (the free-stream Mach cone) and has the following physical basis.

The upper segment of the boundary is the top of the Mach cone appropriate to the free-stream velocity (and to the first characteristic of the Prandtl-Meyer fan from the leading edge). The lower segment is a section of the Mach cone appropriate to the resulting expanded (and yawed) velocity corresponding to the last characteristic of the fan. The intervening space may be thought of as occupied by the family of Mach cones appropriate to the intermediate characteristics of the Prandtl-Meyer fan, and the central segment of the boundary is the locus of the points of tangency of these

characteristics to their respective Mach cones.

The f distribution in the apex domain was determined by means of the relaxation method, and a comparison is given in Fig. 5 of the exact and linearized f distributions on the wing expansion surface ($X_3 = 0$).

(3) Expansion Surface—Discontinuous Case

(3.1) The Upper Limit to the Continuous Solution

It was apparent from Fig. 4 that the lower bound to the central segment of the boundary approaches the line of symmetry ($X_2 = 0$) as the angle of attack is increased. For angles of attack such that this point reaches or passes the line $X_2 = 0$ the original assumption of a continuous solution leads to a contradiction. By symmetry, the v component of velocity must be zero on the centerline. By the assumption of continuity, the outboard solution (for which finite v's directed toward the wing centerline are produced by the expansions over the leading edges) applies up to and including the points of the parabolic line. Hence, in the case of the lower bound coincident with or having crossed $X_2 = 0$, the outboard solution specifies two equal and opposite velocities, while symmetry requires zero velocity normal to the plane $x_2 = 0$—i.e., the original assumption of a continuous solution leads to a solution discontinuous at $X_2 = 0$.

The critical condition of the boundary meeting or crossing $X_2 = 0$ is

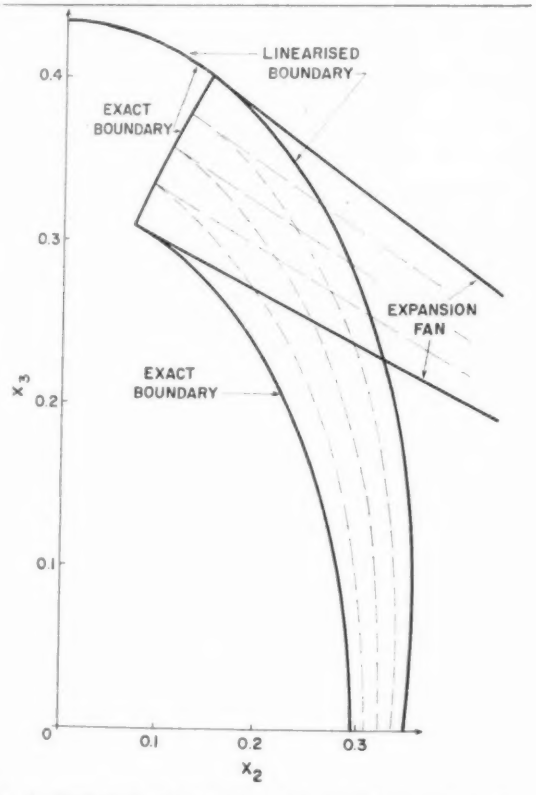

Fig. 4. Boundary of inboard region, expansion surface, for $M_\infty = 3$, $\bar{\alpha} = 4°$, $\bar{\gamma} = 45°$.

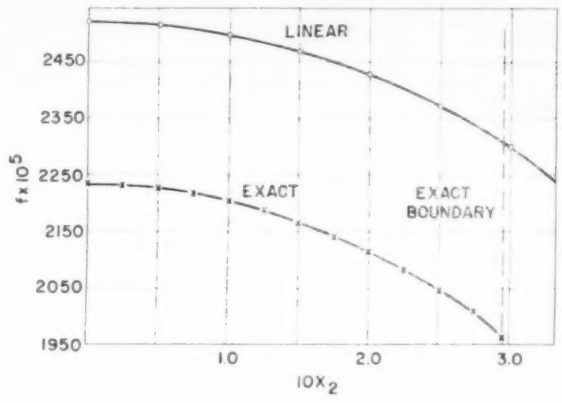

Fig. 5. Comparison of f distributions on the wing expansion surface.

$$\sin(\lambda\theta_2^*)\cos\theta_2 \geq \Phi_{\partial L}\tan\bar{\gamma}\,c^{*\,-1} \qquad (3.1.1)$$

(3.2) An Approximate Method for the Discontinuous Case

The boundary conditions on the flow may be satisfied by a flow containing discontinuities as well as by one which is continuous. Having been informed by the exact analysis that such a discontinuous solution is the only one that can exist above certain angles of attack, one may consider a simplified flow structure of this type and devise an approximate method of solution for the flow adjacent to the wing surface.

The discontinuity was interpreted to be an indication of a shock wave bounding the inboard region of the flow field, replacing in this sense the parabolic line of the continuous case. It was assumed that this inboard shock existed for the purpose of turning the outboard velocity (which is directed towards the wing centerline by the leading edge expansion) into parallelism with the central wing chord (see Fig. 6).

In particular, it was assumed that the shock would be of such a strength as to completely account for the change in direction of the outboard velocity, and that the two-dimensional shock relations could be used to connect the states on either side of the wave. The shock was considered to be planar and normal to the wing surface in the region adjacent to the wing. In the physical case, some of the flow deviation may occur behind the shock rather than being entirely accomplished in the discontinuity. Thus from the assumptions made, one would expect the shock given by theory to provide an upper limit in strength and an outboard limit in position for the shock wave occurring in practice.

While it may be inferred that the shock wave is weakened and dissipated by the interaction with the expansion wave as shown by the dashed line in Fig. 6, only the flow adjacent to the wing was considered in detail.

The flow field adjacent to the wing is thus known. The outboard velocity

$$M_3 = (\bar{M}_2^2 + \Phi_{\partial L}^2)^{1/2}(a_0/a_2) \qquad (3.2.1)$$

at an angle to the centerline of

$$\zeta = \tan^{-1}(\bar{M}_2/\Phi_{\partial L}) - \bar{\gamma} \qquad (3.2.2)$$

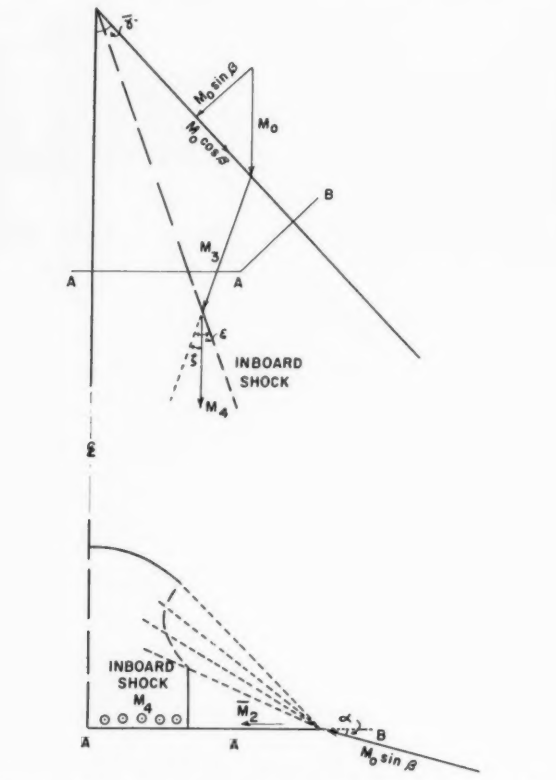

FIG. 6. Flow structure assumed for discontinuous case on the expansion surface.

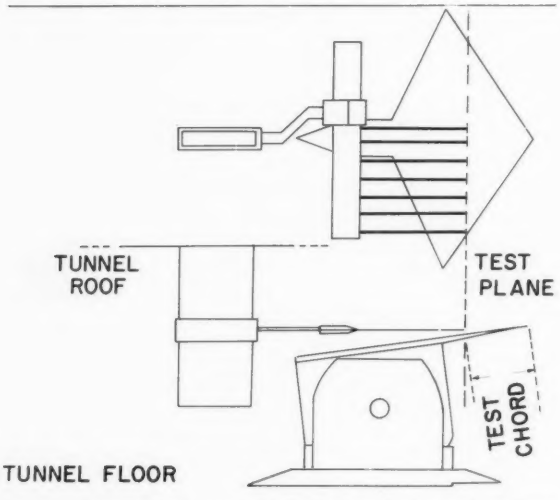

FIG. 7. Schematic diagram of installation of wing and pressure rake in tunnel.

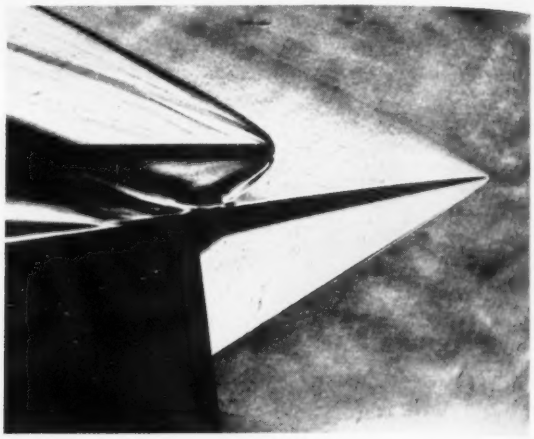

FIG. 8. Schlieren photograph of flow over wing and probes for $M_0 = 2.50$, $\bar{\gamma} = 60°$, $\bar{\alpha} = 8°7'$.

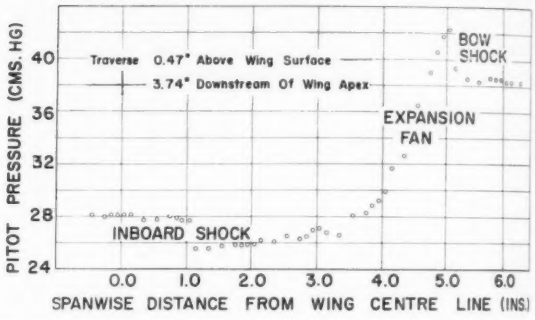

FIG. 9. Spanwise pitot pressure traverse for $M_0 = 2.50$, $\bar{\gamma} = 60°$, $\bar{\alpha} = 10°5'$.

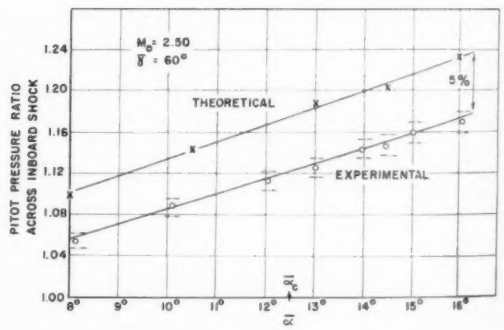

FIG. 10. Variation of inboard shock strength with $\bar{\alpha}$.

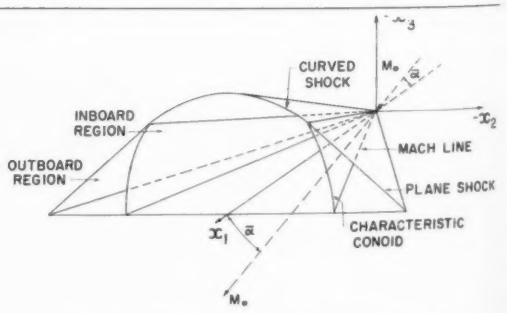

FIG. 11. Flow structure on compression side.

is given by the exact solution. The shock is that two-dimensional shock deflecting M_3 through the angle ζ and, by the assumption of conical flow, passing through the wing apex.

(3.3) *Experimental Investigation*

An experimental study of the flow on the expansion side of a supersonic delta wing was made in the Institute of Aerophysics 16- by 16-in. intermittent wind tunnel at a Mach Number of 2.50.

In particular, it was desired to ascertain (a) whether or not there was a quantitative agreement between the suggested discontinuous (shock) mechanism and that of the physical case [the validity of the method of Section (3.2)], and (b) whether or not there was a sudden transition from the continuous to the discontinuous type of solution in the neighborhood of the critical angle of attack, $\bar{\alpha}_c$, at and above which theory implies that only the discontinuous solution can exist [see Section (3.1)].

A model wing was designed having a flat upper surface, a semi-apex angle of 60°, and a 4.5° wedge angle perpendicular to the leading edge. Detailed pitot pressure surveys were taken throughout the field of flow above the wing for each angle of attack in a range of angles bracketing $\bar{\alpha}_c$, by means of a pitot rake adjustable in three dimensions (see Fig. 7). A schlieren photograph of the flow over the wing and probes is shown in Fig. 8.

It was found that the pressure field did indicate the presence of an inboard shock as predicted (see typical pitot traverse, Fig. 9). The theoretical and experimental strengths of the shocks were plotted (see Fig. 10) in the form of the pitot pressure ratios across them. These ratios agreed within 5 per cent and showed the theoretical values to be in excess of the experimental as expected. No sudden transition from a continuous to a discontinuous flow field was noted in the region of $\bar{\alpha}_c$. The experimental results showed the shock wave to be established at relatively low angles of attack, increasing in strength as the angle increased.

The strength of the inboard shock is quite small, being of the same order as the weak bow shock on the expansion side of the wing. This bow shock is neglected in first-order theories. The method of Section (3.2) is, thus, one considering effects of second-order or smaller in magnitude, and its reasonable agreement with the experimental data indicates that it can give useful results.

(4) Compression Surface—Exact Solution

(4.1) *Boundary of the Inboard Region*

As in the case of the expansion surface, the boundary of the field of influence of the apex was sought to delineate the outboard region, for which the yawed two-dimensional wing solution can be used, from the inboard more complex region (see Fig. 11). The outboard region, below the bow shock, is isentropic such that the potential equation applies. By the assumption of a continuous solution between the wing and the bow shock, the outboard solution applies up to and including the boundary of the inboard region; such that Eq. (2.2.1) again yields this boundary in the region between the wing and the shock.

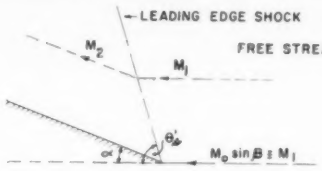

Fig. 12. Plane perpendicular to leading edge, compression side.

The upper, curved shock, segment of the boundary was first estimated by fitting a quadratic to the shock from the leading edge at its intersection by the parabolic line and to a point on $X_2 = 0$ (where the shock slope in the X_2, X_3 plane was assumed to be zero) found by averaging the shock positions corresponding to a flow deviation through the same $\bar{\alpha}$ by a right circular cone and a two-dimensional wedge. The accuracy of this segment was later improved by an iteration process in conjunction with the relaxation solution of the inboard region.

(4.2) *Solution for the Outboard Region*

A section perpendicular to the leading edge was considered in which the shock angle θ_s' as measured from $M_0 \sin\beta$ (see Fig. 12) was found from

$$\theta_s' = \sin^{-1}\left\{(M_0 \sin\beta)^{-2}[\sin\theta_s' - 2^{-1}(\gamma+1)\sin\alpha\sec(\theta_s' - \alpha)]^{-1}\right\} \quad (4.2.1)$$

which gave satisfactory convergence. The angle between the shock and the wing is then $\theta_s = \theta_s' - \alpha$ such that the equation of the leading-edge shock is

$$X_3 = -(1 + X_2)\sin\bar{\gamma}\tan\theta_s$$

The Mach Number of the velocity after the shock in the plane normal to the leading edge was given by

$$M_2 = 2^{1/2}(\csc\theta_s)[(\gamma+1)\tan\theta_s'\cot\theta_s - (\gamma-1)]^{-(1/2)}$$

and expressed in terms of the free-stream velocity of sound in the form

$$\bar{M}_2 = [2 + (M_0\sin\beta)^2(\gamma-1)]^{1/2} \times [2 + M_2^2(\gamma-1)]^{-(1/2)} M_2$$

The outboard velocity components u, v, w were then known as

$$\begin{aligned} u &= \Phi_{\partial L}\cos\bar{\gamma} + M_2\sin\bar{\gamma} \\ v &= \bar{M}_2\cos\bar{\gamma} - \Phi_{\partial L}\sin\bar{\gamma} \\ w &= 0 \end{aligned}$$

Substitution of these into Eq. (2.2.1) yielded the parabolic line segment of the inboard boundary.

$$X_3 = \left\{ \begin{matrix} [(\Phi_{\partial L} \cos \bar{\gamma} + \bar{M}_2 \sin \bar{\gamma}) - (\Phi_{\partial L} \sin \bar{\gamma} - \bar{M}_2 \cos \bar{\gamma}) X_2]^2 \times \\ \{2^{-1}\bar{M}_2^2(\gamma+1) + 2^{-1}M_0^2[(\gamma+1)\cos^2\beta - (\gamma-1)] - 1\}^{-1} \\ - [1 + X_2^2] \end{matrix} \right\}^{1/2}$$

(4.3) *Equations Governing the Inboard Region*

The equation of motion in conical coordinates for rotational adiabatic flow, the stagnation enthalpy being assumed constant, yielded the set

$$v(X_2 v_{\partial X_2} + X_3 v_{\partial X_3} + u_{\partial X_3}) + w(X_2 w_{\partial X_2} + X_3 w_{\partial X_3} + u_{\partial X_3}) = -a^2(X_2 s_{\partial X_2} + X_3 s_{\partial X_3}) \tag{4.3.1}$$

$$u(X_2 v_{\partial X_2} + X_3 v_{\partial X_3} + u_{\partial X_2}) + w(w_{\partial X_2} - v_{\partial X_3}) = -a^2 s_{\partial X_2} \tag{4.3.2}$$

$$u(X_2 w_{\partial X_2} + X_3 w_{\partial X_3} + u_{\partial X_3}) + v(v_{\partial X_3} - w_{\partial X_2}) = -a^2 s_{\partial X_3} \tag{4.3.3}$$

where

$$s = S[(\gamma - 1)\gamma c_v]^{-1}$$

S being the entropy and c_v the specific heat of the gas at constant volume.

The equations of energy and continuity were combined to yield

$$a^2(v_{\partial X_2} + w_{\partial X_3} - X_2 u_{\partial X_2} - X_3 u_{\partial X_3}) = 2^{-1}[(v - uX_2)(\partial/\partial X_2) + (w - uX_3)(\partial/\partial X_3)](u^2 + v^2 + w^2) \tag{4.3.4}$$

The determination of the flow in the inboard region then required the solution of this set of four first-order partial differential equations for the four dependent variables u, v, w, s.

The equation of the isentropic lines was seen to be

$$(v - uX_2)s_{\partial X_2} + (w - uX_3)s_{\partial X_3} = 0$$

and a quantity τ was defined as follows:

$$\tau \equiv \left\{ \frac{-(v - uX_2)}{(w - uX_3)} = \frac{s_{\partial X_2}}{s_{\partial X_3}} = (-X_{2\,dX_3})_{s\,=\,\text{const.}} \right\} \tag{4.3.5}$$

A velocity function f^* was defined as

$$f^* = [u - M_0 \cos \bar{\alpha} + X_2 v + X_3(w - M_0 \sin \bar{\alpha})][M_0 \cos \bar{\alpha}]^{-1} \tag{4.3.6}$$

and the following notation was introduced for convenience in writing:

$$U^* = (1 + f^* - X_2 f_{\partial X_2}{}^* - X_3 f_{\partial X_3}{}^*)$$

$$A^* = [2 + (\gamma - 1)M_0^2](2M_0^2 \cos^2 \bar{\alpha})^{-1} - 2^{-1}(\gamma - 1)[f_{\partial X_2}{}^{*2} + (\tan \bar{\alpha} + f_{\partial X_3}{}^*)^2 + U^{*2}]$$

$$\begin{aligned} B^* &= (X_2 U^* - f_{\partial X_2}{}^*) \\ C^* &= (X_3 U^* - f_{\partial X_3}{}^* - \tan \bar{\alpha}) \\ N &= (B^* + \tau C^*) \\ E &= (X_2 + \tau X_3) \end{aligned} \qquad \begin{aligned} L^* &= 1 + EX_2 \\ M^* &= \tau + EX_3 \\ H &= 1 + \tau^2 + E^2 \end{aligned}$$

The inboard velocities were then given by

$$\begin{aligned} u &= (M_0 \cos \bar{\alpha})[U^* - ENH^{-1}] \\ v &= (M_0 \cos \alpha)[f_{\partial X_2}{}^* + NH^{-1}] \\ w &= (M_0 \cos \bar{\alpha})[\tan \bar{\alpha} + f_{\partial X_3}{}^* + \tau NH^{-1}] \end{aligned}$$

The combination of these relations with Eq. (4.3.4) yielded one of two final governing equations,

$$f_{\partial X_2 \partial X_2}{}^*(1 + X_2{}^2 - B^{*2}A^{*-1}) + f_{\partial X_3 \partial X_2}{}^*(1 + X_3{}^2 - C^{*2}A^{*-1}) + 2f_{\partial X_2 \partial X_3}{}^*(X_2X_3 - B^*C^*A^{*-1}) = (A^*H^3)^{-1}[G_0(f^*, \tau) + G_1(f^*, \tau) + G_2(f^*, \tau) + G_3(f^*, \tau)] \tag{4.3.7}$$

where

$$G_0(f^*, \tau) \equiv (H^2A^*) \left\{ \begin{matrix} f_{\partial X_2 \partial X_2}{}^*(L^{*2}) + f_{\partial X_3 \partial X_3}{}^*(M^*)^2 \\ + f_{\partial X_2 \partial X_3}{}^*(2L^*M^*) - \tau_{\partial X_2}(L^*C^*) \\ - \tau_{\partial X_3}(M^*C^*) - HU^* \end{matrix} \right\}$$

$$G_1(f^*, \tau) \equiv (NH) \left\{ \begin{matrix} f_{\partial X_2 \partial X_2}{}^*(-2B^*HL^*) - f_{\partial X_2 \partial X_3}{}^*(2C^*HM^*) \\ -f_{\partial X_3 \partial X_3}{}^*(2H)(M^*B^* + C^*L^*) \\ +\tau_{\partial X_2}[H(B^*C^* - A^*X_2X_3) + 2M^*L^*A^*] \\ + \tau_{\partial X_3}[H(C^{*2} - A^*[1 + X_3{}^2]) + 2M^{*2}A^*] \\ + [A^*HE] \end{matrix} \right\}$$

$$G_2(f^*, \tau) \equiv (N^2H)\begin{Bmatrix} f_{\partial X_2 \partial X_2}{}^*[L^{*2}2^{-1}(\gamma+1) - 2^{-1}(\gamma-1)H(1+X_2^2)] \\ +f_{\partial X_3 \partial X_3}{}^*[M^{*2}2^{-1}(\gamma+1) - 2^{-1}(\gamma-1)H(1+X_3^2)] \\ +2f_{\partial X_2 \partial X_3}{}^*[M^*L^*2^{-1}(\gamma+1) - 2^{-1}(\gamma-1)HX_2X_3] \\ +\tau_{\partial X_2}[-B^*M^* - 2^{-1}C^*L^*(\gamma+1)] \\ +\tau_{\partial X_3}[-M^*C^*2^{-1}(\gamma+3)] - H[2^{-1}U^*(\gamma-1)] \end{Bmatrix}$$

$$G_3(f^*, \tau) \equiv (N^3)\begin{Bmatrix} \tau_{\partial X_2}[\gamma M^*L^* - 2^{-1}(\gamma-1)HX_2X_3] \\ +\tau_{\partial X_3}[\gamma M^{*2} - 2^{-1}(\gamma-1)H(1+X_3^2)] \\ +H[2^{-1}E(\gamma-1)] \end{Bmatrix}$$

In the case of irrotational flow f^*, A^*, B^*, C^* reduce to f, A, B, C, respectively, τ reduces to $-BC^{-1}$, and N, $G_0(f^*, \tau)$, $G_1(f^*, \tau)$, $G_2(f^*, \tau)$, $G_3(f^*, \tau)$ all vanish such that Eq. (4.3.7) reduces to the equation in the perturbation velocity potential, f, as used on the expansion surface. Thus, the magnitude of N provides a measure of the departure of the flow from irrotationality. The magnitudes of the $G_i(f^*, \tau)$ are indicated by the occurrence in each of the factor N^i. Since N is commonly $\ll 1$, the magnitudes of the $G_i(f^*, \tau)$ may be expected to decrease rapidly for increasing values of i. The possibility is, thus, provided—in solving the inboard region by a method of successive approximations—of using the irrotational solution as the first approximation and regarding the $G_i(f^*, \tau)$ as rotationality correction terms of successively higher order. While the inclusion of all these terms will yield an exact solution, labor may be saved by neglecting those $G_i(f^*, \tau)$ which are of too small a magnitude to affect the accuracy desired.

Eq. (4.3.7) represents the combination of three relations obtained from the governing four. For the remaining available condition, Eq. (4.3.2) itself was chosen and written in terms of f^* and τ to become

$$\sum_0^6 K_i\tau^i + \sum_0^3 (k_i\tau_{\partial X_2} + \bar{k}_i\tau_{\partial X_3})\tau^i = 0 \quad (4.3.8)$$

where

$$K_0 \equiv [(\bar{X}_2{}^2 s_{\partial X_2})(\bar{X}_2 A^* + \tilde{\gamma}B^{*2}) - B^*\bar{X}_2\tilde{A} - \bar{F}_{1,1}\bar{J}]$$

$$K_1 \equiv \begin{Bmatrix} (2\bar{X}_2 s_{\partial X_2})(3X_2X_3\bar{X}_2A^* + B^*\bar{H}_{1,2}\tilde{\gamma}) - B^*\bar{X}_2\tilde{C} \\ -\bar{H}_{1,2}\tilde{A} + \bar{E}_{1,1}\bar{J} - \bar{F}_{1,1}\bar{K} \end{Bmatrix}$$

$$K_2 \equiv \begin{Bmatrix} s_{\partial X_2}[3\bar{X}_2\bar{I}_{1,4}A^* + (\bar{H}_{1,2}{}^2 + 2B^*\bar{X}_2\bar{G}_{1,2})\tilde{\gamma}] \\ -B^*\bar{X}_2\tilde{B} - \bar{H}_{1,2}\tilde{C} - \bar{G}_{1,2}\tilde{A} + \bar{E}_{1,1}\bar{K} - \bar{F}_{1,1}\bar{L} \end{Bmatrix}$$

$$K_3 \equiv \begin{Bmatrix} 2s_{\partial X_2}[2X_2X_3\bar{I}_{3,2}A^* + (B^*C^*\bar{X}_2\bar{X}_3 + \bar{G}_{s,2}\bar{H}_{1,2})\tilde{\gamma}] \\ -\bar{H}_{1,2}\tilde{B} - \bar{G}_{1,2}\tilde{C} - C^*\bar{X}_3\tilde{A} + \bar{E}_{1,1}\bar{L} - \bar{F}_{1,1}\bar{M} \end{Bmatrix}$$

$$K_4 \equiv \begin{Bmatrix} s_{\partial X_2}[3\bar{X}_3\bar{I}_{1,4}A^* + (\bar{G}_{1,2}{}^2 + 2C^*\bar{X}_3\bar{H}_{1,2})\tilde{\gamma}] - \bar{G}_{1,2}\tilde{B} \\ -C^*\bar{X}_3\tilde{C} + \bar{E}_{1,1}\bar{M} + \bar{F}_{1,1}\bar{N} \end{Bmatrix}$$

$$K_5 \equiv \begin{Bmatrix} 2\bar{X}_3 s_{\partial X_2}(3X_2X_3\bar{X}_3A^* + C^*\bar{G}_{1,2}\tilde{\gamma}) - C^*\bar{X}_3\tilde{B} \\ -\bar{E}_{1,1}\bar{N} \end{Bmatrix}$$

$$K_6 \equiv s_{\partial X_2}\bar{X}_3{}^2(\bar{X}_3A^* + C^{*2}\tilde{\gamma})$$

and

$$k_0 \equiv -B^*\bar{X}_2\bar{F}_{1,1} \qquad \bar{k}_0 \equiv \bar{F}_{1,1}\bar{F}_{1,2}$$
$$k_1 \equiv \bar{X}_2(B^*\bar{E}_{1,1} - 2C^*\bar{F}_{1,1}) \qquad \bar{k}_1 \equiv -(\bar{E}_{1,1}\bar{F}_{1,2} + 2B^*\bar{X}_3\bar{F}_{1,1})$$
$$k_2 \equiv (2C^*\bar{X}_2\bar{E}_{1,1} + \bar{E}_{1,2}\bar{F}_{1,1}) \qquad \bar{k}_2 \equiv \bar{X}_3(2B^*\bar{E}_{1,1} - C^*\bar{F}_{1,1})$$
$$k_3 \equiv -\bar{E}_{1,1}\bar{E}_{1,2} \qquad \bar{k}_3 \equiv C^*\bar{X}_3\bar{E}_{1,1}$$

while

$$\tilde{A} \equiv U^* + X_2 f_{\partial X_2}{}^* \qquad \tilde{G}_{l,m} \equiv lB^*\bar{X}_3 + mC^*X_2X_3$$
$$\tilde{B} \equiv U^* + X_3(f_{\partial X_3}{}^* + \tan\bar{\alpha}) \qquad \bar{H}_{l,m} \equiv lC^*\bar{X}_2 + mB^*X_2X_3$$
$$\tilde{C} \equiv X_3 f_{\partial X_2}{}^* + X_2(f_{\partial X_3}{}^* + \tan\bar{\alpha}) \qquad \bar{I}_{l,m} \equiv l\bar{X}_2\bar{X}_3 + m(X_2X_3)^2$$
$$\bar{E}_{l,m} \equiv lB^*\bar{X}_3 - mC^*X_2X_3 \qquad \bar{J} \equiv \bar{X}_2(X_2X_3 f_{\partial X_3 \partial X_3}{}^* + \bar{X}_2 f_{\partial X_3 \partial X_3}{}^*)$$
$$\bar{F}_{l,m} \equiv lC^*\bar{X}_2 - mB^*X_2X_3 \qquad \bar{K} \equiv (\bar{I}_{1,2} f_{\partial X_3 \partial X_3}{}^* - \bar{X}_2{}^2 f_{\partial X_2 \partial X_2}{}^* + 2X_2X_3\bar{X}_2 f_{\partial X_3 \partial X_3}{}^*)$$
$$\bar{X}_2 \equiv 1 + X_2^2$$
$$\bar{X}_3 \equiv 1 + X_3^2$$
$$\tilde{\gamma} \equiv 2^{-1}(\gamma - 1)$$

The system of equations to be solved thus consists of Eqs. (4.3.7) and (4.3.8) for the two dependent variables f^* and τ. The boundary values for the inboard region were obtained by substituting the outboard velocities into Eq. (4.3.6). $f_{\partial X_3}{}^*$ at the wing surface was taken to be $= -\tan\bar{\alpha}$ in accordance with the assumption of an isentropic region of infinitesimal depth associated with the stream surface represented by the wing.

The procedure chosen to satisfy this system was numerical and iterative. A first approximation was made for τ,

$$\tau^{(0)} = (f_{\partial X_2}{}^* - X_2 U^*)(X_3 U^* - f_{\partial X_3}{}^* - \tan \bar{\alpha})^{-1} \tag{4.3.9}$$

and Eq. (4.3.7) was solved under this assumption (being thus reduced to a form identical with the irrotational equation for the perturbation velocity potential), yielding the first approximation $f^{*(1)}$. The values $s_{\partial X_2}{}^{(0)}$ and the coefficients of τ in Eq. (4.3.8) were calculated from the $f^{*(1)}$ solution and this equation solved for improved values, $\tau^{(1)}$. The $\tau^{(1)}$, $f^{*(1)}$ values were then used to calculate the functions $G_i(f^*, \tau)$, thus obtaining corrections to the residuals found in the relaxation solution of Eq. (4.3.7) and leading to the next approximation $f^{*(2)}$. The cycle is then free to continue with an improvement of the solution of Eq. (4.3.8), and so on, until convergence to the desired accuracy is obtained.

(4.4) *The Adjusted Linearized Solution*

It is important in such a numerical procedure to select the best available approximation as a starting solution. It was noted from Fig. 5 that the discrepancy between the exact and linearized solutions in the apex domain is almost entirely a matter of translating the f curve with only a slight change in shape. Therefore, one can obtain a close approximation to the exact solution in this domain by translating the linearized solution parallel to the f axis until it matches the exact solution at the boundary of the inboard region.

The linearized methods of solution—e.g., reference 13—use a coordinate system $\bar{x}_1$, $\bar{x}_2$, $\bar{x}_4$ in which one of the axes ($\bar{x}_1$, say) is coincident with the free-stream velocity. To compare the exact and linearized solutions one must consider the latter in a plane normal to the wing chord, and translate the line $\bar{X}_3 = 0$ (the assumed wing position in linearized theory) to coincide with the line $X_3 = 0$ (the actual wing position). The resulting relationships between the coordinates are

$$\left.\begin{aligned} X_2{}^* &= \bar{x}_2(\bar{x}_1 \tan \bar{\mu})^{-1} = X_2 \cot \bar{\mu} \times (\cos \bar{\alpha} + X_3 \sin \bar{\alpha})^{-1} \\ X_3{}^* &= \bar{x}_3(\bar{x}_1 \tan \bar{\mu})^{-1} = \cot \bar{\mu} \times \left[\tan \bar{\alpha} + \left(\frac{X_3 \cos \bar{\alpha} - \sin \bar{\alpha}}{\cos \bar{\alpha} + X_3 \sin \bar{\alpha}}\right)\right] \end{aligned}\right\} \tag{4.4.1}$$

such that

$$f = (M_0{}^{-1} \sec \bar{\alpha}) \left\{\begin{matrix} u(\cos \bar{\alpha} + X_3 \sin \bar{\alpha}) \\ + vX_2 + w(X_3 \cos \bar{\alpha} - \sin \bar{\alpha}) \\ - M_0(X_3 \sin \bar{\alpha} + \cos \bar{\alpha}) \end{matrix}\right\} \tag{4.4.2}$$

These permit calculation of the linearized values of f [or $f^{*(1)}$] at the points desired in the X_2, X_3 field. Here $\bar{u}$, $\bar{v}$, $\bar{w}$ are the linearized velocity components along the $\bar{x}_1$, $\bar{x}_2$, $\bar{x}_3$ axes, respectively.

The linearized solution for f was plotted along grid lines X_2 = constant, X_3 = constant and the values of f (linear), extrapolated if necessary, were noted at intersections with the exact boundary of the inboard region. The f (linear) values of each grid line were then increased by the quantity [f(exact) − f(linear)] as evaluated at the point of intersection by the boundary. A "smoothing" of these values gave the starting solution.

(4.5) *Solution of the Inboard Region*

The relaxation method was applied to the solution of Eq. (4.3.7), the relaxation operator being of the same form as Eq. (2.4.7). With the elimination of residuals on the chosen finite difference grid, the position of the shock segment of the boundary was improved. An iteration procedure was proposed, starting from the known point at the parabolic-line - leading-edge shock intersection. For a specified X_2 a pair of values X_3 and X_{3dX_2} were found for the shock trace in the X_2, X_3 plane, matching the relaxation field with the free stream across the shock and satisfying a finite difference equation relating them to the preceding points of the shock boundary.

When the new boundary position was thus found, new residuals were calculated and eliminated and the boundary position again improved. With the convergence of this cycle for a given grid size, accuracy was increased by repeating the cycle on a refined grid.

When the degree of accuracy obtained in this process was sufficient to raise the question of rotationality effects, the solution of Eq. (4.3.8) as a boundary value problem in τ was considered. The first approximation for τ was calculated throughout the field (as $-B^* C^*$ from the distribution obtained in the relaxation process. The boundary values of τ were given by the velocities of the outboard solution, those for the shock boundary segment being approximate to the same order as the location of the boundary.

The entropy distribution throughout the field was obtained by calculating the entropy distribution along the curved shock and plotting the isentropes from it into the field. The isentropes were plotted by means of the τ distribution which gave their slopes at every point in the field. Entropy, S, was defined by the form

$$JdS = JT^{-1}di^* - (g^*\rho T)^{-1}dp$$

such that the change in entropy across the shock boundary was given by[14]

$$\Delta s = [\gamma(\gamma - 1)]^{-1} \left\{\begin{matrix} \ln [(2\gamma q_\nu{}^2 - \gamma + 1)(\gamma + 1)^{-1}] \\ + \gamma \ln [(2 + \{\gamma - 1\} q_\nu{}^2)(\gamma + 1)^{-1} q_\nu{}^{-2}] \end{matrix}\right\}$$

Here q_ν is the free-stream velocity component normal to the shock surface, J is the mechanical equivalent of heat, T is absolute temperature, p is pressure, ρ is density, g^* is the acceleration of gravity and i^* is the enthalpy.

The exact values of τ were known on the lines $X_2 = 0$ and $X_3 = 0$ from its definition in terms of the velocity components, being 0 and ∞, respectively. This expresses the fact that for $X_2 = 0$ the isentrope is normal to the wing while for $X_3 = 0$ it is parallel to the wing, and all the isentropic lines bearing different values of entropy pass through the same point ($X_2 = 0$, $X_3 = 0$) representing

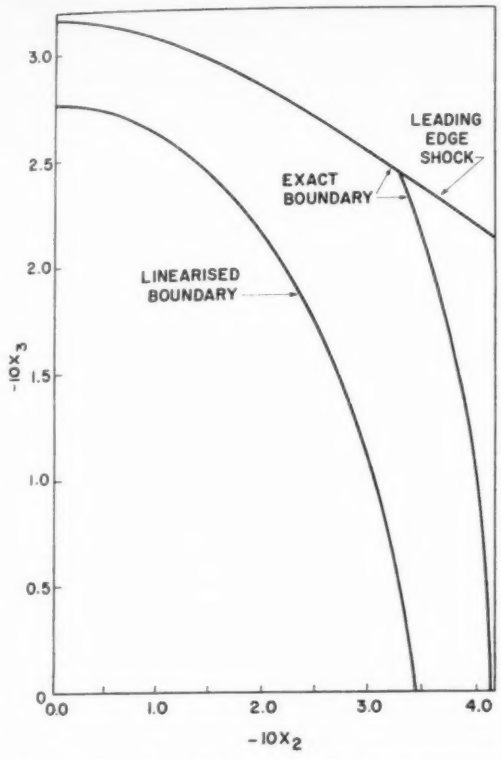

FIG. 13. The boundary of the inboard region on the compression surface for $M_0 = 3$, $\bar{\gamma} = 45°$, $\bar{\alpha} = 4°$.

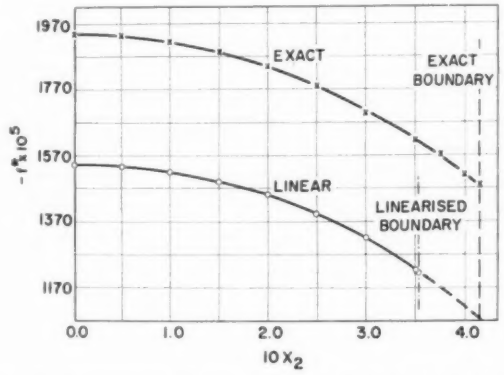

FIG. 15. Comparison of linear with exact f^* distribution on compression surface of wing for $M_0 = 3$, $\bar{\gamma} = 45°$, $\bar{\alpha} = 4°$.

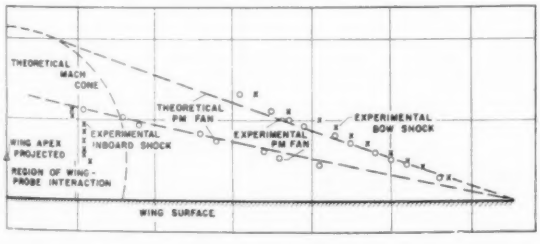

FIG. 17. Composite plot showing wave structure above the wing for $M_0 = 2.50$, $\bar{\gamma} = 60°$, $\bar{\alpha} = 8°7'$ (typical of the range $8° \leq \bar{\alpha} \leq 16°$) in a plane perpendicular to the free stream.

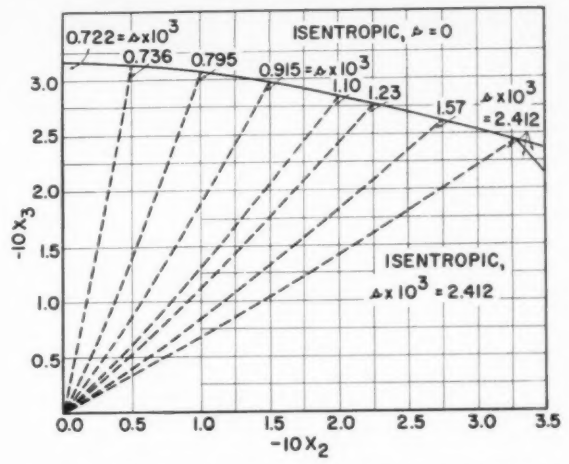

FIG. 14. Isentropes through the inboard region appropriate to the $f^{*(1)}$ solution for $M_0 = 3$, $\bar{\gamma} = 45°$, $\bar{\alpha} = 4°$.

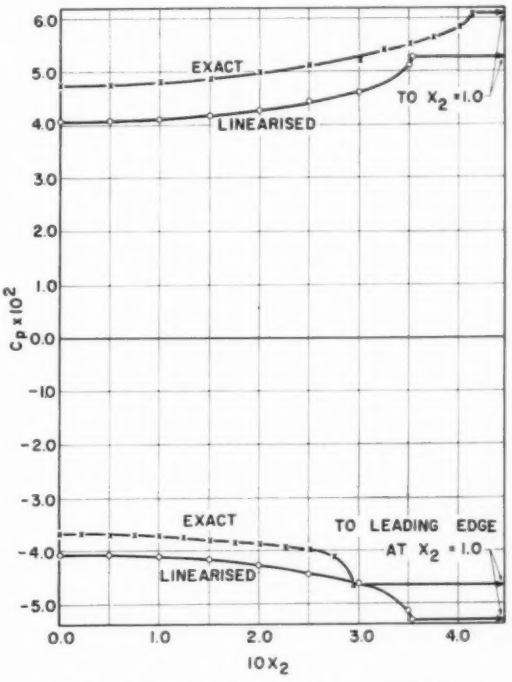

FIG. 16. The linearized and exact C_p distributions.

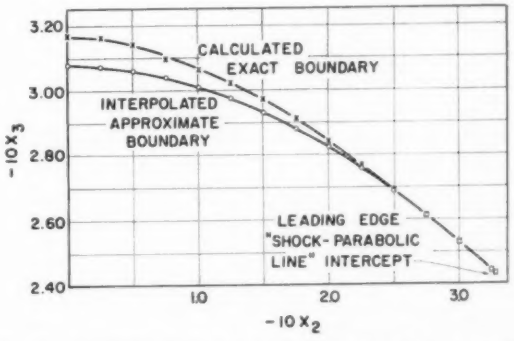

FIG. 18. Comparison of the quadratic boundary of Section (4.1) with the exact boundary.

the wing centerline—a singular line with respect to entropy.† The central region of non-zero entropy gradients in which Eq. (4.3.8) must be solved is, thus, a curvilinear triangle bounded by $X_2 = 0$, the shock boundary segment and the isentrope proceeding from the parabolic line–leading-edge shock intersection to the wing centerline.

A relaxation method was considered for the solution of Eq. (4.3.8) and residuals were calculated using the first finite difference approximation with a square grid. The elimination of these residuals yields a $\tau^{(1)}$ distribution satisfying Eq. (4.3.8), allowing calculation of corrections to the residuals for Eq. (4.3.7) and the repetition of the cycle.

(4.6) *An Example*

For $\bar{\alpha} = 4°$, $\bar{\gamma} = 45°$, $M_0 = 3$, $\gamma = 1.402$ as on the expansion side, the solution was calculated. The linearized and exact boundaries of the inboard region for this case are shown in Fig. 13. In the case of Eq. (4.3.8) the relaxation operator based on the first finite difference approximation did not give satisfactory convergence and a graphical method was used to eliminate the residuals. A modified method of attack was indicated, such as a relaxation operator based upon a higher order finite difference approximation. The region of non-zero entropy gradients and plots of several isentropes are shown in Fig. 14.

The residuals for Eq. (4.3.7) were calculated to the nearest 1×10^{-5}. For a particular field point, the contributions to the residuals of the $G_i(f^*, \tau)$ terms were -1.2783×10^{-5} for $i = 0$, 4.8304×10^{-6} for $i = 1$, 5.1442×10^{-9} for $i = 2$, and 1.2670×10^{-11} for $i = 3$, illustrating the negligible order of magnitude of the higher order rotationality correction terms.

A comparison of the linearized and exact f^* distributions on the wing surface in the apex domain is shown in Fig. 15.

(5) The Exact and Linearized Solutions Compared

The magnitude of the f (or f^*, as applicable) values as calculated by the linearized theory is seen from Figs. 5 and 15 to be, on the average, 13 per cent too high in the apex domain on the expansion surface and 32 per cent too low in the same region on the compression surface of the wing.

When the linearized solution is translated parallel to the f (or f^*) axis until it matches the exact solution at the exact boundary of the inboard region, Section (4.4), quite good agreement with the exact solution is obtained (see Figs. 5 and 15). This indicates that the main part of the error made by the linearized solution is due to the approximation of the boundary conditions on the inboard region rather than to the approximation of the governing equations.

† Subsequent to the submission of this paper it has been brought to the attention of the author that such entropy singularities are discussed in Volume VI, Chapter H 15, of the Princeton Series, "High Speed Aerodynamics and Jet Propulsion."

The comparison between the exact C_p and the ordinary linearized C_p is given in Fig. 16 for both wing surfaces. The linearized magnitudes in the apex domain average 11 per cent greater than the exact on the expansion surface and 16 per cent less on the compression surface. The relatively better agreement of the C_p values, considering that shown for the f (or f^*) values, is due to the manner in which the latter functions enter into the equations determining C_p. Finally, the relative distribution of the linearized and exact C_p values is such that the integrated areas to determine lift differ by 2 per cent, the linearized values showing an underestimation by this amount.

(6) The Methods Reviewed

The "inboard shock model" of Section (3.2) provides a simple solution considering second-order effects on the expansion surface of the wing. The experimental results indicate that the actual flow mechanism is reasonably well described (see Fig. 17).

The "adjusted linearized solution" of Section (4.4) permits the attainment of a solution very near the exact by the relatively simple procedure of calculating the exact outboard solution and the usual linearized solution. A further refinement results from the accumulation of exact solutions which provide an empirical factor, k^*, capable of matching the f (or f^*) distributions at the field centerline as well as at the boundary, the example considered indicating $k^* = -0.24$ on the expansion surface and $k^* = -0.31$ on the compression surface. The improved value for f (or f^*) along a line $X_2 =$ constant is then

$$f = f_{\text{linear}}\{1 + \Delta f_b[1 + k^* X_{2b}^{-1}(X_{2b} - X_2)]\}$$

Δf_b is $(f_{\text{exact}} - f_{\text{linear}})\,(f_{\text{linear}})^{-1}$ evaluated at the boundary and X_{2b} is the boundary intersection coordinate.

Similarly, an empirical factor arises to improve the initial shock boundary estimate. The wedge-cone arithmetic mean of Section (4.1) is shown with the calculated boundary in Fig. 18, and it is noted that weighting the average in favor of the wedge in a 3 to 2 ratio would have given much better agreement.

While considerable labor was required to calculate the rotationality corrections, it is apparent from the example considered that for many purposes one would not be concerned with this, the magnitude of the corrections being small. On the other hand, the exact f and f^* (uncorrected for rotationality) distributions are reasonably easy to obtain.

References

[1] Busemann, A., *Infinitesimal Conical Supersonic Flow*, NACA TM 1100, 1947.

[2] Taylor, G. I., and Maccoll, J. W., *The Air Pressure Over a Cone Moving At High Speeds*, Proc. Roy. Soc. (London), A, Vol. 139, No. 838, pp. 278–311, February, 1933.

[3] Maslen, S. H., *Supersonic Conical Flow*, NACA TN 2651, March, 1952.

[4] Webster, A. G., *Partial Differential Equations Of Mathematical Physics*, G. E. Stechert & Co., New York, 1933.

(*Continued on page 770*)

The Integrated Use of Analog and Digital Computing Machines for Aircraft Dynamic Load Problems†

BERNARD MAZELSKY‡ AND ROBERT F. O'CONNELL††

Lockheed Aircraft Corporation

SUMMARY

This paper describes the techniques and methods used in investigating aircraft dynamic loads problems such as vibration, flutter, gust loads, taxi and landing loads, based on an integration of both analog and digital facilities to provide maximum information on a problem in a minimum of time with a guarantee that the results are correct. The last requirement is an important consideration since high-speed computing machines not only provide the possibility of investigating far more complex dynamic problems but, unfortunately, also extend the probability of introducing errors due to the additional complexities of the problem.

The advantages and disadvantages of both the digital and analog computers in terms of the requirements specified for the aircraft dynamic problems are discussed; a method of analysis is suggested using the best features of each in a closely integrated manner. Numerous examples are presented of several dynamic loads problems for typical air frame configurations.

SYMBOLS

h = bending deflection, positive down
α = torsional deflection, positive leading edge up
y = spanwise coordinate
$b'/2$ = exposed wing semispan
η^* = normalized span coordinate, $2y/b'$
c = local chord
$\bar{c}$ = reference chord (usually taken as mean aerodynamic chord)
ρ = density of air
V = forward velocity of wing
ω = circular frequency
k_1 = reduced frequency $[k_1 = (\omega\bar{c}/V)]$
l = running load, positive down
l' = concentrated load, positive down
L = accumulated load, positive down
t = running torque, positive leading edge up
t' = concentrated torque, positive leading edge up
T = accumulated torque, positive leading edge up
M = bending moment
GJ = torsional stiffness parameter
EI = bending stiffness parameter
μ = running mass
r = radius of gyration
e_A = distance from elastic axis to center of gravity in chords, positive aft
P_α = aerodynamic lift coefficient due to torsional deflection
P_h = aerodynamic lift coefficient due to bending deflection
T_α = aerodynamic torque coefficient due to torsional deflection
T_h = aerodynamic torque coefficient due to bending deflection
λ = nondimensional eigenvalue parameter defined by Eq. (13)
g_s = structural damping parameter
$[A_{\alpha\alpha}]$, $[A_{\alpha h}]$, $[A_{h\alpha}]$, $[A_{hh}]$ = aeroelastic matrices defined by Eqs. (11), (12), (22) and (23), respectively
$A_{\alpha\alpha}$, $A_{\alpha h}$, $A_{h\alpha}$, A_{hh} = reduced aeroelastic coefficients defined by Eqs. (31), (32), (33), and (34), respectively
$[I]$, $[I]''$, $[II]$ = integrating matrices
p = differential operator, $p = (d/dt)$
m_s, S_α, I_α = concentrated mass, unbalance, and moment of inertia, respectively
i = electrical current
e = electrical voltage
C = capacitance
L_α, L_e = inductance in torsion and bending circuits, respectively
K_α, K_e = concentrated stiffness parameters

Subscripts

t = tip
N = coordinate station number

Matrix notation

$[\ ]$ = square or rectangular matrix
$\lfloor\ \rfloor$ = row matrix
$\{\ \}$ = column matrix

Received March 22, 1955.

† The authors wish to express their sincerest gratitude and appreciation to Hermann J. Hassig and Friedrich H. Nuernberg who were directly responsible for the digital calculations on the IBM 701 Computer as well as the necessary digital checks for the analog computations.

‡ Group Engineer, Flight Dynamics Research.

†† Dynamics Engineer.

INTRODUCTION

As a result of higher airplane speeds due to more powerful engines and of increased flexibility due to thinner lifting surfaces necessary for optimum performance, the aircraft designer must give considerably more attention to aircraft dynamics problems such as flutter, gust, landing, and taxi loads in airplane designs. In many cases the representation of the elastic structure for adequate predictions of the vibration, flutter, and dynamic load characteristics of the airplane must be considered to a higher degree of complexity. Prior to the final acceptance of an analysis requiring the increased complexity, two important problems must be considered.

(1) The elapsed time involved in determining a network of solutions, which will be shown to be a definite characteristic of the problem due to required variations of the structure and the aerodynamics, should be well within the time the airplane design is "frozen" in order that the results obtained may be of use.

(2) The results should enjoy some reasonable guarantee that they are correct as well as make "engineering sense."

The realization of treating problems to a high degree of complexity—prior to the development of high-speed computing machines, both digital and analog—appeared remote. However, in recent years the computing facilities necessary to overcome these difficulties have not only been developed but apparently have been incorporated in the engineering forces of major aircraft companies. The purpose of the present paper is to review the possible approaches to the various phases of aircraft dynamics problems and also to examine the optimum methods in terms of both the analog and digital facilities for successful solution of these highly complex problems. The optimum method should be based on integrating both the analog and digital facilities such that the best features of each would be available to overcome the two previously mentioned problems.

Details of a suggested method are given as well as numerous examples for various dynamics problems. The advantages and disadvantages of the method are discussed. Finally, examples are given which not only illustrate the methods but also point out the manner in which the two basic problems previously mentioned are overcome. In addition, detailed examination of the examples provides numerous suggestions for future research.

Aircraft Dynamic Load Problems and Solutions at Various Design Stages

As implied by the word "dynamic," the aircraft problems of interest in this paper are those which involve the element of time. Specifically, they are aeroelastic problems such as flutter, airplane dynamic stability as affected by wing and tail elasticity, gustloads, as well as vibration problems which involve landing and taxi load investigations. Examination of the characteristics of each problem indicates that a major portion of each is common to all of the problems. As a result the study of a variety of phases of airplane dynamics could be made with the same computer set-up with relatively minor modifications. The study of these problems can be broken up into stages which are predicated by the design development of the airplane. These stages consist of: (1) preliminary design, (2) shake test, (3) final analysis. In this section the need and significance of each stage will be discussed and the character of the required solutions will be indicated.

Preliminary Design Stage

The preliminary design stage of an airplane offers the dynamicist the opportunity of determining the adequacy of a design which is primarily set by performance, stability, and maneuverability criteria at a time when the design is still not frozen. As noted in the Introduction, the trend of present and future airplanes indicates the need of increased consideration of elasticity effects in the overall optimum design. In the past the role played by the dynamicist at this design stage has been to offer an opinion, on the basis of experience on previous designs, as to the possible difficulties the configuration would encounter. These difficulties, if still present after the configuration is built, could be counteracted by beefing up the structure or by judicious use of balance or ballast weights. On the present and future designs such a philosophy may not be adequate and could result in a final configuration that is unduly penalized by an unnecessary weight increase since an easy "fix" may not be possible. In addition the airplane would be placarded in the interim resulting in an expensive and time-consuming flight-test program. Such a state of affairs must obviously be avoided if possible. Such a predicament could be anticipated if the dynamicist could reliably catch the dynamics problem in the preliminary design stage. Similarly, a desirable configuration from other viewpoints may be discarded as too great a gamble flutterwise, merely because the flutter analysis will not be available until the airplane is built, and it is too late to change.

The principal difficulty in determining significant "engineering results" in the preliminary design stage is the restricted availability and accuracy of the data, both structural and perhaps aerodynamic (if the design is radically different, requiring experimental testing to help define the aerodynamic coefficients). Two possibilities exist at this point:

(1) The analyst can direct his efforts principally to refining the data to a higher degree of accuracy and therefore postpone the preliminary analysis until such time as the data are accurate enough to warrant an analysis that would lead to significant "engineering results."

(2) An analysis can be made based on available data realizing its inadequacies and shortcomings with the intention of first getting a "feel" for the problem and of determining what structural or aerodynamic parameters have the most effect on the solutions. In contrast, those parameters which have a relatively minor effect can also be determined. At this point further investigation of those parameters which must be known to a higher degree of accuracy for adequate engineering results can be pursued by more detailed study or by experimental techniques involving carefully scaled models.

In view of the limited time available for performing a successful analysis while the airplane is in the early design stage, the second choice appears to be the most logical. During the investigation of the preliminary design an unsatisfactory condition in terms of stability, such as flutter, may appear. Through the use of many parameter variations the most logical "fix"—that is,

the one requiring the least weight increase and complexity—can be determined. Recommendations could then be given to the design group for possible incorporation in the design.

In the preliminary design stage some verification of the aerodynamic force and moment representations for the flutter and gust problems should be obtained. In some cases, depending upon the speed range and configuration, the aerodynamic representation used may be similar to previous designs for which the aerodynamics have been verified by flight-test experience. However, in investigation of configurations which are radically different and can attain speeds well beyond those of previous designs, the validity of the aerodynamics must be established. Careful experimentation employing wind-tunnel or free-flight models together with careful analytical studies appears to be the most logical approach. Once again the same problems face the analyst. The models and the desired information obtained from their study must be available prior to the final analysis stage in order to be of use. Consequently, the models cannot be made to represent the airplane exactly in stiffness and mass properties and, of course, cannot represent all of the degrees of freedom except at impractical cost of both money and time. However, the results from the preliminary analysis provide some information as to the critical degrees of freedom or modes that are coupling to cause a possible flutter problem. In some cases several such problems may exist, on the wing as well as on the tail. The models can be constructed to simulate the aerodynamic shape exactly but unfortunately can simulate only the mechanical modes of significance approximately. In some cases several significant modes may have to be ignored, such as those due to fuselage motions. As a result an analysis of each model is required to insure that the differences between the model and the airplane are properly accounted for in interpreting the significance of the aerodynamics used in the analysis when comparisons of the calculated model response with the observed model response characteristics are made. Since agreement of analysis with one or two test points may be only fortuitous, it is desirable to have sufficient test points in each range of Mach Number to give a real test of the aerodynamics used for each range. This is usually accomplished by varying such parameters as stiffness, weight, inertia, and unbalance of the model. Thus, a complete structural, vibration, and aerodynamic analysis should be made for each model in addition to the previously mentioned work necessary on the airplane. Also, variations of the aerodynamics may be necessary to determine the proper adjustments to match the observed model test results. All of these calculations must be made prior to the final analysis of the airplane.

Thus an analysis in this stage has many desirable features. However, the following requirements must be recognized if the results of the analysis are to be useful.

(1) A large number of degrees of freedom are often needed since significant degrees of freedom—say, for flutter—may not be readily predicted for a new design. Also the aerodynamic terms become increasingly larger compared to the corresponding structural inertia terms for thinner, more flexible lifting surfaces at transonic and supersonic speeds indicating the need for sufficient degrees of freedom for good representation of the flutter modes.

(2) A large number of solutions are required.

(3) Some means of guaranteeing that the calculations are correct must be established.

These requirements are impossible to meet without a high-speed computing facility. Once such a facility is available, then the requirements are only difficult to meet. However, these difficult requirements can be satisfied by an integrated method of analysis involving both analog and digital facilities.

Shake Test Stage

The next stage of importance to the dynamicist involves the vibration or shake test of the airplane. As many dynamicists know, the results obtained in these tests play an important role in the studies that follow; consequently, careful attention should be given to these tests to insure adequate correlation with the calculations made in the preliminary design stage. Correlation of the observed and calculated vibration results allows for a means of determining the validity of the mechanical representation used. Differences that occur can be attributed to two primary reasons: (1) selection of proper as well as adequate number of degrees of freedom, and (2) accuracy of structural data.

Detailed comparisons of the modes are usually sufficient for evaluation of the first item. The second item, however, is not readily evaluated by mere inspection but usually necessitates numerous calculations involving a large number of variations of structural parameters. Such a network of solutions supplies the dynamicist with a means of determining the optimum match of the observed shake test results requiring the most reasonable adjustment of the initial structural data. The optimization should be based on not only the match of frequencies but also mode shapes, node lines, and relative phasings and amplitudes among the modes. The effects of the landing gear or airplane suspension may be significant in the observed shake test results, and consequently, its effect should be included in the analysis when adjustments to the structural data are made. Of course, this stage also presents a crisis (except in those fortunate cases where it is obvious that no serious dynamic problems exist) in view of the allowable time required to match the observed shake tests since the first flight date of the airplane is not far off. A final analysis check, say for flutter, has to be made prior to the first flight date, and time must be allowed for this investigation.

Thus the success of refining the analysis at this stage depends again upon the previously mentioned requirements: (1) large number of degrees of freedom, (2) large number of solutions, (3) limited time for deter-

mining solutions, and (4) a guarantee solutions are free of errors.

Final Analysis Stage

The final analysis stage permits the dynamicist to determine the effects of changes in structural representation necessary to match the shake tests as well as in aerodynamic representation to match observed wind-tunnel or free-flight model responses on the final results. In addition a reorganization of the pertinent degrees of freedom may appear warranted as a result of the knowledge obtained in matching the observed shake test results together with the aeroelastic stability or dynamic load results obtained in the preliminary analysis. For instance, the flutter investigations may indicate that the critical flutter speed of the airplane involves the coupling of essentially two or three vibration modes on a particular surface. The modes on the remaining surfaces or structure may have a relatively minor effect on the critical mode. Consequently, a more refined definition of the critical modes could be made by redistributing the degrees of freedom. In addition the pertinent degrees of freedom for gust, landing, and taxi loads may not necessarily be compatible for optimum representation for each problem. Thus a certain amount of further reorganization (much of it should be already planned from the results of the preliminary analysis) may be necessary and must, of course, be done rapidly and accurately, implying again the need of an integrated method of analysis.

Since the representation of aerodynamic forces and moments are usually neglected in the landing and taxi load investigations, these studies should be considered as final since the refinements, which resulted from the shake tests, have been included.

Possible flutter difficulties in the speed range of the airplane may appear not only as a result of changes in the structure to match observed shake tests but also due to changes in the aerodynamics to match observed wind-tunnel or free-flight model responses. Thus the "fix" required for minimum weight increase should be determined by parameter variations as quickly as possible, since the initial flight date of the airplane could be within a few days. Numerous additional configurations could also be anticipated and investigated at this time, such as addition of external stores.

In summarizing the characteristics of the work involved in the final analysis stage, the same pattern indicated for the other two stages is seen to exist for this stage.

(1) The problem may be complex due to the large number of degrees of freedom required.

(2) A large number of solutions may be necessary to cover completely the possible loading conditions and configurations of the airplane over its speed range.

(3) The time required to obtain the large number of solutions is even more critical at this stage since the flight date of the airplane is within a few days from the time the airplane is shake tested.

(4) The calculations must enjoy some reasonable guarantee of correctness as well as make good engineering sense.

This section has provided some light on the nature of the dynamic analysis problems involved in the development of an airplane and has indicated the philosophy of the solutions required for each design stage. It is felt that in order for the dynamicist to be of assistance to the design group before the design is frozen, the dynamic analyses must be obtained according to the repeatedly mentioned requirements. The attainment of this goal is impossible without the aid of high-speed computing machines. Once these machines are available, the feasibility of performing the necessary calculations exists. The remaining problem faced by the dynamicist is one of determining the optimum use of the computing facilities to attain the desired goals defined herein. In the next section, the characteristic features of available computing facilities, both analog and digital, as well as existing methods for studying aircraft dynamic problems, will be reviewed and discussed in light of the existing needs previously outlined.

Analog and Digital Methods of Analysis

In describing a complex physical structure for the purpose of analysis by means of any computing technique, a primary consideration is that of reducing the given physical system to a system having a finite number of degrees of freedom. In general, all computational methods are restricted to the consideration of a limited number of degrees of freedom. The problem then becomes one of retaining all of the significant characteristics of the physical system within the limitations imposed by the particular method employed. Various representations have therefore been evolved which accomplish this reduction. Since each of these representations is necessarily an approximation, the final evaluation of each must be made in terms of the particular application. Certain conclusions, however, may be drawn from a consideration of the general characteristics of some of these methods.

Analog Methods

(A) *Modal*—A common means of representation of a physical system is through the use of a modal-type analysis. Here, the motion of the physical system is assumed to be represented by the linear combination of a limited number of modes. These modes must be chosen to include all the relevant types of motion of all coordinates of significant importance in the system. In practice, the modes chosen are usually the lower order vibration modes (either normal or uncoupled) in the important degrees of freedom of the system.

The description of a mode of a distributed physical system involves the assumption of a deflection curve which is a function of a space-wise dimension. The deflection curve should approximate the true deflection of the system in the particular mode and is chosen either on the basis of analytical or experimental results

or from previous experience. Once this deflection curve has been prescribed, the generalized inertial, elastic, and aerodynamic properties of the system may be determined for motions of this mode. The determination of these generalized properties involves an integration with respect to a space-wise dimension. The differential equations of the modal system are then derived from the Lagrangian energy principles as applied to these generalized properties. Electronic differential analyzers such as BEAC or REEVES computers are normally used to simulate the resulting differential equations.

It will be noted that the modal approach results in a two-fold simplification of the distributed physical system:

(1) The number of degrees of freedom is restricted to those of importance to the particular analysis.

(2) The three-dimensional properties of the distributed physical system are replaced by equivalent two-dimensional properties.

(B) *Finite difference*—As an alternative analog method, a distributed physical system may be represented by assuming the properties of the system to be concentrated at discrete intervals. This lumped-parameter system is then described by means of finite difference equations, which are in turn represented by an analog computer. The computer which most commonly utilizes this method of representation is the network analyzer or direct analog computer. The network analyzer utilizes passive electrical circuit elements to represent the discrete structural parameters of the approximate physical system. In the direct analog computer, both the electrical quantities, voltage, and current, are analogous to quantities of the mechanical system. Two analogies are widely used: the loop analogy, wherein electrical voltage is analogous to mechanical force; and the nodal analogy, wherein electrical current is analogous to mechanical force. The nodal analogy is generally preferred in the representation of structural systems; this is due in part to the close topological similarity between the resulting electrical circuit and the structural system. Since mechanical quantities are usually translated directly into electrical quantities without reference to the differential equations of either the mechanical or electrical system, this topological similarity is an important characteristic of the nodal analogy. The external forces applied to the mechanical system, e.g., aerodynamic forces, are represented by the analogs of the differential equations of these forces, much as is done in the case of the differential analyzer. In this case, however, current generators are required as well as voltage amplifiers, since current and voltage both represent mechanical quantities.

Although each of the two methods, modal and finite difference, has been identified with a particular type of analog computer, variations of these methods are used in conjunction with either type. Differential analyzers have frequently been used to represent the finite difference equations of distributed mechanical systems. More recently, a method has been devised wherein mechanical properties are simulated in differential form by elements of the differential analyzer, and these elements are interconnected in accordance with finite difference equations of the mechanical system. In the case of the network analyzer, frequent use is made of modal representation in order to achieve a saving of electrical circuit elements. This is usually done in representing a subsidiary portion of the structure, such as a fuselage, where detailed information is not a required part of the solution.

Digital Methods

The methods used in the solution of aircraft dynamics problems with high-speed digital computers parallel quite closely those described in conjunction with analog computers. Modal-type analyses are commonly used with digital computers in much the same manner as with analog computers, with one principal difference: the generalized coordinates in the digital analysis are usually assumed to be prescribed functions of time—i.e., to have only simple harmonic motions. In some cases, as for landing or taxi loads, limited time histories are computed for discrete forcing functions. The assumption of harmonic motion is certainly true in the case of the free vibrations of a conservative system, and while it is not in general true of a mechanical system under the influence of aerodynamic forces, the assumption is valid for those critical cases where the aeroelastic system becomes neutrally stable. In other cases, harmonic motions are obtained by the addition of an appropriate damping or driving force to the mechanical system. The differential equations of the modal system are then expressed as homogeneous equations containing an unknown frequency. The solutions of the characteristic equation of the system are then obtained by numerous methods such as matrix iteration, or fraction series, etc., and the frequencies so obtained are the desired vibration frequencies or flutter modes, as the case may be. The magnitude and sign of the required damping (if any) is then taken as a measure of the stability of the given root of the system.

Finite difference techniques may also be applied to the solution of dynamics problems on digital computers. The mechanical and aerodynamic properties of the system are described in terms of discrete stations or panels of the distributed structure. The equations of motion of each station are expressed in matrix form in terms of the summation of forces at each station. The summation of these forces—elastic, inertial, and aerodynamic—is performed by the use of integrating matrices which prescribe the distribution of these forces. This formulation results in equations of motion of finite difference form which replace the partial differential equations of the distributed physical system. The equations obtained in this manner are time-dependent functions. As such, they are not in an expedient form for solution by digital means, especially when aerodynamic forces must be considered. The

motions of the system are therefore normally restricted to harmonic oscillations, and the equations written as functions of frequency. This set of equations is then solved as an eigenvalue problem by means of matrix iteration.

Comparison and Evaluation of Methods

(*A*) *Analog*—(1) *Modal systems:* The use of modal systems with analog computers has the advantage that it requires a minimum of electrical circuit parameters for a given complexity of structure. This feature is, indeed, the principal attraction of modal analyses. As might be expected, however, this simplicity of representation gives rise to other characteristics which are less desirable:

(a) The fact that the generalized structural parameters are obtained from space-wise integrations of the original system parameters means that localized structural or inertial changes are not simple to perform.

(b) The deflection curves which are assumed in modal analyses represent constraints on the system, which may have a significant effect unless the advantage of simplicity is lost by using many modes. The inclusion of these constraints assumes that external forces have no significant effect on the mode shapes.

(2) *Direct analog systems:* Direct analog representations as applied to the network analyzer offer several formidable advantages:

(a) Complex structural systems may usually be analyzed without specific reference to the differential equations of the systems.

(b) Since the mechanical system is represented directly on the computer, the complete aircraft dynamics problem may be solved with one general set-up. The changes in set-up from static deflection tests to free vibrations, to flutter analysis, to gust response studies, etc., are accomplished in a very short time.

(c) The high degree of identification between electrical quantities results in extreme convenience in making localized changes of structural parameters. To expedite these parameter changes, the passive electrical circuit components of the network analyzer are variable over a wide range of values in small increments.

(d) The short time required for the actual machine solution, coupled with the ease of making parameter changes, makes possible the investigation of a wide range of structural configurations in a relatively short time. In this way, the significant parameters in a particular analysis are readily ascertained and investigated in detail.

The use of the network analyzer in the solution of dynamics problems is not, however, free of disadvantages:

(a) The analysis of complex structural systems necessarily results in complex electrical circuits. Each element of the circuit representing the structure must be set to the appropriate value and correctly connected into the structure. The aerodynamic forces are simulated through the use of active elements, and these electronic devices are, of course, subject to failure or malfunction. One of the most difficult phases of the analysis is that of ascertaining that the set-up is correct.

(b) Although the electrical elements used in the network analyzer are the best quality obtainable, they are not perfect. The parasitic effects associated with these imperfections may be minimized by the proper choice of element values, but in some cases these effects are difficult to evaluate. This is particularly true of the small amount of damping which is necessarily present in any circuit containing inductors or transformers.

(c) Since the network analyzer has been used principally in analyses employing classic two-dimensional incompressible theory, the use of other aerodynamic theories generally requires some development of the associated circuits. Although this is not an inherent limitation of the computer, it may be a serious difficulty if close cooperation between the aerodynamics group and the computer group is not maintained.

(B) *Digital*—(1) *Modal systems:* The use of digital computers in modal analyses is characterized by the same general advantages and disadvantages as were mentioned in conjunction with modal analyses with analog computers. The principal differences between these two methods are:

(a) The accuracy of solution is inherently better in the case of the digital computer.

(b) The digital computer requires a solution time which is considerably longer than that of the analog computer—that is, when many parameter variations must be considered.

(2) *Finite difference methods:* The use of finite difference techniques with high-speed digital computers is in many respects similar to the use of direct analog representation. This method of formulation eliminates the necessity of prescribing deflection shapes; the motions which are represented are not limited by artificial constraint except due to the number of panels which may be included in the analysis. Successive stages of the analysis—static deflection tests, vibration test, flutter—may be performed using digital programs which are very similar to those required for the analog. The resulting eigenvalue problem is solved by means of matrix iteration; this technique provides the means of discontinuing the solution after a specified number of roots are obtained. This number, of course, depends on the problem and its counterpart solution obtained on the analog for comparisons.

The time required for the formulation and set-up of the problem is comparable to the time required for the same operation using the network analyzer. The principal advantage of the digital method over the corresponding analog method is due to the inherent accuracy of the digital computer. In general, the digital computer may be considered to solve exactly the problem which is programmed, while the network analyzer involves certain inaccuracies even under optimum conditions. The digital method, however, requires an appreciably larger solution time than the analog for repetitous solutions of the kind required by parameter studies. Although this longer solution time may not

be significant if the number of solutions is small, the nature of the dynamics problem indicates that the number of solutions required is large. Therefore, the use of the digital method by itself is seriously restricted.

Suggested Method Based on Integration of Analog and Digital Machines

As noted previously, the analysis of a complex dynamic system usually requires a large number of solutions involving wide variations of the significant parameters of the system. These solutions, however, must often be obtained with a minimum of elapsed time and must be free both of system errors and errors in machine set-up. The finite difference or "panel" method using the digital and analog computers in an integrated manner provides a means of achieving these desired results. The advantages of both computational systems are obtained—the ease of parameter variations and speed of solution using the direct analog computer as well as a continued check on the accuracy of the solution using the digital computer. The very fact that the analysis is performed by two independent methods is of course advantageous in assuring elimination of errors. The realization of the full capabilities of the integrated digital-analog method is most nearly attained when both computers use the finite difference or "panel" approach. This formulation results in optimum compatibility between the digital and analog systems and provides for comparative checks of the two systems at each stage of the analysis—elasticity, vibration, and aeroelastic stability checks. The description of these check procedures will be given in detail.

Description of Direct Panel and Analog Methods

In the previous section the various methods for dynamic analysis as well as their solution on both analog and dig tal computers were reviewed and examined for determining an improved approach for solving aircraft dynamics problems. A suggested method, in terms of the requirements for dynamic analyses at each design stage, is an integrated approach employing both the analog and digital computers. This method, which utilizes finite difference approximations for both computers, is described in this section by a simple example.

Example of Digital Finite Difference Solutions for Cantilever Wing Bending-Torsion Motion

Consider a wing restrained such that its torsional and bending deflection as well as its bending slope is zero at the root. Assume that the wing acts as a simple beam—that is, its structural properties can be represented by a torsional stiffness parameter, GJ, a bending stiffness parameter, EI, and an elastic axis, *e.a.* Also assume that its properties are given at specified spanwise stations such as illustrated in Fig. 1. The differential equation relating the torsional deflection α, positive leading edge up, as a function of accumulated torque, T, can be written in several forms. The most convenient, from the standpoint of numerical evaluation, is the integral form given as

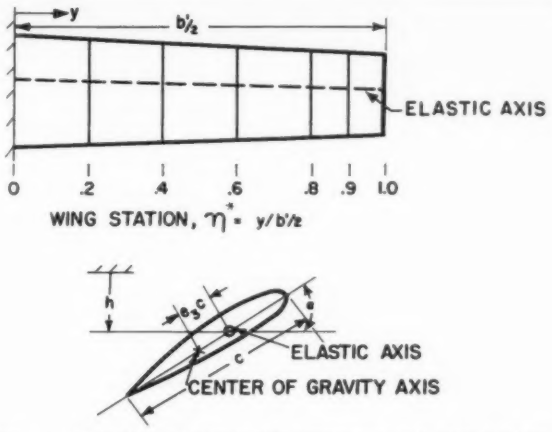

FIG. 1. Definition of geometrical parameters and wing stations used in analysis.

$$\alpha = \frac{b'}{2} \int_0^{\eta^*} \frac{T}{GJ}\, d\eta^* \tag{1}$$

where $b'/2$ is the exposed or structural span of the wing, and η^* is the normalized span coordinate illustrated in Fig. 1. The accumulated torque, T, can be conveniently expressed in terms of the running torque, t, which at specified spanwise stations are due to inertia or aerodynamic loading.

$$T = \frac{b'}{2} \int_{\eta^*}^{1.0} t\, d\eta^* \tag{2}$$

The equations relating the running torque to the torsion and bending motions of the wing are quite complex since for the general dynamics problem both inertial and aerodynamic forces and moments give rise to this quantity. For convenience general expressions can be used to illustrate the digital approach without specifying the details of the aerodynamics of the wing. Assume that the running torque, positive leading edge up, is due to aerodynamic and inertial forces.

$$t = t_{\text{aero.}} + t_{\text{inertia}} \tag{3}$$

The expression for the inertia contribution in terms of the coordinates α and h, where h is positive down and α is positive leading edge up, is

$$t_{\text{inertia}} = -\mu e_3 c \ddot{h} - \mu[(e_3 c)^2 + r^2]\ddot{\alpha} \tag{4}$$

where μ is the running mass, $e_3 c$ is the distance of the center of gravity from the elastic axis, positive aft, and r is the radius of gyration of the section.

The aerodynamic running torque is extremely complex for time-dependent motion; as a result numerous simplifying assumptions are necessary to permit evaluation. A general expression for aerodynamic torque can be written which will allow for introduction of its principal characteristics.

$$t_{\text{aero.}} = (1/2)\rho V^2 c^2 [T_\alpha \cdot \alpha + T_h \cdot (h/\bar{c})] \tag{5}$$

where ρ is the density of air, V is the forward velocity of the wing, c is the local chord, and $\bar{c}$ a reference chord (usually the mean aerodynamic chord). The aerodynamic coefficients T_α and T_h are of course the quantities which depend upon the particular transient aerodynamic theory used and the type of motion. For digital analysis simple harmonic motion is assumed such that solutions can be obtained in terms of eigenvalues. Similarly, this assumption is applied to the inertial terms which then provide not only compatibility of the inertial and aerodynamic terms but also a means of determining the natural frequencies of the system. On this basis Eq. (4) simplifies to

$$t_{\text{inertia}} = \omega^2 \mu e_3 c \bar{c}(h/\bar{c}) + \omega^2 \mu [(e_3 c)^2 + r^2]\alpha \qquad (6)$$

The remaining step is that of combining Eqs. (1), (2) (5), and (6) into a single equation and providing a means of performing the required integrations with the viewpoint of rapid and efficient evaluation by digital operations. The nodal analog representation provides a means of performing these two operations automatically. If one were to attempt to simulate the analog representation, the first step would be to relate the integral expressions, Eqs. (1) and (2), by trapezoidal approximation. Such a numerical approximation is the most convenient from the standpoint of the analogy. For the digital representation no restriction is required as to the type of numerical approximation. In fact to provide increase in accuracy for a given number of degrees of freedom (spanwise stations) and length of time, for evaluation, the parabolic type of integrating approximation such as Simpson's rule (with modifications for nonuniform increments) is suggested for digital evaluation. On this basis Eq. (1) can be written as

$$\{\alpha\} = \frac{b'/2}{(GJ)_{\text{root}}} [\text{I}]'' \left[\frac{(GJ)_{\text{root}}}{GJ}\right] \{T\} \qquad (7)$$

where $\{\ \}$ denotes a column matrix where the first value represents the value at the root and the last corresponds to the tip. The square matrix $[\text{I}]''$ performs the desired numerical integration from the root to a spanwise location for a set of spanwise stations. The diagonal matrix $[(GJ)_{\text{root}}/GJ]$ is a nondimensional torsional stiffness matrix describing the stiffness values along the span of the wing. A typical set of values for the $[\text{I}]''$ matrix based on parabolic arc approximations at spanwise stations $\eta^* = 0, 0.2, 0.4, 0.6, 0.8, 0.9$, and 1.0 is given in Table I. A derivation of the numbers in Table I is given in reference 1. For the convenience of the reader the notation used throughout the digital presentation is similar to that also used in reference 1.

The numerical equivalent of Eq. (2) can be written in matrix form using numerical integrating approximations.

$$\{T\} = b'/2[\text{I}]\{t\} \qquad (8)$$

where the square matrix [I] performs the numerical integration from the tip to a spanwise location for a set of spanwise stations. A typical set of values for the [I] matrix based on parabolic arc approximations at the spanwise stations indicated for the $[\text{I}]''$ matrix is also given in Table I. The two integrating matrices are related approximately by the double transpose. If equally spaced spanwise stations had been selected, then the $[\text{I}]''$ matrix would be exactly the double transpose of the [I] matrix. This characteristic follows directly from the noted integral operations.

The expression for running torque, t, due to aerodynamic and inertia load can be written in matrix form to give

$$\{t\} = \omega^2\{[\mu e_3 c\bar{c}]\{h/\bar{c}\} + [\mu((e_3 c)^2 + r^2)]\{\alpha\}\} + (1/2)\rho V^2 \bar{c}^2 [(c/\bar{c})^2]\{[T_\alpha]\{\alpha\} + [T_h]\{h/\bar{c}\}\} \qquad (9)$$

TABLE 1

Values of Integrating Matrices: [I], $[\text{I}]''$, and [II] for Spanwise Stations $\eta^* = 0, 0.2, 0.4, 0.6, 0.8, 0.9, 1.0$, Based on Parabolic Arc Approximation

$$[\text{I}] = \begin{bmatrix} 0.06667 & 0.26667 & 0.13333 & 0.26667 & 0.10000 & 0.13333 & 0.03333 \\ -0.01667 & 0.13333 & 0.15000 & 0.26667 & 0.10000 & 0.13333 & 0.03333 \\ 0 & 0 & 0.06667 & 0.26667 & 0.10000 & 0.13333 & 0.03333 \\ 0 & 0 & -0.01667 & 0.13333 & 0.11667 & 0.13333 & 0.03333 \\ 0 & 0 & 0 & 0 & 0.03333 & 0.13333 & 0.03333 \\ 0 & 0 & 0 & 0 & -0.00833 & 0.06667 & 0.04167 \\ 0 & 0 & 0 & 0 & 0 & 0 & 0 \end{bmatrix}$$

$$[\text{I}]'' = \begin{bmatrix} 0 & 0 & 0 & 0 & 0 & 0 & 0 \\ 0.08333 & 0.13333 & -0.01667 & 0 & 0 & 0 & 0 \\ 0.06667 & 0.26667 & 0.06667 & 0 & 0 & 0 & 0 \\ 0.06667 & 0.26667 & 0.15000 & 0.13333 & -0.01667 & 0 & 0 \\ 0.06667 & 0.26667 & 0.13333 & 0.26667 & 0.06667 & 0 & 0 \\ 0.06667 & 0.26667 & 0.13333 & 0.26667 & 0.10833 & 0.06667 & -0.00833 \\ 0.06667 & 0.26667 & 0.13333 & 0.26667 & 0.10000 & 0.13333 & 0.03333 \end{bmatrix}$$

$$[\text{II}] = \begin{bmatrix} 0 & 0.05333 & 0.05333 & 0.16000 & 0.08000 & 0.12000 & 0.03333 \\ -0.00167 & 0.01000 & 0.02500 & 0.10667 & 0.06000 & 0.09333 & 0.02667 \\ 0 & 0 & 0 & 0.05333 & 0.04000 & 0.06667 & 0.02000 \\ 0 & 0 & -0.00167 & 0.01000 & 0.01833 & 0.04000 & 0.01333 \\ 0 & 0 & 0 & 0 & 0 & 0.01333 & 0.00667 \\ 0 & 0 & 0 & 0 & -0.00042 & 0.00250 & 0.00292 \\ 0 & 0 & 0 & 0 & 0 & 0 & 0 \end{bmatrix}$$

Eqs. (7), (8), and (9) can then be combined to give a final matrix equation.

$$\begin{Bmatrix} \alpha \end{Bmatrix} = \frac{1}{\lambda}\left[[A_{\alpha\alpha}]\ [A_{\alpha h}] \right] \begin{Bmatrix} \begin{Bmatrix} \alpha \end{Bmatrix} \\ \begin{Bmatrix} h \\ \bar{c} \end{Bmatrix} \end{Bmatrix} \tag{10}$$

where $[A_{\alpha\alpha}]$, $[A_{\alpha h}]$, and λ are defined as

$$[A_{\alpha\alpha}] = [\mathrm{I}]'' \left[\frac{(GJ)_{\text{root}}}{GJ} \right] [\mathrm{I}] \left[\left(\frac{c}{\bar{c}} \right)^2 \right] [T_\alpha] + \frac{k_1^2}{(\rho/2)\bar{c}^4} [\mu((e_3 c)^2 + r^2)] \tag{11}$$

$$[A_{\alpha h}] = [I]'' \left[\frac{(GJ)_{\text{root}}}{GJ} \right] [\mathrm{I}] \left[\left[\left(\frac{c}{\bar{c}} \right)^2 \right] [T_h] + \frac{k_1^2}{(\rho/2)\bar{c}^4} [\mu e_3 c \bar{c}] \right] \tag{12}$$

$$\lambda = \frac{(GJ)_{\text{root}}}{(b'/2)^2 \bar{c}^2 (\rho/2)\, \mathrm{V}^2} \tag{13}$$

The aerodynamic terms T_α and T_h are written as square matrices, implying that aerodynamic influence coefficients are available—that is, the aerodynamic torque at a particular station is due to the motions of all the spanwise stations. Unfortunately these coefficients are not readily available; however engineering approximations are available which provide estimates of these terms and consequently the aerodynamics is written in this form. If a strip analysis is employed, the matrices $[T_\alpha]$ and $[T_h]$ simplify to diagonal matrices, implying that the aerodynamic torque at any station is due only to the motion at that station.

The aerodynamic terms are usually written as a function of a nondimensional frequency parameter defined in this case as

$$k_1 = (\omega \bar{c}/\mathrm{V}) \tag{14}$$

In flutter work this parameter is usually called the "reduced frequency." Note that this term appears in the expressions for $[A_{\alpha\alpha}]$ and $[A_{\alpha h}]$.

It might be noted that the quantities λ, $[A_{\alpha\alpha}]$, and $[A_{\alpha h}]$ are all dimensionless.

The same approach can be applied to describe the bending motion of the built-in wing. The differential equation in a convenient form for numerical evaluation, which relates the bending slope of the wing as a function of the bending moment, M, and the bending stiffness, EI, is

$$\frac{dh}{d\eta^*} = \left(\frac{b'}{2} \right)^2 \int_0^{\eta^*} \frac{M}{EI}\, d\eta^* \tag{15}$$

but the slope can be written in terms of the deflection, h, as

$$h = \int_0^{\eta^*} \frac{dh}{d\eta^*}\, d\eta^* \tag{16}$$

and the bending moment, M, can be expressed in terms of the running load, l, positive down, as follows:

$$M = (b'/2)^2 \int_{\eta^*}^1 (\eta^*_0 - \eta^*) l\, d\eta^*_0 \tag{17}$$

where η_0^* is a dummy spanwise variable. The running load, l, similar to the running torque, is due to both aerodynamic and inertia forces.

$$l = l_{\text{aero.}} + l_{\text{inertia}} \tag{18}$$

The expression for running load inertia is

$$l_{\text{inertia}} = -\mu h - \mu e_3 c \ddot{\alpha} \tag{19}$$

The aerodynamic running load (positive down) is

$$l_{\text{aero.}} = (1/2)\rho \mathrm{V}^2 c [P_\alpha \cdot \alpha + P_h \cdot (h/\bar{c})] \tag{20}$$

Assuming harmonic motion and parabolic arc approximations for the numerical evaluation of the required integrations, Eqs. (15) through (20) can be combined to give the expression equivalent to Eq. (10) for torsion. This expression is

$$\begin{Bmatrix} h \\ \bar{c} \end{Bmatrix} = \frac{1}{\lambda}\left[[A_{h\alpha}]\ [A_{hh}] \right] \begin{Bmatrix} \begin{Bmatrix} \alpha \end{Bmatrix} \\ \begin{Bmatrix} h \\ \bar{c} \end{Bmatrix} \end{Bmatrix} \tag{21}$$

where $[A_{h\alpha}]$ and $[A_{hh}]$ are defined as

$$[A_{h\alpha}] = \frac{(b'/2)^2}{\bar{c}^2} ([\mathrm{I}]'')^2 \left[\frac{(GJ)_{\text{root}}}{EI} \right] [\mathrm{II}] \times \left[\left[\frac{c}{\bar{c}} \right] [P_\alpha] + \frac{k_1^2}{(\rho/2)\bar{c}^2} \left[\frac{\mu e_3 c}{\bar{c}} \right] \right] \tag{22}$$

$$[A_{hh}] = \frac{(b'/2)^2}{\bar{c}^2} ([\mathrm{I}]'')^2 \left[\frac{(GJ)_{\text{root}}}{EI} \right] [\mathrm{II}] \times \left[[P_h] + \frac{k_1^2}{(\rho/2)\bar{c}^2} [\mu] \right] \tag{23}$$

Note that the special integrating matrix, [II], appearing in Eq. (22) and (23), is required to perform the integration indicated in Eq. (17). A typical set of values for the [II] matrix for spanwise stations $\eta^* = 0, 0.2, 0.4, 0.6, 0.8, 0.9$, and 1.0 is given in Table I.

Note that all of the required operations for solving the torsion and bending equations have been put in a form such that their numerical evaluation has consistently required integration rather than differentiation. Inherently such an approach provides maximum accuracy for a given number of stations or "panels."

Eqs. (10) and (21) can be combined to give the final aeroelastic matrix from which the flutter stability of the wing can be determined.

$$\begin{Bmatrix} \begin{Bmatrix} \alpha \end{Bmatrix} \\ \begin{Bmatrix} h \\ \bar{c} \end{Bmatrix} \end{Bmatrix} = \frac{1}{\lambda} \begin{bmatrix} [A_{\alpha\alpha}]\ [A_{\alpha h}] \\ [A_{h\alpha}]\ [A_{hh}] \end{bmatrix} \begin{Bmatrix} \begin{Bmatrix} \alpha \end{Bmatrix} \\ \begin{Bmatrix} h \\ \bar{c} \end{Bmatrix} \end{Bmatrix} \tag{24}$$

It should be noted that Eq. (24) is in canonical form.

The square matrices $[A_{\alpha\alpha}]$, $[A_{\alpha h}]$ etc., are complex matrices due to the aerodynamic forces and moments. These forces and moments are, as noted previously, given as a function of a nondimensional frequency parameter, k_1. Several values of this parameter are selected and solutions for the parameter "λ" are ob-

tained. Since the $[A]$ matrices are complex, the values of "λ" will usually be complex. The physical interpretation of these complex values of "λ" is as follows:

The structural damping, g_s, required to sustain harmonic oscillation at the given reduced frequency is

$$g_s = \lambda_I/\lambda_R \tag{25}$$

and the speed for which this condition exists is

$$V = \sqrt{\frac{(GJ)_{\text{root}}}{(b'/2)^2\bar{c}^2(\rho/2)\lambda_R}} \tag{26}$$

where λ_R is the real part and λ_I is the imaginary part of the complex "λ."

If the stations $\eta^* = 0$, 0.2, 0.4, 0.6, 0.8, 0.9, and 1.0 had been taken as the degrees of freedom, the final aeroelastic matrix would be twelfth order and complex implying that the determination of the complex eigenvalues, λ, and the eigenvectors $\{\alpha\}$ and $\{h/\bar{c}\}$ would be extremely difficult and time consuming without the aid of a high-speed digital computer. Since the aero elastic equation is in canonical form, simple matrix iteration is an ideal method of solution. As many roots as desired can be extracted at a time without determining all of the roots. Usually for a simple wing configuration (no concentrated weights such as engines or external stores are present) determination of two or three eigenvalues would be sufficient for providing the necessary information to plot the critical stability diagram.

The possibility of simplifying the aeroelastic matrix given by Eq. (24) for certain configurations should be considered in light of the assumptions made in a modal analysis—that is, a specified bending and torsion mode can be assumed. Such an assumption could provide for a tremendous reduction of the order of the aeroelastic matrix. The introduction of these modes can readily be made in the formulation given herein. Rather than a detailed explanation of the technique, a simple example will be considered.

The modes $\{\alpha\}$ and $\{h/\bar{c}\}$ can be rewritten as follows:

$$\left.\begin{aligned} \{\alpha\} &= \alpha_t \{\alpha/\alpha_t\} \\ \begin{Bmatrix} h \\ \bar{c} \end{Bmatrix} &= \frac{h_t}{\bar{c}} \begin{Bmatrix} h/\bar{c} \\ h_t/\bar{c} \end{Bmatrix} \end{aligned}\right\} \tag{27}$$

where the subscript, t, denotes the value at the wing tip. Eq. (10) can be written as

$$\{\alpha_t\} \begin{Bmatrix} \alpha \\ \alpha_t \end{Bmatrix} = \frac{1}{\lambda} \left\{ [A_{\alpha\alpha}] \begin{Bmatrix} \alpha \\ \alpha_t \end{Bmatrix} \alpha_t + [A_{\alpha h}] \begin{Bmatrix} h/\bar{c} \\ h_t/\bar{c} \end{Bmatrix} \frac{h_t}{\bar{c}} \right\} \tag{28}$$

Similarly Eq. (21) can be rewritten as

$$h_t \begin{Bmatrix} h/\bar{c} \\ h_t/\bar{c} \end{Bmatrix} = \frac{1}{\lambda} \left\{ [A_{h\alpha}] \begin{Bmatrix} \alpha \\ \alpha_t \end{Bmatrix} \alpha_t + [A_{hh}] \begin{Bmatrix} h/\bar{c} \\ h_t/\bar{c} \end{Bmatrix} \frac{h_t}{\bar{c}} \right\} \tag{29}$$

Eq. (28) may be premultiplied (both left- and right-hand side) by a row matrix, designated by $\lfloor\ \rfloor$, consisting of the mode α/α_t; Eq. (29) can also be premultiplied in the same way except by the mode $(h/\bar{c})/(h_t/\bar{c})$. When these operations are applied and the resulting two equations combined, a simple 2×2 matrix is obtained.

$$\begin{Bmatrix} \alpha_t \\ h_t/\bar{c} \end{Bmatrix} = \frac{1}{\lambda} \begin{bmatrix} A_{\overline{\alpha\alpha}} & A_{\overline{\alpha h}} \\ A_{\overline{h\alpha}} & A_{\overline{hh}} \end{bmatrix} \begin{Bmatrix} \alpha_t \\ h_t/\bar{c} \end{Bmatrix} \tag{30}$$

where the bar quantities are complex numbers (not matrices) and are defined as

$$A_{\overline{\alpha\alpha}} = \frac{\lfloor \alpha/\alpha_t \rfloor [A_{\alpha\alpha}] \{\alpha/\alpha_t\}}{\lfloor \alpha/\alpha_t \rfloor \{\alpha/\alpha_t\}} \tag{31}$$

$$A_{\overline{\alpha h}} = \frac{\left\lfloor \dfrac{\alpha}{\alpha_t} \right\rfloor [A_{\alpha h}] \begin{Bmatrix} h/\bar{c} \\ h_t/\bar{c} \end{Bmatrix}}{\lfloor \alpha/\alpha_t \rfloor \{\alpha/\alpha_t\}} \tag{32}$$

$$A_{\overline{h\alpha}} = \frac{\left\lfloor \dfrac{h/\bar{c}}{h_t/\bar{c}} \right\rfloor [A_{h\alpha}] \begin{Bmatrix} \alpha \\ \alpha_t \end{Bmatrix}}{\left\lfloor \dfrac{h/\bar{c}}{h_t/\bar{c}} \right\rfloor \begin{Bmatrix} h/\bar{c} \\ h_t/\bar{c} \end{Bmatrix}} \tag{33}$$

$$A_{\overline{hh}} = \frac{\left\lfloor \dfrac{h/\bar{c}}{h_t/\bar{c}} \right\rfloor [A_{hh}] \begin{Bmatrix} h/\bar{c} \\ h_t/\bar{c} \end{Bmatrix}}{\left\lfloor \dfrac{h/\bar{c}}{h_t/\bar{c}} \right\rfloor \begin{Bmatrix} h/\bar{c} \\ h_t/\bar{c} \end{Bmatrix}} \tag{34}$$

The solution of Eq. (30) will provide two complex values of "λ"; one will represent the stability of the bending mode, h/h_t, and the other the torsion mode, α/α_t. If the proper mode was selected and the effect of changes in spanwise phasing of the modes is negligible, then the values obtained should be excellent approximations to the first two values obtained from the twelfth order complex equation.

Example of Analog Finite Difference Solution for Cantilever Wing

The basic formulation of a simple dynamics problem on the network analyzer will now be considered. In order to demonstrate the compatibility of the digital and analog methods, the same physical system will be considered as in the digital example. The subdivision of the wing into "panels" or stations and the definitions of coordinates shown in Fig. 1 also correspond to those quantities of the digital analysis.

As an aid in the physical interpretation of the finite difference approximations used here, the equivalent mechanical system represented by the electrical circuit analogy is shown in Fig. 2. The distributed properties of the wing are replaced by concentrated properties at each cell or station. The method of parameter representation used here corresponds in general to the use of trapezoidal integration matrices in the digital example. The use of an analogy corresponding to the higher order integration matrices which are possible in the digital analysis would in most cases involve circuits which are prohibitively complex or nonrealizable. The

errors due to this type of approximation vary with the number of panels chosen, the types of motion to be considered, and the distribution of the system parameters. It has been shown, however, that these errors are small for practical physical systems when sufficient coordinate stations are included.[2, 3]

A conventional electrical circuit analogy is used in the representation of the finite difference wing of the present example and is shown in Fig. 3. Since the derivation of this analogy appears in the literature,[4–7] the derivation will not be repeated here in detail. The identification of electrical circuit quantities with mechanical system quantities may be made, however, without resorting to a complete derivation of the analogy.

In the nodal circuit analogy, electrical currents are proportional to mechanical forces and electrical voltages are proportional to the time derivatives of coordinates in the mechanical system. In the following discussion, operational notation is used [$p = (d/dt)$].

The discrete coordinate stations are designated as η^*_N where $N = 0, 1, 2, 3, 4, 5, 6$, numbered from root to tip. The subscript N refers to quantities at these stations, and the subscripts $N + (1/2)$ and $N - (1/2)$ refer to quantities half way between stations.

The equations of the running inertia forces (Eqs. 4 and 19 of the previous section) must be modified in terms of the discrete inertia load stations and may be expressed as

$$\begin{Bmatrix} l' \\ t' \end{Bmatrix}_N = -\begin{bmatrix} m & S_\alpha \\ S_\alpha & I_\alpha \end{bmatrix}_N \begin{Bmatrix} p^2 h \\ p^2 \alpha \end{Bmatrix}_N \tag{35}$$

where l', t' refer to concentrated rather than running loads and moments. All quantities refer to the discrete coordinate station, N, and

$$m_N = \frac{b'}{2} \int_{\eta^*_{N-(1/2)}}^{\eta^*_{N+(1/2)}} \mu \, d\eta^* \tag{36}$$

$$S_{\alpha_N} = b'/2 \int_{\eta^*_{N-(1/2)}}^{\eta^*_{N+(1/2)}} \mu e_3 c \, d\eta^* \tag{37}$$

$$I_{\alpha_N} = b'/2 \int_{\eta^*_{N-(1/2)}}^{\eta^*_{N+(1/2)}} \mu((e_3 c)^2 + r^2) d\eta^* \tag{38}$$

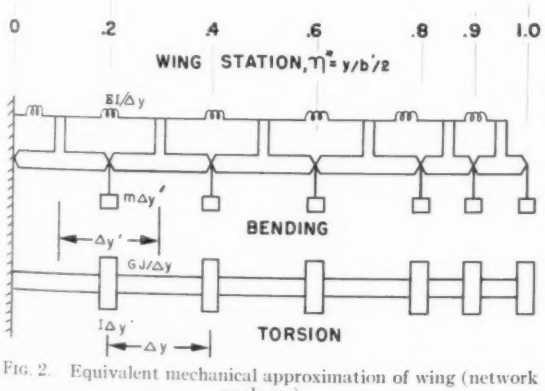

FIG. 2. Equivalent mechanical approximation of wing (network analyzer).

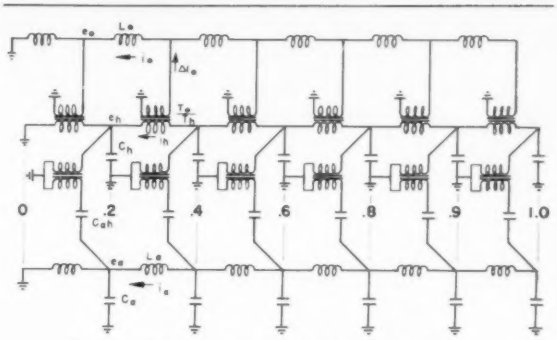

FIG. 3. Electrical circuit analogy (structure).

The expression for the electrical currents resulting from the introduction of the network of capacitors C_h, C_α, and $C_{\alpha h}$ (Fig. 3) at a particular station $\eta_N{}^*$ is

$$\begin{Bmatrix} i_h' \\ i_\alpha' \end{Bmatrix}_N = -\begin{bmatrix} (C_h + C_{\alpha h}) & C_{\alpha h} \\ C_{\alpha h} & (C_\alpha + C_{\alpha h}) \end{bmatrix}_N \begin{Bmatrix} pe_h \\ pe_\alpha \end{Bmatrix} \tag{39}$$

The transformer associated with $C_{\alpha h}$ in Fig. 3 provides for the correct sign of the inertial coupling term. The comparison of the last equation with Eq. (39) reveals that the capacitors represent inertias and that the quantities $(C_h + C_{\alpha h})$, $(C_\alpha + C_{\alpha h})$, and $C_{\alpha h}$ are proportional to the concentrated mass, moment of inertia, and static moment assumed to be acting at that station. In a similar manner, the expression for the accumulated torque of Eq. (2) becomes the summation of all the concentrated inertial torques introduced at stations outboard of the particular section.

$$T_{N-(1/2)} = \sum_{N'=N}^{N'=6} t'_{N'} \tag{40}$$

where N' is a dummy index.

These summations follow naturally from the summation of currents in the electrical circuit. The accumulated torque $T_{N-(1/2)}$ is proportional to the current $(i_\alpha)_{N-(1/2)}$ at each section. The finite difference equation for the chordwise rotation is

$$\alpha_N = \sum_{N'=1}^{N'=N} \frac{T_{N'-(1/2)}}{(K_\alpha)_{N'-(1/2)}} \tag{41}$$

where

$$\frac{1}{(K_\alpha)_{N-(1/2)}} = \frac{b'}{2} \int_{\eta^*_{N-1}}^{\eta^*_N} \frac{d\eta^*}{GJ} \tag{42}$$

These equations correspond to Eq. (1) of the previous section. From electrical circuit considerations, the analogous equation

$$(e_\alpha)_N = \sum_{N'=1}^{N'=N} (i_\alpha)_{N'-(1/2)} \cdot p \cdot (L_\alpha)_{N'-(1/2)} \tag{43}$$

it will be noted that the inductor, $(L_\alpha)_{N-(1/2)}$ shown in Fig. 3 is proportional to $1/(K_\alpha)_{N-(1/2)}$ as defined by Eq. (42).

The combination of these equations into the complete difference equation for torsion, as represented in the digital method by Eqs. (7), (8), (9), and (10) above, is implicit in the interconnection of the elastic

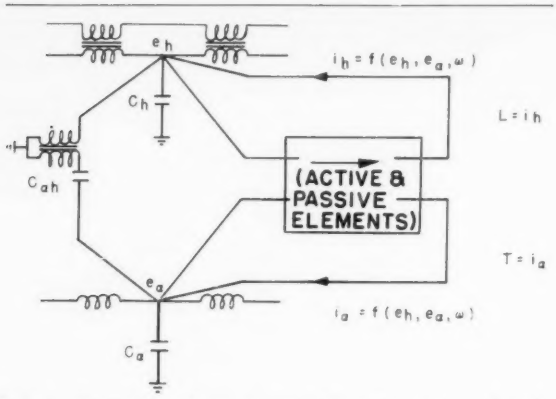

FIG. 4. Generation of aerodynamic forces (network analyzer).

and inertial portions of the electrical circuit. Although only inertial forces have been considered, aerodynamic loads are inserted from external sources in the same manner as inertial loads.

The bending circuit may be described in a manner similar to that of the torsion circuit by replacing the differential bending equations with the finite difference approximations. The concentrated loads are summed at each section

$$L_{N+(1/2)} = \sum_{N'=N+1}^{N'=6} l'_{N'} \tag{44}$$

and the accumulated load $L_{N+(1/2)}$ is represented electrically by the current $(i_h)_{N+(1/2)}$ in the transformer winding $(T_h)_{N+(1/2)}$ at each section. The finite difference approximation of the equation for bending moment [Eq. (17)] is expressed as

$$M_N = \sum_{N'=N}^{N'=5} \Delta M_{N'+(1/2)} \tag{45}$$

where $$\Delta M_{N+(1/2)} = (b'/2)\,(L_{N+(1/2)})\,(\eta^*_{N+1} - \eta_N{}^*) \tag{46}$$

Electrically, Eq. (46) may be expressed as

$$(\Delta i_\theta)_{N+(1/2)} = (i_h)_{N+(1/2)}\,(T_h/T\theta)_{N+(1/2)} \tag{47}$$

which describes the constraint imposed by the transformer, T_h/T_θ, providing this turns ratio is equal to the length $b'/2(\eta^*_{N+1} - \eta^*_N)$. The bending slope at any section $(dh/d\eta^*) = (b'/2)\theta$ may be written as

$$\theta_{N+(1/2)} = \sum_{N'=0}^{N'=N} \frac{M_{N'}}{(K_\theta)_{N'}} \tag{48}$$

where $$\left(\frac{1}{K_\theta}\right)_N = \frac{b'}{2}\int_{\eta^*_{N-(1/2)}}^{\eta^*_{N+(1/2)}} \frac{d\eta^*}{EI}$$

and corresponds to the differential Eq. (15). The analogous circuit equation

$$(e_\theta)_{N+(1/2)} = \sum_{N'=0}^{N'=N} (i_\theta)_{N'}(L_\theta)_{N'} \cdot p \tag{49}$$

indicates that the inductor L_θ as shown in Fig. 3 is proportional to $1/K_\theta$. The relationship between slope and displacement, as expressed in Eq. (16) may be replaced in finite difference form by

$$\left.\begin{aligned} h_N &= \sum_{N'=0}^{N'=N-1} (\Delta h)_{N'+(1/2)} \\ (\Delta h)_{N+(1/2)} &= (b'/2)\,[\theta_{N+(1/2)}]\,(\eta^*_{N+1} - \eta^*_N) \end{aligned}\right\} \tag{50}$$

The second of these equations is a coordinate transformation and is imposed by the transformer T_h/T_θ

$$\left.\begin{aligned} e_{h_{N+1}} - e_{h_N} &= (T_h/T_\theta)_{N+(1/2)}(e_\theta)_{N+(1/2)} \\ \text{where} \quad (T_h/T_\theta)_{N+(1/2)} &= b'/2(\eta^*_{N+1} - \eta^*_N) \end{aligned}\right\} \tag{51}$$

The summation of incremental deflections of each section is then the summation of voltages across the transformer windings.

Again, only inertial forces have been considered, but aerodynamic forces may be included in the same manner. The currents representing aerodynamic forces are applied at each coordinate station in the manner shown symbolically in Fig. 4. The circuits—amplifiers, current generators, and passive transfer function networks—sense the appropriate coordinates as inputs and insert currents (forces and moments) which are functions of these coordinates. Although the diagram indicates that the aerodynamic forces are functions of the local coordinates only (as would be true of two-dimensional flow), spanwise flow distributions may be included by sensing all the coordinates which affect the aerodynamic forces at a particular station.

The complete electrical circuit corresponds to the mathematical description of the system as expressed in Eq. (24) of the digital example. Here, however, the equations are functions of time rather than frequency. With the aerodynamic portions of the circuit removed, the vibrations problem of the structural system is studied by means of the resonance response of the electrical circuit. In aeroelastic studies, stability, load factors, etc., are determined directly from the transient response of the electrical circuit.

Extensions to More Complicated Systems

It should be noted that the structural system chosen for the example is not a very complex one. This choice was made to facilitate the description of the analysis and should not be interpreted as restricting either the digital or analog method to the consideration of such systems. Such additional complexities as concentrated inertial loads, elastically coupled external stores, and additional degrees of freedom are readily represented, as are discontinuities in the elastic distribution or the elastic axis. Digitally such discontinuities may be represented by special interpolating matrices; similarly for the analog these effects can be represented by appropriate electrical circuits.

In either method, the elastic system may be represented through the use of deflection influence coefficients rather than explicit elastic properties. In general, the extent of such complexities which may be considered is limited only by the size or capacity of the particular computing facility.

Description of Check Procedures

In the determination of the optimum methods for aircraft dynamic analyses, involving both analog and digital facilities, one of the most important problems is guaranteeing the calculations to be correct within the initial assumptions. The use of the finite difference digital method, which defines the degrees of freedom almost identically as the network analog, permits the dynamicist to have a completely independent check of the results at several stages of the computations.

One of the best techniques to insure constant checks is to keep the analog and digital set-ups completely independent. Fortunately the approach used in the integrated methods continually allows for such independence except from errors in the basic physical data used in both computers. The analog employing the nodal analogy permits the dynamicist to obtain an electrical model of the mechanical system by physical considerations such as a blueprint or drawing and does not require a description by a mathematical model as represented by a set of differential equations. (What system could have a more direct approach than this one?) Should an inconsistency between the analog and digital results exist—say in a flutter problem which involves complex elastic, inertial, and aerodynamic representations—the determination of the inconsistency may be difficult and time-consuming. Since all of these problems must be solved in a limited time in order that the results obtained be effective, the desirability of performing check procedures during the problem is obvious. These check procedures have a dual purpose:

(1) Prevent inconsistencies or errors from occurring readily.

(2) Inconsistencies that do occur will be located and eliminated rapidly.

The logical approach to these check procedures is to first consider the problem in as many small pieces as feasible without consuming so much time as to render the check procedures impractical and undesirable. Experience has shown that the aircraft problem lends itself to three main check points: (1) elasticity or static deflection check, (2) vibrations check, and (3) aerodynamics check.

In this section a brief description and the significance of each check will be given employing both the analog and digital facilities in the optimum integrated method previously discussed.

Elasticity or Static Deflection Check

The initial check of the physical interpretation of the mechanical system can be made by comparing deflections (voltages on the analog) for specifically applied forces or moments (currents on the analog). The deflections can be computed from the digital finite difference approximations completely independent of the analog results. The representation on both set-ups at this stage is relatively simple; therefore, any inconsistencies can be found rapidly and corrected immediately. Since both systems should be identical in terms of physical representation, the comparison of the deflections should agree within measurements (1 or 2 per cent). If larger differences exist, implying the possibility of an error, then attention should be given to corrective measures so that the stiffness representations are completely compatible between the two systems.

Vibration Check

Once the elasticity and the physical representation of the system have been checked, the addition of the mass and inertia parameters on both the analog and digital set-ups allows for the determination of the natural frequencies and mode shapes of the physical system. As usual, complete independence of the two methods should be retained, although the mass and inertial data supplied to both methods must be checked to be consistent.

In the digital method the most efficient method of obtaining the frequencies and mode shapes is to first introduce the concept of harmonic motion for the degrees of freedom. Since the formulation of the problem has introduced an abnormally large number of degrees of freedom of which the higher orders have relatively little physical significance, the modes of primary interest are the lower order ones with decreasing interest as the higher modes are obtained. Since the principal purpose of the digital calculations is to check the results obtained from the analog, it is felt that if the first six or eight modes agree in frequency and shape, then the correlation is considered sufficient for most practical configurations. The most practical method of obtaining this information for the digital set-up is by simple matrix iteration. More elaborate methods or modified versions may be used, but details are not the purpose of the present paper and therefore will not be discussed. One point should be made concerning the compatibility of the set-up of the digital approach and the determination of the eigenvalues by the iteration methods. In the previous section the matrix defining the stiffness is written as the reciprocal of stiffness or simply as the deflection matrix. In this form the final aeroelastic matrix required for solution of its eigenvalues and eigenvectors is in canonical form without the necessity of any matrix inversions. Should experimental deflection influence coefficients be available, the information can be used in this form without matrix inversions. In cases where modes are included that have no structural stiffness or deflection counterpart such as the rigid body motions of an airplane, then the final aeroelastic matrix for iteration will be in noncanonical form and consequently will require a matrix inversion for solution if simple iteration techniques are used.

The method of determining the natural frequencies and modes by the analog is very similar to the technique used in the shake test of an airplane. A sinusoidal current excitation (force or moment) is applied at a point somewhere on the structure; the frequency of excitation is varied until a resonance is determined. This resonance appears as a minimum current required

to sustain a constant amplitude oscillation. In the actual shake test of an airplane the reverse procedure is usually used. The shaker input is kept constant as the frequency excitation is varied until a resonance is reached. This resonance is indicated as the maximum observed deflection of the structure. The modes for both the analog and the shake tests of the actual structure are determined by reading the relative amplitudes and phases on as many points on the structure as desired. Other natural frequencies can be obtained by variation of the excitation frequency until the desired range of resonant frequencies is determined.

Since the analog and digital methods have been developed with the intent of minimizing their differences, the correlation of frequencies and modes should be within engineering accuracy (4 or 5 per cent). Should errors larger than this amount be present, then the dynamicist can logically assume the results are uncorrelated. Since the elasticity representations for both the digital and analog set-up have been checked, the difficulty must lie in the mass and inertial representations. By comparison of frequencies and modes, the existing error can be found and corrected rapidly. Note that the separation of the elasticity and inertial checks allows for these rapid guaranteed correlations.

Some of the existing differences between the analog and digital methods in determining the natural frequencies and modes should be discussed. As noted previously one obvious difference is the method of excitation (if one can consider the determination of eigenvalues of a matrix as a means of excitation). Actually this method implies that the "excitation" is uniform for all the degrees of freedom. In order that the analog be comparable to the digital method, the excitation must be made not at one or two points on the electrical representation, but on all circuit nodal points defining degrees of freedom. Unfortunately such a procedure would be impractical, as it would be to attempt to excite the actual airplane at an equivalent number of locations as the analog, say 30 to 40 points. Although this difference has relatively little effect on the natural frequency determinations and the normalized mode shapes, it could have an appreciable effect on the relative amplitudes since the analog is not a "perfect" representation as indicated by the following discussion.

Inconsistencies in relative amplitudes necessitate mentioning one of the most important differences and perhaps the most difficult to evaluate between the analog and digital methods. This is the problem of estimating the effects of parasitic impedances in the analog representations. The electrical elements involved in causing these impedances are the passive elements. In general the circuitry associated with the active elements (those elements dealing with the aerodynamic representations) do not affect the final results. The two electrical elements of primary interest are transformers and inductors. The high quality capacitors available in the analog computer can be assumed to have negligible parasitic impedance in comparison to the transformers and inductors which also are high quality but unfortunately not good enough compared to the capacitors.

The transformers experience the following parasitic impedances which result in the following inconsistencies not usually present in the digital set-up:

(1) leakage inductance—represents shear compliance
(2) magnetizing inductance—represents tension in beam
(3) series resistance—represents shear damping
(4) shunt resistance—represents slope damping
(5) shunt capacity—represents rotary inertia

The inductors experience the following parasitics which introduce the corresponding mechanical effects:

(1) series resistance—structural damping
(2) shunt capacity—inertia, direct or coupling, depending on location of inductor

Since the transformer parasitics are dependent on the turns ratio (they vary as the square of the turns ratio), their parasitics are considerably more significant in a typical vibrations (or flutter) problem than the inductor parasitics. Although these parasitics have somewhat of a parallel to the actual structure, unfortunately they are difficult to evaluate and consequently are difficult to represent by comparable digital methods. One of the most apparent effects of the parasitics appears as "structural" damping. Although this effect has a negligible effect on the frequency, the relative amplitudes can be affected appreciably. In the next major section of this paper details of the differences to be expected for a typical problem will be illustrated.

Aerodynamics Check

The addition of the aerodynamic forces and moments to the vibration set-up provides a means of determining the suitability of the dynamic system in terms of stability such as flutter, as well as load responses due to gusts. Since the aerodynamic representations are perhaps the most difficult physical quantities to describe electronically on the analog, a great deal of care must be taken in their representation. Once again complete independency of the digital and analog set-ups is required. An individual aerodynamic cell check on the analog is recommended. The procedure consists of separating each cell inputs from their corresponding nodes and then the inputs are driven with individual sinusoidal voltages representing the velocities of the particular degrees of freedom. The output of the cell is measured by a current representing either a lift or moment or perhaps some part of each. The output current with respect to a unit input voltage is evaluated in terms of modulus and phase for a range of input frequencies. These modulus and phase functions can be compared readily with the values used in the digital analysis which in the eigenvalue form necessitates representation in terms of a frequency response. Once all the cells are checked for the frequency range to be expected for flutter, dynamic stability, and gust load con-

siderations, the analog set-up can be considered as checked.

A discussion of the additional differences between the analog and the digital methods due to the inclusion of the aerodynamics appears warranted. The first obvious difference is once again the method of "excitation." The digital method, due to practical considerations, is handled once again as an eigenvalue problem. As usual all of the roots are not obtained since the higher roots have relatively little significance, and therefore, simple matrix iteration is used. However, a sufficient number must be obtained to insure that the critical roots have been obtained. Although no set rule can be established as to the number of roots to be determined, approximately six to eight should be considered as a maximum satisfactory number. Since these results are used basically for checking the results obtained on the analog, it is felt that with the aid of good judgement on the part of the dynamicist, a minimum number of roots need be obtained for insuring not only the attainment of the critical roots but also the correctness of the results of the analog. The method of excitation for the analog depends of course on the problem under investigation. For stability investigations, such as flutter, a highly damped sine wave excitation at one location on the structure would be sufficient in general. By variation of the frequency of the damped sine wave a certain degree of selectivity of the roots is possible. In general the computer automatically selects the least damped root, and if the system is unstable or at neutral stability usually no excitation is required. If the roots are damped at an air speed below neutral stability, particular roots can be excited and examined for its characteristics such as damping and frequency by variation of the frequency of the damped sine wave excitation as well as its location on the structure. The results from the analog assures the dynamicist the determination of the critical roots, consequently this information provides a reasonable guarantee for determining the maximum number of roots required in the digital method.

One of the most important additional differences between the analog and the digital techniques is the representation of the aerodynamics. The digital technique requires representation by numerical values as a function of a parameter which resulted from the assumption of harmonic motion. These numerical values must be represented by some continuous mathematical function which must have a simple electrical counterpart for use on the analog. Aside from the differences due to mathematical and electronic approximations, differences in the responses when not at neutral stability also exist since the motions are not harmonic as assumed to be in the digital methods. When the responses are positively or negatively damped, the significance of these differences must be interpreted in light of the original assumptions involved in the aerodynamic representations. These interpretations can best be discussed by examples and will be given in the next section.

Example of Methods and Check Procedures for Typical Production Problems

The method outlined in the preceding sections was recently applied to the tail symmetric flutter analysis of a transport-type airplane being built at Lockheed. The network analyzer was used together with the IBM 701 digital computer. The problem required analysis of the coupled stabilizer, elevator, and fuselage motions. In view of the complex nature of the configuration to be analyzed, a large number of degrees of freedom was required to adequately describe the natural vibration characteristics of the configuration as well as the flutter modes.

Distribution of Structural and Aerodynamic Cells

The full capacity of the network analyzer was utilized as well as the maximum programming techniques available at the time of investigation on the IBM 701 Computer. Six spanwise stations for the stabilizer and elevator combination were chosen as well as five sections for the fuselage. This combination provided six bending and six torsion modes on the stabilizer, six elevator flapping and torsion modes, as well as five fuselage vertical vending modes. Simple beam theory was used for representing the structure in bending and torsion. The elevator was assumed to have a flapping mode with a restraint determined by the boost system. The torsional rigidity of the torque tube required to transfer the elevator hinge moments into the fuselage through the boost system was also represented. In addition an elevator balance weight located at the fuselage centerline was assumed as a separate degree of freedom because of its large concentrated weight on the relatively flexible torque tube extending from the inboard end of the elevator to the balance weight linkage. The whole airplane was free to pitch and plunge. Unfortunately, the wing flexibility was not included due to the limited capacity of the computer. This problem illustrates very well the degree of complexity of airplane structure that can be handled by such a computing facility; its justification was substantiated by observed shake tests of the airplane.

The aerodynamic representation on the computer was based on standard-type two-dimensional incompressible flow considerations together with strip theory to account for three-dimensional effects. The transient aerodynamics were applied to the bending and torsion cells of the stabilizer and to the elevator cells. No aerodynamic representation was assumed for the fuselage. A sketch of the degrees of freedom previously discussed is given in Fig. 5.

Comparison of Static Deflections for Elasticity Checks

In order to provide a continued check on the validity of the analog computer results, a corresponding set of IBM calculations were made using a breakdown of the structure on a "panel" basis similar to that required on the analog. The first stage in the correlation was to check the stiffness circuits on the analog as well as

the stiffness values. This was accomplished by applying loads, moments, and hinge moments and recording the deflections. A comparison of the deflections was then made with those calculated from the IBM "panel" representation for the same loading conditions. These comparisons are given in detail in Fig. 6, for bending and torsion of the stabilizer as well as the elevator deflection. Note the remarkable agreement between the two approaches. No detailed structural deflection measurements were made for the fuselage. It was found that the description of the fuselage mode required a modification in the stiffness and mass distribution from the actual representative values. This was necessary due to the presence of a wing bending mode occurring approximately at the same frequency as the fuselage mode. Since the full capacity of the computer was utilized for description of the stabilizer-elevator-fuselage modes, the wing flexibility could not be included in the computations. In order to provide the effects of wing flexibility in the fuselage mode, the fuselage stiffness and mass distribution were altered, such that their effects on the stabilizer and elevator modes, which were of primary interest in this flutter study, were correct. This alteration required numerous parameter variations and, as a result, was ideally suited for the analog. The net result, then, was a pseudo fuselage which represented a wing and fuselage that had the proper "impedance" as viewed by the stabilizer and elevator. Since this "impedance" representing the wing and fuselage appeared as one natural frequency (the higher modes were not important in the natural modes of the stabilizer and elevator) and no aerodynamics was assumed for the fuselage and wing combination in the tail analysis, such an approximation did not appear to be serious. These approximations were made on the basis of available shake tests of the airplane.

The elasticity checks, which were made concurrently on the digital and analog computers, took approximately 1 week from the time the structural data were made available to the engineers.

Analog and Digital Ground Vibration Test Correlations

The next step in the provision of a continued check on the validity of the analog computer results required the addition of appropriate masses, inertias, together with the proper center of gravity locations of the masses in order that a vibration test correlation could be made. Since the fuselage modes were matched on the analog with observed shake tests and no aerodynamics would be present on the fuselage, the correlations were made with the fuselage rigid and restrained in pitch and plunge. A summary of the natural frequencies obtained by the two computers is given in Table 2.

Note the close agreement between the two completely independent solutions. The differences in frequencies between the digital and analog are most likely due to the differences in integrating matrices used in the digital method and the method of lumping of structural parameters in the analog circuits. The analog approach implies a trapezoidal type of integrating approximation while the digital representation consistently employed parabolic-type approximations similar to Simpson's rule.

TABLE 2
Comparison of Analog and Digital Natural Frequencies

Analog (c.p.s.)	Mode	Digital (c.p.s.)
6.4	Stabilizer first bending	6.12
7.34	Elevator flapping (boost on)	7.30
16.8	Elevator first torsion	16.23
22.85	Elevator second torsion	23.1
28.0	Stabilizer second bending	26.4
32.1	Stabilizer first torsion	33.3

The corresponding mode shapes and relative phasings were also compared. A typical comparison is shown in Fig. 7 for the stabilizer first bending mode. Examination of the results in Fig. 7 as well as those for the other modes indicated that, in general, the agreement of the mode shapes and relative phasings agree remarkably well; the relative amplitudes, however, experience appreciable differences. These differences are primarily a result of the inherent "structural" damping of the order of one to two per cent present in the analog computer. The corresponding digital calculations were made, of course, with no structural damping. As would be expected, the small damping would have little effect on the natural frequencies, mode shapes, and relative phasings, but a noticeable effect on the relative amplitudes of the modes. If the distribution of "structural" damping was known for the analog, then this distribution could be simulated on the digital representation and more favorable comparisons could be obtained. In addition, the compatibility of the method of excitation of the modes on the analog and digital set-ups must be considered since structural damping would be present on both. This implies, then, that the analog excitation at possibly all the degrees of freedom is necessary to be comparable with the results obtained digitally. However, the differences that do exist between analog and digital calculations are relatively minor; they can be explained readily but unfortunately would require a prohibitive amount of additional work to eliminate them. On this basis, the present correlation appears sufficient for engineering purposes.

An estimate of the time involved to set up this problem on the analog and digital computers was made. Since both set-ups are made completely independent of each other, both problems were solved simultaneously and took approximately 1 week from the time the elasticity checks were made. Parameter variations made on the analog for several days to determine the adequacy of the degrees of freedom selected as well as the structural data determined from preliminary calculations. One conclusion drawn from this study is that the large number of degrees of freedom used in the analysis were necessary to adequately describe the stabilizer and elevator natural frequencies.

Flutter Stability Diagrams

In view of the excellent correlation obtained in the natural vibration study, the aerodynamics were applied to the stabilizer and elevator to determine the flutter characteristics. The aerodynamic representation on the analog was first checked using "aerodynamic cell checks," where sinusoidal inputs to the aerodynamic cell circuit are applied at several frequencies. The output to input ratios, both modulus and phase, can then be compared directly with the corresponding numerical values used in the digital representation. These checks were made for lift, pitching, and hinge moments due to bending, torsion, and elevator motion. Once these checks were made, the flutter stability calculations were determined on both set-ups. The significant results are plotted in Fig. 8 as a function of logarithmic increment of damping versus speed, normalized to the flutter speed obtained on the analog. Although other modes were present on both the analog and digital solutions, the one shown in this figure represents the most critical, that is, the mode having the lowest flutter speed. Also shown are the frequencies of oscillation for the analog and IBM at various stability and speed conditions. Comparison of the two solutions indicates that the frequency of oscillation at flutter agrees remarkably well. The flutter speed for the analog, however, is higher than the speed obtained by the digital set-up. This difference can best be explained by interpreting the use of the damping parameter, g, when applied to analog and digital calculations together with the inherent "structural" damping present in the analog. As noted previously, the proper interpretation of "g" for the analog is the actual aerodynamic damping present on the system, while for the digital solutions the "g" represents the amount of structural damping required to sustain an oscillation. This difference in "g" interpretation is due, of course, to the difference in aerodynamic representations on the digital and analog computers. To account for this difference approximately the digital computations can be plotted such that the "structural" damping in the analog is accounted for in the digital solutions. Although the exact distribution of the damping is difficult if not impossible to determine, an average value can readily be obtained and assumed to be uniform in the structural representation. For the calculations shown in Fig. 8 approximately one to two per cent damping was observed to exist. If a value of $g_s = 0.015$ is used for the digital calculations, the revised digital stability curve corresponds almost identically to the analog curve. Thus the necessary correlation has been established. At this point the effect of numerous variations of structural or aerodynamic parameters on the critical flutter speed can be investigated in a relatively short time.

The amount of time required to make this correlation from the time the vibration checks were completed depended to a large extent on the complexity of the aerodynamic representation, the dependability of the active elements in the analog computer such as amplifiers and associated power supplies, as well as the extent of programming techniques available on the digital computer. If complete familiarity of the aerodynamic circuitry for the analog representation is available and no failures in equipment are present, then approximately 1 to 2 weeks are required to obtain the desired set-up on the analog. Similarly, if the programming techniques for solving the required eigenvalues on the digital set-up are available, approximately 1 to 2 weeks are required. Experience has indicated that the time involved in arriving at a satisfactory set-up on the analog or digital computers for the flutter problem depends on numerous factors, and thus a definite time requirement is difficult to state. Such problems as availability of personnel, their training, cooperation, and understanding of the problem, enter as important and necessary considerations in determining the time requirements as well as the feasibility of computing such problems by this approach. These problems are, of course, difficult to evaluate except by actual operating experience.

Extension of Dynamic Representation to Landing and Taxi Load Studies

Once the vibrations are checked a landing gear representation may be added to the existing structural representation. Dynamic load studies for different landing approaches or runway profiles may be made. No digital checks for these studies are necessary since the addition of the landing gear is relatively simple and presents little chance for error. The time required for simulating the landing and taxi load representations is usually from 1 to 2 days. The aerodynamics are usually eliminated since, in general, these studies are made at extremely low airplane speeds and the forces and moments derived from this source are considered negligible.

(A) *Dynamic Landing Loads*—Due to the complex oleo-pneumatic action of most landing gears no attempt is made to represent the component actions of the gear on the computer. Instead, recourse is had to drop tests of the actual or a similar landing gear. The load time histories obtained from these tests may be considered to be applicable to the airplane for the same conditions of vertical velocity at contact and static load on the gear. These load time histories are used as the excitations on the computer. In Fig. 9 a sketch of the landing gear representation is shown for the landing load investigation together with some typical time histories of vertical and drag loads. The drag load is determined by the coefficient of friction times vertical force and acts up to time, t_s, required for the wheels to reach maximum spin-up speed. At that time the drag excitation ceases. The drag impulse, defined as the area under the drag-time curve, is usually made equal to the angular impulse of the wheel at airplane touch-down speed.

The quantities measured on the analog computer are time histories of accelerations of pertinent mass sta-

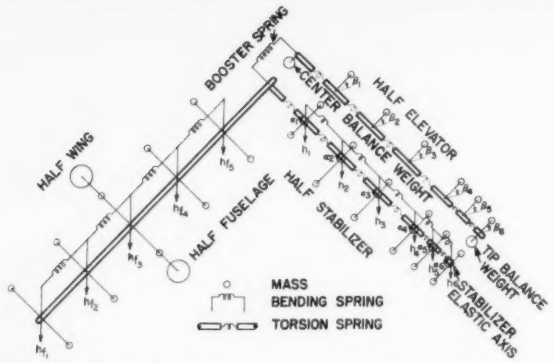

FIG. 5. Schematic of degrees of freedom for symmetric tail flutter.

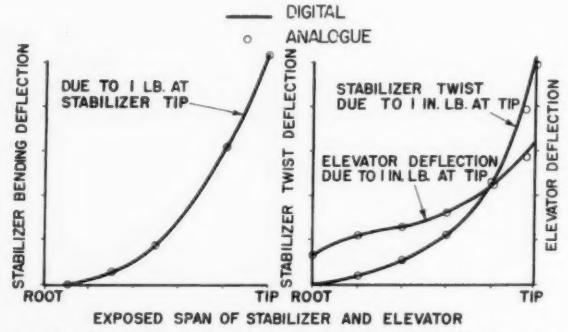

FIG. 6. Comparison of analog and digital static deflections due to unit tip load and moments.

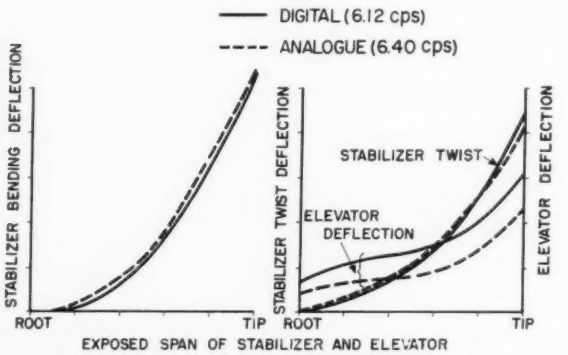

FIG. 7. Comparison of vibration modes for stabilizer first bending determined on digital and analog computers.

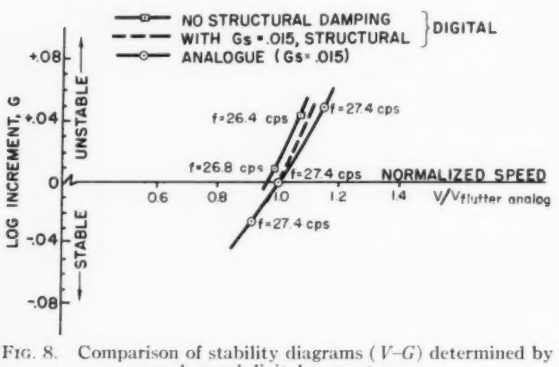

FIG. 8. Comparison of stability diagrams (V–G) determined by analog and digital computers.

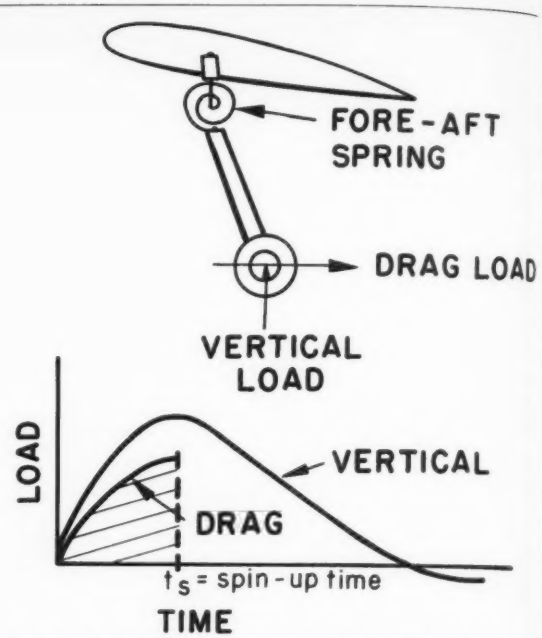

FIG. 9. Typical landing gear representation and time histories for dynamic landing load studies.

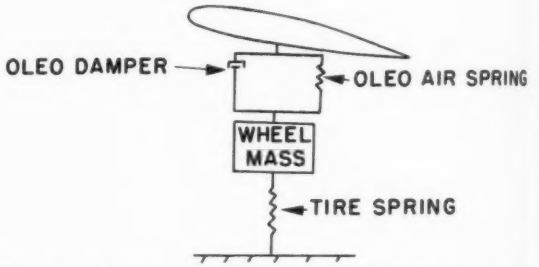

FIG. 10. Typical landing gear representation for dynamic taxi load studies.

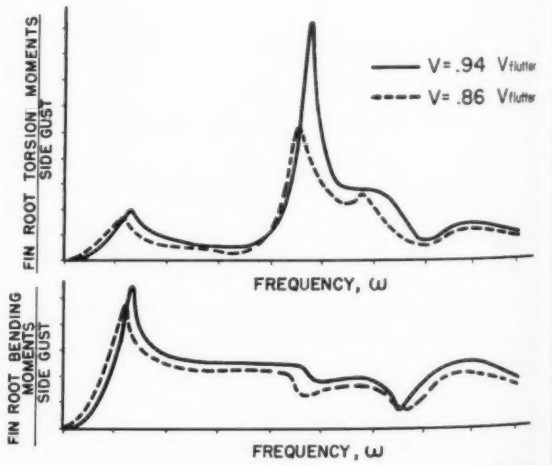

FIG. 11. Transfer functions (modulus) of fin root bending and torsion moments due to sinusoidal side gust at two speeds.

tions such as engines, fuselage (at wing elastic axis), or the wing tip. If a flexible fuselage representation is present, the nose and tail fuselage accelerations are also recorded. These accelerations could be used to determine load factors for the masses from which a spanwise variation of load factor may be obtained directly for design. Some discretion may be necessary in use of simultaneous maxima of different quantities for design.

(B) *Dynamic Taxi Loads*—The normally small displacements of the gear oleo while taxiing provides the possibility of representing the landing gear by a linear system of springs, mass, and damping components over the range of displacements of interest. A typical gear representation is shown in Fig. 10 for the oleo, wheel, and tire spring. This representation is added to the original analog set-up, and excitation is introduced as a displacement time history of the gear. The specific form of the displacement depends to a large extent on the method of analysis. One of the most promising approaches is the use of power spectral methods which provides a means of determining a rational criteria of the loads experienced based on probability techniques for random gear displacement inputs as would be represented by the roughness profile of a runway. The details of this approach are unfortunately too complicated to describe in this paper; in fact their description could readily be the subject of a separate paper. What should be described is the information required for such an analysis and how it can be obtained from the analog computer. This information is basically the desired transfer function relating the accelerations of pertinent masses previously described in the landing loads section to sinusoidal gear inputs. Usually the modulus as a function of input frequency is the desired quantity rather than the phase-frequency curve. This function can readily be obtained by using a sinusoidal input displacement on the gear (tire) and observing the amplitude of acceleration of desired masses on the airplane over a wide range of input frequencies. The transfer functions determined for the desired accelerations on the airplane can then be used in the power spectral analysis.

Extension of Dynamic Representation to Gust Load Studies

With the availability of the structural and aerodynamic representations for flutter investigations the use of special aerodynamic forcing functions desired for simulating the penetration of a wing or tail into a gust allows for an evaluation of the gust load experience of the airplane. Once again the type of forcing function (gust profile) used on the computer depends entirely on the method of analysis. Although in the past the discrete gust-type analysis has been used predominantly, the introduction of power spectral methods, using the transfer function concept, has attained increased importance recently. Here again the gust loads for design may be determined by more rational requirements employing probability criteria as well as recognizing the continuous randomness of the gust structure in the atmosphere. The simulation of the applied gust forces and moments is relatively simple, requiring a small fraction of computer set-up time, say, 1 day, and consequently requiring no digital checks. The desired information is in the form of transfer functions relating the accelerations of certain masses critical for gust load factors, bending and/or torsion moments of primary beam structures, etc., to sinusoidal gust inputs of varying frequency. A typical set of transfer functions of the bending and torsion moments at the root of a fin are given in Fig. 11. The results are for an elastic fin, stabilizer, and fuselage combination which is also free to roll and yaw. The calculations were made for two speeds below the flutter speed of the configuration. Note the pronounced effect of speed on the pertinent modes. Such calculations provide the necessary information for more rational gust load analysis of not only rigid, but highly flexible airplane structures.

In addition to the gust investigations, other related problems, such as the loads due to buffeting of wings and tail surfaces, may be studied. Such studies also require definition of the load response in terms of transfer functions and therefore can be readily obtained on the analog once a flutter problem has been simulated.

Thus the integrated use of such a computing facility provides innumerable applications for aircraft dynamics problems and is limited only to the extent of available computing equipment and the ingenuity of the dynamics engineer.

Suggestions for Future Research

In the design of a dynamics-type analog computing facility, such as the one available at Lockheed, a great deal of emphasis has been directed to permit rapid variations in airplane structural properties—that is, the passive electrical elements, such as inductors, capacitors, and resistors can be changed quickly and in sufficiently small increments. In contrast, little development work has been done for possible rapid variations of the aerodynamic representations. That is, the circuitry associated with the active elements—amplifiers and current generators—is relatively inflexible to parameter variations. The flutter and associated aerodynamic loads problems admittedly require precise knowledge of the structural characteristics of the airplane, but unfortunately knowledge of the transient aerodynamic properties of the lifting or control surfaces is considerably less available in comparison to the structural properties. Thus, investigation of the proper transient aerodynamics by closely correlated analytical and experimental studies such as Lockheed's rocket model program implies the necessity of providing rapid and accurate variations of the transient aerodynamics.

Since the present approach of investigating aircraft dynamics problems implies an integration of analog and digital computers, the compatibility of the computing potential of both machines is therefore an extremely important consideration. The principal factor which prevents complete compatibility is again the

aerodynamic representations on the analog computer. Specifically, the problem is the proper balance of active to passive elements available in the computer. Lockheed's present computer has an optimum balance of active to passive elements if a conventional incompressible two-dimensional transient theory such as Theodorsen's is represented. For any other transient aerodynamic theory, the required number of active elements per structural cell is usually doubled or tripled, and therefore the use of the computer for dynamic load or stability problems becomes extremely limited if not entirely useless. Thus, considerable development work by the electronics designers should be directed along these lines to insure compatible capacity for the analog to that available on high speed-large memory digital computers.

An additional aerodynamic problem on the analog for future study is one with which aerodynamicists should be concerned. Those familiar with the available transient aerodynamic theories know that the aerodynamics is so complicated that the information is usually given in tabular form for a specific type of motion such as constant amplitude sinusoidal motion. These tables, which are a function of a nondimensional frequency parameter, are difficult to represent on the analog computer since their equivalent representation is done by an electrical circuit which approximates the tabulated aerodynamic values over a range of nondimensional frequencies. Fortunately, such approximations are relatively simple for the familiar and most used theory—two-dimensional incompressible flow. Again if any other theories are considered the associated electronic circuitry becomes increasingly complex; in most instances, a large development program must be initiated to even determine the general form of the electronic circuitry. For instance, the representation of two-dimensional transient supersonic aerodynamics is possible with a variety of circuits, requiring anywhere from five to ten amplifiers per structural cell for describing the lift and moment due to bending and torsion motions. The question of the optimum reference axis for maximum accuracy also arose and was finally decided by extensive development studies. In some cases, the mathematical expressions for optimum approximation lead to physically unrealizable circuits, such as negative resistors and capacitors. Thus the overall optimization was extremely complex and involved an intensive study. The investigation of the other theories for which information exists for use in digital calculations must be examined and explored such that once again a reasonable degree of analog and digital computing compatibility is attained. In the same light the development of new aerodynamic theories as well as their solution should be considered with the viewpoint of representation not only in tabular form for digital calculation but also by electronic circuitry for analog computers.

Several remarks concerning the existing differences among the analog and digital results are apparently warranted. One problem in interpreting the significance of an analog and digital correlation is the errors induced in the analog results due to residual inductance, capacitance, and resistance of the electrical elements. Although in the successful development of the computer these factors were considered, unfortunately they cannot be entirely eliminated. Consequently their existence must be recognized and understood in the interpretation of analog and digital comparisons. On the other hand, if these residuals can be evaluated quantitatively, possible modifications of the digital calculations are feasible which will provide additional assurance of the correlations. These modifications can include arbitrary but known distributions of structural damping as determined from the analog. Knowledge of this damping distribution is not only important for digital comparisons, but is one of the principal factors in taxi and landing load studies where the inherent "structural" damping of the computer represents almost the entire damping present in the system. A possible modification for digital aerodynamic representation is the use of aerodynamic coefficients which are not only a function of a steady-state sinusoidal motion but also of the degree of positive or negative damping of the motions. Such aerodynamic representations will eliminate the differences in interpretation of the stability-speed diagram (g-V) usually used in flutter investigations; that is, "g" would then represent the actual aerodynamic damping for both the analog and digital computations.

It is apparent, therefore, that numerous worth-while development programs can be undertaken to extend the usefulness of both the analog and digital computing facilities for dynamic load problems in a still faster and more accurate manner than that indicated in the present paper.

Concluding Remarks

This paper attempts to define the major phases of the dynamic loads problem faced by the dynamicist at various design stages of the airplane. Such problems as vibration, flutter, gust loads, taxi and landing loads are described at three design stages of the airplane. At each stage the nature of these problems was investigated and the following characteristics were found to exist for each:

(1) The dynamic problems are becoming increasingly complex due to higher airplane speeds and increasingly flexible due to thinner lifting surfaces necessary for optimum performance.

(2) The amount of time required for obtaining accurate results which make good "engineering sense" is critically limited since accurate structural and aerodynamic data are not readily available.

(3) As a result of the lack of data a large number of parameter variations are required in the preliminary design stage. Examination of the other two stages—shake test and final analysis—also indicates the requirement of a large number of parameter variations.

(*Continued on page 780*)

An Analysis of the Performance of an Axial-Flow Compressor at Low Reynolds Number*

ROBERT L. SOHN†

Propulsion Research Corporation

SUMMARY

An analysis of the performance of an axial-flow compressor of low Reynolds Number has been made. The performance of the machine at low Reynolds Numbers is explained in terms of the behavior of the boundary layer attached to the blades. It is hypothesized that, under ordinary operating conditions, the blade boundary layer forms a laminar separation bubble shortly downstream of the point of minimum pressure, reattaching in turbulent form after transition has taken place. At very low Reynolds Numbers, the separated boundary layer is so stable that transition fails to take place upstream of the blade trailing edge. Under these conditions, the fluid turning accomplished by the blade decreases abruptly, and the blade profile losses increase with attendant loss in efficiency.

The existence of a "critical" Reynolds Number as described above is verified by test data. An empirical method based on cascade data is derived for use in predicting the critical Reynolds Number and is shown to be in good agreement with test results.

SYMBOLS

A = boundary layer parameter $\equiv \left[0.45\left(\frac{V}{V_1}\right)^{-6}\int_0^{x/c}\left(\frac{V}{V_1}\right)^6 d\left(\frac{x}{c}\right)\right]^{1/2}$

c = blade chord

C_a = axial velocity

C_D = overall loss coefficient $\equiv \frac{(\Delta p)_{ideal} - (\Delta p)_{actual}}{(1/2)\rho V_{av}^2}$

D_L = diffusion factor $= A^2\frac{d(V/V_1)}{d(x/c)}$

H = shape factor $= \delta^*/\theta$

R = Reynolds Number

V = local velocity outside the boundary layer

u_t = rotor tip speed

x = distance along the airfoil surface

Δp = pressure rise through a blade row

β = rotor air inlet or discharge angle

δ = boundary-layer thickness at $v/V = 0.707$

δ^* = boundary-layer displacement thickness $\equiv \int_0^\infty\left(1 - \frac{V}{V_1}\right)dy$

η = adiabatic efficiency

θ = boundary layer momentum thickness $\equiv \int_0^\infty\left(1 - \frac{V}{V_1}\right)\left(\frac{V}{V_1}\right)dy$

λ = ratio of length of separated region to the boundary-layer thickness at separation

ν = kinematic viscosity

ρ = density (slugs per cu.ft.)

φ = flow coefficient $= C_a/u_t$

ψ = power coefficient $= \frac{2u\Delta C_u}{u_t^2} = \frac{\text{power/unit mass flow}}{(1/2)u_t^2}$

ψ' = pressure coefficient $= \frac{CpgJT_1[(PR)^{(\gamma-1)/\gamma} - 1]}{(1/2)u_t^2}$

Subscripts

e = refers to Reynolds Number based on axial velocity

av = average velocity through a blade passage

s = conditions at separation

1 = inlet to a passage

2 = discharge from a passage

Received June 6, 1955.

* The author gratefully acknowledges the contributions of personnel at Propulsion Research Corporation and the University of California at Los Angeles who performed the careful experimental work. Particular thanks go to R. L. Greengard, R. M. Jacobsen, J. P. Dutt, and to Dr. A. F. Charwat.

† Senior Engineer and Head, Thermodynamics Group.

INTRODUCTION

THE INFLUENCE of Reynolds Number on the performance of axial-flow machines is becoming a major consideration in design work for two reasons. First, conventional turbojets are being designed for flight at extreme altitudes, and second, widespread application of small, auxiliary fans and blowers is becoming common in the air-frame industry. To date, few tests have been conducted on axial-flow components at very low Reynolds Numbers, and few if any methods exist for predicting performance under these conditions.

It is hoped that the present paper will give the designer of axial-flow machinery a better understanding of Reynolds Number effects as well as a method for meeting the design requirements. Additional investigations in this field are suggested herein.

THE LAMINAR SEPARATION BUBBLE

At normal angles of incidence, the boundary layer over the forward portion of an airfoil is usually laminar. Downstream of the point of minimum pressure, the flow begins the diffusion process, the adverse pressure gradient causing the laminar boundary layer to separate from the blade. Depending upon the local Reynolds Number at the point of separation, the separated laminar boundary layer goes into transition and soon becomes turbulent. The turbulent motion enables the boundary layer to spread and reattach itself to the surface of the blade. However, if the local Reynolds Number is very low, the boundary layer is quite stable and resists transition until the flow has passed over the airfoil trailing edge. A sketch of the laminar separation bubble phenomenon is shown in Fig. 1.

A high angles of incidence, sharp minimum pressure peaks are encountered very near the leading edge, causing the separation point to move to the leading edge. The same bubble mechanism takes place, but

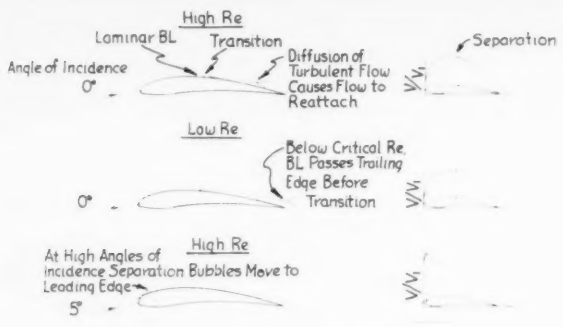

FIG. 1. The laminar separation bubble.

failure to reattach occurs at a slightly lower inlet Reynolds Number (because the flow has a greater distance in which to reattach).

Finally, an angle of incidence is reached at which separation will occur regardless of Reynolds Number. The pressure gradients are too steep even for the turbulent boundary layer to negotiate, and the flow goes into stall.

When the boundary layer fails to reattach, the amount of turning accomplished by the blade abruptly decreases. The blade wakes widen out, and the profile losses increase accordingly. Below this critical Reynolds Number, the airfoil performance can be expected to deteriorate rather rapidly.

The laminar separation bubble is, however, a rather remarkable, and a very fortunate, natural phenomenon. In a sense, it is an automatic, high-performance boundary-layer trip that goes into operation as soon as the flow must negotiate an adverse pressure gradient. The turbulence created by the bubble causes almost immediate transition, the resulting turbulent motion providing a mechanism for reattachment. The reattached turbulent boundary layer can negotiate much higher rates of diffusion. The "natural trip" takes only a fraction of the chord to effect transition, follows the peak pressure point unfailingly, and has none of the drag losses of a mechanical trip.

In brief, cascade performance at low Reynolds Number seems intimately connected with the performance of the laminar separation bubble.

Review of Experimental Work

The laminar separation bubble was first noticed in connection with the stalling of isolated airfoils and was reported by Jones[1] in 1934. Von Doenhoff[2] made some measurements of boundary-layer profiles in a separation bubble and reported the results in 1938. Later investigations[3–5] included more detailed mappings of the extent and shape of the separated regions, there being at that time an extensive effort to achieve low-drag airfoil sections by preserving the laminar boundary layer as far aft on the chord as possible.

A recent study[6] of the laminar separation bubble not only mapped the shape and boundary-layer characteristics of the bubble but also made an important correlation between the boundary-layer Reynolds Number* at separation and the length of the separated region—that is, the distance required for the boundary layer to reach transition and reattach to the surface.

That such a relation exists seems reasonable because transition is dependent upon the boundary-layer Reynolds Number, turbulence level, and pressure gradient. Furthermore, boundary-layer growth along the airfoil is likewise dependent upon the Reynolds Number and upon the pressure distribution. For a given airfoil and given turbulence level, one would expect the point of transition and reattachment to have a definite relationship with the boundary-layer Reynolds Number at separation. This is shown to be the case in Fig. 2, which summarizes the results of the NACA isolated airfoil data.[6] Two curves are shown, one for low angles of incidence where the separated region occurs near the midchord, and the other for high angles of incidence where the bubble is located very close to the leading edge. The bubble apparently shifts rapidly to the leading edge at angles of incidence above about 5°.

Unfortunately, little work has been done on local separation regions for airfoils in cascade, particularly at high angles of incidence (near peak efficiency or peak pressure coefficient). The bubble does exist, however, and effects can be seen very clearly in the cascade pressure distribution summaries of reference 7.

Sawyer[8] has made one of the few comprehensive studies of cascade performance at low Reynolds Numbers. The separated region was mapped as to length over a wide range of Reynolds Number. A critical Reynolds Number was reached, at which point the flow failed to reattach. The same series of tests was carried out at different turbulence levels and, in one case, with a transition strip attached. Complete velocity profiles were included for each case so that the laminar boundary-layer growth could be calculated.

Sawyer's cascade performance is summarized in Fig. 3, where the Reynolds Number at which the flow fails

* Reynolds Number based on the boundary-layer thickness and on the local velocity immediately outside the boundary layer.

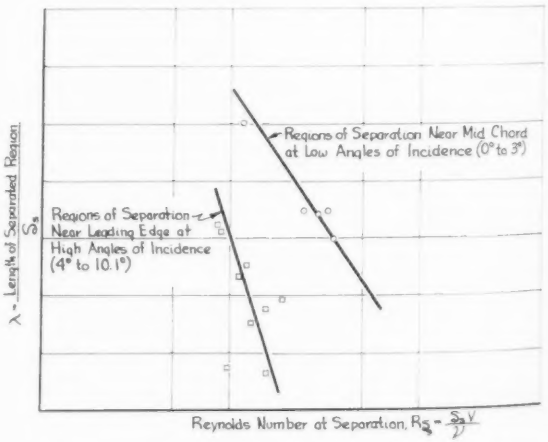
Regions of Separation Near Mid Chord at Low Angles of Incidence (0° to 3°)
Regions of Separation Near Leading Edge at High Angles of Incidence (4° to 10.1°)
Reynolds Number at Separation, Rs = Ss V / ν

FIG. 2. Length of separation bubble for isolated airfoils.

to reattach is clearly defined by the abrupt change in turning or discharge angle. It will be shown later that the separation bubble shape can be related to the boundary-layer Reynolds Number in a manner similar to that shown in Fig. 2 for the isolated airfoils.

One other set of cascade data exists which is quite useful in the boundary-layer analysis. Australian researchers[9] have mapped the extent of the separated boundary layer over a range of angles of incidence, indicating the shift of the bubble from midchord to leading edge as angle of attack is increased. The results are shown in Fig. 4 for two cascade configurations. Reynolds Number variations were not investigated.

Maekawa and Atsumi[10] reported in 1948 on some experiments designed to illustrate transition caused by laminar flow separation. Their results are not directly applicable to cascade analysis, although they did indicate that the breakdown of separated flow into transition occurred at a fixed Reynolds Number based on the distance traveled downstream from the point of separation. The diffusion angles of the turbulent flow are presented, but details of the boundary layer—thickness and velocity distribution—are not given.

Observed Performance of an Axial-Flow Compressor

The brief description of boundary-layer behavior on both isolated and cascaded airfoils given above suggests the performance of an axial-flow compressor at low Reynolds Number. Some unpublished data obtained by Propulsion Research Corporation are qualitatively summarized to verify the anticipated trends.

Fig. 5 indicates the variation of maximum efficiency and peak pressure coefficient with Reynolds Number.

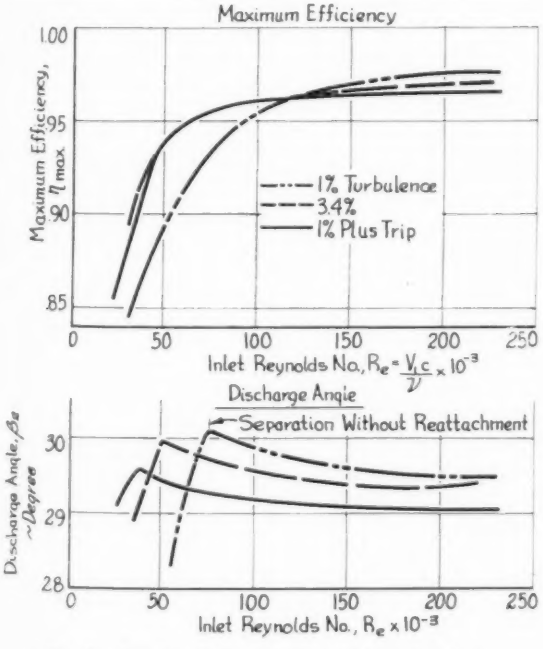

Fig. 3. Results of Sawyer's cascade investigations.

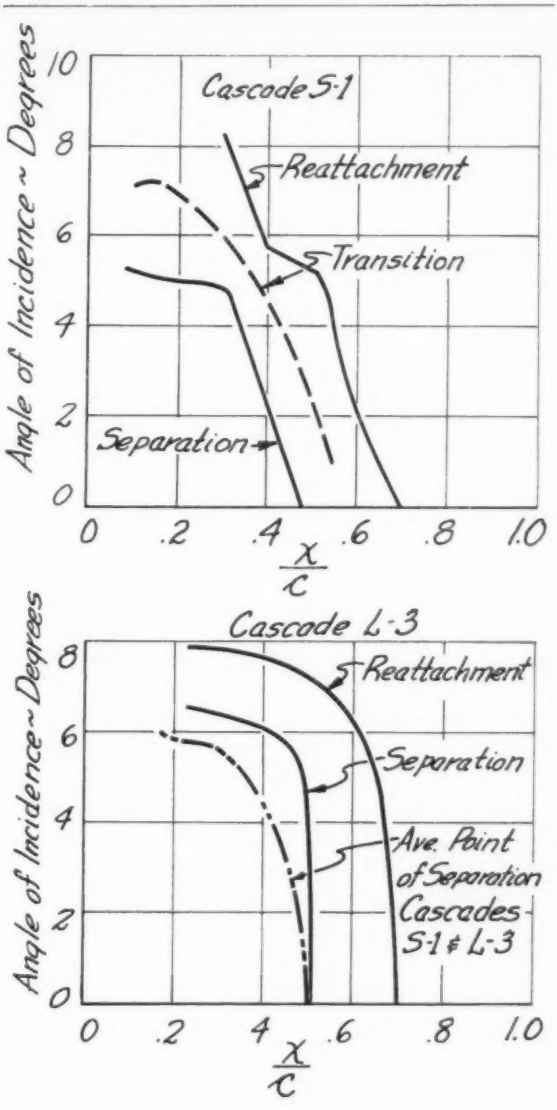

Fig. 4. Chordwise location of separation bubble.

The distinct break in the data at the critical Reynolds Number is noted. The slight shift in the critical Reynolds Number is due to the fact that the above performance parameters do not occur at the same flow coefficient. (The influence of flow coefficient is discussed later.)

The influence of Reynolds Number on power coefficient is shown in Fig. 6. The critical Reynolds Number is clearly defined in this figure. Increasing the angle of incidence of the flow (decreasing flow coefficient) causes the critical Reynolds Number to decrease since the separation bubble moves to the leading edge. As stall is approached, the critical Reynolds Number tends to approach a minimum.

The existence of the critical Reynolds Number is further emphasized by graphs of blade turning and blade wakes shown in Figs. 7 and 8, respectively. The magnitudes of the loss in rotor and stator blade turning

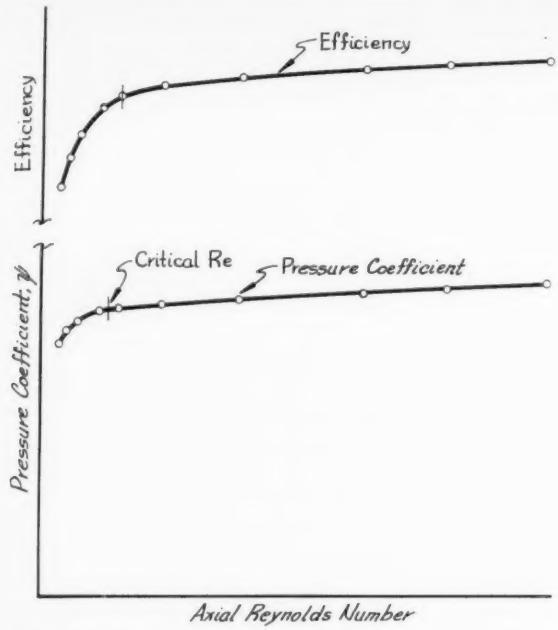

FIG. 5. Variation of maximum efficiency and peak. Pressure coefficient.

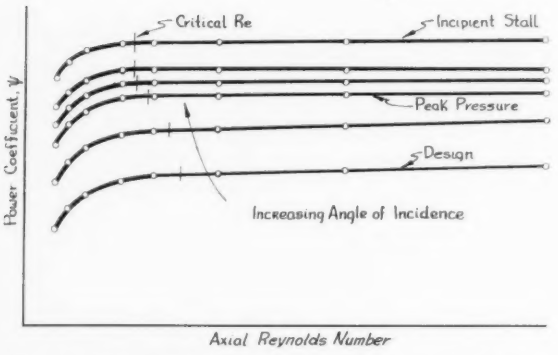

FIG. 6. Influence of Reynolds Number on power coefficient.

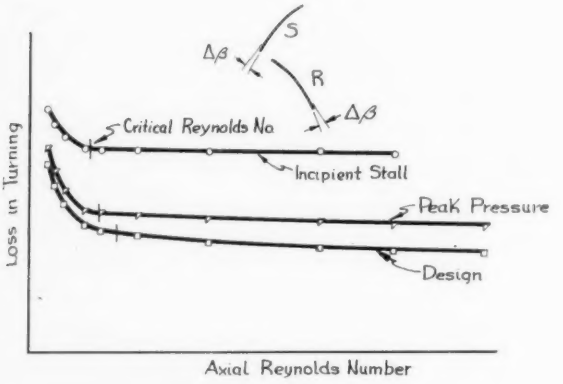

FIG. 7. Loss of turning.

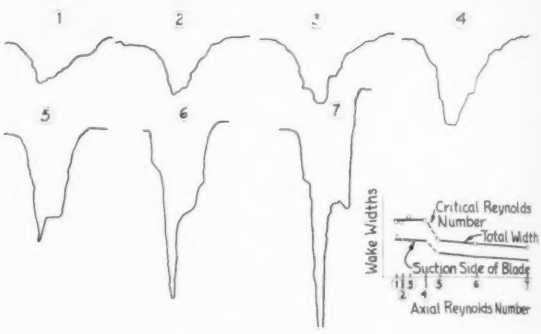

FIG. 8. Blade wakes.

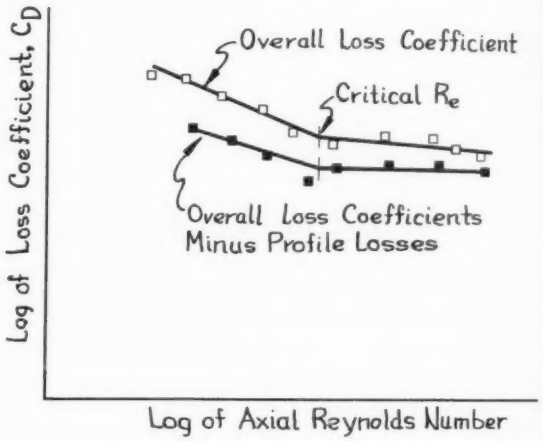

FIG. 9. Blade profile loss coefficients.

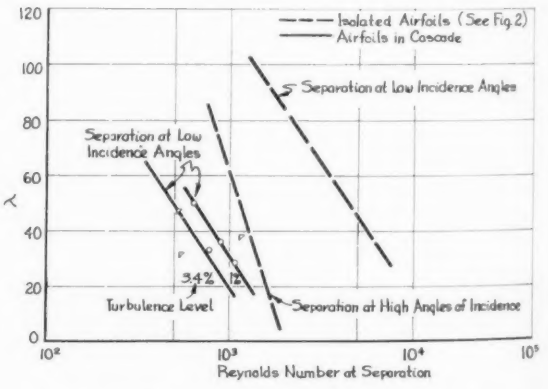

FIG. 10. Length of separation bubble for cascaded airfoils.

have been assumed to be equal. The blade profile losses corresponding to the blade wake pressure distribution shown in Fig. 8 are given in Fig. 9.

Prediction of the Critical Reynolds Number

As described previously, the laminar boundary layer on the upper surface of an airfoil separates immediately downstream of the peak velocity point. The boundary layer must then go into transition so that a turbulent mechanism can be set up to cause the flow to reattach.

In general, transition is dependent upon a Reynolds Number, R_δ calculated from the boundary-layer thickness and local velocity at a given point. The stream turbulence level and the pressure gradient influence this number considerably, however. For cascades with about the same general configuration, some empirical relation should exist between R_δ at separation and the length of the separated region (such as was shown in Fig. 2 for isolated airfoils). Such a relation will be discussed later.

Transition occurs when the laminar boundary layer becomes unstable to certain disturbances. The exact mechanism of transition is imperfectly understood, but apparently two distinct types of transition can take place—one holding for very low turbulence levels (less than 0.1) and the other occurring when the turbulence level is relatively high.[11, 12]

Transition occurring at a high turbulence level was predicted by a theory of G. I. Taylor. He assumed that transition occurs when fluctuations in the laminar layer reach a magnitude such that $\partial v/\partial y$ at the surface has momentary values less than zero (so that sporadic flow reversals take place). The scale and level of turbulence are determining factors in this type of transition. The transition at low turbulence level (less than 0.1) is preceded by instability waves as predicted by the Tollmien-Schlichting theory.

Certainly, in an actual compressor, the high-turbulence-level type of transition takes place since the effective turbulence level is greater than 0.1. Unfortunately, analytical means are not available for predicting the exact point of transition in the case of a separated boundary layer so that empirical relations are sought.

The cascade data of Sawyer[9] have been used to construct the relation between the R_δ at separation and the length of the bubble as shown in Fig. 10. Two curves have been derived for turbulence levels of 1 per cent and 3.4 per cent, respectively. By use of these empirical curves, the distance between the separation point and the point of reattachment can be estimated for any similar type of cascade if R_δ at separation is known. Furthermore, these curves can be used to find the case where the bubble will extend to the trailing edge of the airfoil, thus giving the critical Reynolds Number. It is noted that the Sawyer data describe the bubble formation at low angles of incidence only and cannot be used at high angles of incidence.

R_δ at the separation point can be calculated if the velocity distribution and inlet Reynolds Number are known. Thwaites[13] gives the following expression for the boundary-layer growth:

$$\theta^2 = 0.45\,\nu(V)^{-6}\int_0^x V^5\,dx \tag{1}$$

where

θ = momentum thickness
V = local velocity outside the boundary layer

In terms of the blade chord, inlet velocity, and Reynolds Number at the inlet, the above expression is

$$R_{V_1}\left(\frac{\theta}{c}\right)^2 = 0.45\left(\frac{V}{V_1}\right)^{-6}\int_0^{x/c}\left(\frac{V}{V_1}\right)^5 d\left(\frac{x}{c}\right) \equiv A^2 \tag{2}$$

where $R_{V_1} = (V_1 c)/\nu$

R_δ can be related to the above equation:

$$\left.\begin{aligned} R_2 = (V\delta)/\nu &= R_{V_1}(V/V_1)(\delta/c) \\ &= R_{V_1}(V/V_1)(\theta/c)(\delta^*/\theta)(\delta/\delta^*) \\ &= A\sqrt{R_{V_1}}(V/V_1)(\delta^*/\theta)(\delta/\delta^*) \end{aligned}\right\} \tag{3}$$

where δ^* = displacement thickness. The shape factor, $H = \delta^*/\theta$, at separation, is generally about 2.7 or 2.8 and can be assumed constant at this value. Likewise, at separation, δ/δ^* and R_{V_1} can be related to the axial Reynolds number since

$$R_c = R_{V_1}(C_a/V_1)$$

so that

$$R_\delta = \left[AH\frac{\delta}{\delta^*}\frac{V_s}{V_1}\sqrt{\frac{V_1}{C_a}}\right]\sqrt{R_c} \tag{4}$$

The quantity δ/δ^* has been evaluated from a typical boundary-layer velocity distribution just prior to separation and has been assumed to be constant with Reynolds Number. The term inside the brackets is now dependent on the velocity distribution alone and does not vary with Reynolds Number. Actually, Sawyer's data show some slight variation in the velocity distribution—and, hence, in the separation point—but the change is quite small.

The equivalent expression for δ/c is

$$\frac{\delta}{c} = \left(\frac{AH}{\sqrt{V_1/C_a}}\frac{\delta}{\delta^*}\right)\frac{1}{\sqrt{R_c}} \tag{5}$$

where again the quantity in parentheses is assumed to be unaffected by changes in Reynolds Number.

At the critical Reynolds Number, the length of the separated region is simply the distance from the separation point to the trailing edge:

$$\begin{aligned} \lambda &= \frac{1-(x/c)_s}{\delta/c} \\ &= \frac{1-(x/c)_s}{\left(\dfrac{AH}{\sqrt{V_1/C_a}}\dfrac{\delta}{\delta^*}\right)}\sqrt{R_c} \\ &= \left[\frac{1-(x/c)_s}{\left(\dfrac{AH}{\sqrt{V_1/C_a}}\dfrac{\delta}{\delta^*}\right)}\frac{1}{AH\dfrac{\delta}{\delta^*}\dfrac{V_s}{V_1}\left(\dfrac{V_1}{C_a}\right)^{1/2}}\right]R_\delta \end{aligned} \tag{6}$$

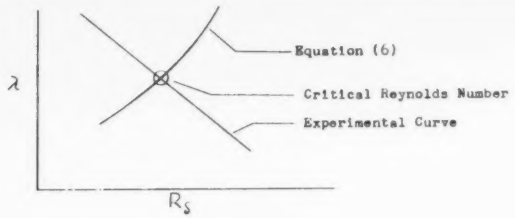

SKETCH A.

thus giving a relation between R_δ and λ at the critical Reynolds Number. Another relation exists that must be satisfied at separation—namely, the experimental curve shown in Fig. 10. Graphing these two relations simultaneously gives the critical Reynolds Number. (See Sketch A.)

The separation point can be found if the boundary-layer geometry and velocity distribution are known. Loitsianskii (in reference 14) indicates that laminar separation will occur if the diffusion factor D_L reaches a value of $= -0.0888$. In terms of the already derived expression, A,

$$\left.\begin{aligned} D_L &= A^2 \frac{d(V/V_1)}{d(x/c)} \\ &= -0.0888 \end{aligned}\right\} \qquad (7)$$

COMPARISON OF CALCULATED AND ACTUAL CRITICAL REYNOLDS NUMBER

The procedure outlined above was followed in estimating a critical Reynolds Number for comparison with the unpublished data shown in Figs. 5–9. Velocity distributions as shown in Fig. 11 were taken from Rannie's compressor test results[15] and were used to estimate the chordwise separation point and the parameter A. The separation point as determined by Eq. (7) is shown.

The shape factor H, and the ratio δ/δ^* at separation were based on the boundary layer velocity distribution shown in reference 6 and were taken as 2.84 and 1.313, respectively.

Since the empirical curve relating λ and R_δ for cascades applied only for low angles of incidence, the critical Reynolds Number was not calculated for an incidence angle above 5° (as suggested by Fig. 4).

The calculated and actual critical Reynolds Numbers are compared in Fig. 12. The values compare closely at design angle of incidence.

CONCLUSIONS AND RECOMMENDATIONS

(1) In normal operation at any operating Reynolds Number, a laminar separation bubble forms on the suction side of the compressor blade. At very low Reynolds Number this bubble fails to reattach to the surface, causing a loss in turning and a loss in efficiency. This phenomenon is clearly discernible in the performance data of a typical compressor.

(2) It is possible to predict the critical Reynolds Number at low angles of incidence with good accuracy by an empirical method provided that the compressor geometry is similar to that implied in the empirical relations.

(3) Future analyses might include an attempt to correlate the experimental relation between bubble geometry and the separation Reynolds Number (R_δ vs. λ) with cascade geometry and cascade performance parameters. A combination of the solidity and the rate of diffusion parameters probably can furnish some common denominator between isolated and cascaded airfoil data.

(4) Future experimental work should include some analysis of the bubble geometry for cascaded airfoils at high angles of incidence.

(5) Transition phenomena for a free-floating boundary layer should be investigated both analytically and experimentally.

REFERENCES

[1] Jones, B. M., *Stalling*, J. RAeS., Vol. 38, No. 285, September, 1934.

[2] Von Doenhoff, A. E., *A Preliminary Investigation of Boundary-Layer Transition Along a Flat Plate with Adverse Pressure Gradient*, NACA TN 639, 1938.

[3] Von Doenhoff, A. E., and Tetervin, N., *Investigation of the Variation of Lift Coefficient with Reynolds Number at a Moderate Angle of Attack on a Low-Drag Airfoil*, NACA CB, November, 1942.

[4] Gault, D. E., *Boundary-Layer and Stalling Characteristics of the NACA 63-009 Airfoil Section*, NACA TN 1894, 1949.

(*Continued on page 791*)

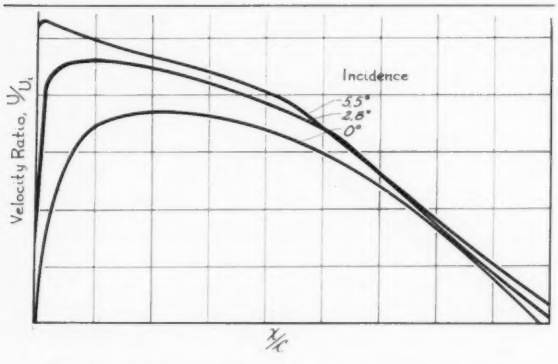

FIG. 11. Velocity distribution over a cascaded airfoil.

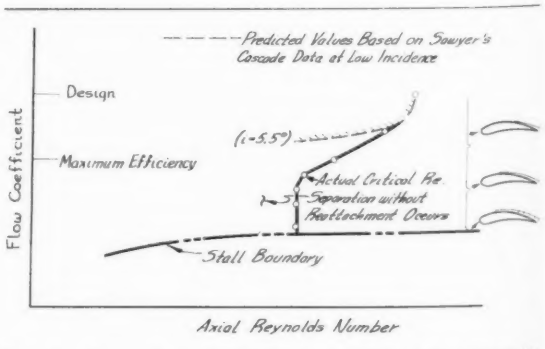

FIG. 12. Comparison of calculated and actual critical Reynolds Numbers.

The Oscillations of a Supersonic Gas Jet Embedded in a Supersonic Stream

D. C. PACK*

The Royal Technical College, Glasgow

SUMMARY

The general problem of the behavior of a supersonic jet emerging into a medium in supersonic motion is of interest, since it represents the motion relative to a rocket in supersonic flight of the flow of exhaust gases from the rocket motor. In this paper an examination is made, on the basis of the linearized theory of gas dynamics, of both two-dimensional and axially symmetrical jets. The findings of Pai and Kawamura on the reflection and transmission of waves in two-dimensional jets are confirmed and the subject treated in generality. In axially symmetrical jets it is found that the displacement of the jet boundary may be divided into three parts; the first is a constant (the asymptotic width of the jet), the second may be expressed as an infinite integral, and the third is obtained as the superposition of an infinite number of damped harmonic oscillations. The latter may be strongly damped and for certain choices of Mach Number of the outer and inner streams may be absent. Comparisons are made between the two-dimensional and axially symmetrical flows. The final change in the width of the axially symmetrical jet is just one-half of the change in the two-dimensional jet.

SYMBOLS

a	= speed of sound
M	= Mach Number
P	= pressure
ΔP	= excess of pressure in jet
U	= speed of uniform flow
x,r	= coordinates
t	= modified x-coordinate
R	= radius of jet
R'	= ultimate radius of jet
α	= $\sqrt{(M^2-1)}$
β	= α_2/α_1
γ	= ratio of specific heats
k	= $\gamma_1 M_1^2\beta/\gamma_2 M_2^2$
ρ	= density
ϵ	= $\Delta P/\rho_2 U_2^2$
$F(x)$, $f(t)$	$\propto$ displacement of jet boundary
p, ξ	= coordinates used in Laplace transforms
μ	= $(1-k)/(1+k)$
Φ	= velocity potential
$U\phi$	= perturbation potential
$H(t)$	= step function

Suffix 1 refers to the jet.
Suffix 2 refers to the outer medium.
Bars are used for Laplace transforms.

INTRODUCTION

THE GENERAL PROBLEM OF THE BEHAVIOR of a supersonic jet emerging into a medium in supersonic motion is of interest, since it represents the motion relative to a rocket in supersonic flight of the flow of exhaust gases from the rocket motor. Studies have recently been made by Pai[1] and Kawamura[2] of the oscillations of a two-dimensional supersonic jet of gas embedded in a supersonic stream, assuming steady motion and only small variations in pressure throughout. The methods of approach in these studies are particular to two-dimensional flow. In the following paragraphs an analysis is made of the oscillations of both two-dimensional and axially symmetrical jets of gas moving at supersonic speed in an infinite medium which is likewise in supersonic motion. As in the earlier papers the basis is the linearized equation of steady motion in gas dynamics, pressure changes are assumed to be everywhere small, and both heat conduction and viscosity are neglected.

The analysis of the oscillations of two-dimensional supersonic jets sets up the procedure and presents the findings of Pai and Kawamura in a general form. Some new features are illustrated. The study of the oscillations of axially symmetrical jets presents greater analytical difficulties. However, particular attention is paid to the differences between the reflection and transmission phenomena in the two-dimensional and axially symmetrical cases. An examination is made of the flow near to and at a large distance from the orifice from which the jet flows. It is found that the ultimate change in the width of an axially symmetrical jet is just one-half that of the two-dimensional jet under the same conditions at the orifice. Some remarks are made concerning the singularities within the jet as well as those which occur in the gradient of the boundary.

EQUATIONS AND BOUNDARY CONDITIONS

The pressure changes are assumed to be everywhere small, heat conduction and viscosity are neglected, and the motion is supposed to be steady.

Let the jet issue as a uniform parallel stream of ideal gas with ratio of specific heats γ_1 from an orifice of radius (or semi-width in two-dimensional flow) R with Mach Number M_1 (>1), velocity U_1, and density ρ_1 at pressure P_1; let it issue into an ideal gas with ratio of specific heats γ_2 which, upstream from the orifice, flows as a uniform parallel stream in the same direction as the jet with Mach Number M_2 (>1), velocity U_2, density ρ_2, and pressure P_2. Suppose that the pressure difference $\Delta P = P_1 - P_2$ is small compared with P_2 or $\rho_2 U_2^2$. Write

$$\Delta P/\rho_2 U_2^2 = \epsilon$$

The fluctuations of the two streams from uniform parallel flows are assumed to be small, and the lin-

Received June 17, 1955.

* Professor of Mathematics.

earized equation of supersonic motion is used for the velocity potential. Let x be the distance measured from the orifice in the direction of the motion of the uniform streams and let r be the distance measured from and perpendicular to the axis of symmetry. Then the velocity potentials Φ_1, Φ_2 in the inner and outer streams, respectively, may be written

$$\Phi_1 = U_1(x + \phi_1), \quad \Phi_2 = U_2(x + \phi_2) \tag{1}$$

Let a_1, a_2 be the speeds of sound at $x = 0$ in the jet and outer medium, respectively. To a first approximation

$$\rho_2/\rho_1 = \gamma_2 a_1^2/\gamma_1 a_2^2 = (U_1^2/\gamma_1 M_1^2)/(U_2^2/\gamma_2 M_2^2)$$

giving
$$\rho_1 U_1^2/\rho_2 U_2^2 = \gamma_1 M_1^2/\gamma_2 M_2^2 \tag{2}$$

The pressure in the jet is

$$P = P_1 - \rho_1 U_1^2(\partial\phi_1/\partial x)$$

and in the outer medium it is

$$P = P_2 - \rho_2 U_2^2(\partial\phi_2/\partial x)$$

to the first order of small quantities. The condition for the continuity of pressure across the boundary between the two streams, when this boundary is assumed to have the equation

$$r = R[1 + F(x)], \quad F(x) = O(\epsilon) \tag{3}$$

is thus

$$(\partial\phi_2/\partial x) - [(\gamma_1 M_1^2)/(\gamma_2 M_2^2)](\partial\phi_1/\partial x) = -\epsilon \quad \text{on } r = R \tag{4}$$

The condition for continuity of the direction of flow across the boundary is simply

$$\partial\phi_2/\partial r = \partial\phi_1/\partial r \quad \text{on} \quad r = R \tag{5}$$

The Two-Dimensional Supersonic Jet in a Supersonic Stream

The velocity potentials ϕ_1 and ϕ_2 in the two-dimensional case satisfy the differential equation

$$\partial^2\phi/\partial r^2 = (M^2 - 1)(\partial^2\phi/\partial x^2)$$

The Laplace transform of ϕ is

$$\bar{\phi} = \int_0^\infty e^{-px}\phi(x,r)dx$$

and it satisfies the differential equation

$$\partial^2\bar{\phi}/\partial r^2 = (M^2 - 1)p^2\bar{\phi} \tag{6}$$

Write $M_1^2 - 1 = \alpha_1^2$, $M_2^2 - 1 = \alpha_2^2$, $\beta = \alpha_2/\alpha_1$, $k = \gamma_1 M_1^2\alpha_2/\gamma_2 M_2^2\alpha_1 = \gamma_1 M_1^2\beta/\gamma_2 M_2^2$. The solution of Eq. (6) which is chosen for the outer medium must be one which represents waves propagated downstream, since, in the supersonic flow, the disturbances caused by the emergence of the jet from the orifice can have no effect upstream of the leading Mach line from the edge of the orifice when boundary-layer effects, produced by viscosity of the gas on the outer surface of the nozzle from which the jet flows, are neglected as here. Thus,

$$\bar{\phi}_2 = Ae^{-\alpha_2 pr}$$

In the jet itself waves are reflected at the boundaries, and the form of the potential which includes both incident and reflected waves is

$$\bar{\phi}_1 = Ce^{-\alpha_1 pr} + De^{\alpha_1 pr}$$

The boundary conditions (4) and (5) impose the following conditions upon the Laplace transforms $\bar{\phi}_1$, $\bar{\phi}_2$ on $r = R$:

$$\bar{\phi}_2 - k\beta^{-1}\bar{\phi}_1 = -\epsilon p^{-2} \tag{7}$$

$$\partial\bar{\phi}_2/\partial r = \partial\bar{\phi}_1/\partial r \tag{8}$$

The condition that the r-component of velocity vanishes on the plane $r = 0$ becomes

$$\partial\bar{\phi}_1/\partial r = 0 \quad \text{on } r = 0 \tag{9}$$

By means of Eq. (7), (8), and (9) the values of the constants A, C, and D are obtained. Thus,

$$\bar{\phi}_1 = \frac{\epsilon\beta}{p^2}\frac{\cosh \alpha_1 pr}{\sinh \alpha_1 pR + k \cosh \alpha_1 pR}$$

and
$$\bar{\phi}_2 = -\frac{\epsilon}{p^2}\frac{\sinh \alpha_1 pR\, e^{-\alpha_2 p(r-R)}}{\sinh \alpha_1 pR + k \cosh \alpha_1 pR}$$

The Laplace transform $\bar{F}(p)$ of the function $F(x)$ which occurs in Eq. (2) of the jet boundary is given by the boundary condition

$$Rp\bar{F}(p) = (\partial\bar{\phi}/\partial r)_{r=R} \tag{10}$$

$$= \frac{\alpha_2\epsilon}{p}\frac{\sinh \alpha_1 pR}{\sinh \alpha_1 pR + k \cosh \alpha_1 pR}$$

Write $F(x) = \epsilon\alpha_1\alpha_2 f(t)$, $t = x/\alpha_1 R$, $\xi = \alpha_1 pR$. Then

$$\bar{F}(p) = R\alpha_1^2\alpha_2\epsilon\bar{f}(\xi) \tag{11}$$

with
$$\bar{f}(\xi) = \frac{1}{\xi^2}\frac{\sinh \xi}{\sinh \xi + k \cosh \xi}$$

With $\mu = (1 - k)/(1 + k)$, this may be written

$$\bar{f}(\xi) = (1 + k)^{-1}\xi^{-2}(1 - e^{-2\xi})/(1 - \mu e^{-2\xi})$$

Since $k > 0$, $|\mu| < 1$.

A study of the wave formation in the boundary may be made by expanding $\bar{f}(\xi)$ in ascending powers of $e^{-2\xi}$ and transforming the resulting series term by term. Since

$$\bar{f}(\xi) = (1 + k)^{-1}\xi^{-2}[1 - (1 - \mu)e^{-2\xi}(1 + \mu e^{-2\xi} + \mu^2 e^{-4\xi} + \ldots)]$$

$$f(t) = (1 + k)^{-1}\{t - (1 - \mu)[(t - 2)\,H\,(t - 2) + \mu(t - 4)\,H\,(t - 4) + \mu^2(t - 6)\,H\,(t - 6) + \ldots]\}$$

where
$$H(t) = 1, t \geq 0$$
$$= 0, t < 0$$

The values of the gradient $f'(t)$ are: $(1 + k)^{-1}$ between $t = 0$ and $t = 2$; $\mu(1 + k)^{-1}$ between $t = 2$ and $t = 4$; $\mu^2(1 + k)^{-1}$ between $t = 4$ and $t = 6$; etc. Thus, if $\mu > 0$, the jet is expanding or contracting monotoni-

cally as the distance downstream increases; on the other hand, if $\mu < 0$, the gradient of the jet oscillates in sign. In either event the jet tends asymptotically to a finite width given by $f(t) = (1 + k)^{-1} \sum_{n=0}^{\infty} 2\mu^n = k^{-1}$—i.e., $F(\infty) = \epsilon\alpha_1\alpha_2/k$.

When the ratios of specific heats in the jet and the outer medium are equal, the conditions may be expressed simply as follows:

Expanding or contracting if *either* $M_1 > M_2$ and $\alpha_1\alpha_2 < 1$ *or* $M_1 < M_2$ and $\alpha_1\alpha_2 > 1$.

Oscillating if *either* $M_1 > M_2$ and $\alpha_1\alpha_2 > 1$ *or* $M_1 < M_2$ and $\alpha_1\alpha_2 < 1$.

These conditions are the same as those given by Kawamura in his paper. There is a *singular case* when $k = 1$ ($\mu = 0$). This arises when either $M_1 = M_2$ or $\alpha_1\alpha_2 = 1$. The latter case is not trivial. When $\alpha_1\alpha_2 = 1, f(\xi) = (2\xi^2)^{-1}(1 - e^{-2\xi})$, giving

$$f(t) = [t - (t - 2)\, H\,(t - 2)]/2$$

The jet "expands" from the orifice to $f(2) = 1$, and the jet remains thereafter at constant width given by $f(t) = 1$ or $F(x) = \epsilon$.

Reflection and Transmission Coefficients in Two-Dimensional Flow

In order to see the nature of the reflected and transmitted waves and to obtain the reflection and transmission coefficients defined by Pai, it is only necessary to expand the expressions for $\bar{\phi}_1$, $\bar{\phi}_2$ in powers of exponentials. Thus

$$\bar{\phi}_1 = \frac{\epsilon\beta\alpha_1{}^2R^2}{\xi^2}\frac{e^{-\xi(1 - r/R)}}{(1 + k)}\frac{(1 + e^{-2\xi r/R})}{(1 - \mu e^{-2\xi})}$$

$$= \frac{\epsilon\beta\alpha_1{}^2R^2}{\xi^2}\frac{e^{-\xi(1 - r/R)}}{(1 + k)}[1 + e^{-2\xi r/R} + \mu e^{-2\xi} + \mu e^{-2\xi(1 + r/R)} + \mu^2 e^{-4\xi} + \mu^2 e^{-4\xi - 2\xi r/R} + \ldots]$$

which gives, on interpreting term by term,

$$\phi_1 = \frac{\epsilon\beta\alpha_1 R}{(1 + k)}\left[\left(t + \frac{r}{R} - 1\right) H\left(t + \frac{r}{R} - 1\right) + \left(t - \frac{r}{R} - 1\right) H\left(t - \frac{r}{R} - 1\right) + \mu\left(t + \frac{r}{R} - 3\right) \times H\left(t + \frac{r}{R} - 3\right) + \mu\left(t - \frac{r}{R} - 3\right) \times H\left(t - \frac{r}{R} - 3\right) + \ldots\right]$$

This shows that there is no disturbance in the jet upstream of the leading characteristics from the edges of the orifice $[t \pm (r/R) - 1 < 0]$, as is to be expected on general principles. If the upper half of the jet is considered in detail, the first term represents the wave downstream of the leading characteristic from the upper edge—the wave that first appears in the region 1 of Fig. 1. The second term represents the disturbance associated with the leading characteristic from the lower edge; it crosses the axis of symmetry at $t = 1$ and

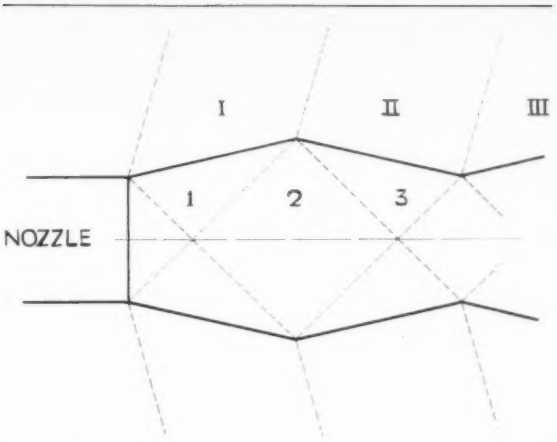

FIG. 1. Sketch illustrating the domains of influence of successive reflected and transmitted waves.

affects the upper half-plane in region 2 and downstream of this. The third term represents the reflection of this wave at the boundary of the jet. The amplitude of this reflected wave is μ times that of the incident wave. This confirms the finding of Pai, whose reflection coefficient is identical with μ of this paper when γ_1 and γ_2 are made equal in the latter. Since μ may be greater or less than zero according as $k <$ or > 1, the implication is that a wave of expansion, for example, may be reflected either as a wave of expansion or of compression according to the sign of μ. The singular case $\mu = 0$ corresponds to no reflected wave. These results are illustrated in the behavior of the boundary between the jet and the outer medium, which has already been considered.

When $\bar{\phi}_2$ is expanded in powers of exponentials and interpreted term by term one obtains

$$\phi_2 = -\frac{\epsilon\alpha_1{}^2R^2}{(1 + k)}\left[\left(t - \frac{\beta r}{R} + \beta\right) H\left(t - \frac{\beta r}{R} + \beta\right) - (1 - \mu)\left(t - \frac{\beta r}{R} + \beta - 2\right) H\left(t - \frac{\beta r}{R} + \beta - 2\right) - \mu(1 - \mu)\left(t - \frac{\beta r}{R} + \beta - 4\right) H\left(t - \frac{\beta r}{R} + \beta - 4\right) - \ldots\right]$$

In the upper half-plane the successive terms on the right-hand side first affect the flow in the regions in Fig. 1 marked I, II, III, ..., respectively. The transmission coefficient, defined as the ratio of the amplitude of the transmitted wave to the incident wave at $t = 2n (n = 1, 2, \ldots)$, $r = R$, is clearly $(1 - \mu)/\beta$, which is the value obtained by Pai.

The Axially Symmetrical Supersonic Jet in a Supersonic Stream

When the flow possesses axial symmetry, the velocity potentials satisfy the equation

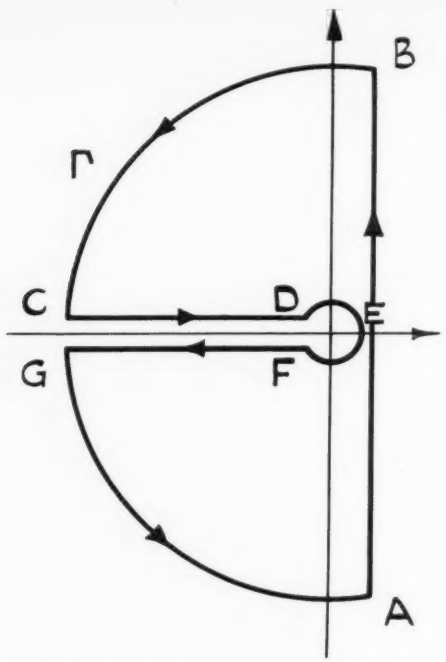

FIG. 2. Contour for the inversion of the Laplace transform.

$$(\partial^2\phi/\partial r^2) + [(1/r)(\partial\phi/\partial r)] = (M^2 - 1)(\partial^2\phi/\partial x^2)$$

and the corresponding transforms satisfy the equation

$$(d^2\bar{\phi}/dr^2) + [(1/r)(d\bar{\phi}/dr)] - \alpha^2 p^2 \bar{\phi} = 0 \qquad (12)$$

The solutions of Eq. (12) appropriate to the inner and outer streams are, respectively,

$$\left.\begin{aligned} \bar{\phi}_1 &= AI_0(\alpha_1 pr) \\ \text{and} \quad \bar{\phi}_2 &= BK_0(\alpha_2 pr) \end{aligned}\right\} \qquad (13)$$

where A and B are constants and $I_0(\xi)$, $K_0(\xi)$ are Bessel functions of the first and second kinds of imaginary argument. $\bar{\phi}_1$ is the solution of Eq. (12) which is regular at $r = 0$ and which satisfies the boundary condition (9); $\bar{\phi}_2$ is the solution that tends to zero at an infinite distance from the axis of the jet.

Substitution from Eqs. (13) into Eqs. (7) and (8) gives

$$BK_0(\alpha_2 pR) - k\beta^{-1}AI_0(\alpha_1 pR) = -\epsilon/p^2$$

$$\alpha_2 BK_1(\alpha_2 pR) + \alpha_1 AI_1(\alpha_1 pR) = 0$$

With the same notation as in the two-dimensional problem, these equations lead to the following transforms of the potentials:

$$\left.\begin{aligned} \bar{\phi}_1 &= \frac{\epsilon\beta\alpha_1^2 R^2}{\xi^2} \frac{I_0(r\xi/R)K_1(\beta\xi)}{[I_1(\xi)K_0(\beta\xi) + kI_0(\xi)K_1(\beta\xi)]} \\ \bar{\phi}_2 &= -\frac{\epsilon\alpha_1^2 R^2}{\xi^2} \frac{I_1(\xi)K_0(\beta r\xi/R)}{[I_1(\xi)K_0(\beta\xi) + kI_0(\xi)K_1(\beta\xi)]} \end{aligned}\right\} \qquad (14)$$

The transform of the function $f(t)$ which gives the oscillations of the boundary [see Eqs. (10) and (11)] is given by

$$\bar{f}(\xi) = I_1(\xi)K_1(\beta\xi)/\{\xi^2[I_1(\xi)K_0(\beta\xi) + kI_0(\xi)K_1(\beta\xi)]\} \qquad (15)$$

In the following paragraphs the oscillations of the jet boundary are discussed and some consideration is given to the singularities within the jet which are indicated by Eqs. (14).

The form of the jet boundary will be known when the transform of Eq. (15) is found. In order to discuss the properties of the transform most simply, it is necessary to examine the singularities of this equation; these consist of a logarithmic branch point at $\xi = 0$ and poles at the other zeros of the denominator.

THE POLES OF $\bar{f}(\xi)$

The poles of $\bar{f}(\xi)$ are given by the zeros of the expression

$$D(\xi) \equiv I_1(\xi)K_0(\beta\xi) + kI_0(\xi)K_1(\beta\xi)$$

For large values of $|\xi|$,

$$D(\xi) \sim \left[\frac{e^{\xi} \mp ie^{-\xi}}{(2\pi\xi)^{1/2}}\right]\left(\frac{\pi}{2\beta\xi}\right)^{1/2} e^{-\beta\xi} + k\left[\frac{e^{\xi} \pm ie^{-\xi}}{(2\pi\xi)^{1/2}}\right]\left(\frac{\pi}{2\beta\xi}\right)^{1/2} e^{-\beta\xi}$$

where the upper sign is to be taken in the upper half-plane, the lower sign in the lower half-plane. On rearranging the terms,

$$D(\xi) \sim E(\xi) = [e^{-\beta\xi}/(2\beta^{1/2}\xi)][(1 + k)e^{\xi} \mp i(1 - k)e^{-\xi}] \qquad (16)$$

This vanishes at the points

$$\xi = \frac{1}{2}\log\left|\frac{1 - k}{1 + k}\right| \pm i\pi\left[N + \frac{1}{4}\operatorname{sgn}(1 - k)\right] \qquad (17)$$

with N integral (or zero) subject to the conditions $N \geq 0$ if $k < 1$, $N \geq 1$ if $k > 1$, and with the upper and lower signs applying to the upper and lower half-planes, respectively.

If $k = 1$, $E(\xi)$ certainly has no zeros in the finite part of the ξ-plane.

Let $E(\xi) = E_u(\xi)$ in the upper half-plane and $E(\xi) = E_l(\xi)$ in the lower half-plane.

The zeros of $D(\xi)$ which are at some distance from the origin will be given closely by Eq. (17). At this stage it is useful to see whether the number of zeros of $D(\xi)$ is equal to the number of zeros of $E(\xi)$; if so, it may be hoped that each zero of $D(\xi)$ is represented approximately by one and one only of the zeros of $E(\xi)$. The check may be made in the upper half-plane by comparing the change in argument of $D(\xi)$ with that of $E_u(\xi)$ round a large semicircle with center at the origin and with the real axis as the bounding diameter, indented by means of a vanishingly small semicircle above the origin; in the lower half-plane the change in the argument of $D(\xi)$ may be compared with that of $E(\xi)$ round a similar contour indented below the origin.

Consider the change in argument of $D(\xi)$ and $E_u(\xi)$ round the contour (taken anti-clockwise) in the upper

half-plane. It is evident that the arguments change by the same amount round the semicircle of radius λ in the limit as $\lambda \to \infty$. Round the small semicircle indenting the origin, on which $D(\xi) \sim k\,\beta\xi$, the arguments of $D(\xi)$ and $E_u(\xi)$ alike increase by π. Along the negative real axis, with $\xi = \eta e^{i\pi}$, $D(\xi)$ has always a negative real part; arg $D(\xi)$ increases by $(1/2)\pi \times \mathrm{sgn}(1-k)$. Arg $E_u(\xi)$ increases by $\mathrm{sgn}\,(1-k) \times \left(\frac{1}{2}\pi - \tan^{-1}\frac{1-k}{1+k}\right)$ along the negative real axis. Along the positive real axis $D(\xi)$ is always real and positive; thus arg $D(\xi)$ is constant. Arg $E_u(\xi)$ increases by $\mathrm{sgn}\,(1-k)\tan^{-1}\left|\frac{1-k}{1+k}\right|$. The total change along the real axis with the indentation is therefore $+(3/2)\pi$ $(k<1)$ or $+(1/2)\pi (k>1)$ for both functions. It follows that they have the same number of zeros in the upper half-plane. A similar check shows that $D(\xi)$ and $E_l(\xi)$ have the same number of zeros in the lower half-plane. The zeros of the function $D(\xi)$ are therefore one-to-one with the zeros of $E(\xi)$. The extent to which the members of one set may be viewed as approximations to the members of the other depends upon the adequacy of the asymptotic expressions replacing the Bessel functions. The accuracy should be good provided $|\xi|, |\beta\xi| > 1$. This precludes small values of β; even for small k, with β not small, $|\xi| = O(1)$, so that the requirements will be satisfied in general.

The Oscillations of the Boundary

The oscillations of the boundary are given directly by the integral

$$I_1 = \frac{1}{2\pi i}\int_{\gamma-i\infty}^{\gamma+i\infty} e^{t\xi}\bar{f}(\xi)d\xi = f(t) \qquad (18)$$

by the inversion theorem for Laplace transforms, γ being a constant greater than the real part of all the singularities of $\bar{f}(\xi)$—i.e., $\gamma > 0$. The integral I_1 is uniformly convergent for all t and therefore represents a mathematically continuous oscillation of the jet boundary; also $f(0) = 0$ as it should be.

When Eq. (18) is differentiated with respect to t, the resulting integral is uniformly convergent for $t > 0$, except at the points $t = 2r$ $(r = 1, 2, \ldots)$. An expansion of $\bar{f}(\xi)$ by the binomial theorem in powers of $e^{-2\xi}$ for large ξ shows that, at the points $t = 4m - 2$ $(m = 1, 2, \ldots)$, there are logarithmic infinities in the gradient $f'(t)$, while at the points $t = 4m$ $(m = 1, 2, \ldots)$, there are finite discontinuities. The value of dI_1/dt is zero for $t < 0$; for $t = +0$ it is $1/(1+k)$. The discontinuity of gradient across $t = 0$ represents the expansion (or contraction) that, when boundary-layer effects are neglected, is produced at the rim of the orifice by the pressure difference between the inner and the outer media.

The value of $f(t)$ may be expressed in terms of real variables by considering the integral

$$I = \frac{1}{2\pi i}\int_\Gamma e^{t\xi}\bar{f}(\xi)\,d\xi \qquad (t>0)$$

where Γ is the contour ABCDEFGA illustrated in Fig. 2. The large semicircle is chosen so as not to pass through a pole of the integrand. For all k the value of the integral taken round this semicircle tends to zero as the radius tends to infinity. By Cauchy's theorem, the value of the integral I is equal to the sum of the residues at the poles of the integrand within Γ; call this sum $s(t)$. Each residue yields a term to $s(t)$ which contains the factor $\mu^{t/2}$—i.e., $\exp[(1/2)\,t\log|\mu|]$, insofar as the zeros of $E(\xi)$ may be used to represent the poles of the integrand. Since the logarithm in this factor is negative for all permitted values of μ, the amplitude of each oscillatory term falls off exponentially with the distance downstream; each term represents a damped oscillation. For $k \doteq 1$ the damping is very strong; for $k = 1$ the oscillatory terms vanish completely. The contribution to I from the vanishingly small circle DEF is $-1/2k$; the contributions from CD and FG combine to give an infinite integral. The result is that

$$f(t) = s(t) + \frac{1}{2k} + \frac{1}{\beta}\int_0^\infty \frac{e^{-t\xi}I_1^2(\xi)\xi^{-3}d\xi}{\{[I_1(\xi)K_0(\beta\xi) + kI_0(\xi)K_1(\beta\xi)]^2 + \pi^2[I_1(\xi)I_0(\beta\xi) - kI_0(\xi)I_1(\beta\xi)]^2\}} \qquad (19)$$

This relation shows that the ultimate radius R' of a jet issuing from an orifice of radius R is

$$R' = R(1 + \epsilon\alpha_1\alpha_2/2k)$$

indicating a slight expansion of radius when there is an initial excess pressure in the jet $(\epsilon > 0)$, and a slight shrinking when there is an initial excess pressure in the outer medium $(\epsilon < 0)$. The change is exactly one-half that obtained in a two-dimensional jet (see above).

The limiting value of R' may be obtained directly from a consideration of the flux of mass at the orifice and at a large distance downstream.

If the approximations of Eq. (16) are made, the series $s(t)$ may be found by the calculus of residues in the form

$$s(t) = \frac{-(1-\mu^2)}{2\mu}|\mu|^{t/2} \times \sum_{N=0}^{\infty} \frac{\{(1/4)\log^2|\mu| - [N+(1/4)]^2\pi^2\}\cos[N+(1/4)]t\pi + (\pi\log|\mu|)[N+(1/4)]\sin[N+(1/4)]t\pi}{\{(1/4)\log^2|\mu| + [N+(1/4)]^2\pi^2\}^2}$$

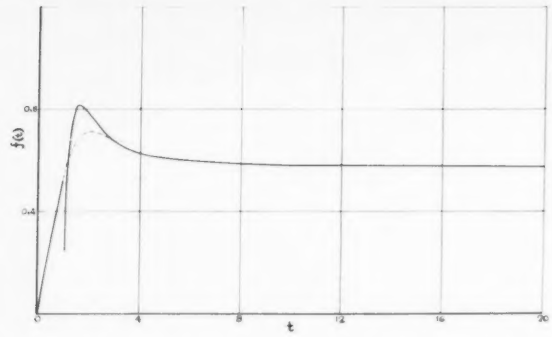

FIG. 3. Form of the jet boundary for axially symmetrical flow with $M_1 = \sqrt{2}$, $M_2 = 2$.

when $k < 1$ ($\mu > 0$); when $k > 1$ ($\mu < 0$) the lower limit of the summation becomes $N = 1$ and $N - (1/4)$ must be written for $N + (1/4)$ throughout the series.

The behavior of the derivative $s'(t)$ of this series exhibits the singularities of the boundary of the jet. A study of the terms of $s'(t)$ with large values of N reveals that there is a discontinuity in the gradient at points corresponding to $t = 4m$ ($m = 1, 2, \ldots$) of magnitude $(1/2)(-1)^{m-1}(1-\mu^2)\mu^{2m-1}$. This result is true for both positive and negative values of μ. While the magnitudes of the discontinuities are equal to those in the two-dimensional case, the signs of alternate discontinuities are opposite. At the points $t = 4m - 2$ ($m = 1, 2, \ldots$), the singularities are of logarithmic type; in fact $s'(t)$ has a singular part represented by $(1/2\pi)(-1)^{m-1}(1-\mu^2)\mu^{2m-2}\log|4m-2-t|$. This behavior may be compared with that of the flow in a quasi-cylindrical tube[3] and also in the flow of an axially symmetrical jet issuing at supersonic speed into a medium at rest.[4]

THE BEHAVIOR FOR LARGE AND SMALL DISTANCES DOWNSTREAM

Eq. (19), although complicated, may be used for computing the shape of the boundary of the jet. For the present purpose, however, it will be sufficient to examine in some detail the behavior near the orifice and at large distances. This may be done by means of well-known theorems on Laplace transforms.[5]

Near $\xi = 0$, $\bar{f}(\xi)$ possesses the expansion

$$\bar{f}(\xi) = \frac{1}{2k\xi} + \frac{\beta}{4k^2}\,\xi\log\xi + \frac{\beta^2}{8k^3}(1-\beta k)\xi^3\log^2\xi + \frac{\beta}{k^2}\left[\frac{1}{16}(2\beta^2-1) + \frac{\beta}{4k}(1-\beta k)\left(\log\frac{1}{2}\beta + C\right)\right]\times \xi^3\log\xi + \ldots + a_1\xi + a_3\xi^3 + \ldots \quad (20)$$

consisting of a power series in ξ together with a series containing mixed powers of ξ and $\log\xi$. In Eq. (20) C denotes Euler's constant and $a_1, a_3, \ldots$ are constants that do not need to be evaluated explicitly for the present purpose.

Corresponding to Eq. (20) there is the asymptotic expansion*

$$f(t) = \frac{1}{2k} + \frac{\beta}{4k^2t^2} - \frac{3\beta^2}{2k^3}(1-k\beta)\frac{\log t}{t^4} + \frac{2\beta^2(1-k\beta)\Gamma'(4) + 3\beta\{(2\beta^2-1)k + 4\beta(1-k\beta)[\log(1/2)\beta + C]\}}{8k^3t^4} \quad (21)$$

The discontinuities in the gradient of the jet at the points $t = 2r$ are not revealed by the above transformations, which yield only the contribution from the singularity of $\bar{f}(\xi)$ with the greatest real part—i.e., from the singularity at $\xi = 0$. However, while the contributions to the gradient from the poles, which are on a line approximately parallel to the imaginary axis, have a discontinuous sum, the sum is very strongly damped for large t, so that the profile given by the series (21) is not significantly in error. It will be noticed that $\lim_{t\to\infty} f(t) = 1/2k$, as deduced previously from Eq. (19).

The form of $f(t)$ near the origin is obtained by a transformation of the asymptotic form of $\bar{f}(\xi)$. As $\xi \to \infty$

$$\bar{f}(\xi) \sim \frac{1}{1+k}\,\xi^{-2} + \frac{1-k\beta}{2\beta(1+k)^2}\,\xi^{-3} - \frac{[(1-k\beta)^2 + 3k(1+\beta)^2]}{8\beta^2(1+k)^3}\,\xi^{-4} + \ldots$$

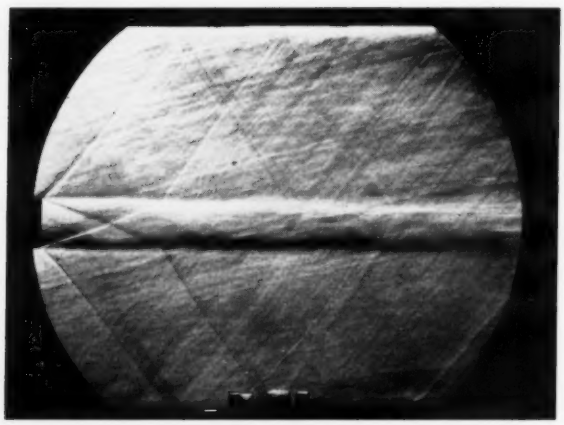

FIG. 4. Axially symmetrical supersonic jet embedded in a supersonic stream. ($M_1 = 2.6$, $M_2 = 1.3$; $P_1 = 5.28$ lb./sq.in., $P_2 = 5.23$ lb./sq.in. Photograph taken at Cornell Aeronautical Laboratory by J. G. Wilder, Jr., and reproduced by courtesy of the United States Air Force.)

* See reference 5, Section 126. An additional theorem is required to supplement those given by Carslaw and Jaeger. This is that, subject to the same conditions as are required for the transformation of a series of terms such as $\log\xi\sum_{n=0}^{\infty} b_n\xi^n$, the transform of $\log^2\xi\sum_{n=0}^{\infty} c_n\xi^n$ has the asymptotic expansion

$$2\sum_{n=0}^{\infty}(-1)^{n+1}c_n t^{-(n+1)}[\Gamma'(n+1) - \Gamma(n+1)\log t]$$

to which corresponds the expansion for small t (see reference 5, Section 123)

$$f(t) = \frac{1}{1+k}\,t + \frac{1-k\beta}{4\beta(1+k)^2}\,t^2 - \frac{[(1-k\beta)^2 + 3k(1+\beta)^2]}{48\beta^2(1+k)^3}\,t^3 + \ldots \quad (22)$$

The gradient of the jet at $t = 0$ is $+\epsilon\alpha_2/(1+k)$, showing a small initial increase in jet width downstream from the orifice when there is an initial excess pressure in the jet ($\epsilon > 0$), as was to be expected.

In order to give an idea of the form of the jet as indicated by the linearized theory presented here, an example has been worked out with $\gamma_1 = \gamma_2$, and the results are illustrated in Fig. 3. The Mach Numbers in the jet and outer medium were taken to be $\sqrt{2}$ and 2, respectively; then $\alpha_1 = 1$, $\alpha_2 = \sqrt{3}$, $\beta = \sqrt{3}$, and $k = \sqrt{3}/2$. This case was chosen as leading to the smallest possible value of k for $M_2 = 2$. The ordinate in Fig. 3 is $f(t)$ and is therefore proportional to the increase in width of the jet after leaving the orifice. Since $\alpha_1 = 1$, $x = tR$; thus t measures in this instance the distance downstream in orifice radii. Limitation of space requires a severe compression of the abscissas.

The boundary is closely linear for a radius downstream and settles down quickly to a fairly uniform width; it is almost within 5 per cent of its asymptotic thickness at five orifice radii downstream of the nozzle. The expansions in t and $1/t$ found above are not to be expected to give reliable results between $t = 1$ and $t = 4$; however, since $f(t)$ is initially rising and finally falling, the shape of the jet may be supposed to be something like that indicated by transferring from the one calculation to the other along the dotted line. It is clear that for a small pressure difference the disturbance of the boundary will appear to be very slight; when at overpressure the jet will have a small initial bulge but will quickly settle down to almost uniform thickness with a radius that is greater than its initial radius. An example of an axially symmetric supersonic jet in a supersonic stream obtained in the course of some experiments is given in Fig. 4. The photograph shows some of the reflected and transmitted waves in the jet.

Discontinuities in the Axially Symmetrical Flow

The discontinuities in the axially symmetrical flow may be examined by the same methods as those employed by Ward[3] in his study of flow inside a quasi-cylindrical tube, and they are, in fact, similar. When the Bessel functions in the expression for $\bar{\phi}_2$ in Eq. (14) are replaced by their asymptotic expansions and only first terms are retained

$$\partial\bar{\phi}_2/\partial r \sim (1+k)^{-1}\beta\epsilon\alpha_1^2 R^{3/2} r^{-1/2}\xi^{-1} \exp(\beta\xi - \beta\xi r/R)$$

This shows that there is a discontinuity in velocity which falls off as $r^{-1/2}$ across the line $t = \beta(r - R)/R$; this is the representation in the linearized flow of the shock wave or expansion occurring in the outer medium and springing from the rim of the orifice.

Consideration of the form of $\bar{\phi}_1$ shows that there are discontinuities within the jet of the same character as those found by Ward. In particular, on the leading Mach cone from the rim of the orifice, $\bar{\phi}_1 \sim \beta\epsilon(1+k)^{-1} \times \alpha_1^2 R^{5/2} r^{-1/2}\xi^{-2} \exp[-\xi(1 - r/R)]$, showing that $\bar{\phi}_1$ tends to infinity as $r^{-1/2}$ as r tends to zero.

As Ward has remarked, the singularities indicated by the solutions of the linearized equation of gas dynamics are not to be accepted; however, they do indicate the presence of focusing effects and enable an understanding of the general nature of the flow while an exact solution of the nonlinear differential equation is awaited.

Conclusion

The linearized equation of gas dynamics indicates the character of the flow when a supersonic jet emerges into an outer medium which is itself in supersonic motion. There are notable differences between the two-dimensional and axially symmetrical flow. In two dimensions, the jet first expands if at overpressure. Thereafter, at successive reflections of waves on the boundary, it either continues to expand with reducing gradient or it oscillates, according to whether the sign of $\mu = (1-k)/(1+k)$, with $k = \gamma_1 M_1^2\alpha_2/\gamma_2 M_2^2\alpha_1$, is positive or negative. (For overpressure in the outer medium read contraction for expansion in the above.) The ultimate radius of the jet is $(1 + \epsilon\alpha_1\alpha_2/k)$ times the orifice radius.

The axially symmetrical jet has singularities in its boundary gradient which are alternately logarithmic singularities and simple discontinuities. The signs of the discontinuities are only alternately the same as those in the two-dimensional case, although the magnitudes are always equal at corresponding points. An analysis of the boundary oscillations shows that there is a quick convergence to the asymptotic thickness of the jet, which is $(1 + \epsilon\alpha_1\alpha_2/2k)$ times the orifice radius; ultimate expansion (or contraction) of the jet is seen to be one-half that in the corresponding two-dimensional jet.

Transmission and reflection coefficients obtained for two-dimensional jets agree with those previously obtained by Pai. Some remarks are made on the singularities other than those on the boundary both for two-dimensional and axially symmetrical jets.

Acknowledgments

The author is indebted to Professor S. I. Pai of the University of Maryland for interesting him in this problem and to Professor M. J. Lighthill, F. R. S., of the University of Manchester for his assistance and advice during the work, most of which was carried out while the author was at the University of Manchester. The computations for Fig. 3 were carried out by D. F. Ferguson.

The paper was presented at the International Mathematical Congress at Amsterdam, September, 1954.

(Continued on page 764)

Effect of Wind-Tunnel Contraction on Free-Stream Turbulence*

MAHINDER S. UBEROI†

University of Michigan

SUMMARY

The effect of wind-tunnel contraction on free-stream turbulence is determined by passing a well-defined turbulence through three contractions of ratios 4:1, 9:1, and 16:1. Turbulent velocity measurements show that, in absolute magnitudes, the longitudinal component decreases and the lateral component increases as the flow accelerates through the contraction. Post- and precontraction spectra are measured to get an idea about the distortion of turbulence structure.

Corresponding to the test section of a wind tunnel, a uniform section was placed after the contraction. The turbulence is fairly homogeneous and axisymmetric at the end of the contraction, and the turbulent energy in three velocity components slowly equalizes as the flow goes through the uniform section. Measurements show that the lateral (larger) component is losing more energy due to viscosity than by transfer to the longitudinal (smaller) component. The longitudinal component is receiving enough energy to compensate for its decay, and, in fact, it is slowly increasing.

For supersonic nozzles, elementary considerations show that the effects of increase in the mean speed and decrease in the density are both beneficial in reducing the flow irregularities.

The relation of this investigation to the general problem of turbulent flows is discussed, particularly in connection with local isotropy and the concept of a cascade process in shear flows.

SYMBOLS

c	=	U_2/U_1
E	=	longitudinal spectrum of $\overline{u^2}$
F	=	longitudinal spectrum of $\overline{v^2}$
k	=	$2\pi n/U$ = wave number
M	=	mesh length of grid
n	=	frequency, cycles per sec.
R_M	=	$U_1 M/\nu$
U	=	mean speed
u, v, w	=	components of turbulent velocity
u_t	=	"eddy" turbulence
u_s	=	velocity due to sound waves
ξ, η, ζ	=	components of vorticity
ρ	=	density
ν	=	kinematic viscosity

An overbar denotes mean value.

Subscripts 1 and 2 denote pre- and postcontraction values of a quantity, respectively.

Presented at the Aerodynamics Session, Twenty-Second Annual Meeting, IAS, New York, January 25–29, 1954. Revised and received September 25, 1955.

* This work was financially supported by the Office of Naval Research, U.S. Navy, under contract NR 062-175. The author is indebted to Dr. Arnold M. Kuethe for helpful suggestions. The assistance of Sture Karlsson, K. Raman, Stanley Wallis, and Ellen Kurath during various phases of this investigation is gratefully acknowledged.

† Department of Aeronautical Engineering.

INTRODUCTION

THE ATTAINMENT of uniform flow, free of turbulence and pulsations, is of foremost importance in many experimental investigations of fluid dynamics problems. It was first pointed out by Prandtl[1] that a sharp decrease in the cross-sectional area of a pipe with consequent increase in the mean speed smooths out the flow irregularities. In most modern wind tunnels, the air first enters a relatively large duct or "pressure box" and reaches the test section through a rapidly converging nozzle or a contraction. Additional reduction in flow nonuniformities can be obtained by placing fine screens in the pressure box which attenuate the precontraction irregularities with little loss since the speed in the pressure box is quite low. With great physical insight, Prandtl considers vorticity to be the primary variable in a turbulent fluid. In an extensive volume of incompressible fluid, the velocity changes can only be produced by vorticity—i.e., neglecting the effect of walls the turbulent velocity fluctuations are entirely due to random distribution of vorticity. The mathematical proof follows from the fact that, for an incompressible fluid without vorticity, if the velocity is zero at the surface enclosing the fluid, then it is zero everywhere inside the enclosure. Consequently, the effect of contraction on free-stream turbulence can be determined by considering its effect on vorticity. For simplicity we assume axisymmetric contraction; the results may be easily extended to other cases.

Fig. 1 gives a physical picture of Prandtl's semiquantitative theory. He assumed that the velocity fluctuations in the x direction, the direction of mean flow, are

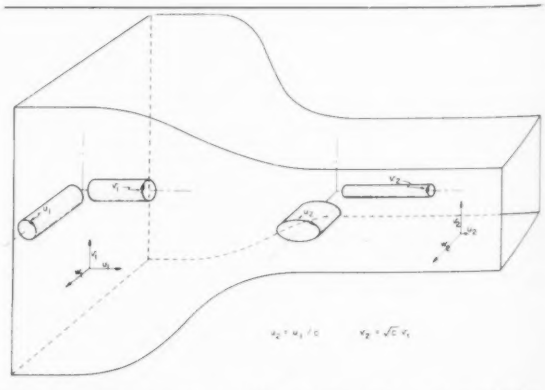

FIG. 1. Pictorial representation of Prandtl's semiquantitative theory.

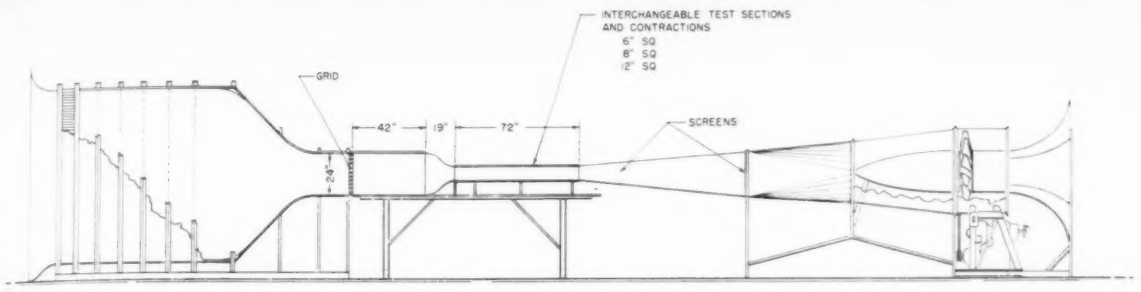

FIG. 2. Experimental arrangement I.

mainly due to vortex filaments lying perpendicular to the x direction. Similarly, the velocity fluctuations in the y direction are mainly due to the vortices lying perpendicular to the y axis. As the flow goes through the contraction, the vortex filaments in the x direction are elongated by a factor c, and those in the y and z directions are contracted by a factor $\sqrt{c}$, where $c = U_2/U_1$ is the ratio of the test section mean velocity to that in the pressure box. Neglecting viscosity, the total strength of a vortex filament or the circulation around it remains constant—i.e., the product of the angular velocity and the cross-sectional area of the vortex filament remains constant. The angular velocity of the vortex filament lying along the tunnel axis increases by a factor c while its radius decreases by a factor $\sqrt{c}$, and hence the peripheral velocity increases by a factor $\sqrt{c}$—i.e.,

$$v_2/v_1 = w_2/w_1 = \sqrt{c}$$

On the other hand, the cross-sectional area of a vortex filament lying perpendicular to the x axis increases by a factor $\sqrt{c}$, and hence its angular velocity decreases by a factor $\sqrt{c}$. The distance of the periphery of the vortex tube from its center decreases by a factor of $\sqrt{c}$, and therefore the peripheral velocity decreases by a factor of c—i.e.,

$$u_2/u_1 = 1/c$$

Prandtl also shows that decrease in the longitudinal turbulent velocity can be obtained by consideration of the Bernoulli equation. Although the flow is turbulent, and therefore rotational, we can apply the Bernoulli equation separately for each streamline—i.e., $U_2^2 = (2/\rho)(p_1 - p_2) + U_1^2$. The pressure drop or the energy gain is the same for all streamlines; therefore, the change in the longitudinal velocity from streamline to streamline is $U_2\delta U_2 = U_1\delta U_1$ or $\delta U_2/\delta U_1 = U_2/U_1 = 1/c$. The consideration of Bernoulli's equation can give only the effect of contraction on u fluctuations. We prefer Prandtl's original idea of taking vorticity as the primary variable since it gives the effect of contraction on all three components of turbulence and since, as we shall see later, it can be generalized to the case of a supersonic contraction.

Prandtl's theory is based on the behavior of discrete vortex filaments, while in a turbulent fluid there is a continuous distribution of vorticity. Taylor[2] took this into account and investigated the effect of contraction on some special distributions of vorticity (cellular flows). If ξ_1, η_1, ζ_1 and ξ_2, η_2, ζ_2 are the components of vorticity before and after the contraction, the Lagrangian equations of vorticity, neglecting viscosity, are[16]

$$\left.\begin{aligned}(\rho_1/\rho_2)\xi_2 &= \xi_1(\partial x_2/\partial x_1) + \eta_1(\partial x_2/\partial y_1) + \zeta_1(\partial x_2/\partial z_1)\\ (\rho_1/\rho_2)\eta_2 &= \xi_1(\partial y_2/\partial x_1) + \eta_1(\partial y_2/\partial y_1) + \zeta_1(\partial y_2/\partial z_1)\\ (\rho_1/\rho_2)\zeta_2 &= \xi_1(\partial z_2/\partial x_1) + \eta_1(\partial z_2/\partial y_1) + \zeta_1(\partial z_2/\partial z_1)\end{aligned}\right\} \quad (1)$$

where x_1, y_1, z_1 and x_2, y_2, z_2 are the positions of a particle at the entrance and the exit of the contraction and ρ_1 and ρ_2 are the corresponding densities. Eqs. (1) are based on the assumption that the density is a unique function of pressure. For the present, we assume that fluid is incompressible and, later, discuss the effect of contraction on turbulence in compressible flows. Taylor assumes, as Prandtl did, that, for a rapid contraction, the relative motion of two neighboring particles due to contraction is large compared with that due to turbulence—i.e., (for an axisymmetric contraction),

$$\partial x_2/\partial x_1 = c \qquad \partial y_2/\partial y_1 = \partial z_2/\partial z_1 = 1/\sqrt{c} \quad (2)$$

and $\partial x_2/\partial z_1 \ldots$ etc., are zero and Eqs. (1) simply reduce to

$$\xi_2 = c\xi_1 \qquad \eta_2 = \eta_1/\sqrt{c} \qquad \zeta_2 = \zeta_1/\sqrt{c} \quad (3)$$

Taylor's results for most of the cellular flows which he investigated were of the same form as Prandtl's except for numerical factors. Taylor's linearized equations and the formalism of statistical analysis can be used to get the effect of contraction on isotropic (or homogeneous) turbulence.

It is well known that, if two random functions are related by a *linear* operator, it is always possible, subject to some mild restrictions, to predict the correlation or spectrum of one variable in terms of the corresponding quantities of the other variable.[3] In the present case, the linear operator is a set of constants given by Eqs. (2). The postcontraction vorticity spectrum is obtained by properly multiplying the known precontraction vorticity spectrum with these constants. The postcontraction velocity spectrum can be obtained using the fact that the velocity and vorticity spectra of a homogeneous turbulence are simply related. Calcu-

lations made by Ribner and Tucker[4] and independently by Batchelor[5] show that

$$\left.\begin{aligned}\frac{\overline{u_2}^2}{\overline{u_1}^2} &= \frac{3c^{-2}}{4}\left[\frac{2-c^{-3}}{(1-c^{-3})^{3/2}}\times \tanh^{-1}(1-c^{-3})^{1/2} - \frac{1}{1-c^{-3}}\right] \\ &\simeq (3c^{-2}/4)(\log 4c^3 - 1) \qquad \text{for } c >> 1 \\ \frac{\overline{v_2}^2}{\overline{v_1}^2} &= \frac{3c}{8}\left[\frac{2-c^{-3}}{1-c^{-3}} - \frac{c^{-6}}{(1-c^{-3})^{3/2}}\tanh^{-1}(1-c^{-3})^{1/2}\right] \\ &\simeq 3c/4 \qquad \text{for } c >> 1\end{aligned}\right\} \quad (4)$$

The results for u fluctuations give the same dependence on the contraction ratio c as that obtained by Prandtl since $(\log 4c^3 - 1)$ varies slowly, and, for v fluctuations, even the constant of proportionality is close to the value given by Prandtl.

A number of experiments on the subject have been reported in the literature; however, no two experiments give the same results. These experiments will be discussed later. The present experiments were conducted to see if the neglect of viscosity and linearization of the equations are justified. A priori we expect deviations from the linearized theory, and the problem is to get an estimate and an understanding of these deviations.

Experimental Arrangement

The experiments were conducted in 2- by 2-ft. low-turbulence wind tunnel. Approximately isotropic turbulence was produced by placing grids of various mesh sizes in the test section. Axisymmetric nozzles of various contraction ratios (4:1, 9:1, and 16:1) were placed some distance downstream of the grid, and these were followed by uniform sections. Fig. 2 shows one arrangement which was used for 4:1 contraction. A separate fan was installed for use with 9:1 and 16:1 as well as 4:1 contraction. Fig. 3 shows the second arrangement, the reason for which will be explained later. The dimensions of the three contractions are shown in Fig. 4. All three contractions are quite rapid, and careful examinations showed no separation in any contraction. The measurements were made on the tunnel axis with a probe attached to a long wooden rod. The rod was counterweighted and was attached at one end to a movable carriage. Standard hot-wire technique and equipment were used to measure the turbulence levels and the spectra.

Turbulence Intensity Changes in a Contraction

Effect of Contraction Ratio

Turbulence generated by a biplanar 2-in. square mesh grid made of 1/2-in. round rods was passed through the three contractions of ratios 4:1, 9:1, and 16:1. The mean speed at the entrance of all three contractions for this set of experiments was 3.6 ft./sec., and, therefore, the grid Reynolds Number R_M was 3,710. The measurements of $\overline{u^2}$ and $\overline{v^2}$ were made on the axes of the contractions and are shown in Figs. 5–7. Here, and in all other figures, the mean velocities are those actually measured on the axes, although no experimental points are shown. In accordance with Prandtl's prediction, $\overline{u^2}$ decreases and $\overline{v^2}$ increases as the flow accelerates through 4:1, and 9:1, but, for 16:1 contraction, $\overline{u^2}$ first decreases and then increases to a final value which is higher than the initial value. We note that the turbulence behind the grid is anisotropic, but, soon after reaching the contraction, $\overline{u^2}$ and $\overline{v^2}$ equalize.* We shall take this point as the beginning of the contraction so that we can assume that turbulence is isotropic as it enters the contraction. This is not necessary, but it makes it easy to compare the experimental results with the computations of linear theory which are available for the effect of contraction on isotropic turbulence. The differences between the values of $\overline{u^2}$ and $\overline{v^2}$, even if real, are small compared with the changes produced by the contraction so that new calculations, based on linear theory, for the effect of contraction on anisotropic turbulence do not seem justified.

In Figs. 8 and 9 we have plotted the data for the three contractions as a function of U/U_1, where U is the local mean velocity and U_1 is the precontraction mean velocity. The results of the linear theory [Eq. (4)] are also shown in these figures. We see that u^2/u_1^2 is greater and

* Most investigators,[6, 7] except the ones[17, 18] at the Cavendish Laboratory, have reported that $\overline{u^2} > \overline{v^2}$ for turbulence generated by grids.

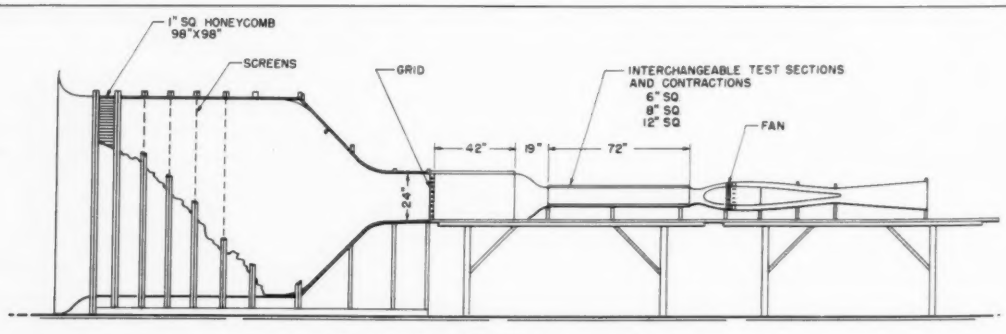

Fig. 3. Experimental arrangement II.

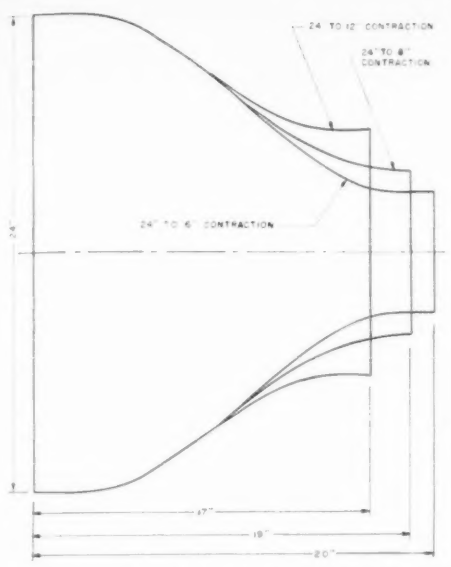

FIG. 4. Dimensions of nozzles. The cross section is a square.

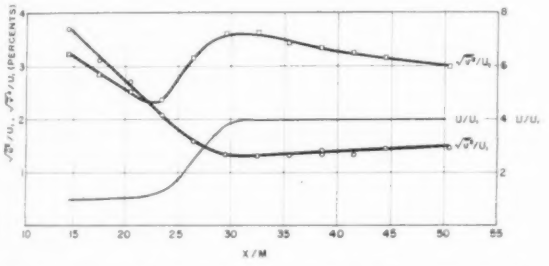

FIG. 5. Effect of 4:1 contraction on turbulence generated by 2-in. square mesh grid, $R_M = 3{,}710$.

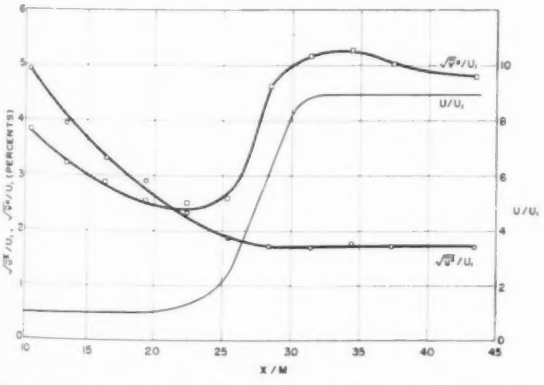

FIG. 6. Effect of 9:1 contraction on turbulence generated by 2-in. square mesh grid, $R_M = 3{,}710$.

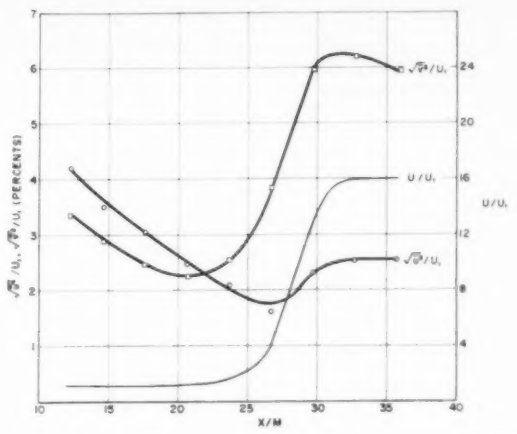

FIG. 7. Effect of 16:1 contraction on turbulence generated by 2-in. square mesh grid, $R_M = 3{,}710$.

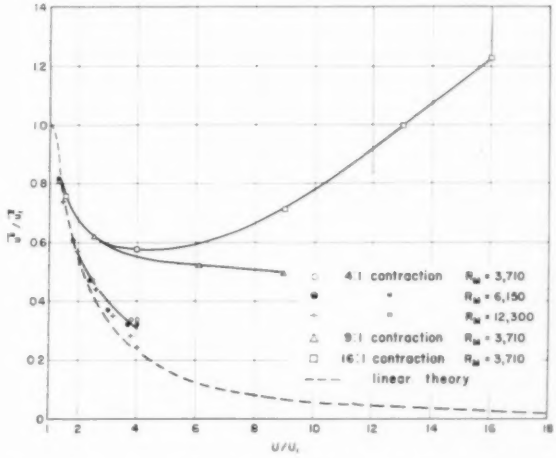

FIG. 8. Change of $\overline{u^2}$ as a function of increase in the mean speed.

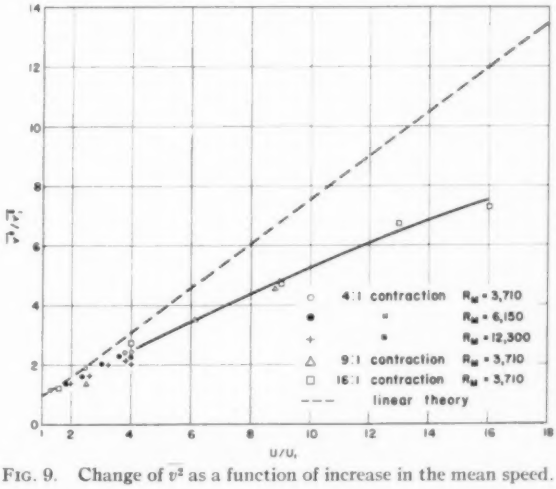

FIG. 9. Change of $\overline{v^2}$ as a function of increase in the mean speed.

that $\overline{v^2}/v_1^2$ is smaller than predicted by the linear theory. In the theory it is contended that, for a sufficiently rapid contraction, the following assumptions can be made: (1) neglect of viscosity, (2) the relative motion of two neighboring particles due to turbulence is small compared with that produced by the contraction—i.e., the stretching or contraction of a vortex filament due to turbulence is small compared with that produced by the contraction. Neglect of viscosity does not explain the observed deviations from the theory since its effect would be to decrease both $\overline{u^2}/u_1^2$ and $\overline{v^2}/v_1^2$. The second assumption is therefore questionable.

There is continuous movement and mixing in a turbulent fluid, and vortex filaments which started out parallel to the main flow will not remain so as they go through the contractions and, consequently, will not be stretched as much as assumed in the theory. Similarly, the vortex filaments which started out perpendicular to the main stream will not contract as much. Naturally, fairly large random movement due to turbulence would nullify the preferential stretching and contraction of vortex filaments due to increase in the mean speed. This tendency toward isotropy or the equipartition of turbulence energy among the three velocity components is the important feature which deserves further investigation. The study of equipartition of turbulence energy inside the nozzle is complicated by rapidly changing mean velocity and turbulence fields. However, the conditions in the uniform section are ideal for such a study. In Fig. 5 we see that, in the uniform section, $\overline{u^2}$ and $\overline{v^2}$ slowly equalize. We shall return to this later, but at the moment we are mainly interested in the turbulence intensities just before and after the contraction. It is usually assumed that, for rapid convergence, the effect of contraction should conform to the linear theory. The rapidity of contraction alone does not determine the deviations from the linearized theory, and the total contraction also enters into the picture. All three contractions are equally rapid or slow, but, for 16:1 contraction, even the direction of change given by linearized theory is reversed, and $\overline{u^2}$ increases at the end of the contraction instead of continuing to decrease. If the change of total energy is compared with that predicted by the linear theory, then the comparison would be little more favorable since the largest deviations are for $\overline{u^2}$, which makes small contribution to the total energy.

At the point on the axis of 16:1 contraction where the mean speed has risen to four times its original value, $\overline{u^2}$ is not the same as that at the end of 4:1 contraction. This is because, at this point in 16:1 contraction, there are sharp mean velocity gradients while, at the corresponding point in the 4:1 contraction, the mean flow is uniform. It is not possible to predict the performance of all nozzles of contraction ratios between one and 16 from that of contraction ratio 16.

Effect of Reynolds Number

The effect of turbulence Reynolds Number on the performance of 4:1 contraction was studied by changing the mesh size of the turbulence generating grid as well as the mean speed. In the first experiment of this set, the mesh Reynolds Number was 6,150 which is about twice that in previous experiments. The turbulence was generated by a 1-in. square mesh biplanar grid made of 1/4-in. rods. The measurements on the contraction axis are shown in Fig. 10.

In the second experiment of this set, a 2-in. square mesh grid was used, giving a mesh Reynolds Number of 12,300 which is four times that of previous experiments. Turbulence intensity measurements are shown in Fig. 11.

Comparison of Figs. 5, 10, and 11 shows that turbulence Reynolds Number has insignificant effect on the performance of a nozzle. The above measurements are also compared with other measurements in Figs. 8 and 9. The 4:1 contraction used in the two experiments described above is not identical with that used earlier, but this is of little consequence.

Performance Analysis of a Low-Turbulence Wind Tunnel

It is desirable to analyze the actual performance of a low-turbulence wind tunnel before we compare the present measurements with other data available on the subject. This will serve to explain the inconsistencies among different sets of data.

It was found that the free-stream turbulence level in the 2- by 2-ft. low-turbulence open return wind tunnel used for the present investigation increased with speed and that turbulence consisted of bursts. The 16:1 contraction used in the tunnel is quite rapid, and it was suspected that turbulent bursts are due to separation in the contraction. However, careful examination showed no separation. We finally came to the conclusion that, as the speed is increased, the turbulent fluid from the fan reaches the pressure box with little decay—i.e., swirling masses of fluid are drawn into the tunnel before they have time to decay. The four fine screens used in the pressure box were unable to damp out the bursts, and it was finally decided to use a honeycomb of 1-in. square and 9-in. deep cells. This eliminated the bursts and considerably reduced the turbulence level; $\overline{v^2}/U = 0.015$ per cent, and $\overline{u^2}/U = 0.03$ per cent. However, the fact that $\overline{u^2} > \overline{v^2}$ is in contradiction to our previous measurements of the effect of contraction on free-stream turbulence. Dryden and Schubauer[5] have already shown that when free-stream turbulence level in a wind tunnel is reduced by screens and a contraction, the remaining fluctuations are mainly sound waves coming from the fan. These sound waves are not of discrete frequency but form a more or less continuous spectrum which is no doubt dominated by the frequency of the fan blade. The pulsations, being of very large wave lengths, are not reflected from the tunnel walls and are, therefore, plane sound waves which should contribute only to $\overline{u^2}$. Furthermore, the velocity associated with these sound waves should be perfectly correlated across the entire section. Measurement of

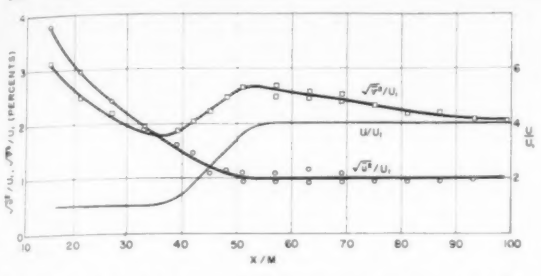

FIG. 10. Effect of 4:1 contraction on turbulence generated by 1-in. square mesh grid, $R_M = 6{,}150$.

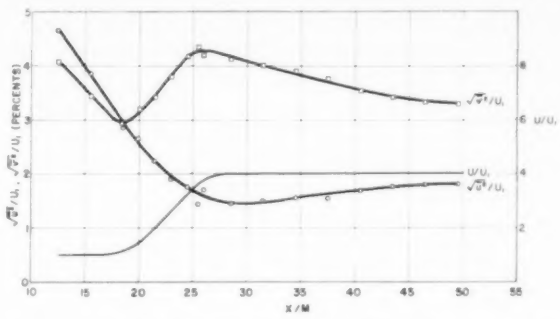

FIG. 11. Effect of 4:1 contraction on turbulence generated by 2-in. square mesh grid, $R_M = 12{,}300$.

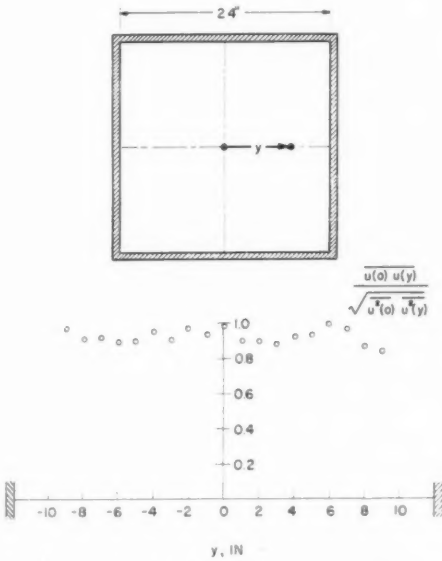

FIG. 12. Lateral correlation of free-stream turbulence in 2- by 2-in. tunnel.

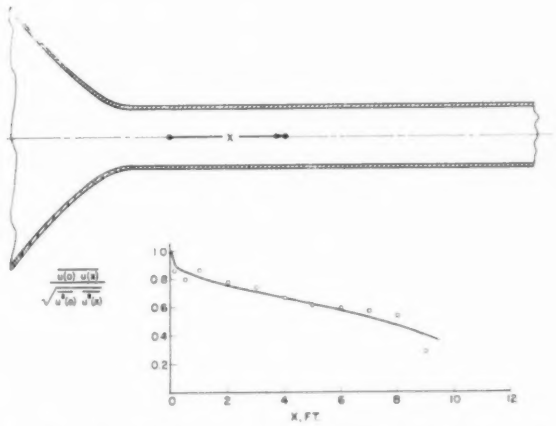

FIG. 13. Longitudinal correlation of free-stream turbulence in 2- by 2-in. tunnel.

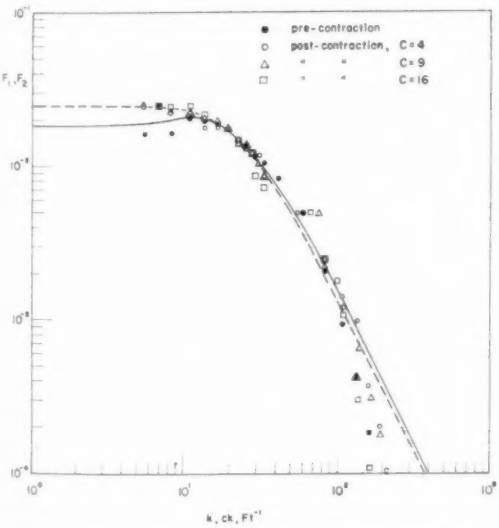

FIG. 14. The spectra of v^2. If the measured precontraction spectrum is approximated by the solid line, then the dotted line is the postcontraction spectra predicted by the linear theory.

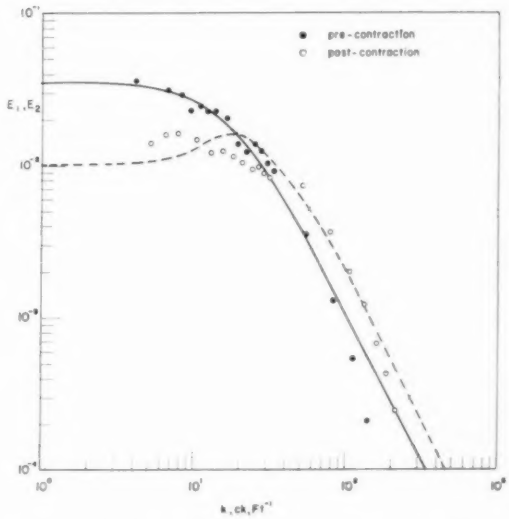

FIG. 15. The spectra of u^2 for 4:1 contraction. If the measured precontraction spectrum is approximated by the solid line, then the dotted line is the postcontraction spectra predicted by the linear theory.

lateral correlation coefficient of u components is shown in Fig. 12, and almost perfect correlation (0.9) confirms the above conjecture. The longitudinal correlation coefficient was also measured and is shown in Fig. 13. The total u component of the fluctuating velocity is made up of eddy turbulence and random sound. The former is of relatively small scale and its correlation rapidly disappears, while the latter, being of large wave length, shows appreciable correlation for 10–12 ft.

It is possible to determine the intensities of sound and turbulence by measuring the lateral correlation of u. Let u_t and u_s denote the contribution of turbulence and sound, respectively, to the total velocity fluctuation. The measured lateral correlation coefficient of u at two points for large separation y of the points is

$$\{\overline{[u_t(0) + u_s(0)][u_t(y) + u_s(y)]}\} \div [\overline{u_t^2(0) + u_s^2(0)}] \simeq [\overline{u_s^2}/(\overline{u_t^2} + \overline{u_s^2})] = 0.9$$

where we have made use of the fact that $\overline{u_t(0)u_t(y)} = 0$ for large y and that $\overline{u_s(0)u_t(y)} = \overline{u_t(y)u_s(0)} = 0$ since the sound and turbulence are statistically independent under the present conditions. Making use of the fact that $\overline{u_t^2}/U^2 + \overline{u_s^2}/U^2 = (0.0003)^2$, we find that $\sqrt{\overline{v_s^2}}/U$, the true eddy turbulence, is 0.009 per cent which is smaller than $\sqrt{\overline{v^2}}/U$, the latter having a value of 0.015 per cent.

The intensity of sound waves in the 2- by 2-ft. tunnel was considerably reduced by using a twelve-bladed fan of improved quality.* However, when 16:1 contraction is placed in the test section, it is necessary to use a 1:16 diffuser. The turbulence increases considerably in the diffuser, and the flow reaching the fan is quite disturbed. This increases the sound generated by the fan. It was therefore decided to use a small fan, as shown in Fig. 3, for 9:1 and 16:1 contractions. Even then, the contribution of sound waves to u was subtracted out at every point by making the measurement without the grid and assuming that sound and turbulence are uncorrelated. The sound generated is mainly determined by the quality of the fan and the fan loading, and the latter changes little with or without the grid which is in the low-speed section of the duct. There was appreciable correction for 16:1 contraction only.

Another method of subtracting out noise is to use two wires placed so far apart that eddy turbulence is uncorrelated. The difference of the signal from the two wires gives the eddy turbulence, and the sound is automatically subtracted out.

We are now in a position to discuss other available data on the subject. The first reported experiments to check Prandtl's theory were conducted by Fage[9] in 1934. He found that, in contradiction to Prandtl's prediction, the absolute value of $\overline{v^2}$ decreased and $\overline{u^2}$ remained about the same. Some measurements were made by MacPhail,[10] who found that $\overline{v^2}$ increased and $\overline{u^2}$ decreased initially but that, toward the end of the contraction, the two components tended to equalize in a rapid and oscillatory fashion. Other measurements have been reported by Hall[11] and by Dryden and Schubauer.[8] These data are not very accurate since no attempt was made to eliminate the extraneous effects. Recently, Townsend[12] has published a paper in the uniform distortion of homogeneous turbulence. Although his results cannot be directly compared with present investigation, both have one common feature—distortion of homogeneous turbulence.

Turbulence Structure Changes in a Contraction

Effect on Turbulence Spectra

The post- and precontraction longitudinal spectra of $\overline{u^2}$ and $\overline{v^2}$ were measured for all three contractions. The turbulence was generated by a 2-in. square mesh grid at an R_M of 3,170. A special low-frequency wave analyzer, covering a range from 2–200 cycles per sec., was designed using three operational amplifiers. This was necessary since we are particularly interested in the spectra at low wave numbers or frequencies. The spectra were measured as a function of frequency n and were later expressed as functions of wave number by using Taylor's hypothesis of interchangeability of instantaneous time and space variable—i.e., $t = x/U$. Using this assumption, the wave number $k = 2\pi n/U$. The precontraction one-dimensional longitudinal spectra of $\overline{u^2}$ and $\overline{v^2}$ are defined by the following relations:

$$E_1(k) = \frac{2}{\pi \overline{u_1^2}} \int_0^\infty \overline{u_1(0)u_1(x)} \cos k\,x\,dx \qquad (5)$$

$$F_1(k) = \frac{2}{\pi \overline{v_1^2}} \int_0^\infty \overline{v_1(0)v_1(x)} \cos k\,x\,dx \qquad (6)$$

The spectra, so defined, are normalized—i.e., $\int_0^\infty E_1(k)\,dk = \int_0^\infty F_1(k)\,dk = 1$. The postcontraction spectra are similarly defined:

$$E_2(ck) = \frac{2}{\pi \overline{u_2^2}} \int_0^\infty \overline{u_2(0)u_2(x)} \cos ck\,x\,dx \qquad (7)$$

$$F_2(ck) = \frac{2}{\pi \overline{v_2^2}} \int_0^\infty \overline{v_2(0)v(x)} \cos ck\,x\,dx \qquad (8)$$

$$\left(\int_0^\infty E_2(ck)\,d(ck) = \int_0^\infty F_2(ck)\,d(ck) = 1\right)$$

For reasons given later, the postcontraction spectra are expressed as function of ck instead of k, where c $(= U_2/U_1)$ is the contraction ratio.

The measured post- and precontraction spectra for the three contractions are shown in Figs. 14–17. Since the linear theory does not correctly predict the postcontraction turbulence intensities, it is improbable that it will correctly predict the postcontraction spectra. However, it is still of interest to compare the results with the predictions of the linear theory. Using the linear theory, the postcontraction spectra can be com-

* Louis C. Garby designed the 2- by 2-ft. low-turbulence open return wind tunnel used in this investigation. He has further reduced the sound and turbulence by improved design and will report elsewhere on this tunnel.

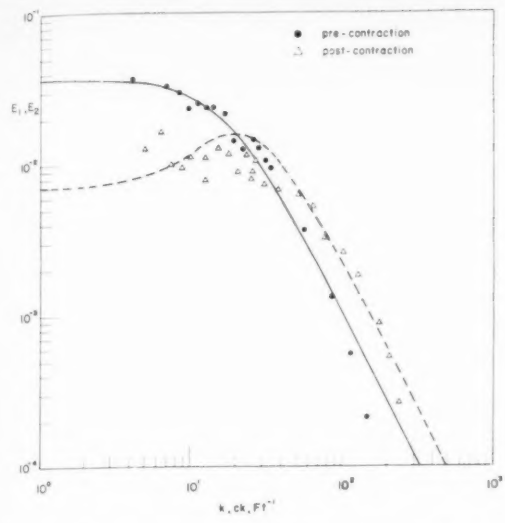

FIG. 16. The spectra of $\overline{u^2}$ for 9:1 contraction. If the measured precontraction spectrum is approximated by the solid line, then the dotted line is the postcontraction spectra predicted by the linear theory.

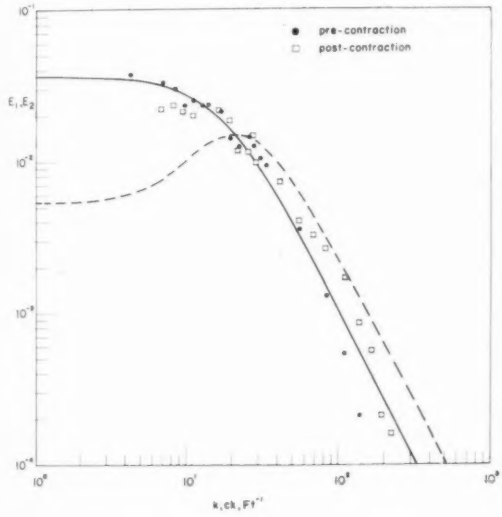

FIG. 17. The spectra of $\overline{u^2}$ for 16:1 contraction. If the measured precontraction spectrum is approximated by the solid line, then the dotted line is the postcontraction spectra predicted by the linear theory.

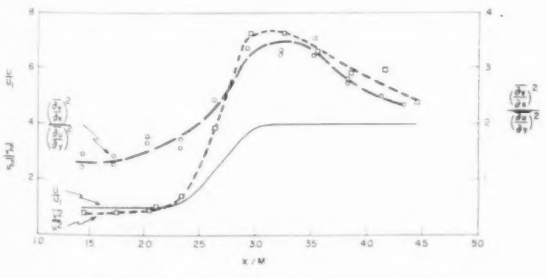

FIG. 18. Local isotropy in 4:1 contraction.

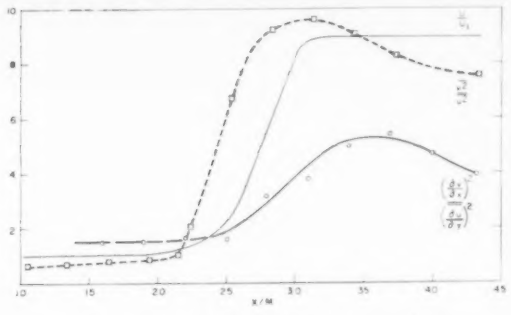

FIG. 19. Local isotropy in 9:1 contraction.

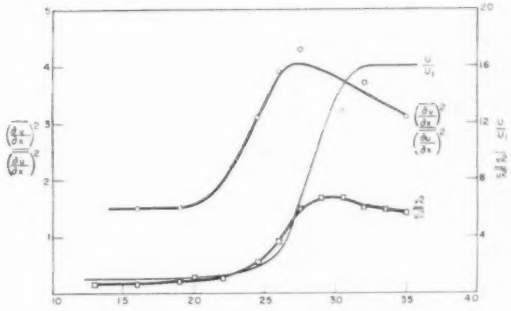

FIG. 20. Local isotropy in 16:1 contraction.

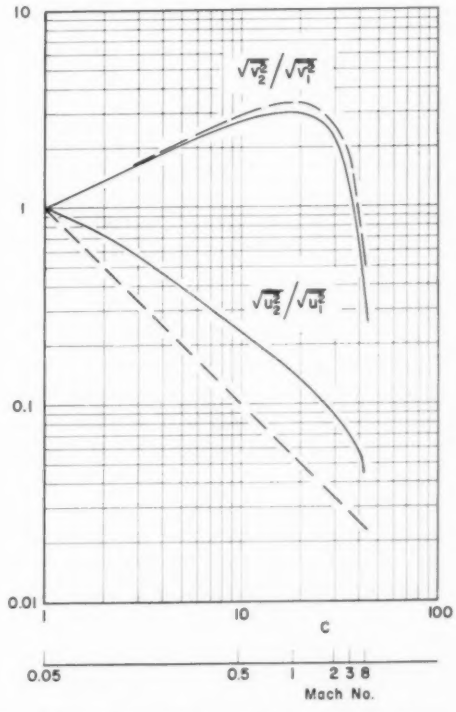

FIG. 21. Effect of supersonic nozzle on eddy turbulence; solid line, exact linear theory; dotted line, approximate linear theory.

puted from the precontraction spectra. These lengthy numerical calculations are not justified, and simpler procedure is used. We assume that the three-dimensional spectrum of the precontraction turbulence is isotropic, and it can be approximated by the relation $(k/k_0)^4/[1 + (k/k_0)^2]^3$, or that one-dimensional measured spectra can be approximated by the following:

$$E_1 = (2/\pi\, k_0)[1 + (k/k_0)^2]^{-1} \tag{9}$$

$$F_1 = (1/\pi\, k_0)[\{1 + (k/k_0)^2\}^{-1} + 2\,(k/k_0)^2\{1 + (k/k_0)^2\}^{-2}] \tag{10}$$

A reasonably good agreement with experiments (Figs. 14 and 15) is obtained with $k_0 = 17.6$ ft.$^{-1}$. The postcontraction spectra have been computed using the linear theory and the above approximations for the precontraction spectra. The details of similar calculation are given by Ribner and Tucker[4] and will not be repeated here.

According to the linearized theory, the postcontraction spectra of v^2 for all three contractions should fall on a single curve when plotted as a function of ck. Fig. 14 shows that there is fair agreement on this point. There is no agreement between the predicted and the measured spectrum of u^2 (Figs. 15–17). The disagreement gets worse with increased contraction ratio. This was to be expected from the measured turbulence intensities. Of course, there would be still greater discrepancy if the comparison were based on absolute instead of normalized spectra. For all these measurements, the spectrum of sound was subtracted from the combined spectrum of sound and turbulence on the basis that the two are uncorrelated.

Local Isotropy in a Contraction

The ratio $\overline{(\partial v/\partial x)^2}/\overline{(\partial u/\partial x)^2}$ was determined on contraction axes by electrical differentiation and assuming interchangeability of space and time derivatives. The measurements for the three contractions are shown in Figs. 18–20. The ratio should be two for locally isotropic turbulence, and the fact that, for precontraction turbulence, it is not exactly two is either due to some error in measurement or slight deviation of grid-generated turbulence from local isotropy. Inside the contraction, the turbulence is far from being locally isotropic. For 4:1 contraction, the measurements made in the uniform section after the contraction show that the turbulence is becoming locally isotropic faster than equipartition of turbulent energy among the three components is being realized. From his work on uniform distortion of homogeneous turbulence, Townsend[12] also found that return to local isotropy is faster than equipartition of energy. However, his interpretation that even highly anisotropic turbulence dissipates its energy through nearly isotropic eddies should be taken with caution.

Equipartition of Turbulent Energy

The effect of the contraction or mean rate of strain is to produce anisotropic turbulence, and the random rate of strain of turbulence tends to produce isotropy or to equalize the turbulence energy in three components. The transfer of energy takes place throughout the nozzle, although it is striking for 16:1 contraction. There is little energy in $\overline{u^2}$ compared with that in $\overline{v^2}$ and $\overline{w^2}$, and even a small transfer to $\overline{u^2}$ will change the actual value from $\overline{u^2}$ from that predicted by the linear theory. Things are complicated in the contraction, and equipartition of turbulence energy is best studied in uniform section after the contraction. Measurements in the uniform section after the 4:1 contraction show that the turbulence is fairly homogeneous and that the energy in $\overline{u^2}$ and $\overline{v^2}$ ($\overline{w^2} = \overline{v^2}$) slowly equalizes. Since the mean flow is uniform, it does not interact with the turbulence, and changes in $\overline{u^2}$ and $\overline{v^2}$ are due to mutual transfer and viscosity.

The expressions for transfer can easily be obtained from the equation of motion. The energy equation for fluctuating velocity is

$$(1/2)[(\partial u^2/\partial t) + u(\partial u^2/\partial x) + v(\partial u^2/\partial y) + w(\partial u^2/\partial z)] = -(u/\rho)(\partial p/\partial x) + \nu\, u\Delta u \tag{11}$$

After making some transformation and using continuity equation for incompressible flow, we have

$$(1/2)[(\partial u^2/\partial t) + (\partial u^3/\partial x) + (\partial v u^2/\partial y) + (\partial w u^2/\partial z)] = -(1/\rho)(\partial p u/\partial x) + (p/\rho)(\partial u/\partial x) + \nu\,\Delta u^2 - \nu[(\partial u/\partial x)^2 + (\partial u/\partial y)^2 + (\partial u/\partial z)^2] \tag{12}$$

For a statistically homogeneous field, the average of the above equation is

$$\frac{1}{2}\frac{\partial \overline{u^2}}{\partial t} = \frac{1}{\rho}\overline{p\frac{\partial u}{\partial x}} - \nu\left[\overline{\left(\frac{\partial u}{\partial x}\right)^2} + \overline{\left(\frac{\partial u}{\partial y}\right)^2} + \overline{\left(\frac{\partial u}{\partial z}\right)^2}\right] \tag{13}$$

Now, if $\partial/\partial s$ is the gradient in the direction making equal angles with all three axes, then

$$3\overline{\left(\frac{\partial u}{\partial s}\right)^2} = \overline{\left(\frac{\partial u}{\partial x} + \frac{\partial u}{\partial y} + \frac{\partial u}{\partial z}\right)^2} = \left[\overline{\left(\frac{\partial u}{\partial x}\right)^2} + \overline{\left(\frac{\partial u}{\partial y}\right)^2} + \overline{\left(\frac{\partial u}{\partial z}\right)^2}\right] +$$

some cross products which vanish because the turbulence is axisymmetric about the x axis.

Substituting this result in Eq. (13), we get

$$\frac{1}{2}\frac{\partial \overline{u^2}}{\partial t} = \frac{1}{\rho}\overline{p\frac{\partial u}{\partial x}} - 3\nu\overline{\left(\frac{\partial u}{\partial s}\right)^2} \tag{14}$$

Similarly

$$\frac{1}{2}\frac{\partial \overline{v^2}}{\partial t} = \frac{1}{\rho}\overline{p\frac{\partial v}{\partial y}} - 3\nu\overline{\left(\frac{\partial v}{\partial s}\right)^2} \tag{15}$$

From the continuity equation it follows that

$$\overline{p\frac{\partial u}{\partial x}} + \overline{p\frac{\partial v}{\partial y}} + \overline{p\frac{\partial w}{\partial z}} = 0 \quad \text{or} \quad 2\overline{p\frac{\partial v}{\partial y}} = -\overline{p\frac{\partial u}{\partial x}}$$

and the decay equations, Eqs. (14) and (15), become*

$$\frac{1}{2}\frac{\partial \overline{u^2}}{\partial t} = \frac{1}{\rho}\overline{p\frac{\partial u}{\partial x}} - 3\nu\overline{\left(\frac{\partial u}{\partial s}\right)^2} \tag{16}$$

$$\frac{1}{2}\frac{\partial \overline{v^2}}{\partial t} = -\frac{1}{2\rho}\overline{p\frac{\partial u}{\partial x}} - 3\nu\overline{\left(\frac{\partial v}{\partial s}\right)^2} \tag{17}$$

There may be transfer of energy from one component to another, but the total energy is decreasing due to viscosity alone. We have measured $\overline{u^2}(t)$, $\overline{v^2}(t)$, and $\overline{(\partial u/\partial s)^2}$; the last quantity was determined by measuring the correlation of u for small distances in the direction s. These measurements were made in the uniform section after the 4:1 contraction. The remaining quantities can be calculated from Eqs. (16) and (17). From these data we find that

$$\frac{1}{\rho}\overline{p\frac{\partial u}{\partial x}}\Big/3\nu\overline{\left(\frac{\partial u}{\partial s}\right)^2} \simeq 1.5$$

i.e., $\overline{u^2}$ is gaining 50 per cent more energy from $\overline{v^2}$ or $\overline{w^2}$ than is needed for its decay. Also,

$$\frac{1}{2\rho}\overline{p\frac{\partial u}{\partial x}}\Big/3\nu\overline{\left(\frac{\partial v}{\partial s}\right)^2} \simeq 0.2$$

i.e., $\overline{v^2}$ or $\overline{w^2}$ is losing 1/5 as much energy by transfer as it is due to viscosity. Townsend[14] has found that, when isotropic turbulence is passed through a wire gauze, the resulting turbulence is anisotropic and $\overline{u^2}$ and $\overline{v^2}$ equalize slowly. Further research along these lines is in progress, and, without attaching great significance to the above numbers, it is safe to say that, in homogeneous turbulence, the equipartition of energy is taking place rather slowly.

Supersonic Nozzles

When considering the effect of a supersonic nozzle on flow irregularities, it is necessary to distinguish between two types of fluctuations that are possible in a compressible fluid. One is "eddy" turbulence which is associated with vorticity, and the other is random sound. In a supersonic nozzle, there will be fluctuations which are generated in the test section or are due to pulsations. For example, the turbulent boundary layer can cause a fluctuating Mach wave pattern in the test section. If we consider eddy turbulence alone, as was done in the incompressible case, we can readily generalize the Prandtl theory to the supersonic case without performing any lengthy calculations. It is only necessary to assume that pressure is a unique function of density, a condition which is satisfied to a high approximation in nozzles.

As in the incompressible case, let us assume that the u fluctuations are mainly due to vortex filaments lying perpendicular to the x axis and that the v fluctuations are due to those lying perpendicular to the y axis. Since we have assumed that pressure is a unique function of density, then, neglecting viscosity, the circulation or the product of angular velocity and cross-sectional area of a vortex tube remains constant. Let us assume axisymmetric contraction; the results can be easily extended to contractions of other shapes. In going through the nozzle, a fluid element will be stretched along the x axis by a factor c ($= U_2/U_1$) and will be changed in the y direction by a factor $\sqrt{\rho_1/\rho_2 c}$. The angular velocity of a vortex filament lying along the nozzle axis changes by a factor $c(\rho_2/\rho_1)$, and its radius changes by a factor $\sqrt{\rho_1/c\rho_2}$, and hence the peripheral velocity changes by a factor $\sqrt{c\rho_2/\rho_1}$—i.e.,

$$v_2/v_1 = w_2/w_1 = \sqrt{c\rho_2/\rho_1} \tag{18}$$

The decrease in density reduces v_2. The angular velocity of a vortex filament lying along the y axis changes by a factor $\sqrt{\rho_2/c\rho_1}$, and the distances of the periphery from the center of the vortex tube changes by a factor $\sqrt{\rho_1/c\rho_2}$. Hence, the peripheral velocity changes by a factor $1/c$—i.e.,

$$u_2/u_1 = 1/c \tag{19}$$

For large density changes, both u_2 and v_2 are reduced to an insignificant value relative to the test section speed. As an example, let us assume that for a Mach 8 hypersonic air tunnel, the Mach Number in the pressure box is 0.05 and $u_1/U_1 = v_1/U_1 = w_1/U_1 = 5$ per cent. Using Eqs. (18) and (19) and isentropic relations between density and Mach Number ratios we have

$$u_2/U_2 = 0.003 \text{ per cent} \qquad v_2/U_2 = 0.03 \text{ per cent}$$

The value for v_2/U_2 is the upper limit since decay and transfer have been neglected. Using linear theory, Ribner and Tucker[4] have calculated the effect of supersonic nozzle on free-stream (eddy) turbulence, and their results are compared with the above approximate calculations in Fig. 21 for an air tunnel with pressure box Mach Number of 0.05. Experience with incompressible flow has shown that difference between the approximate and exact calculations is significant compared with that due to linearization of the equations.

Corrsin[15] has extended Prandtl's results for the compressible case including temperature fluctuations but using isentropic relations. His analysis gives the effect of contraction on one component, $\overline{u^2}$, only, and for no temperature fluctuations his results are consistent with present analysis.

Remarks on Turbulent Flows

The original investigation was undertaken to study the properties of homogeneous turbulence, such as equipartition of turbulent energy and local isotropy. Research on these topics is in progress and will be reported elsewhere. The following remarks are in order here.

The recent work on the theory of turbulence at high

* The decay equations were first derived by Batchelor[13] using axisymmetric tensors. For the present purpose we are not interested in these tensors, and therefore a simpler derivation is used here.

Reynolds Number is based on the assumption that the entire turbulent motion is made up of a hierarchy of eddies or scales of motion. The large eddies receive their energy from the mean motion of the shear flow whose overall dimensions determine their scale or, in the case of grid-generated turbulence, their scale is determined by the mesh size. The large eddies loose their energy to small eddies which in turn pass it on to still smaller eddies. The smallest eddies dissipate most of the energy by direct action of viscosity. Any directional effect of the shear flow gets progressively less as we go from large to small eddies; the latter are isotropic.

From the foregoing, it follows that the turbulence should be locally isotropic in the contraction while the measurement (Figs. 18–20) show anisotropy. It is quite possible that the Reynolds Number of the present experiments is too low for local isotropy to apply. However, at Reynolds Numbers of the same order of magnitude, local isotropy in shear flows has been confirmed by various investigators. The mean square derivatives of turbulent velocity were measured, and it was shown that they satisfy the isotropic relation. In the contraction, the measurements refer to the principal axis of the rate of deformation of the fluid since x, y, and z are the principal axes for this case. Naturally, directional influence of shear flow on the turbulence is most pronounced in the direction of the principal axes. In shear flow, the measurement of mean square turbulent velocity gradients along the principal axis of the rate of deformation might reveal anisotropy.

The cascade process implies that, if the agency causing the anisotropy disappears, then the turbulence should fast become isotropic. At the end of the contraction, the velocity gradient causing the anisotropy disappears, and references to Figs. 5, 10, and 11 show that turbulence is not rapidly becoming isotropic.

References

[1] Prandtl, L., *Attaining a Steady Air Stream in Wind Tunnels*, NACA TM 726, 1933.

[2] Taylor, G. I., ZAAM, Bed 15, Heft 1, 1935.

[3] Uberoi, M. S., and Kovasznay, L. S. G., *On Mapping and Measurement of Random Fields*, Quart. Appl. Math., Vol. 10, No. 4, 1953.

[4] Ribner, H. S., and Tucker, M., *Spectrum of Turbulence in a Contracting Stream*, NACA TN 2606, 1952.

[5] Batchelor, G. K., *Theory of Homogeneous Turbulence;* Cambridge University Press, 1953.

[6] Corrsin, S., A.E. Thesis, California Institute of Technology, 1942.

[7] Laufer, J., Private correspondence.

[8] Dryden, H. L., and Schubauer, G. B., *The Use of Damping Screens for the Reduction of Wing-Tunnel Turbulence*, Journal of the Aeronautical Sciences, Vol. 14, No. 4, pp. 221–228, April, 1947.

[9] Fage, A., *Effect of a Contraction on the Turbulence in a Fluid Stream*, British R&M 1584, 1934.

[10] MacPhail, D. C., *Turbulence Changes in Contracting and Distorted Passages*, British R&M 2437, 1951.

[11] Hall, A. A., *Measurement of the Intensity and Scale of Turbulence*, British R&M 1842, 1938.

[12] Townsend, A. A., *The Uniform Distortion of Homogeneous Turbulence*, Quart. Jour. Mech. & Appl. Math., Vol. 7, Pt. 1, 1954.

[13] Batchelor, G. K., Proc. Roy. Soc., Vol. 186, 1946.

[14] Townsend, A. A., *The Passage of Turbulence Through Wire Gauzes*, Quart. Jour. Mech. & Appl. Math., Vol. 4, Pt. 3, 1951.

[15] Corrsin, S., *Effect of Wind-Tunnel Nozzle on Steady-Flow Nonuniformities*, Journal of the Aeronautical Sciences, Readers' Forum, Vol. 19, No. 2, pp. 135, 136, February, 1952.

[16] Lamb, H., *Hydrodynamics*, 6th Ed., p. 205; Cambridge University Press, 1932.

[17] MacPhail, D. C., *An Experimental Verification of the Isotropy of Turbulence Produced by a Grid*, Journal of the Aeronautical Sciences, Vol. 8, No. 2, pp. 73–75, December, 1940.

[18] Batchelor, G. K., and Stewart, R. W., *Anisotropy of the Spectrum of Turbulence at Small Wave-Numbers*, Quart. Jour. Mech. & Appl. Math., Vol. 3, Pt. 1, 1950.

Oscillations of a Supersonic Gas Jet . . .

(*Continued from page 753*)

References

[1] Pai, S. I., *On Supersonic Flow of a Two-Dimensional Jet in Uniform Stream*, Journal of the Aeronautical Sciences, Vol. 19, No. 1, p. 61, January, 1952.

[2] Kawamura, R., *Reflection of a Wave at an Interface of Supersonic Flows and Wave Patterns in a Supersonic Compound Jet*, Journal of the Physical Society of Japan, Vol. 7, p. 482, 1952.

[3] Ward, G. N., *The Approximate External and Internal Flow Past a Quasi-Cylindrical Tube Moving at Supersonic Speeds*, Quarterly Journal of Mechanics and Applied Mathematics, Vol. 1, Part 2, p. 225, 1948.

[4] Taunt, D. R., and Ward, G. N., *The Axially Symmetrical Supersonic Free Jet*, Admiralty Report D.A.E.R./Airflow, 39 (unpublished); see *Modern Developments in Fluid Dynamics: High Speed Flow*, Howarth, L., Ed., Vol. 1, p. 319, Oxford, 1953.

[5] Carslaw, H. S., and Jaeger, J. C., *Operational Methods in Applied Mathematics*, Second Ed., Oxford, 1949.

The Human Pilot and the High-Speed Airplane

JAMES L. DECKER*
The Glenn L. Martin Company

Introduction

As aircraft attain higher and higher speeds, the ability of the human pilot to maintain control becomes marginal in some cases. Recognizing that pilot-induced oscillations of large magnitude have been experienced in high-speed low-altitude flight, it is necessary to predict accurately whether the pilot will be able to achieve stable flight with a particular aircraft.

Consequently, analytical expressions, which interpret the dynamic characteristics of a human pilot, are needed for stability analysis. Investigations of pilot response which provide data on such physiological factors as reaction time and muscular lag have been supported by both the United States Air Force and Navy Bureau of Aeronautics. Under specific test conditions experimental data establishing human transfer functions have been obtained. Some of these investigations have taken place at the Franklin Institute, Goodyear Aircraft, and Langley Field,[4] and their findings are included in reference 2.

The purpose of the present study is to investigate human dynamics as it affects the airplane in pitch, and to present a means of predicting the pilot transfer function during pitching flight. In detailing the longitudinal stability of a human pilot–aircraft combination, the type of control the pilot attempts to apply has been rationalized, and the physiological factors of reaction time and muscular lag have been included.

Development of Pilot Transfer Function

A pilot, while flying, senses certain physical displacements or accelerations, and after his particular period of response time has passed, produces the action he calculates will return the airplane to the desired flight condition or attitude. The basic problems involved in expressing this cycle in mathematical form suitable for aircraft–pilot stability analyses are: (1) determining what the pilot employs as sensory cues for the required control action, (2) determining the reaction time of the pilot, and (3) determining the pilot's muscular lag time constant.

Items (2) and (3) above have been studied by several investigators; this analysis will use the typical reaction time of 0.25 sec. and muscular lag time constant of 0.125 sec. established in BuAer Report AE 61-6.[1]

To understand what these factors mean, consider the idealized case of a step input which the pilot attempts to follow. As shown in Fig. 1, there will be a finite time delay between the instant the step function is generated and the instant the pilot initiates his movement. This is the pilot reaction time, τ.

After the signal to move has reached the muscles, an immediate instantaneous displacement is not possible. This muscular lag time, T_2, is defined as the time taken to achieve $(e-1)/e$, or 63.3 per cent of the final value of displacement, measured from the inception of the motion—that is, from the end of the reaction time. Therefore, it is apparent that the time of reaction and the muscular lag introduce a phase lag in the pilot response.

To use these concepts in a stability analysis, it is necessary to express them in mathematical form. The reaction time transfer function is expressed as

$$P_R/\theta_i = e^{-\tau s} \tag{1}$$

(where P_R is the pilot response, θ_i is the input function to which the pilot is sensitive, τ is the pilot reaction time, and s is the Laplace transform variable taken as $j\omega$, where ω is the frequency in radians per sec.

The muscular lag transfer function is

$$P_R/\theta_i = K_0/(0.125s + 1) \tag{2}$$

where K is the gain constant.

Including both the reaction time and the muscular lag, we have

$$P_R/\theta_i = K_0\, e^{-0.25s}/(0.125s + 1) \tag{3}$$

The above transfer function, in which the reaction time, τ, is 0.25 sec., is plotted in Fig. 2. The remaining factor in the determination of the overall pilot transfer function is the selection of the cues to which the pilot is sensitive and to which he responds by moving the controls. During pitching flight, as shown in Fig. 3, the pilot could, for example, react to:

(1) pitch attitude, θ
(2) flight path attitude, γ
(3) pitch rate, $\dot{\theta}$
(4) load factor increment, $\Delta n = V\dot{\gamma}/g$
(5) pitch acceleration, $\ddot{\theta}$
(6) rate of change of load factor, $\dot{n} = V\ddot{\gamma}/g$

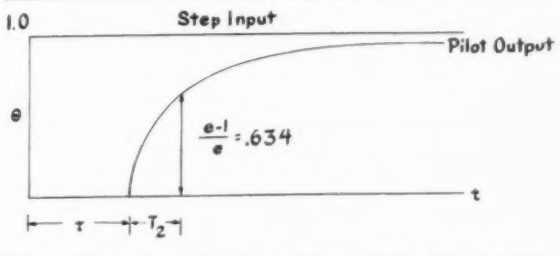

Fig. 1. Effect of reaction time and muscular lag on the response to a step input.

Received May 5, 1955. Revised and received January 6, 1956.
* Chief, Aerodynamics Staff.

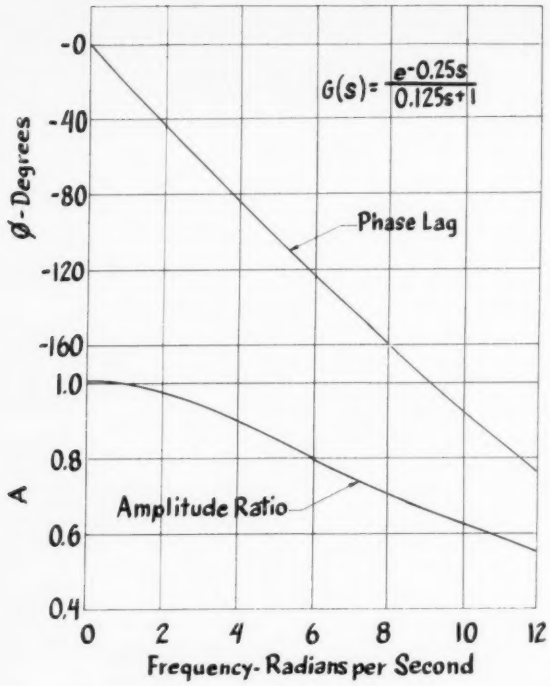

FIG. 2. Pilot reaction time and muscular lag.

Since the load factor and the angle of attack are interrelated, α and $\dot{\alpha}$ are included in items (4) and (6).

Including all of the six items listed above as sensory cues to which the pilot responds is not considered practical. Rather, in selecting a more workable set of cues, it is necessary to choose the basic variable, θ or γ, to which the pilot is sensitive. In this respect, we are guided by the fact that the pilot associates a certain stick force per g with a particular airplane flying at a given weight, speed, altitude, and center of gravity location. On this basis, the flight path attitude, γ, was selected as the primary variable, since $\Delta n = V\dot{\gamma}/g$.

The next step is the determination of the specific function of the flight path attitude which describes the control motion the pilot would like to produce, neglecting his reaction time and muscular lag.

It is evident the pilot uses an angular position reference in flying an aircraft, inasmuch as he is successful in stabilizing a machine that has some static instability. As previously mentioned, a load factor reference enters naturally through the stick force per g. Although this may be expressed as a control proportional to $\dot{\gamma}$, and, therefore, could be considered a damping term, it is not primarily one. This situation results from the fact that load factor is proportional to the angle of attack, and the effect of a control motion applied as a function of load factor is similar to the effect of a change in C_{M_α} of the aircraft. It is not until we introduce a control motion proportional to the rate of change of load factor, $\dot{n}$ or $V\ddot{\gamma}/g$, that we have added a predominantly damping term. It is clear that the pilot is sensitive to $\dot{n}$ in a physiological sense, and consequently is readily capable of providing the control motion proportional to $\ddot{\gamma}$.

The general ideal control law which the pilot may be expected to follow can then be expressed as

$$P_R = k\gamma + k_1\dot{\gamma} + k_2\ddot{\gamma}$$

The pilot reaction P_R may be evidenced either as a control force or as a control motion. Since the control motions for high-speed airplanes in particular are very small, it appears that the primary pilot response is evidenced as a control force application. Therefore, we may write

$$F_p = k\gamma + k_1\dot{\gamma} + k_2\ddot{\gamma} \tag{4}$$

The pilot gain constants must be determined to permit a stability analysis to be made.

In order to do this, the air-frame equations for the short period pitching motion will be considered in conjunction with an idealized control system. A synthetic feel system providing a control feel force proportional to elevator deflection, employed in conjunction with a power operated elevator control, has been assumed. For the purposes of evaluating the pilot gain constants, the control system will be assumed to be frictionless and inertialess. These latter two simplifying assumptions involve little error at the frequencies of interest—namely, those less than approximately one cycle per sec. In passing, it may be mentioned that an extension of the analysis for the case of a manual control system may be made by including the effect of the elevator hinge moment coefficient due to angle of attack.

Consider the air-frame equations for the short period pitch motion.

$$\left.\begin{aligned} C_{L_\alpha}\Delta\alpha &= C_L\frac{V}{g}(\dot{\theta} - \dot{\alpha}) \\ C_{M_\alpha}\Delta\alpha + C_{M_{\dot{\alpha}}}\dot{\alpha} + C_{M_{\dot{\theta}}}\dot{\theta} + C_{M_\delta}\delta &= \frac{I_y}{qS\bar{c}}\ddot{\theta} \end{aligned}\right\} \tag{5}$$

We have the additional relationship

$$\gamma = \theta - \alpha, \qquad F_p = k_3\delta$$

from which can be obtained

$$\left.\begin{aligned} \delta &= K(\theta - \alpha) + K_1(\dot{\theta} - \dot{\alpha}) + K_2(\ddot{\theta} - \ddot{\alpha}) \\ K &= k/k_3; \qquad K_1 = k_1/k_3; \qquad K_2 = k_2/k_3 \end{aligned}\right\} \tag{6}$$

Eqs. (5) and (6) may be combined to yield the characteristic equation for the system consisting of the ideal pilot and the air frame.

$$\begin{aligned} s^3C_L(V/g)(I_y/qS\bar{c}) + s^2\{C_{L_\alpha}[-K_2C_{M_\delta} + (I_y/qS\bar{c})] - C_L(V/g)(C_{M_{\dot{\theta}}} + C_{M_{\dot{\alpha}}})\} + \\ s[-C_{L_\alpha}(K_1C_{M_\delta} + C_{M_{\dot{\theta}}}) - C_L(V/g)C_{M_\alpha}] - KC_{L_\alpha}C_{M_\delta} = 0 \end{aligned} \tag{7}$$

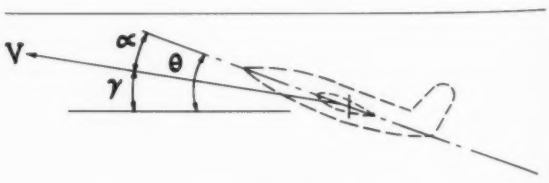

FIG. 3. Cues pilot may react to in pitch case.

The constants K, K_1, and K_2 are yet to be established.

Since the pilot may be expected to attempt to damp any airplane oscillation which exists, it seems reasonable to assume he will aim for a critically damped motion. This assumption provides one boundary condition for the determination of the K values.

For simplicity, Eq. (7) may be written

$$s^3 + (B/A)s^2 + (C/A)s + (D/A) = 0$$

This may be factored into

$$(s^2 + as + b)(s + c) = 0$$

where

$$\left.\begin{aligned} a + c &= B/A \\ b + ac &= C/A \\ bc &= D/A \end{aligned}\right\} \quad (8)$$

From the requirement of critical damping, the damping ratio $\zeta = 1.0$, and we have

$$a^2 = 4b \quad (9)$$

Eqs. (8) and (9) may be combined to give the following expression for a:

$$a = (2/3)(B/A) \pm 2\sqrt{(B^2/9A^2) - (C/3A)} \quad (10)$$

If we apply a second condition that a must be single valued, then

$$\left.\begin{aligned} a &= (2/3)(B/A) \\ b &= B^2/9A^2 \\ c &= B/3A \\ D &= B^3/27A^2 \\ \text{Also, } &\left[\frac{B^2}{9A^2} - \frac{C}{3A}\right] = 0, \quad \text{whence } B = \sqrt{3CA} \end{aligned}\right\} \quad (10a)$$

and

$$C = -C_{L_\alpha}(K_1 C_{M_\delta} + C_{M_{\dot\theta}}) - C_L (V/g) C_{M_{\dot\alpha}}$$

$$A = C_L (V/g)(I_y/g\,Sc)$$

The consequence of the second assumption is the establishment of a particular time for the ideal pilot—control system—air-frame motion to damp to half amplitude. Computational simplicity is the primary reason for making a single valued. The time to half amplitude of the resulting motion under this condition is

$$T_{1/2} = 2.09/(B/A) \text{ sec.} \quad (11)$$

In terms of the aircraft parameters and pilot gain,

$$T_{1/2} = \frac{2.09}{\dfrac{-K_2 C_{L_\alpha} C_{M_\delta}}{C_L (V/g)(I_y/qS\bar{c})} + \dfrac{C_{L_\alpha}}{C_L}\dfrac{g}{V} - (C_{M_{\dot\alpha}} + C_{M_{\dot\theta}})\dfrac{qS\bar{c}}{I_y}} \quad (11a)$$

For an example aircraft, flying at $M = 0.8$ at sea level, Eq. (11a) yields a value of $T_{1/2} = 0.137$ sec. The requirements of reference 3 state that the short period pitching motion shall damp to 1/10 amplitude in one cycle. This is equivalent to requiring $T_{1/2}$ to be 0.301 P, where P is the period of the motion. For the same example aircraft, the reference 3 requirement $T_{1/2}$ is 0.360 sec. It should also be noted that the specification requirement corresponds to a damping ratio of 32 per cent of critical damping.

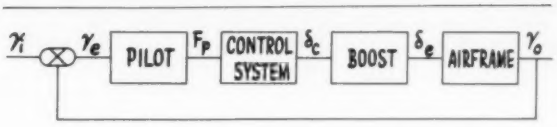

FIG. 4. Block diagram of pilot to air-frame loop.

Since the pilot would be expected to attempt to improve the aircraft damping significantly, it seems that reasonable results are obtained from the computations which are based upon the second assumption.

A third boundary condition to be applied utilizes the assumption that the value of K_1 may be found from the known value of elevator per g.

It is assumed that, in correcting for a load factor disturbance, the pilot will deflect the elevator in a manner equal and opposite to the deflection required to generate an equal load factor in an intentional pull-up. For example, if an up elevator deflection of 1° will produce a load factor increment of 1/2 g, the pilot would react to produce a down elevator deflection of 1° in response to a disturbance which causes a 1/2 g increment in load factor.

We know $\Delta n = V\dot\gamma/g$, therefore,

$$\frac{\partial\delta}{\partial\dot\gamma} = K_1 = \frac{V}{g}\frac{\partial\delta}{\partial n} = \frac{C_L V}{g}\frac{\partial C_M/\partial C_L}{C_{M_\delta}} + \frac{l_t}{V(\partial\alpha/\partial\delta)} \quad (12)$$

This establishes a value for C. Since A is known, B and D may be calculated from Eq. (10). The gain constants K and K_2 may now be determined.

$$K = \frac{-D}{C_{L_\alpha} C_{M_\delta}} \quad (13)$$

$$K_2 = \frac{B + C_L \dfrac{V}{g}(C_{M_{\dot\alpha}} + C_{M_{\dot\theta}}) - C_{L_\alpha}(I_y/qS\bar{c})}{-C_{L_\alpha} C_{M_\delta}} \quad (14)$$

The ideal pilot transfer function is now

$$\frac{\delta}{\gamma} = (K + K_1 s + K_2 s^2) \quad (15)$$

When the pilot reaction time and muscular lag are considered, we have

$$\frac{\delta}{\gamma} = \frac{e^{-0.25s}}{0.125s + 1}(K + K_1 s + K_2 s^2) \quad (16)$$

Eq. (16) expresses the total pilot transfer function.

Application to Typical Airplanes

Having established an expression representative of the pilot transfer function in pitch, application of this equation to a typical airplane will be considered.

Fig. 4 represents the complete loop from pilot to air frame. The pilot's sensitivity to a function of the flight path attitude, γ, results in his producing a force on the control column.

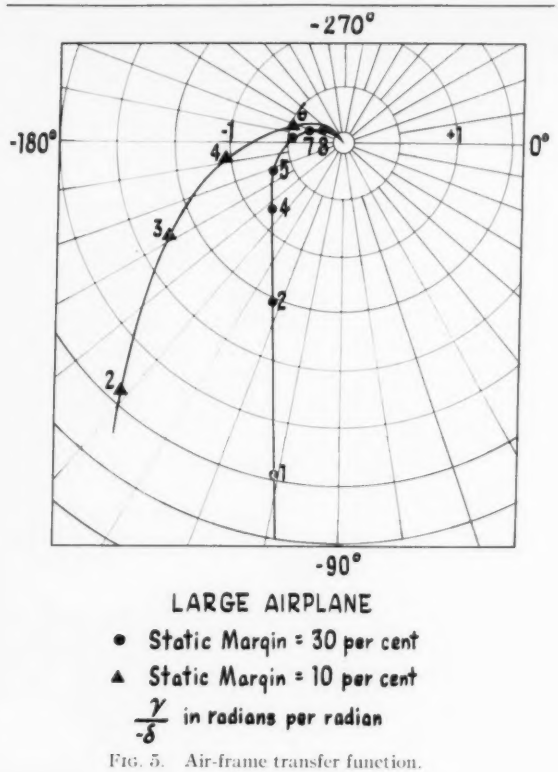

FIG. 5. Air-frame transfer function.

An irreversible power operated longitudinal control has been assumed. The synthetic feel device in the control system provides a stick force proportional to the dynamic pressure and the control deflection change from the trim position. Control system friction and inertia have been considered. The control system transfer function used in the analysis is

$$\frac{\delta c}{F_p} = \frac{1.0}{s^2 + 4s + 2{,}770} \tag{17}$$

A simple time lag has been employed as a mathematical representation of the power boost transfer function. A time constant of 0.033 sec. has been assumed for the hydraulic boost servo.

$$\frac{\delta_e}{\delta_c} = \frac{-0.553}{0.033s + 1} \tag{18}$$

The air-frame transfer function is developed from Eq. (5) for the case of two degrees of freedom. A sea-level flight condition at a speed of 528 knots has been assumed. The flight Mach Number is 0.8. The aircraft parameters are tabulated in Table 1 for a center of gravity location for which $\partial C_M / \delta C_L = -0.3$.

TABLE 1
Aerodynamic and Inertia Parameters of Example Aircraft

Item	Airplane 1	Airplane 2
V	528 knots	528 knots
q	945 lbs./sq.ft.	945 lbs./sq.ft.
altitude	sea level	sea level
C_L	0.0556	0.0556
C_{L_α}	4.59	4.59
$\partial C_M/\partial C_L$	−0.3	−0.3
$C_{M_{\dot\alpha}}$	−0.041	−0.014
$C_{M_{\dot\theta}}$	−0.137	−0.046
C_{M_δ}	−1.75	−1.75
G.W	100,000 lbs.	11,100 lbs.
S	1,900 sq.ft.	211 sq.ft.
I_y	1.65×10^6 slug ft.^{2}	6.12×10^4 slug ft.^{2}
l_t	70 ft.	23.3 ft.
$I_y/qS\bar{c}$	0.0456	0.0456

$$\frac{\gamma}{-\delta} = \frac{C_{L_\alpha} C_{M_\delta}}{-s^3 \frac{I_y}{qS\bar{c}} C_L \frac{V}{g} + s^2 \left[C_L \frac{V}{g} (C_{M_{\dot\alpha}} + C_{M_{\dot\theta}}) - \frac{I_y}{qS\bar{c}} C_{L_\alpha} \right] + s \left[C_{M_\theta} C_{L_\alpha} + C_{M_\alpha} C_L \frac{V}{g} \right]} \tag{19}$$

For a center of gravity location which gives a 10 per cent stability margin, the aerodynamic transfer function for the example aircraft is

$$\frac{\gamma}{-\delta} = \frac{114.5}{s^3 + 6.79s^2 + 19.1s} \tag{20}$$

When a 30 per cent stability margin is present, the transfer function is

$$\frac{\gamma}{-\delta} = \frac{114.5}{s^3 + 6.79s^2 + 39.2s} \tag{21}$$

Fig. 5 presents the airplane Nyquist diagrams.

Establishing the stick force gain of the pilot is the next step. The work of the previous section has established the pilot control transfer function, δ/γ. With the specified feel system at the constant speed assumed for the aerodynamic equations, the stick force varies directly as the control deflection. We know

$$F_p/\gamma = (F_p/\delta)_{ss} (\delta/\gamma) \tag{22}$$

For the airplane under consideration, using Eqs. (17) and (18),

$$(F_p/\delta)_{ss} = -5{,}000 \qquad \text{at} \quad \omega = 0$$

Therefore, the ideal pilot transfer function is

$F_p/\gamma = 167\ (s^2 + 5.00s + 11.9)$(stability margin = 10 per cent)

$F_p/\gamma = 368\ (s^2 + 4.64s + 15.9)$(stability margin = 30 per cent)

The above transfer functions are plotted in Fig. 6. It should be noted that the pilot gain is approximately twice as high at the forward center of gravity position than at the aft position. This indicates the large effect of the aircraft characteristics upon the pilot response.

It is now possible to combine the transfer functions for the pilot, control system, boost, and air frame to determine the stability of the overall system.

The Nyquist plots of the open loop transfer function are presented in Fig. 7. It can be seen that the pilot is able to stabilize the airplane successfully at aft c.g. (10 per cent static margin). The period of the airplane motion in this case is 2.3 sec., and the air-frame damping ratio is $\zeta = 0.775$ for the short period motion. However, neutral stability is indicated at the forward c.g. location (static margin of 30 per cent) and the indications are that the pilot would have difficulty flying the airplane. It should be pointed out that the calculations are critically dependent upon the pilot reaction time, and, with a reaction time of less than 0.25 sec., a stable situation would exist. Conversely, a longer reaction time would result in an instability of the piloted air frame if the pilot continued his efforts to control the aircraft. The air-frame period in this case is 1.2 sec., with a short period $\zeta = .54$.

The higher short-period air-frame oscillatory frequency is responsible for the increased difficulty experienced by the pilot in stabilizing the aircraft at forward c.g. location. The increase in phase lag due to pilot reaction time and muscular lag is 50° greater at the forward c.g. resonant frequency than at the aft c.g. resonant frequency. This points out the basic reason for the reduced capability of a pilot to stabilize an aircraft with a high resonant frequency.

The basic airplane which has been studied is a large one with a 70-ft. tail length. The long tail length produces a high degree of aircraft damping. A small airplane with the same natural frequency would have appreciably less air-frame damping, and therefore may be expected to be considerably more difficult for the pilot to stabilize.

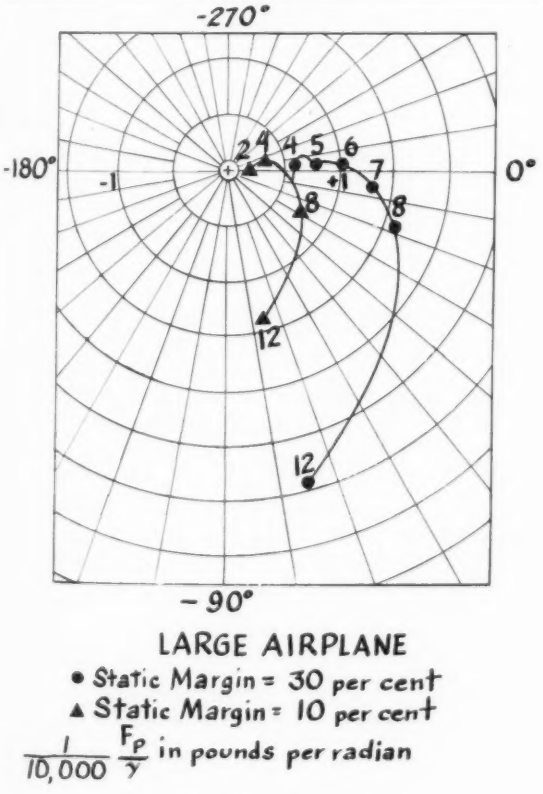

FIG. 6. Pilot transfer function.

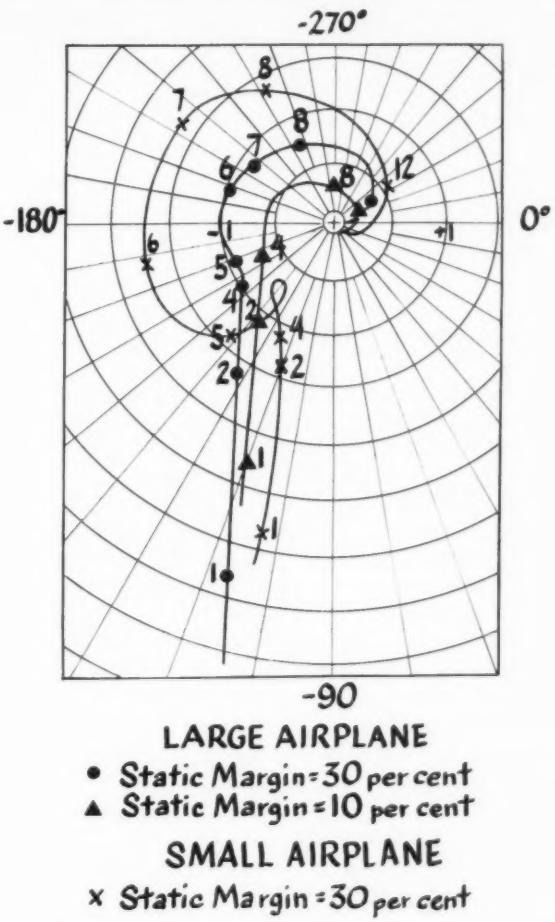

FIG. 7. Pilot-aircraft open loop transfer function.

Calculations have been made for the stability of a second aircraft with the same aerodynamic parameters and flying at the same speed and altitude as the large aircraft. The second aircraft, however, was assumed to be one-third the scale of the first aircraft with respect to external dimensions. The aerodynamic and inertia parameters of both aircraft are tabulated in Table 1. The only differences in the parameters influencing the computations appear in $C_{M_{\dot{\alpha}}}$ and $C_{M_{\dot{\theta}}}$, which become one-third of the values for the first airplane. The undamped resonant frequency remains the same as for the larger aircraft, but with equal values of 30 per cent static margin, the period of the aircraft motion drops to 1.06 sec. from 1.2 sec., and the damping ratio deteriorates from 0.54 to 0.33. As may be seen from Fig. 7, the pilot is incapable of stabilizing this motion. The large influence of aircraft scale on the ability of a pilot to control an aircraft short period pitching motion at high aircraft frequencies is evident from these results.

Limitations of Analysis

These results have been obtained from an analysis which have rationalized the response of a human pilot in flying an aircraft. The foundations upon which an analysis of this type may be built are obviously none too firm at the present time. In particular, the rationalization of the desired state of flight, in terms of damping, frequency, etc., of the controlled motion is somewhat nebulous. Another formidable obstacle, from an analytical point of view, which the human presents is his adaptability to change his gain, dead zone, phase lag, and other dynamic characteristics. It is clear that the results of stability analyses based upon the precepts presented in this paper cannot be taken in a completely literal sense. However, the author does believe that the present methods will serve to identify problem areas. If the results indicate an instability with the human in the loop, the pilot will at least have to make abundant use of his gain changing facilities in flying the aircraft. In short, although the aircraft may be flyable in the particular condition with a human pilot, it will probably not be a desirable airplane for him to fly.

Even at this early stage in work of this type, it seems evident that any transfer function which successfully approximates the human response must (1) account for reaction time and muscular lag, and (2) account for the influence of the aircraft and control system characteristics upon the pilot response.

The importance of accounting for the pilot's ability to change gain is undoubtedly significant. However, in some cases, instabilities may develop in such a rapid fashion that the pilot may be unable to put into effect his transfer function changes before difficulties occur.

Concluding Remarks

The method outlined in this study is offered as a "first step" approach to the pilot simulation problem in pitch. The results, however, appear to be reasonable qualitatively and quantitatively. In particular, the deleterious effects of shortening the aircraft period and reducing aircraft size are strikingly apparent. Aircraft periods of a 1-sec. order for small aircraft appear to be well nigh uncontrollable by the human pilot.

It is reemphasized that the quantitative results are highly dependent upon the assumed pilot reaction time.

It is believed essential to consider in some fashion the fact that the human can vary his dynamic characteristics to complement the dynamics of the system he is controlling. This factor is certainly one of the outstanding capabilities of the pilot, and represents a characteristic which is difficult to attain with automatic control.

References

[1] *Flight Controls Human Dynamic Response Study*, BuAer Report AE-61-6, November, 1953.

[2] *Fundamentals of Design of Piloted Aircraft Flight Control Systems*, Vol. III, "The Human Pilot," BuAer Report AE-61-4, August, 1954.

[3] *Flying Qualities of Piloted Airplanes*, Military Specifications R-1815B and SR-119-B, June 1, 1948.

[4] Cheatham, Donald C., *A Study of the Characteristics of Human Pilot Control Response to Simulated Aircraft Lateral Motions*, NACA RM L52 C17.

Exact and Approximate Solutions for the Supersonic Delta Wing

(*Continued from page 720*)

[5] Courant, R., and Hilbert, D., *Methoden der Mathematischen Physik*, Vol. II, Springer, Berlin, 1937.

[6] Fowell, L. R., *An Exact Theory Of Supersonic Flow Around A Delta Wing*, UTIA Report No. 30, March, 1955.

[7] Durand, W. F., Aerodynamic Theory, Vol. III, Springer, Berlin, 1934.

[8] Emmons, H. W., *The Numerical Solution Of Partial Differential Equations*, Quarterly of App. Mathematics, October, 1944.

[9] Southwell, R. V., *Relaxation Methods In Engineering Science*, Oxford University Press, Cambridge, 1940.

[10] Cristopherson, D. G., and Southwell, R. V., *Relaxation Methods Applied to Engineering Problems. III—Problems Involving Two Independent Variables*, Proc. Roy. Soc. (London), A, 168, pp. 317–350, 1938.

[11] Southwell, R. V., and Vaisey, G., *VIII Plane Potential Problems Involving Specified Normal Gradients*, Proc. Roy. Soc. A, 182, pp. 129–151, 1943.

[12] Fox, L., *Mixed Boundary Conditions*, Quarterly of App. Mathematics, p. 251, October, 1944.

[13] Goldstein, S., and Ward, G. N., *The Linearised Theory Of Conical Fields In Supersonic Flow, With Applications To Plane Aerofoils*, Aeronautical Quarterly, Vol. II, Part 1, May, 1950.

[14] Ferri, A., *Elements Of Aerodynamics Of Supersonic Flows*, The Macmillan Co., New York, 1949.

On the Aerodynamic Instability of Thin Panels

JOHN W. MILES*

University of California, Los Angeles

SUMMARY

The self-excited motion of an infinite, approximately plane, thin panel placed in a compressible flow is examined on the basis of linearized theory. The stability boundaries are determined in a plane having as coordinates a speed parameter (the ratio of the wave velocity of the panel in the absence of the air stream to the air speed) and a mass parameter (air density-wave length/panel mass per unit area); the Mach Number appears as the family parameter of these boundaries. The formulation parallels that of Kelvin for the generation of water waves by wind, but compressibility effects render necessary an implicit solution. The results are confirmed by a Cauchy-Nyquist diagram. It is found that the stiffness required to prevent instability increases monotonically with both the aforementioned mass parameter and Mach number, exhibiting a very steep rise with respect to Mach Number for the relatively short wave lengths representative of practical configurations, although tending to independence of the Mach Number for very large wave lengths. No analytical difficulties are found in the transonic range. The results are compared with previous analyses of periodically supported infinite panels (Hedgepeth, Budiansky, and Leonard) and single span finite panels (Shen and Miles), and are found to be fundamentally dissimilar in important respects. The methods of analysis of the latter studies are criticized as being inadequate.

(1) INTRODUCTION

THE PHENOMENON of self-excited motion of a panel under the action of aerodynamic forces has been considered by Isaacs,[1] Hayes,[2] Miles,[3] Shen,[4] Hedgepeth, Budiansky, and Leonard,[5] and Fung.[6] References 1, 2, and 6, however, deal primarily with the question of static stability of a buckled panel in supersonic flow, and the results have little direct bearing on the present analysis.

The dynamic stability of a two-dimensional panel of finite length, either buckled or unbuckled, in supersonic flow was studied by the author[3] on the assumption that terms of the order of the square of the reduced frequency could be neglected in determining the aerodynamic forces. The results indicated instability for all Mach Numbers less than $\sqrt{2}$ in consequence of the reversal of the aerodynamic damping term. The analysis of the unbuckled panel was repeated by Shen[4] without imposing the frequency restriction on the aerodynamic forces. He concluded that the author's approximation was adequate except in the Mach Number (M), reduced frequency (k) neighborhood defined by

$$M^2 - 2 = 0(k^2) \tag{1.1}$$

We shall discuss Shen's results further in Section 6, but note here that his stability boundary for $M = \sqrt{2}$ (and, implicitly, for all M near $\sqrt{2}$) is double valued, with instability being indicated for mass ratios (the parameter μ defined below) that lie either above the upper branch or below the lower branch.

Budiansky et al. attempted to resolve the difficulties presented by the above results by examining an infinite panel having periodic supports, a configuration claimed to approximate design conditions more closely than a panel of finite length. Their results, however, are even more in conflict with the expectations of physical intuition; not only is instability predicted for all M below about 1.25 (and, for most panels, all M below about 1.5), but the stability boundaries exhibit as many as four branches.

The analytical complexities (preventing simple, algebraic expression of the end results) and/or approximations inherent in the studies of references 3–5 render difficult any intuitive appreciation of the seemingly anomalous results. We find that the motion of an infinite panel, on the other hand, is susceptible to a straightforward analysis in finite terms, with no approximations beyond linearization. The results of this analysis appear to conform with intuitive expectations (vide infra), but their *qualitative* extrapolation to supported panels leads to contradictions that can be resolved only by further investigation.

The motion of a panel under aerodynamic excitation finds natural antecedents in the generation of water waves by the wind and the fluttering of flags and sails, as studied by Kelvin[7,8] and Rayleigh,[9] respectively. The surface wave problem presents a particularly striking analogy, insofar as an analysis considering either gravity or capillary waves (of all possible wave lengths) alone yields a critical wind velocity of zero, whereas the inclusion of both types leads to a minimum wind velocity that is proportional to the minimum surface wave velocity and below which no waves are generated (in the absence of viscous forces). Similarly, we may anticipate that a panel characterized elastically by flexural forces only will be unstable at any finite air speed for sufficiently large wave lengths, whereas the introduction of membrane tension† will lead to instability only for air speeds superior to the minimum wave velocity of the panel (this is stated as a necessary, but not sufficient, condition for instability).

A dimensional analysis of the panel problem, based on the foregoing considerations, leads to the conclusion that the ratio of the critical airspeed U_c to the wave

Received June 29, 1955.

*Professor of Engineering. Also, Consultant, Ramo-Wooldridge Corporation.

† A combination of flexural stresses (which depend on curvature) and stresses proportional to displacement (such as might be provided by an elastic foundation or by direct extensional effects) would furnish a better analogy. This combination will be considered in a future paper dealing with flutter of a cylindrical shell.

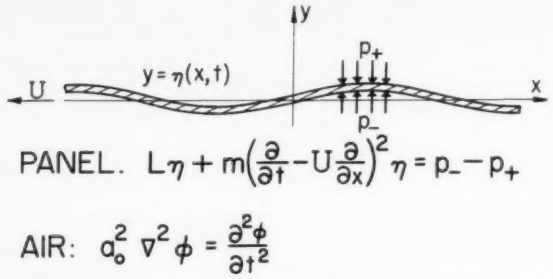

FIG. 1. A thin panel moving with velocity U along the negative x axis and having a small transverse deflection $\eta(x, t)$.

velocity c_0 of the panel at a particular wave length λ may be expressed as a function of a dimensionless mass parameter and a Mach Number according to

$$\frac{U_c}{c_0} = \chi\left(\frac{\rho_0\lambda}{m}, \frac{c_0}{a_0}\right) \tag{1.2}$$

where ρ_0 and a_0 are the mass density and sonic velocity, respectively, of the undisturbed air, and m is the mass per unit area of the panel. An alternative expression, which furnishes a stiffness criterion in the form of a minimum wave velocity c_c, is

$$\frac{c_c}{U} = \psi\left(\frac{\rho_0\lambda}{m}, \frac{U}{a_0}\right) \tag{1.3}$$

There is, of course, no a priori guarantee that the functions χ and ψ will exhibit monotonic dependences on both of their arguments, but we anticipate such a result on physical grounds.

A dimensionless analysis of the stability problem for a finite panel leads again to results like Eqs. (1.2) and (1.3) if the wave length is replaced by the panel length. We no longer would be justified in anticipating monotonic dependences on the mass parameter and Mach Number, however, in consequence of the discrete spectrum of resonant modes of the panel.

(2) THE EQUATIONS OF MOTION

We consider a thin, uniform panel, having the midplane $y = 0$ and placed in an air flow of velocity U directed along the positive x axis (note, in the subsequent analysis the coordinate system will be fixed in the undisturbed air flow). The panel is characterized by a bending stiffness D per unit breadth, a tension load T per unit breadth acting along the x axis, and an areal mass density m; the air by a mass density ρ_0 and a sonic velocity a_0. Small transverse deflections (η) of the panel under a load p per unit area are governed by the elastic equation

$$L\eta \equiv D(\partial^4\eta/\partial x^4) - T(\partial^2\eta/\partial x^2) = p \tag{2.1}$$

The disturbances produced in the surrounding air stream by these deflections may be represented by a velocity potential Φ, which must satisfy the wave equation

$$a_0^2\nabla^2\Phi = \Phi_{tt} \tag{2.2}$$

with respect to a coordinate system at rest in the undisturbed flow.

The equations of motion, Eqs. (2.1) and (2.2), contain essentially all of the assumptions implicit throughout the following analysis, in particular those associated with the linearization of the equations of elastic equilibrium and fluid motion. We remark that the force T may not be negative in the analysis of an infinite panel, for which the Euler buckling load is zero; in the qualitative extrapolation of the results to finite panels, however, we may permit negative values of T insofar as $-T$ is inferior to the minimum buckling load.

We require a solution to the wave Eq. (2.2) subject to the linearized boundary condition

$$(\Phi_y)_{y=0} = \eta_t \tag{2.3}$$

and, subsequent to the assumption of harmonic motion, the Sommerfeld *finiteness* and *radiation* conditions at infinity.* The resulting perturbation pressure on the upper ($y = 0+$) and lower ($y = 0-$) surfaces of the panel then is given by the linearized Bernoulli equation

$$p_\pm = p_0 - \rho_0\Phi_t]_{y=0\pm} \tag{2.4a}$$

$$= p_t \mp \rho_0\Phi_t]_{y=0+} \tag{2.4b}$$

where p_0 is the pressure in the undisturbed air. Eq. (2.4b) follows from Eq. (2.4a) in virtue of the antisymmetry of Φ with respect to $y = 0$, which, in turn, is a direct consequence of Eq. (2.3).

We now regard the panel as moving along the negative x axis with velocity U (see Fig. 1),† so that the inertial load is given by

$$p_i = -m(\partial^2/\partial t^2)[\eta(x, t)]_{(x+Ut)} \tag{2.5a}$$

$$= -m[(\partial/\partial t) - U(\partial/\partial x)]^2\eta(x, t) \tag{2.5b}$$

The total load p is given by

$$p = p_i + p_- - p_+ \tag{2.6}$$

whence the equation of motion of the panel follows from Eqs. (2.1), (2.4b), and (2.5b) as‡

$$L\eta + m(\partial_t - U\partial_x)^2\eta - 2\rho_0\Phi_t]_{y=0+} = 0 \tag{2.7}$$

The deflection η now could be eliminated between Eqs. (2.3) and (2.7) to obtain a homogeneous boundary condition on Φ, but we prefer to preserve the identity of the panel motion.

* We remark that the imposition of the radiation condition is to some extent intuitive, since the usual existence theorems assume the disturbing boundaries to be of finite extent. See, e.g., a recent paper by Stoker.[10]

† Our selection of an axis system moving with the fluid, rather than the panel, is motivated by the greater simplicity of the wave equation, especially as regards the specification of the conditions at infinity.

‡ If we assume the air in $y < 0$ to be at rest with respect to the panel, we have $p_- = p_0$ *approximately*, and the factor of 2 disappears from the last term in Eq. (2.7). More accurately, the air in $y < 0$ could be represented as an access of inertia to the panel, but this generally would be negligible in panel flutter problems; moreover, its precise evaluation for structural configurations would require consideration of adjacent boundaries.

(3) The Eigenvalue Problem

We now consider a traveling wave motion of the form

$$\eta(x, t) = \eta_0 e^{ik(ct-x)}; \qquad k\eta_0 \ll 1 \tag{3.1}$$

We restrict the wave number k to be real, in consequence of the requirement that the solution remain finite at $x = \pm\infty$, but it may be either positive or negative and is related to the wave length λ according to

$$|k| = 2\pi/\lambda \tag{3.2}$$

The *phase* velocity c then appears as an eigenvalue to be determined by the equations of motion; however, we must subject the angular frequency to the a priori restriction

$$Im(kc) \leqq 0 \tag{3.3}$$

Real values of kc correspond to undamped traveling waves moving along the positive or negative x axis as c is positive or negative, respectively, while negative imaginary values of kc imply instability of the assumed, small disturbance. Positive imaginary values of kc would correspond to disturbances tending to infinity at $t = -\infty$ and are not admissible in view of the implicit restriction that any physically realizable, steady-state disturbance such as that specified by Eq. (3.1) must stem from properly specified initial conditions.

In the absence of the air stream ($U = \rho_0 = 0$) the substitution of Eq. (3.1) in the equation of motion (2.7) yields

$$c_0^2 = (T + Dk^2)/m \tag{3.4}$$

We emphasize that c_0 (the phase velocity of transverse waves along the free panel) depends on k, so that the propagation of small disturbances is dispersive except in the limiting case of a pure membrane ($D = 0$).

A solution to the wave Eq. (2.2) that corresponds to the panel deflection of Eq. (3.1) through the boundary condition [Eq. (2.3)] is given by

$$\Phi = -i\beta^{-1}c\eta_0 \exp\,[ik(ct - x) - k\beta|y|]\,\mathrm{sgn}y \tag{3.5}$$

$$\beta = [1 - (c/a_0)^2]^{1/2} \tag{3.6}$$

The Sommerfeld finiteness and radiation conditions impose the respective restrictions

$$Rl(k\beta) \geqq 0 \tag{3.7a}$$

$$Im(\beta) \leqq 0 \qquad \text{as} \qquad Rl(c) \leqq 0 \tag{3.7b}$$

It follows that β is analytic in a c plane cut from $\pm a_0$ to $\pm a_0 + i\infty\,\mathrm{sgn}k$; this choice of branch cuts also is compatible with the restriction of Eq. (3.3). We note that, insofar as the motion is stable, the solution (3.5) represents a *surface wave* that dies out exponentially above the panel.

Substituting Eqs. (3.1) and (3.5) in Eq. (2.7) and noting that $L\eta = mk^2c_0^2\eta$, we obtain the characteristic equation

$$mk^2[c_0^2 - (c + U)^2] - 2\rho_0 k[1 - (c/a_0)^2]^{-(1/2)}c^2 = 0 \tag{3.8}$$

from which the admissible values of c are to be determined. In the determination of these values it is convenient to introduce the dimensionless parameters

$$\zeta = c/U \tag{3.9}$$

$$\zeta_0 = c_0/U \tag{3.10}$$

$$M = U/a_0 \tag{3.11}$$

$$\mu = 2\rho_0/m|k| = \rho_0\lambda/\pi m \tag{3.12}$$

and rewrite Eq. (3.8) in the form

$$f(\zeta) = (\zeta + 1)^2 - \zeta_0^2 + \mu\zeta^2\beta^{-1}\mathrm{sgn}k = 0 \tag{3.13}$$

$$\beta = (1 - M^2\zeta^2)^{1/2} \tag{3.14}$$

where the real part of β is restricted as in Eq. (3.7).

The function $f(\zeta)$ defined by Eq. (3.13) is analytic in a ζ plane cut from $\pm M^{-1}$ to $\pm M^{-1} + i\infty\,\mathrm{sgn}k$, (with $\beta = 1$ at $\zeta = 0$), and the motion of the panel is stable only if f has no zeros in $Im(\zeta\mathrm{sgn}k) < 0$. We consider first the simple, limiting case of incompressible flow, ($M = 0$), for which an explicit solution is possible. The results for compressible flow then will be shown to be qualitatively similar, and, although the actual roots of $f(\zeta)$ can be determined only approximately for $M > 0$, the stability boundary may be determined explicitly.

We remark that the subsequent results may be applied to air blowing over any surface for which the phase velocity $c_0(k)$ and an effective areal mass density m may be determined. Consider, e.g., the classical case of deep water waves in the presence of gravitational and capillary forces; the equation of motion of the surface under the action of a surface pressure p_+ is found to be [see reference 8, §266(5) and §267(1), after solving for and eliminating the velocity potential in the water and allowing for differences in notation]

$$(\rho_1 - \rho_0)g\eta - T_1\eta_{xx} + \rho_1 k^{-1}\eta_{tt} - \rho_0\Phi_t = 0 \tag{3.15}$$

where ρ_1 and T_1 are the mass density and surface tension of the water. Comparing Eq. (3.15) to Eq. (2.7) and allowing for the motion of the axes system in Eq. (2.7), we find the effective values

$$L_1 = (\rho_1 - \rho_0)g - T_1(\partial^2/\partial x^2) \tag{3.16}$$

$$m_1 = \rho_1 k^{-1} \tag{3.17}$$

whence c_0 and μ (deleting the factor of 2 in recognition of the absence of p_-) are given by

$$c_0^2 = (T_1/\rho_1)k + (1 - \rho_0/\rho_1)gk^{-1} \tag{3.18}$$

$$\mu = \rho_0/\rho_1 \tag{3.19}$$

(4) The Incompressible Flow Problem

Setting $M = 0$ in Eqs. (3.13) and (3.14) yields the quadratic equation

$$f(\zeta) = (1 + \mu)\zeta^2 + 2\zeta + (1 - \zeta_0^2) = 0 \tag{4.1}$$

which has the roots

$$\begin{matrix}\zeta_1\\ \zeta_2\end{matrix} = (1 + \mu)^{-1}\{-1 \pm [1 + (1 + \mu)(\zeta_0^2 - 1)]^{1/2}\} \tag{4.2}$$

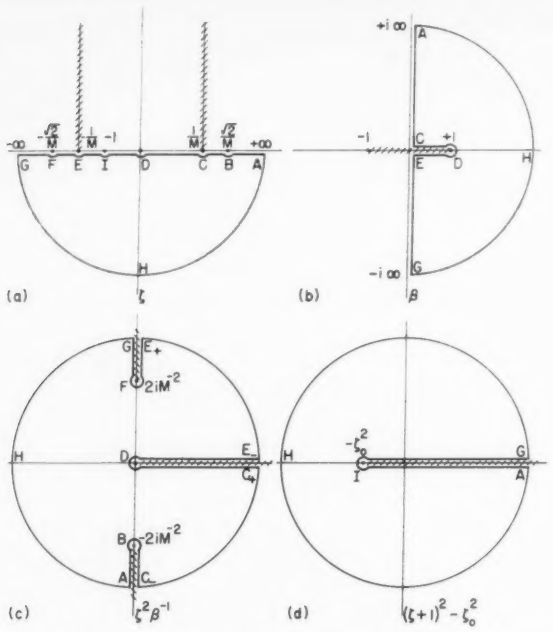

FIG. 2. The contour C in the ζ plane for $k > 0$ and the corresponding contours of β, $\zeta^2\beta^{-1}$, and $(\zeta + 1)^2 - \zeta_0^2$.

Referring to Eqs. (3.9) and (3.10), the corresponding phase velocities *relative to the air* are given by

$$\frac{c_1}{c_2} = (1 + \mu)^{-1}\{-U \pm [(1 + \mu)c_0^2 - \mu U'^2]^{1/2}\} \quad (4.3)$$

We remark that c_1 and c_2 are of opposite sign only if $U < c_0$ ($\zeta_0^2 > 1$), whereas, if $U > c_0$ ($\zeta_0^2 < 1$), c_1 and c_2 are both negative, and no downstream (relative to the undisturbed air) signals are possible.

The phase velocities *relative to the panel* are given by

$$\frac{c_1}{c_2} + U = (1 + \mu)^{-1}\{\mu U \pm [(1 + \mu)c_0^2 - \mu U'^2]^{1/2}\} \quad (4.4)$$

and are of opposite sign if $\zeta_0^2 > \mu$ and both positive if $\zeta_0^2 < \mu$. In the latter instance, no signals can be propagated upstream *relative to the panel;* conversely, signals propagated upstream necessarily correspond to a stable motion.* We note that the result of Eq. (4.4) is identical with air blowing over water if c_0 and μ are substituted from Eqs. (3.18) and (3.19). [Cf. reference 8, §268 (3) and §232 (10) with $U = 0$ therein and U' replaced by the present U.]

The transition to the unstable solution represented by imaginary values of the radical in Eqs. (4.2)—(4.4) occurs at

$$(\zeta_0^2)_c = (c_0^2/U^2)_c = \mu(1 + \mu)^{-1} \quad (4.5)$$

where $(\zeta_0^2)_c$ denotes the critical value of ζ_0^2, below which small disturbances of the panel tend to grow exponentially.† The corresponding phase velocities relative to the panel are given by

$$c_c + U = \mu(1 + \mu)^{-1}U = \mu^{1/2}(1 + \mu)^{-(1/2)}c_0 \quad (4.6)$$

We remark that for small values of μ, such as are found in most practical configurations, $c_c + U$ tends to zero, and the corresponding flow pattern tends to become steady with respect to the panel.

(5) The Stability Boundaries for Compressible Flow

We now proceed to extend the results of the preceding section to compressible flow ($M > 0$), first applying Cauchy's principle of the argument[12] to prove that $f(\zeta)$ has either two zeros on the real axis and no zeros in the half plane $Im\ (\zeta \mathrm{sgn} k) < 0$, or no zeros on the real axis and one zero in $Im(\zeta \mathrm{sgn} k) < 0$, corresponding to stable or unstable motion, respectively.

Assuming first that $k > 0$, we consider the contour C of Fig. 2(a), consisting of the line ABCDEFG just below the real axis and indented under D at $\zeta = 0$, C and E at $\zeta = \pm M^{-1}$, B and F at $\zeta = \pm 2^{1/2}M^{-1}$, and I at $\zeta = -1$ (the location of which, relative to E and F, depends on the value of M), and the semicircle GHA of radius tending to infinity.

The corresponding contours traversed by β, $\zeta^2\beta^{-1}$, and $(\zeta + 1)^2 - \zeta_0^2$ are shown in Figs. 2(b), 2(c), and 2(d), respectively. The β plane is cut from -1 to $+1$, the $\zeta^2\beta^{-1}$ plane from $\pm 2iM^{-2}$ to $\pm i\infty$ and 0 to $+\infty$,

† The result of Eq. (4.5) is not new, at least for the special case of a membrane ($D = 0$), its derivation having been set as a problem in the examination of Constructor Lieutenants at the Royal Naval College.[11] The degenerate case obtained when $D = T = m = 0$ was cited by Rayleigh[9] as illustrating the flapping of flags and sails; in this case *linear* (as opposed to exponential) instability is found for all wave lengths.

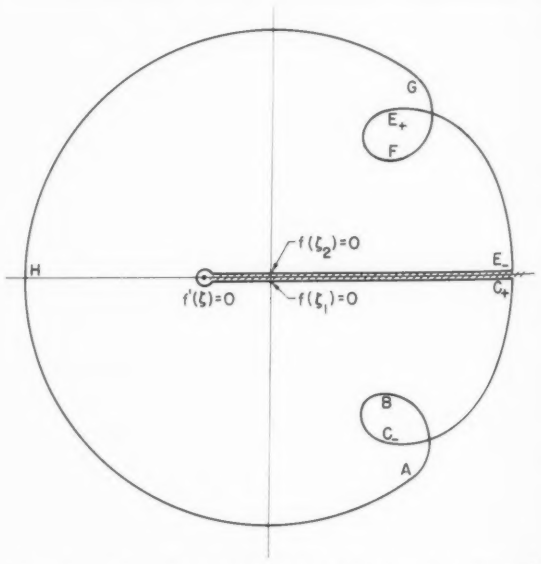

FIG. 3. The Nyquist diagram for $f(\zeta)$ when the motion is stable. The BC and EF loops are drawn on the assumption $M < 1$, and are inverted for $M > 1$.

* This result has a direct bearing on the extrapolation of the results to finite panels, since *standing* waves comprise *traveling* waves in both directions (cf. Section 6).

and the $(\zeta + 1)^2 - \zeta_0^2$ plane from $-\zeta_0^2$ to $+\infty$. The contour (or Nyquist diagram) for $f(\zeta)$, as given by Eq. (3.13), then follows by superposition and is plotted in Fig. 3 on the assumption that ζ_0^2 is sufficiently large to place its branch point (at which f' vanishes and the mapping of C is nonconformal) on the negative real axis.

It is evident from a consideration of the $\zeta^2\beta^{-1}$ and $(\zeta + 1)^2 - \zeta_0^2$ contours that there must exist a critical value $(\zeta_0^2)_c$ depending on μ and M, such that the f contour does not encircle the origin if $\zeta_0^2 > (\zeta_0^2)_c$ and encircles it once if $\zeta_0^2 < (\zeta_0^2)_c$. It then follows from the aforementioned principle of the argument that, since f has no poles within C, it must have respectively, 0 or 1 zeros therein. In the former case, f crosses the imaginary axis twice, say at ζ_1 and ζ_2, the imaginary parts of which tend to zero as the contour A—G approaches the real ζ axis. We also may deduce that:

(a) $|\zeta_{1,2}| < M^{-1}$ (since these points lie between C and E);

(b) if $\zeta_0^2 > 1$ ζ_1 and ζ_2 are of opposite sign [cf. Eq. (4.3)], since then D lies to the left of the origin in the f plane;

(c) $(\zeta_0^2)_c \leqq 1$ for all M [cf. Eq. (4.5)];

(d) if $M < 1$ and $\zeta_0^2 > \mu(1 - M^2)^{-(1/2)}$ $1 + \zeta_1$ and $1 + \zeta_2$ are of opposite sign, since then I lies to the left of the origin in the f plane;

(e) if $\zeta_0 < (1 - M^{-1})$, which can happen only if $M > 1$, the branch point in the f plane (at which f' vanishes) lies on the positive real axis, and the panel motion is unstable for all $\mu > 0$;

(f) the critical value ζ_c, at which ζ_1 and ζ_2 coalesce, lies in the interval $(0, -1)$ or $(0, -M^{-1})$ as M is less or greater than one, respectively, whence signals propagated upstream with respect to the panel cannot be unstable (cf. Section 4).

We next extend the foregoing conclusions to negative k by considering the contour C' in the upper half ζ plane that is obtained from C by reflection in the origin of all points except I (which remains at $\zeta = -1$) as shown in Fig. 4(a). The corresponding β contour, shown in Fig. 4(b), is found to be a reflection in the origin of the contour of Fig. 2(b), and it then follows that the contours traversed by $\zeta^2\beta^{-1}\mathrm{sgn}k$ and $(\zeta + 1)^2 - \zeta_0^2$ as ζ traverses C' are identical with those of Figs. 2(c) and 2(d) except for the relative location of I ($\zeta = -1$).

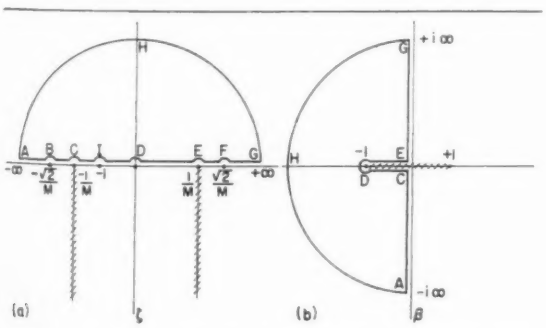

FIG. 4. The contour C' in the ζ plane for $k < 0$ and the corresponding β contour.

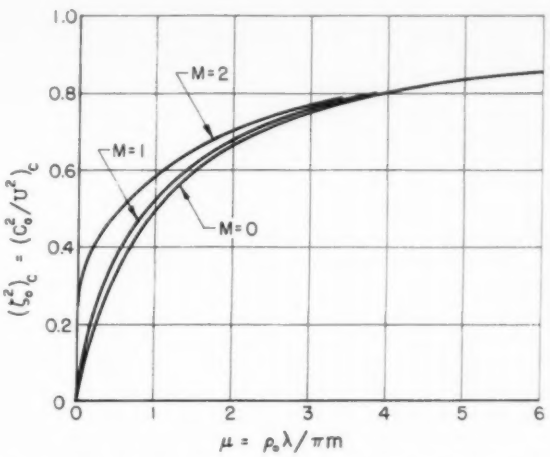

FIG. 5. Stability boundaries. Points above and below a particular boundary correspond to stable and unstable motions, respectively.

We now determine $(\zeta_0^2)_c$ as a function of μ and M by noting that ζ_c, the critical value of ζ at which the real roots ζ_1 and ζ_2 coalesce, must satisfy the simultaneous equations

$$f(\zeta_c) = f'(\zeta_c) = 0 \tag{5.1}$$

Solving Eq. (3.13) for $(\zeta_0^2)_c$ and its derivative for μ then yields the stability boundary in the parametric form

$$\mu = -2(1 + \zeta_c)\zeta_c^{-1}(2 - M^2\zeta_c^2)^{-1}(1 - M^2\zeta_c^2)^{3/2} \tag{5.2a}$$

$$(\zeta_0^2)_c = (1 + \zeta_c)[1 + M^2\zeta_c^3(2 - M^2\zeta_c^2)^{-1}] \tag{5.2b}$$

where the radical now is taken to be positive real for both positive and negative k. The numerical results for $(\zeta_0^2)_c$ vs. μ and ζ_c vs. μ, obtained from Eq. (5.2) by assigning ζ_c values in the intervals $(0, -1)$ or $(0, -M^{-1})$ [cf. conclusion (f) above], are plotted in Figs. 5 and 6 for $M = 0$, 1, and 2.

In the neighborhood of these boundaries we have (for fixed M)

$$0 = (\partial f/\partial\mu)_c(\mu - \mu_c) + (\partial f/\partial\zeta_0^2)_c[\zeta_0^2 - (\zeta_0^2)_c] + (1/2)(\partial^2 f/\partial\zeta^2)_c(\zeta - \zeta_c)^2 + \ldots \tag{5.3}$$

where the subscript c implies the evaluations of the partial derivatives at $\zeta = \zeta_c$, $\mu = \mu_c$, and $\zeta_0^2 = (\zeta_0^2)_c$. Carrying out the indicated operations yields

$$(\zeta - \zeta_c)^2 = -\zeta_c(1 - M^2\zeta_c^2)(2 - M^2\zeta_c^2) \times [2 + M^2\zeta_c^2 + 4M^2\zeta_c^3 - M^4\zeta_c^5]^{-1} \times \{[\zeta_0^2 - (\zeta_0^2)_c] - \zeta_c^2(1 - M^2\zeta_c^2)^{-(1/2)}(\mu - \mu_c)\} \tag{5.4}$$

The square root of the quantity in braces may have either sign if real (stable motion) but must be assigned the phase $-\pi/2$ if imaginary (unstable motion).

The behavior of the stability boundaries for very small and very large values of μ may be determined by approximate reversions of Eq. (5.2), which yield

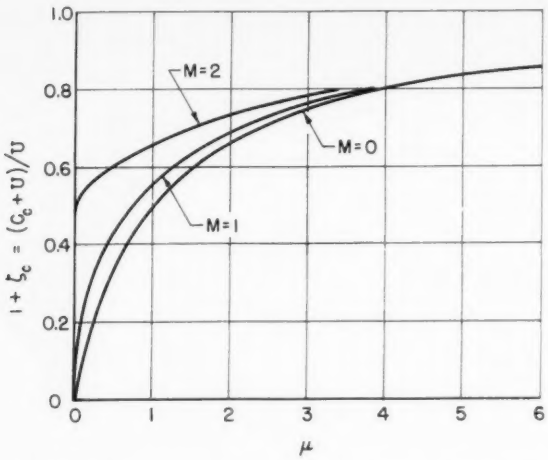

FIG. 6. The parameter $1 + \zeta_e$, representing the ratio of phase velocity relative to the panel to the air speed for points on the stability boundaries.

$$(\zeta_0^2)_e = (1 - M^2)^{-(1/2)}\mu + 0[(1 - M^2)^{-3}\mu^2], \quad M < 1 \tag{5.5a}$$

$$= (5/4)\mu^{4/5} + (M - 1)\mu^{2/5} + 0(\mu^{6/5}), \quad |M - 1| \ll \mu^{2/5} \tag{5.5b}$$

$$= (1 - M^{-1})^2 + 3\cdot 4^{-(1/3)}(M - 1)^{1/3}M^{-2}\mu^{2/3} + 0[(M - 1)^{-(4/3)}\mu^{4/3}], \quad M > 1 \tag{5.5c}$$

$$1 + \zeta_e = [1 - (1/2)M^2](1 - M^2)^{-(3/2)}\mu + 0[(1 - M^2)^{-(5/2)}\mu^2], \quad M < 1 \tag{5.6a}$$

$$= (1/2)\mu^{2/5} + (3/5)(M - 1) + 0(\mu^{4/5}), \quad |M - 1| \ll \mu^{2/5} \tag{5.6b}$$

$$= (1 - M^{-1}) + 2^{-(5/3)}(M - 1)^{-(2/3)} \times M^{-1}\mu^{2/3} + 0[(M - 1)^{-(5/3)}\mu^{4/3}], \quad M > 1 \tag{5.6c}$$

$$(\zeta_0^2)_e \sim 1 + \zeta_e \sim \mu(1 + \mu)^{-1} + 0[M^2\mu(1 + \mu)^{-4}] \tag{5.7}$$

These approximations emphasize the relatively strong sensitivity of the stability boundaries to changes in M for small μ and, on the other hand, the relative independence with respect to M for large μ. We remark that the approximation Eq. (5.5a) for $0 \leqq M < 1$ is related to the incompressible flow result by the Prandtl-Glauert transformation in virtue of the fact that the flow with respect to the panel tends to become steady in the neighborhood of the stability boundary for small μ (cf. the remark at the end of the Section 4).

The nature of the instability in the neighborhood of the stability boundary may be determined from Eq. (5.4). Assuming μ to be small and using Eq. (5.5) and (5.6), we find that the unstable motion in the subsonic regime is approximately of the purely divergent type,* whereas that in the supersonic regime is a divergent oscillation. The latter conclusion is important in comparing the results of this section with those for a finite panel (see Section 6, below).

* The frequency and damping factors, as represented by the real and imaginary parts of $1 + \zeta$, are $0(\mu)$ and $0[\zeta_0^2 - (1 - M^2)^{-(1/2)}\mu]^{1/2}$, respectively.

(6) Stability Criterion for a Periodically Supported Panel

The foregoing results are not directly applicable to supported panels, since, in general, the *two* traveling wave solutions available for a given value of k are not sufficient to construct a standing wave solution that satisfies the boundary condition of zero displacement at the supports.† We should expect, nevertheless, that the assumption

$$|k| = \pi/l \tag{6.1}$$

corresponding to a sinusoidal arch of length l, should furnish an approximation of the right order of magnitude for a panel having periodically spaced supports of separation l.‡ We also shall consider (in Section 7) the extrapolation of our results to a finite panel of length l, but this would appear to be rather less reliable (compared with the periodic support problem) in consequence of the anticipated differences in the aerodynamic forces.

Substituting Eq. (6.1) in Eq. (3.12) and removing the factor of 2, on the assumption that air flows only on the upper side of the panel, yields

$$\mu = (\rho_0 l/\pi m) = \pi^{-1}(\rho_0/\rho_m)(l/h) \tag{6.2}$$

where ρ_m is the mass density and h the thickness of the panel. The ratio $(\rho_0/\pi\rho_m)$ is about $1.5\cdot 10^{-4}$ for duralumin at sea level, while practical values of (l/h) are of the order 10^3, so that we may proceed on the assumption of small μ.

The stiffness D of a thin panel is given by

$$D = E'h^3/12 \tag{6.3}$$

where E' is the *effective* modulus of elasticity (Young's modulus divided by $1 - \sigma^2$, where σ is Poisson's ratio). The corresponding phase velocity of the free panel in the absence of a tension load (i.e., $T = 0$) then is given by Eq. (3.4) as

$$c_0^2 = (\pi^2 E'h^3/12ml^2) = (\pi^2 E'/12\rho_m)(h/l)^2 \tag{6.4}$$

We express the air speed U in terms of the Mach Number M according to

$$U^2 = M^2 a_0^2 = \gamma M^2 p_0/\rho_0 \tag{6.5}$$

where γ is the specific heat ratio ($\gamma = 1.4$ for air) and p_0 the ambient pressure. Dividing Eq. (6.4) by Eq. (6.5) to obtain ζ_0^2 and substituting the result, together with Eq. (6.2), in Eq. (5.5), yields the approximations

† The limiting case of steady flow presents an important exception; cf. the last remarks in Sections 4 and 5 and the paragraph following Eq. (6.9).

‡ The presence of an elastic foundation—or, for a curved structure, extensional stresses—probably would cause the minimum wave speed to occur at a wave length small compared with the panel length, whence the assumption of an infinite length might constitute an adequate approximation—at least for oscillatory instability. This problem is now under investigation.

$$(h/l) = (12\gamma p_0/\pi^3 E')^{1/3} M^{2/3}(1 - M^2)^{-(1/6)}, \quad \mu \ll (1 - M)^{3/2} \quad (6.6a)$$

$$= (15\gamma p_0/\pi^3 E')^{5/14}(\pi\rho_m/\rho_0)^{1/14} + (2/5)(15\gamma p_0/\pi^3 E')^{1/2}(\pi\rho_m/\rho_0)^{1/2}(M - 1), \quad |M - 1| \ll \mu^{2/5} \quad (6.6b)$$

$$= (12\gamma p_0/\pi^3 E')^{1/2}(\pi\rho_m/\rho_0)^{1/2}(M - 1), \quad \mu \ll (M - 1)^{5/2} \quad (6.6c)$$

Assuming duralumin ($E' = 10^7$ lb.in.$^{-2}$, $\rho_m g = 0.1$ lb.in.$^{-3}$) at sea level,* these reduce to

$$(h/l) = 0.0093M^{2/3}(1 - M^2)^{-(1/6)} \quad (6.7a)$$

$$= 0.0135[1 + 2.4(M - 1)] \quad (6.7b)$$

$$= 0.073(M - 1) + 0.001(M - 1)^{-(4/3)} \quad (6.7c)$$

These last results are plotted in Fig. 7, the curves of Eqs. (6.7a), (6.7b), and (6.7c) being faired into one another. We remark that the singularity in Eq. (6.7a) at $M = 1$ [which is a result of the approximation noted in Eq. (5.5a) and not a consequence of the linearization of the equations of motion] is so weak that the critical value of h/l predicted near $M = 1$ exceeds the value given by Eq. (6.7b) at $M = 1$ only for $M > 0.95$.

We note that the effect of a tension load T on the foregoing results may be introduced simply by replacing D by [cf. Eqs. (3.4) and (6.1)]

$$D_{EFF} = D + T(l/\pi)^2 \quad (6.8a)$$

$$= D[1 + (T/N_E)] \quad (6.8b)$$

where N_E is the Euler buckling load (per unit width) for a simply supported, two-dimensional panel—viz.,

$$N_E = (\pi/l)^2 D = (\pi^2 E' h/12)(h/l)^2 \quad (6.9)$$

In attempting to assess the reliability of the results of Eqs. (6.6) and (6.7) for supported panels, we emphasize that the result of Eq. (6.6a) involves no restrictions beyond those applicable to the unsupported panel. This conclusion follows directly from the last remarks of Sections 4 and 5, which establish the steady character of the subsonic flow pattern for points on the stability boundary in the limit $\mu = 0$. Moreover, it is confirmed by the agreement between Eq. (5.5a) and the corresponding result obtained by Hedgepeth et al. [reference 5, Eq. (16)] if a, the distance between supports in their analysis, is replaced by $2l$ in consequence of their use of deflection mode sin $(2\pi x/a)$.†

The validity of the approximations of Eqs. (6.6b) and (6.7b) for supported panels also follows from the foregoing arguments if $M = 1$. We emphasize, however, that the Mach Number range in which the approximation of Eq. (5.6b) furnishes acceptable accuracy tends to zero at the same rate as $1 + \zeta_e$, so that the validity of Eq. (6.6b) for supported panels when $M \neq 1$ remains open to question.

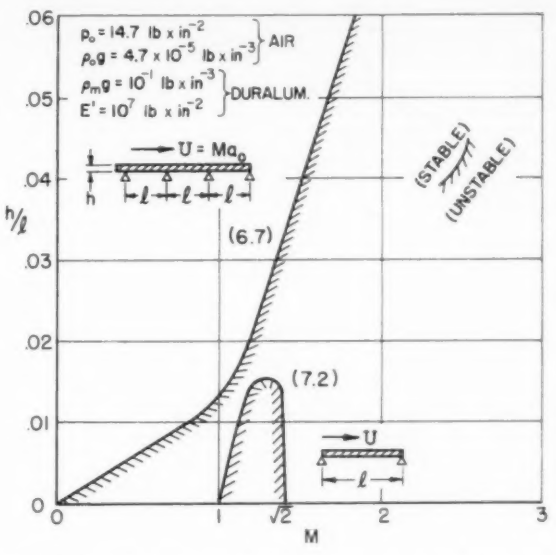

FIG. 7. Approximate stability boundary for two-dimensional panels.

In the supersonic regime the extrapolation of the results for *traveling waves on an infinite, unrestrained panel* to *standing waves on a periodically supported panel* is much more intuitive in character; nevertheless, we should expect any disagreement to be on the conservative side in virtue of the conclusion (deduction *f* from the Nyquist diagram of Section 5) that waves traveling upstream cannot be unstable. The results obtained by Hedgepeth et al. are, however, markedly different from that given by Eq. (6.6c) in $M > 1$; in particular, their stability boundaries are multivalued, so that stability is predicted only for one or more finite ranges of h/l (at least in the Mach Number range considered). A much more detailed investigation would be required to explain in a completely satisfactory manner the *qualitative* differences between the two sets of results, but these differences are so unexpected that we believe it worthwhile to set forth several points on which the analysis of reference 5 is at least questionable.

The most important criticism of the work of Hedgepeth et al. concerns their selection of deflection functions. This choice carries with it the following implicit assumptions: (a) that the panel deflection may be expressed with sufficient generality by the Fourier series $\sum_{-\infty}^{\infty} a_n \exp(in\pi x/l)$; (b) that this series converges rapidly; and (c) that the dominant terms (with respect to panel flutter) in this series are those for which $n = 0$ and ± 2, corresponding to the real deflection modes sin $(2\pi x/l)$ and $1 - \cos(2\pi x/l)$, both of which vanish at $x = 0$ and l.

Now, we may regard it as obvious that the complete set of natural—i.e., free vibration—modes of an infinite, periodically supported panel includes all of the

* We note that the panel thicknesses indicated by Eq. (6.6) decrease with increase in altitude, although the supersonic result, being dependent primarily on the sonic velocity (rather than p_0 and ρ_0 separately) is relatively insensitive to altitude.

† The "odd solution" of reference 5 would correspond to our result if $n = 1$ therein; see also the dashed curve of Fig. 8 therein. The authors' choice of deflection modes is discussed in more detail below.

modes of a single panel having the same length (l) between supports—viz., $\sin(n\pi x/l)$;* on the other hand, the functions $1 - \cos(2n\pi x/l)$, which satisfy the boundary conditions but not the differential equation, are not admissible as natural modes. It also should be evident that the periodicity of the boundary conditions places no constraint on the relative phases of the motion in successive panel bays. Indeed, we may verify that the most general solution to the differential equation

$$\frac{d^4y_n}{dx^4} - \left(\frac{\lambda}{l}\right)^4 y_n = 0; \qquad \lambda = l\left(\frac{m\omega^2}{D}\right)^{1/4}, \qquad nl < x < (n+1)l \quad (6.10)$$

that satisfies the boundary conditions

$$y_n = 0; \qquad x = nl \text{ or } (n+1)l \quad (6.11a)$$

$$y_n' = y_{n+1}'; \qquad x = (n+1)l \quad (6.11b)$$

$$y_n'' = y_{n+1}''; \qquad x = (n+1)l \quad (6.11c)$$

$$y_n \text{ finite}; \qquad x \to \pm\infty \quad (6.11d)$$

is given by†

$$y_n = \sin(m\pi\xi_n); \qquad m = 1, 2, 3, \ldots \quad (6.12)$$

if $\sin\lambda = 0 (\lambda = m\pi)$ or by

$$y_n = e^{i(n+1)\theta}[\sinh\lambda\sin(\lambda\xi_n) - \sin\lambda\sinh(\lambda\xi_n)] + e^{in\theta}[\sinh\lambda\sin\lambda(1-\xi_n) - \sin\lambda\sinh\lambda(1-\xi_n)] \quad (6.13)$$

$$\xi_n = (x/l) - n, \qquad 0 \leqq \xi_n \leqq 1 \quad (6.14)$$

if λ satisfies the equation

$$\cos\theta = \left[\frac{\sinh\lambda\cos\lambda - \cosh\lambda\sin\lambda}{\sinh\lambda - \sin\lambda}\right] \quad (6.15a)$$

$$= \sqrt{2}\cos\left(\lambda + \frac{\pi}{4}\right) + \left[\left(\frac{\cosh\lambda - \cos\lambda}{\sinh\lambda - \sin\lambda}\right) - 1\right]\sin\lambda \quad (6.15b)$$

The right-hand side of Eq. (6.15) is plotted in Fig. 8, assuming θ positive [it also may have the same negative values since Eq. (6.15) is even in θ]. It is found that the smallest value of λ that makes θ real is π; for $\lambda > \pi$ the second term in Eq. (6.15b) is never greater than about 0.02, and the permissible values of λ—i.e., those giving real θ—lie approximately in the intervals

$$m\pi \leqq \lambda \leqq [m + (1/2)]\pi; \quad m = 1, 2, 3 \ldots \quad (6.16)$$

It follows that the spectrum of eigenvalues for an infinite, periodically supported panel is neither discrete, as would be the case for a finite panel, nor continuous, as would the case for an infinite, unsupported panel; rather, it has a *filterlike* character, being made up of discrete bands with a lower cutoff—viz., $\lambda = \pi$.

The discussion of the preceding paragraph reveals

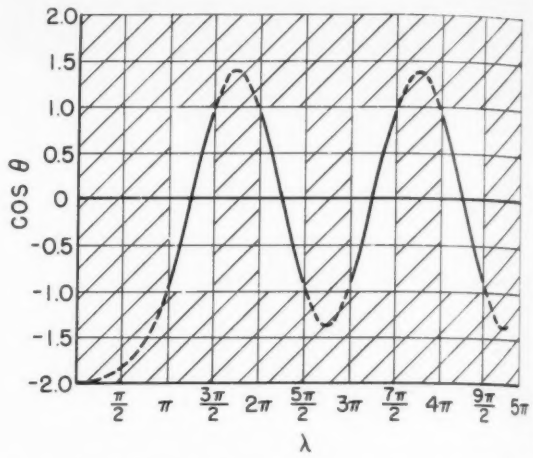

FIG. 8. $\cos\theta$ versus λ, as given by Eq. (6.15). θ is real only in the unshaded regions.

that the expansion functions assumed by Hedgepeth et al. (assumption *a* above) do not form a complete set for the periodically supported panel; more explicitly, their choice imposes an unjustifiable constraint on the spatial periodicity. On the other hand, it is not restricted to natural modes of the freely vibrating panel, in consequence of which there is no reason to expect rapid convergence of the cosine portion of the series in the analysis of the aerodynamically disturbed panel (cf. assumption *b* above). Finally, the dominant mode of the freely vibrating panel is $\sin(\pi x/l)$, and we should anticipate that the departure therefrom of the most important flutter mode in the presence of aerodynamic forces would be of order μ; nevertheless, Hedgepeth et al., in apparent disregard of the trail so clearly blazed by Lord Rayleigh, implicitly regard (assumption *c* above) the deflection functions $\sin(2\pi x/l)$ and $1 - \cos(2\pi x/l)$ as more important than $\sin(\pi x/l)$. We hasten to add that the stability of a flutter mode differing slightly from the dominant natural mode would not necessarily preclude the possibility of other unstable flutter modes (although, on intuitive grounds, their existence is improbable); but we certainly can have but slight confidence in the results of an analysis that both completely neglects the dominant mode and imposes an artificial and unjustified constraint on the admissible types of deflection.

Another criticism of the analysis of Hedgepeth et al. is that, even within the limitations imposed by their assumed deflection, they appear to overlook the possibility of a flutter mode for which (in their notation) $a_n = -a_{-n}$ and $\beta_n + \beta_{-n} = 0$. But this is precisely the type of condition we would expect on the basis of a Rayleigh-Galerkin type of analysis assuming small departures (of order μ) of the deflection mode from $\sin(\pi x/l)$.‡

We emphasize that none of the foregoing arguments prove even the qualitative validity of the approxima-

* n is assumed to be an integer throughout the subsequent discussion.

† Eq. (6.15a) is, of course, satisfied by $\lambda = m\pi$, but Eq. (6.13) then is indeterminate.

‡ Such an analysis is being carried out by one of the writer's students at the University of California, Los Angeles.

tions of Eqs. (6.6c) and (6.7c) for a periodically supported panel in a supersonic stream; nor, on the other hand, do they disprove the results of Hedgepeth et al. Nevertheless, in the face of the disagreement between the results and the questionable assumptions of the latter authors, we believe that there is a need for further study.

(7) Stability Criterion for a Finite Panel

We shall not attempt any direct comparison between the results of Section 5 and those of Shen[4] and the writer[3] for a finite panel in supersonic flow, but it is important to note that there exist serious discrepancies and to offer certain criticisms of the analyses in the latter papers. First, we remark that the instability predicted in Section 5 for sufficiently thin panels in supersonic flow is characterized by negative damping of a single degree of freedom. This type of instability also is predicted by reference 3 for Mach Numbers in the range $(1, \sqrt{2})$ on the assumption of sufficiently small values of the reduced frequency. The approximation of small reduced frequency was not made by Shen,[4] but his results also imply the possibility of negative damping in the range $(1, \sqrt{2})$ as well as the type of instability discussed in the following paragraph.

In addition to the panel instability associated with negative damping of a single degree of freedom, references 3 and 4 both predict a divergence associated with the aerodynamic coupling of the two (natural) modes by which the panel motion is approximated. The fact that such an instability is not predicted for the infinite panel, while by no means conclusive, leads us to suspect that it probably would not be experienced by finite panels and that its prediction by references 3 and 4 is a spurious result of pushing the Rayleigh-Galerkin type of approximation beyond its intrinsic limitations.* In this connection, we remark that such an approximation, being based on the representation of the panel motion in the presence of aerodynamic forces by the first few modes (only two in references 3 and 4) of free vibration, implicitly assumes the aerodynamic forces to be small compared with the structural and inertial forces; i.e., in the notation of Section 5, the parameter μ is assumed small compared with both $(1 + \zeta)^2$ and ζ_0^2; in the neighborhood of the (predicted) stability boundaries in question, however, this does not prove to be the case.

We believe that the statements of the preceding paragraph are sufficient to place the results of references 3 and 4 in considerable doubt insofar as they predict instability due to causes other than simple negative damping.† The latter type of instability, on the other hand, would appear to warrant further investigation. The low frequency approximation of reference 3 is clearly inadequate for this purpose, although it does serve to define approximately the Mach Number regime—viz., $(1, \sqrt{2})$, in which such instability is possible. If μ is sufficiently small, however, we may calculate the zero damping boundary on the basis of the dominant mode $\sin(\pi x/l)$. In Shen's notation, this amounts to requiring the imaginary part of Q_{11}' to vanish, which, using the first three terms in the frequency expansion of the aerodynamic forces,‡ yields [see Eq. (D.7), reference 4, noting that Shen's $\omega' = \pi\zeta_0$ in our notation if we take $k = \pi/l$]

$$\frac{\omega'^2}{\pi^2} = (\zeta_0^2)_c \Big]_{k=\pi/l} = 2M^{-2}(M^2 + 4)^{-1}(2 - M^2) \times (M^2 - 1)^2 \quad (7.1)$$

Comparing Eq. (7.1) with Eq. (5.5c), we find that the critical value of ζ_0^2 for negative damping of single degree of freedom oscillations of a finite panel of length l differs from that for a disturbance of wave length $2l$ on an infinite panel by the factor $2(M^2 + 4)^{-1}(2 - M^2)(M + 1)^2$. The corresponding critical panel thickness ratio for duralumin at sea level [cf. Eq. (6.7c)] is

$$h/l = 0.073\sqrt{2}(M^2 + 4)^{-(1/2)}(2 - M^2)^{1/2} \times (M^2 - 1) \quad (7.2)$$

which is plotted in Fig. 7.

It is, of course, possible to carry out a numerical solution for a finite panel paralleling that of Section 5—i.e., involving no approximations beyond those associated with linearization—indeed, one procedure for such a solution already has been outlined by Goland and Luke.[13]** It would be of considerable interest to compare the results of such a solution with those of Section 5.

We conclude by emphasizing that the foregoing results are not directly applicable to practical configurations, since three-dimensional effects must be expected to be of great importance. It is probable that the next step in the direction of a better understanding of the panel flutter problem should be the analysis of a cylindrical structure.

* This suspicion is supported by a brief (unpublished) investigation of a finite, two-dimensional membrane using the low frequency, aerodynamic approximation. A direct solution of the differential equation yields no instability other than that due directly to negative damping, whereas a two mode Galerkin solution yields a spurious instability similar to that predicted in reference 3. [*Addendum:* Professor Shen has recently informed the author that a direct solution of the differential equation for the panel (with bending stiffness) *confirms* the results of the Galerkin analysis, so that in this case there is no spurious instability.]

† *Addendum:* The analyses of reference 3 and 4 have been extended by Nelson and Cunningham,[15] and they confirm the types of instability previously predicted; see also preceding footnote.

‡ This approximation is justified a posteriori by the smallness of the right-hand side of Eq. (7.1) in the M interval $(1, \sqrt{2})$. It should be emphasized, however, that we have assumed the parameter μ to be small compared with this right-hand side. It appears that the latter condition usually would be satisfied for practical configurations at relatively high altitudes but perhaps not at sea level.

** Goland and Luke also present an asymptotic (in M) solution that predicts stability for sufficiently large M. This result evidently supports the present discussion. [*Addendum:* This result has since been questioned by Shen.[16]]

REFERENCES

[1] Isaacs, R. P., *Translability Flutter of Supersonic Aircraft Panels*, RAND Corp., Santa Monica, California, 1949.

[2] Hayes, W. D., *A Buckled Plate in a Supersonic Stream*, North Amer. Avia. Rep. AL-1029, Downey, California, 1950.

[3] Miles, J. W., *Dynamic Chordwise Stability at Supersonic Speeds*, North Amer. Avia. Rep. AL-1140, 1950.

[4] Shen, S. F., *Flutter of a Two Dimensional Simply Supported Uniform Panel in a Supersonic Stream*, M.I.T. O.N.R. Project, NR-064-259, 1952.

[5] Hedgepeth, J. M., Budiansky, B., and Leonard, R. W., *Analysis of Flutter in Compressible Flow of a Panel on Many Supports*, Journal of the Aeronautical Sciences, Vol. 21, No. 7, p. 475, July, 1954.

[6] Fung, Y. C., *The Static Stability of a Two-Dimensional Curved Panel in a Supersonic Flow, with an Application to Panel Flutter*, Journal of the Aeronautical Sciences, Vol. 21, No. 8, 556–565, August, 1954.

[7] Thomson, William, (Lord Kelvin) Philos. Mag. (4) **42**, 374, 1871; *Papers*, Vol. 4, p. 76; cited from Lamb, loc. cit. infra.

[8] Lamb, H., *Hydrodynamics*, p. 374; Dover Publications, New York, 1945.

[9] Strutt, John William, (Lord Rayleigh) *On the Instability of Jets*, Proc. Lond. Math. Soc., Vol. 10, No. 1, pp. 4–12, 1878; *Scientific Papers*, Vol. 1, p. 361; see also Lamb, loc. cit. supra, p. 374.

[10] Stoker, J. J., *Some Remarks on Radiation Conditions*, Proc. Fifth Symposium in Appl. Math. of the Amer. Math. Soc. 1952, reprinted by McGraw-Hill Book Company, Inc., New York, 1954, p. 97.

[11] Milne-Thomson, L. M., *Theoretical Hydrodynamics*, p. 392, ex. 18; The Macmillan Company, New York, 1950.

[12] Copson, E. T., *Theory of Functions of a Complex Variable*, p. 119; Oxford Univ. Press, 1935.

[13] Goland, M., and Luke, Y., *An Exact Solution for Two-Dimensional Linear Panel Flutter at Supersonic Speeds*, Journal of the Aeronautical Sciences, Vol. 21, No. 4, p. 275, 1954.

[14] Miles, J. W., *Vibrations of Beams on Many Supports*, Proc. A.S.C.E., Vol. 82, No. EM-1, January, 1956.

[15] Nelson, H. C., and Cunningham, H. J., *Theoretical Investigation of Flutter of Two-Dimensional Flat Panels with One Surface Exposed to Supersonic Potential Flow*, NACA TN 3465, July, 1955.

[16] Shen S. F., *Remarks on "An Exact Solution for Two-Dimensional Linear Panel Flutter at Supersonic Speeds*, Journal of the Aeronautical Sciences, Vol. 22, No. 9, p. 656, September, 1955.

Integrated Use of Analog and Digital Computing Machines

(*Continued from page 740*)

(4) As a result of the increased complexity of the dynamics problem, the results must be reasonably guaranteed to be free of errors.

In view of these characteristics a review of possible methods using high-speed computing machines—both digital and analog—was made, and an optimum approach was determined using both the analog and digital computing facilities in an integrated manner. The success of this approach not only depends upon the existence of the computers themselves but, like any other large operating facility, requires a highly trained, fully cooperative team of personnel. The cost of the machines and upkeep as well as the cost and training of adequate personnel is perhaps the largest drawback in this integrated approach.

The techniques described in the paper were illustrated by several dynamics problems involved in production airplanes. Due to the increased amount of information that can be obtained from the computers in the form of various transfer functions, more refined methods can be used to predict critical design factors. In view of the importance of minimum weight for optimum performance, the desirability of obtaining more rational design requirements may very well offset the disadvantage of the large costs involved in a complex computing facility.

REFERENCES

[1] Diederich, Franklin W., *Calculation of the Aerodynamic Loading of Swept and Unswept Flexible Wings*, NACA TR 1000, 1950.

[2] Dixon, W. J., *An Analysis of Errors in Electric Analogue Computers*, California Institute of Technology, Ph.D. Thesis, 1952.

[3] Wilts, C. H., *Finite Difference Errors in the Flutter Speed of a Uniform Wing with an Arbitrarily Placed Mass*, Calif. Inst. Tech. Analysis Lab. Report, June 30, 1954.

[4] McCann, G. D., MacNeal, R. H., *General Methods of Synthesis for Electrical-Mechanical Analogies of Aircraft Structures*, ARDC Technical Report No. 1.

[5] McCann, G. D., MacNeal, R. H., *Beam Vibration Analysis with the California Institute of Technology Analogue Computer*, ASME J. Appl. Mech., Vol. 17, 1950.

[6] MacNeal, R. H., McCann, G. D., Wilts, C. H., *The Solution of Aeroelastic Problems by Means of Electrical Analogies*, Journal of Aeronautical Sciences, Vol. 18, No. 1, January, 1951.

[7] Benscoter, S. U., MacNeal, R. H., *Introduction to Electrical-Circuit Analogies for Beam Analysis*, NACA TN 2785, 1952.

Dynamic Behavior During Accelerated Flight with Particular Application to Missile Launching

TELFORD W. OSWALD*

Aerophysics Development Corporation

(I) Introduction

In the design and development of guided missiles and high performance airplanes, it is often necessary to consider their dynamic behavior in accelerating flight. In the case of airplanes, such accelerations occur during the period immediately following take-off, during high-speed dives, and following the application of dive brakes. In the case of guided missiles the period of interest is the launch or boost phase of the trajectory.

There has been considerable work done to date on the launching of rockets, but in these studies it has been customary to neglect the aerodynamic lift and damping forces. For the usual rocket configuration consisting of a slender body with small stabilizing fins this approximation appears valid since these forces are primarily due to body lift and are small. But in the case of winged missiles which in configuration are more nearly like an airplane than a rocket, the validity of this assumption is questionable.

In the present paper it is found that damping and lift forces may be included in the analysis without complication. The problem is approached from the classical stability theory, assuming small oscillations. The equations of motion are therefore linear but since the speed is variable, the coefficients are not constant. An exact solution in terms of definite integrals of the Fresnel type is obtained. These integrals are functions of the relative damping only; they are independent of the frequency. Consequently, once the relative damping is determined, the effects of acceleration, frequency, launching angle, thrust misalignment, and wind can be readily evaluated. In the appendix the values of these integrals for various values of relative damping are presented.

(II) Coordinates, Notation, and Symbols

The equations of motion for a missile can be referred to a set of body axes that are fixed in the missile and move with it. An orthogonal set of principal body axes with origin in the missile center of gravity (the z-axis in the normally vertical plane) is selected. This coordinate system is shown in Fig. 1. The velocities, moments, angular velocities, displacements, and angular displacements are all defined in accordance with the right-hand rule.

Throughout the text, the usual convention of placing a dot over a quantity to denote differentiation with respect to time is used. Whenever a fractional power of a quantity is involved, the positive real branch of the multivalued function is taken. For the inverse trigonometric functions, the principal branch is taken. In the following list the principal quantities used in this paper are defined.

a	= acceleration, ft./sec.^{2}
c	= reference chord for moment coefficient, ft.
C_L	= $L/(1/2)\rho V^2 S$ = lift coefficient
C_M	= $M/(1/2)\rho V^2 Sc$ = pitching moment coefficient
$C_{L\alpha}$	= $\partial C_L/\partial\alpha$, evaluated at trim position
$C_{M\alpha}$	= $\partial C_M/\partial\alpha$, evaluated at trim position
$C_{M\dot\alpha}$	= $\partial C_M/\partial(\dot\alpha c/2V)$, evaluated at trim position
C_{M_q}	= $\partial C_M/\partial(qc/2V)$, evaluated at $q = 0$
g	= acceleration of gravity, ft./sec.^{2}
I_y	= $\int (x^2 + z^2)dm$ = moment of inertia about y-axis (pitch), lbs. sec.^{2} ft.
l_1	= distance from missile center of gravity to motor nozzle, ft.
L	= lift, lbs.
m	= mass, lb. sec.^{2}/ft.
M	= pitching moment, ft. lb.
$M(\epsilon)$	= $Tl_1 \sin\epsilon$ = pitching moment due to thrust misalignment, ft. lb.

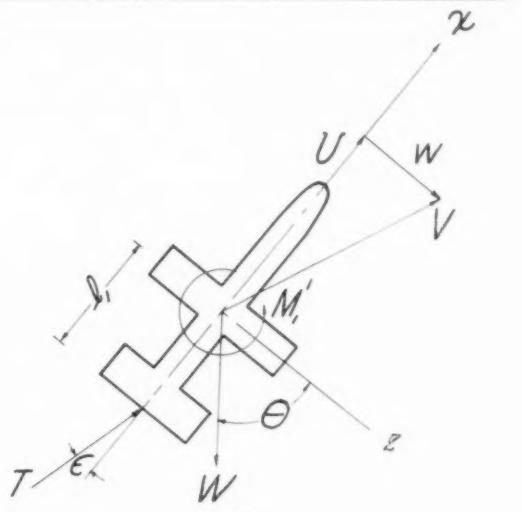

Fig. 1.

Received August 18, 1954. Revised and received May 11, 1955.

* Now, Senior Member of the Technical Staff, Hughes Aircraft Company, Culver City, Calif.

$M'(\epsilon)$ = $M(\epsilon)/I_y$ = angular acceleration in pitch due to thrust misalignment, rad./sec.^{2}
$M'(\delta)$ = $M(\delta)/I_y$ = angular acceleration in pitch due to control deflection, rad./sec.^{2}
q = $\dot{\theta} = \partial\theta/\partial t$ = perturbation in pitch rate (angular velocity about y-axis), rad./sec.
q' = $(1/2)\rho V^2$ = dynamic pressure, lb./ft.^{2}
S = reference area for aerodynamic coefficients, ft.^{2}
t = time, sec.
T = thrust, lb.
T' = (T/m) = axial acceleration due to thrust, ft./sec.^{2}
U = velocity component in x-direction, ft./sec.
V = missile velocity, ft./sec.
w = velocity perturbation in z-direction, ft./sec.
w_g = cross-wind velocity component, ft./sec.
x, y, z = coordinate axis, right handed principal body axes (roll, pitch, yaw axis, respectively)
Z = force in z-direction, lb.
$Z(\delta)$ = force in z-direction due to control deflection, lb.
$Z'(\delta)$ = $Z(\delta)/m$ = acceleration in z-direction due to $Z(\delta)$, ft./sec.^{2}
Z_1' = $Z'(\delta) + T' \sin \epsilon + g \cos \Theta$, ft./sec.^{2}
Z_w = $\partial Z/\partial w$ = resistance derivative, rate of change of force in z-direction due to velocity in z-direction, lb. sec./ft.
$Z_{\dot{w}}$; Z_q = resistance derivatives, lb. sec.^{2}/ft.; lb. sec.
M_w, $M_{\dot{w}}$; M_q = rotary derivatives, lb. sec.; lb. sec.^{2}; ft. lb. sec.
Z_w', Z_q' = Z_w/m, Z_q/m
M_w', $M_{\dot{w}}'$, M_q' = M_w/I_y, $M_{\dot{w}}/I_y$, M_q/I_y
Z_{w_0} = average value of Z_w'/U
M_{q_0} = average value of M_q'/U
M_{w_0} = average value of M_w'/U
$M_{\dot{w}_0}$ = average value of $M_{\dot{w}}'/U$
$M(\delta)_0$ = average value of $M'(\delta)/U^2$
$Z(\delta)_0$ = average value of $Z'(\delta)/U^2$
α = angle of attack, rad.
δ = control surface deflection, rad.
ϵ = angle between thrust axis and missile centerline, rad.
ζ = distance in z-direction, ft.
ζ_0 = η_0/ω_0 = fraction of critical damping
η = damping constant, 1/sec.
η_0 = reduced damping constant (1/ft.)
ϑ = w/U incremental angle of attack, rad.
θ = perturbation angular displacement in pitch, rad.
Θ = angular displacement in pitch measured from horizontal, rad.
Θ_1 = initial value of Θ, rad.
ξ = $\omega_0 x$ = dimensionless independent variable in equation of motion
ρ = mass density of air, lbs. sec.^{2}/ft.^{4}
ψ = phase angle, rad.
ω = circular frequency, rad./sec.
ω_n = natural undamped circular frequency, rad./sec.
ω_0 = ω/U = reduced circular frequency, rad./ft.

(III) Equations of Motion and Their General Solution

The equations of motion are referred to a set of principal body axes; hence all product of inertia terms vanish. The longitudinal motion is assumed to be a uniform acceleration. Furthermore, it is assumed that all other motion is confined to infinitesimals so that the classical theory and the concept of stability derivatives are applicable. The derivatives, being functions of the forward speed, mass, inertia, etc., are variable with time. It is assumed that the missile has a longitudinal plane of symmetry and that it is initially trimmed to fly at zero angle of attack. The forces and moments due to surface incidence and/or control surface deflections, as well as forces and moments arising from thrust misalignment, are treated as forcing functions. The six equations of motion separate into a longitudinal set and a lateral set of three equations each. Neglecting second-order terms and referring to Fig. 1, the longitudinal equations are written

$$m\dot{U} = T \cos \epsilon - mg \sin (\Theta_1 + \theta) \quad (1)$$

$$\dot{w} - Z_w'w - Uq = Z'(\delta) + T' \sin \epsilon + g \cos (\Theta_1 + \theta) \quad (2)$$

where $$\theta = \int_0^t q\, dt$$

$$\dot{q} = M_w'w - M_{\dot{w}}'\dot{w} - M_q'q = M'(\delta) + M'(\epsilon) \quad (3)$$

Where the prime indicates that the quantity has been divided by the appropriate mass or moment of inertia [$Z_w' = (Z_w/m)$, $M_w' = (M_w/I_y)$, etc.]. For small values of θ, Eq. (1) reduces to

$$U = at = V \quad (4)$$

where $$a = T' \cos \epsilon - g \sin \Theta_1 \quad (5)$$

In Eq. (2), if Θ_1 is also small, the quantity $\theta \sin \Theta_1$ in the expansion of $\cos (\Theta_1 + \theta)$ may be neglected and the order of the equation lowered. (This approximation has been found to be acceptable even for large values of Θ_1, provided the axial acceleration a is large compared to g.)

Writing $Z_1' = Z'(\delta) + T' \sin \epsilon + g \cos \Theta_1$

$$q = (\dot{w}/U) - Z_w'(w/U) - (Z_1'/U) \quad (6)$$

Now let $(w/U) = \vartheta$ and substitute in Eq. (6).

$$q = \dot{\vartheta} + [(a/U) - Z_{\dot{w}}']\vartheta - (Z_1'/U) \quad (7)$$

The stability derivatives are defined in terms of body axes and may be written

$$\left.\begin{aligned} Z_w' &= Z_{w_0}U \\ M_q' &= M_{q_0}U \\ M_w' &= M_{w_0}U \\ M_{\dot{w}}' &= M_{\dot{w}_0} \end{aligned}\right\} \quad (8)$$

The terms $Z'(\delta)$ and $M'(\delta)$ in the forcing function are due to the missile lift and moment at $\alpha = 0$ and are given by

$$\begin{aligned} Z'(\delta) &= Z(\delta)_0U^2 \\ M'(\delta) &= M(\delta)_0U^2 \end{aligned}$$

The quantities Z_{w_0}, M_{q_0}, M_{w_0}, $M_{\dot{w}_0}$, $Z(\delta)_0$, and $M(\delta)_0$ are assumed to be constants depending on the missile configuration. (This approximation is reasonably valid for most configurations.) It should be noted that this definition permits variation of mass, moment of inertia, center of gravity, as well as aerodynamic coefficients.

Substituting Eqs. (4) and (8) into Eq. (7) and differentiating

$$\dot{q} = \ddot{\vartheta} + [(a/U) - Z_{w_0}U]\dot{\vartheta} - [(a^2/U^2) + aZ_{w_0}]\vartheta + [a(Z_1')/U^2] - 2a\,Z(\delta)_0 \quad (9)$$

Substituting Eqs. (7), (8), and (9) into Eq. (3)

$$\ddot{\vartheta} + [-Z_{w_0}U - UM_{w_0} - M_{q_0}U + (a/U)]\dot{\vartheta} + [(-M_{w_0} + Z_{w_0}M_{q_0})U^2 - (M_{w_0} + M_{q_0} + Z_{w_0})a - (a^2/U^2)]\vartheta = F(U) \quad (10)$$

where
$$F(U) = M'(\epsilon) + M(\delta)_0U^2 - Z_1'[M_{q_0} + (a/U^2)] + 2aZ(\delta)_0 \quad (11)$$

Defining the damping and frequency parameters, respectively,

$$\eta_0 = (-1/2)(Z_{w_0} + M_{q_0} + M_{\dot{w}_0}) = \eta/U \quad (12)$$

$$\omega_{n_0}^2 = -M_{w_0} + Z_{w_0}M_{q_0} = \omega_n^2/U^2 \quad (13)$$

$$\omega_0^2 = \omega_{n_0}^2 - \eta_0^2 = \omega^2/U^2 \quad (14)$$

$$\zeta_0 = \eta_0/\omega_0 = \eta\ \omega \quad (15)$$

Eq. (11) can be written

$$\ddot{\vartheta} + [2\eta_0U + (a/U)]\dot{\vartheta} + [\omega_{n_0}^2U^2 + 2\eta_0a - (a^2/U^2)]\vartheta = F(U) \quad (16)$$

It is convenient to change the independent variable to x which is essentially the distance along the trajectory. With this change of variable and upon division by $2ax$, Eq. (16) becomes

$$\vartheta'' + \left(\frac{1}{x} + 2\eta_0\right)\vartheta' + \left(\omega_{n_0}^2 + \frac{\eta_0}{x} - \frac{1}{4x^2}\right)\vartheta = \frac{F(U)}{2ax} \quad (17)$$

With the transformations, $\vartheta = y \exp(-\eta_0 x)$, and $\xi = \omega_0 x$, Eq. (17) becomes

$$\frac{d^2y}{d\xi^2} + \frac{1}{\xi}\frac{dy}{d\xi} + \left(1 - \frac{1}{4\xi^2}\right)y = f(\xi) \quad (18)$$

where
$$\left.\begin{aligned} f(\xi) &= (1/\omega_0)\{F[U(\xi)]/2a\xi\}\exp(\zeta_0\xi) \\ U(\xi) &= \sqrt{2(a/\omega_0)\xi} \end{aligned}\right\} \quad (19)$$

The homogeneous equation obtained from Eq. (18) is Bessel's equation of order $1/2$ and has the two general solutions $J_{1/2}(\xi)$ and $J_{-1/2}(\xi)$. Moreover, these may be expressed

$$y_1 = J_{1/2}(\xi) = \sqrt{2/\pi\xi}\sin\xi \quad (20)$$

$$y_2 = J_{-1/2}(\xi) = \sqrt{2/\pi\xi}\cos\xi \quad (21)$$

The particular integral for the nonhomogeneous equation may be obtained by the method of variation of parameters and is given by

$$I(\xi) = V_1y_1 + V_2y_2 \quad (22)$$

where
$$\left.\begin{aligned} V_1 &= -\int [y_2(\xi)/\Delta(y_1y_2)]\,f(\xi)\,d\xi \\ V_2 &= \int [y_1(\xi)/\Delta(y_1y_2)]\,f(\xi)\,d\xi \end{aligned}\right\} \quad (23)$$

and $\Delta(y_1, y_2)$ is the Wronskian. The complete solution to Eq. (18) is then

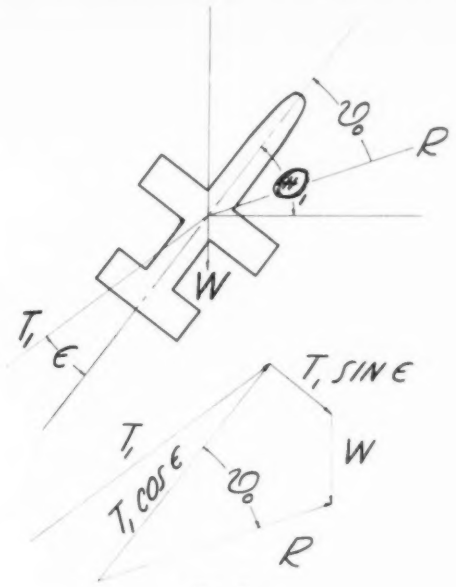

FIG. 2.

$$y = C_1J_{1/2}(\xi) + C_2J_{-1/2}(\xi) + I(\xi) \quad (24)$$

C_1 and C_2 are constants to be determined from the initial conditions. The integrals for V_1 and V_2 are the indefinite integrals with the value of the arbitrary constant taken equal to zero.

The forcing function as given by Eq. (19) may be written in a more convenient form before attempting to evaluate the integrals. Combining Eqs. (11) and (19),

$$f(\xi) = \frac{\exp(\zeta_0\xi)}{2\omega_0a\xi}(\beta\,\xi^{-1} + \Lambda + \Omega\xi) \quad (25)$$

where

$$\left.\begin{aligned} \beta &= -(g\cos\Theta_1 + T_1'\sin\epsilon)\frac{\omega_0}{2} = -\frac{a\omega_0\vartheta_0}{2} \\ \Lambda &= M'(\epsilon) - M_{q_0}(g\cos\Theta_1 + T_1'\sin\epsilon) + aZ(\delta)_0 \\ \Omega &= (2a/\omega_0)\,[-Z(\delta)_0M_{q_0} + M(\delta)_0] \end{aligned}\right\} \quad (26)$$

(IV) Solution for Launching from Rest

It now remains to determine the constants from the initial conditions—i.e., the initial angle of attack, ϑ_0, and the initial angular velocity, q_0. Consider first the case of launching from rest from a zero length launcher with no wind. (The effect of wind will be considered separately.) Referring to Fig. 2, the initial velocity must be in the direction of the initial acceleration which corresponds to the direction of the resultant of all forces acting at time $t = 0$. From the figure it is seen that the initial angle of attack is

$$\left.\begin{aligned} y(0) = \vartheta_0 &= \tan^{-1}\left(\frac{T\sin\epsilon + W\cos\Theta_1}{T\cos\epsilon - W\sin\Theta_1}\right) \\ &= \frac{T'\sin\epsilon + g\cos\Theta_1}{a} \end{aligned}\right\} \quad (27)$$

To determine the second initial condition, $y'(0)$, refer to Eq. (7) and note that $\vartheta = y(\xi) \exp(-\zeta_0\xi)$

$$\dot{\vartheta} = \sqrt{\frac{2a\xi}{\omega_0}} Z_{w_0} y \exp(-\zeta_0\xi) + q - \left(ay \Big/ \sqrt{\frac{2a\xi}{\omega_0}}\right) \exp(-\zeta_0\xi) + Z(\delta)_0 \sqrt{\frac{2a\xi}{\omega_0}} + \left(a\vartheta_0 \Big/ \sqrt{\frac{2a\xi}{\omega_0}}\right) \tag{28}$$

For small values of t; combining Eqs. (2) and (3), integrating, and including the initial angular velocity, q_0,

$$q = [M'(\epsilon) + M_w'a\vartheta_0]t + 0(t^2) + q_0 \tag{29}$$

Hence for small values of ξ

$$\dot{\vartheta} = \sqrt{\frac{2a\xi}{\omega_0}} Z_{w_0} y \exp(-\zeta_0\xi) + [M'(\epsilon) + M_w'a\,\vartheta_0]\sqrt{\frac{2\xi}{\omega_0 a}} - \left(ay \Big/ \sqrt{\frac{2a\xi}{\omega_0}}\right) \exp(-\zeta_0\xi) + Z(\delta)_0 \sqrt{\frac{2a\xi}{\omega_0}} + \left(a\vartheta_0 \Big/ \sqrt{\frac{2a\xi}{\omega_0}}\right) + q_0 \tag{30}$$

Expanding $\exp(\zeta_0\xi)$ and solving for y'

$$\left.\begin{aligned} y'(0) &= \lim_{\xi \to 0}\left[\left(\frac{Z_{w_0}'}{\omega_0} + \zeta_0\right)y + \frac{\vartheta_0 - y}{2\xi} + \frac{M'(\epsilon)}{\omega_0 a} + \frac{M_w'}{\omega_0}\vartheta_0 + \frac{Z(\delta)_0}{\omega_0} + \frac{\vartheta_0\zeta_0}{2} + 0(\xi^2) + \frac{q_0}{\sqrt{2a\omega_0\xi}}\right] \\ &= \frac{2}{3}\left[\left(\frac{Z_{w_0}'}{\omega_0} + \frac{3}{2}\frac{\eta_0}{\omega_0}\right)\vartheta_0 + \frac{M'(\epsilon)}{\omega_0 a} + \frac{M_w'}{\omega_0}\vartheta_0 + \frac{Z(\delta)_0}{\omega_0}\right] + \lim_{\xi \to 0}\left[\frac{q_0}{\sqrt{2a\omega_0\xi}}\right] \end{aligned}\right\} \tag{31}$$

With the initial conditions specified, the complete solution may be determined. For this purpose it is necessary to evaluate the particular integral at $\xi = 0$. Expanding $\exp(\zeta_0\xi)$, $\cos\xi$, and $\sin\xi$, and making use of Eqs. (25) and (26),

$$I(\xi) = \frac{1}{2\omega_0 a}\left[-4\beta + \frac{4}{3}(\Lambda + \zeta_0\beta)\,\xi + 0(\xi^2)\right] \tag{32}$$

$$I(0) = -(2\beta/\omega_0 a) = \vartheta_0 \tag{33}$$

$$I'(0) = \frac{2}{3\omega_0 a}(\Lambda + \zeta_0\beta) = \frac{2}{3}\left[\frac{M'(\epsilon)}{\omega_0 a} - M_{q_0}\frac{\vartheta_0}{\omega_0} + \frac{Z(\delta)_0}{\omega_0} - \zeta_0\frac{\vartheta_0}{2}\right] \tag{34}$$

Comparing $I'(0)$ from Eq. (34) with $y'(0)$ from Eq. (31) [making use of Eq. (12)], it is seen that $y'(0) = I'(0) + \lim_{\xi \to 0}(q_0/\sqrt{2a\omega_0\xi})$. Referring to Eq. (24), since $J_{-1/2}(0) \to \infty$ and $y(0)$ is finite, $C_2 = 0$. Also $J_{1/2}'(0) = \lim_{\xi \to 0}\sqrt{1/2\pi\xi}$, hence $C_1 = \sqrt{\pi/a\omega_0}\,q_0$. The complete solution is then given by

$$\left.\begin{aligned} \vartheta(\xi) &= y(\xi)\exp(-\zeta_0\xi) \\ &= \frac{\exp(-\zeta_0\xi)}{\xi^{1/2}}\left[\sin\xi\int f(\xi)\,\xi^{1/2}\cos\xi\,d\xi - \cos\xi\int f(\xi)\,\xi^{1/2}\sin\xi\,d\xi + \sqrt{\frac{2}{a\omega_0}}\,q_0\sin\xi\right] \end{aligned}\right\} \tag{35}$$

In this form, the solution may include any arbitrary forcing function $f(\xi)$ provided only that $f(\xi)$ be integrable. In the particular case where the functions β, Λ, and Ω which comprise $f(\xi)$ are constants, the form of the solution may be simplified.

In computing $I(\xi)$ it is noted that the indefinite integrals are not expressible in closed form. Hence the evaluation of them is most expediently obtained by graphical or numerical means. Since the quantities β, Γ, and Ω are parameters, it is convenient to express the integrals in the form

$$\vartheta(\xi) = \frac{\exp(-\zeta_0\xi)}{2\omega_0 a}\left\{\beta\left[\frac{\sin\xi}{\xi^{1/2}}\int \exp(\zeta_0\xi)\xi^{-3/2}\cos\xi\,d\xi - \frac{\cos\xi}{\xi^{1/2}}\int \exp(\zeta_0\xi)\xi^{-3/2}\sin\xi\,d\xi\right] + \Omega\left[\frac{\sin\xi}{\xi^{1/2}}\int \exp(\zeta_0\xi)\xi^{1/2}\cos\xi\,d\xi - \frac{\cos\xi}{\xi^{1/2}}\int \exp(\zeta_0\xi)\,\xi^{1/2}\sin\xi\,d\xi\right] + \Lambda\left[\frac{\sin\xi}{\xi^{1/2}}\int \exp(\zeta_0\xi)\xi^{-1/2}\cos\xi\,d\xi - \frac{\cos\xi}{\xi^{1/2}}\int \exp(\zeta_0\xi)\,\xi^{-1/2}\sin\xi\,d\xi\right]\right\} \tag{36}$$

All of the above integrals are the indefinite integrals with the constants of integration taken equal to zero. However, in order to evaluate them graphically or numerically, the definite integral must be taken. Before doing this, it is convenient to integrate by parts the first two integrals, and Eq. (36) becomes

$$\vartheta(\xi) = \frac{1}{2\omega_0 a}\left\{2\beta\left[\frac{\sin\xi\exp(-\zeta_0\xi)}{\xi^{1/2}}\int_0^\xi \exp(\zeta_0\xi)\xi^{-1/2}(\zeta_0\cos\xi-\sin\xi)\,d\xi - \frac{\cos\xi\exp(-\zeta_0\xi)}{\xi^{1/2}}\int_0^\xi \exp(\zeta_0\xi)\,\xi^{-1/2}(\zeta_0\sin\xi+\cos\xi)\,d\xi\right] + \Lambda\left[\frac{\sin\xi\exp(-\zeta_0\xi)}{\xi^{1/2}}\int_0^\xi \exp(\zeta_0\xi)\xi^{-1/2}\cos\xi\,d\xi - \frac{\cos\xi\exp(-\zeta_0\xi)}{\xi^{1/2}}\int_0^\xi \exp(\zeta_0\xi)\,\xi^{-1/2}\sin\xi\,d\xi\right] + \Omega\left[\frac{\sin\xi\exp(-\zeta_0\xi)}{\xi^{1/2}}\int_0^\xi \exp(\zeta_0\xi)\,\xi^{1/2}\cos\xi\,d\xi - \frac{\cos\xi\exp(-\zeta_0\xi)}{\xi^{1/2}}\int_0^\xi \exp(\zeta_0\xi)\,\xi^{1/2}\sin\xi\,d\xi\right]\right\} \quad (37)$$

The above expressions involving four different integrals can be reduced to a form involving only two integrals by noting

$$\int_0^\xi \exp(\zeta_0\xi)\,\xi^{-1/2}\cos\xi\,d\xi = 2\xi^{1/2}\exp(\zeta_0\xi)\cos\xi - 2\int_0^\xi \exp(\zeta_0\xi)\,\xi^{1/2}(\zeta_0\cos\xi-\sin\xi)\,d\xi$$

$$\int_0^\xi \exp(\zeta_0\xi)\,\xi^{-1/2}\sin\xi\,d\xi = 2\xi^{1/2}\exp(\zeta_0\xi)\sin\xi - 2\int_0^\xi \exp(\zeta_0\xi)\,\xi^{1/2}(\zeta_0\sin\xi+\cos\xi)\,d\xi$$

Now define

$$S(\xi) = \xi^{-1/2}\exp(-\zeta_0\xi)\int_0^\xi \exp(\zeta_0\xi)\,\xi^{1/2}\sin\xi\,d\xi \quad (38)$$

$$C(\xi) = \xi^{-1/2}\exp(-\zeta_0\xi)\int_0^\xi \exp(\zeta_0\xi)\,\xi^{1/2}\cos\xi\,d\xi \quad (39)$$

Collecting terms and making use of the trigonometric identities for the sum of two angles, Eq. (37) becomes

$$\vartheta(\xi) = (\beta/\omega_0 a)\{-2 + 2(1+\zeta_0^2)[\sin(\xi+2\psi)\,C(\xi) - \cos(\xi+2\psi)\,S(\xi)]\} + (\Lambda/\omega_0 a)\{\sqrt{1+\zeta_0^2}\,[\cos(\xi+\psi)\,C(\xi) + \sin(\xi+\psi)\,S(\xi)]\} + (\Omega/2\omega_0 a)[\sin\xi\,C(\xi) - \cos\xi\,S(\xi)] \quad (40)$$

where

$$\psi = \tan^{-1}(\zeta_0) \quad (41)$$

With ϑ determined the complete solution is known. From Eqs. (7) and (8)

$$q = \dot{\vartheta} + (\vartheta/t) - Z_{w_0} \quad at\ \vartheta - Z(\delta)_0 \quad at\ -(\vartheta_0/t)$$

and integrating

$$\left.\begin{aligned}\theta &= \int_0^t q\,dt \\ &= \vartheta - \vartheta_0 + \int_0^\xi\left[\frac{\vartheta(x)-\vartheta_0}{2x} - \frac{Z_{w_0}\vartheta(x)}{\omega_0}\right]dx - Z(\delta)_0\frac{\xi}{\omega_0}\end{aligned}\right\} \quad (42)$$

The lateral distance measured in the z body axis direction is

$$\left.\begin{aligned}\zeta &= \int_0^t U\sin(\theta-\vartheta)\,dt \doteq -\int_0^\xi(\theta-\vartheta)\frac{dx}{\omega_0} \\ &= \frac{\vartheta_0\xi}{\omega_0} + \frac{Z(\delta)_0\xi^2}{2\omega_0^2} - \int_0^\xi\frac{1}{\omega_0}\int_0^\lambda\left[\frac{\vartheta(x)-\vartheta_0}{2x} - \frac{Z_{w_0}\vartheta(x)}{\omega_0}\right]dx\,d\lambda\end{aligned}\right\} \quad (43)$$

Eqs. (40), (42), and (43) completely describe the motion. Furthermore, it is noted that the integrals involved are functions of the relative damping, ζ_0, only. Consequently, they form a one parameter family of functions valid for any configuration once the relative damping is known. This being the case, it is convenient to separate the effects of initial angle of attack, aerodynamic forces, and thrust misalignment For this purpose it is convenient to define the following functions.

$$\left.\begin{aligned}f_1(\xi) &= 2(1+\zeta_0^2)[\sin(\xi+2\psi)C(\xi) - \cos(\xi+2\psi)S(\xi)] \\ f_2(\xi) &= \sqrt{1+\zeta_0^2}[\cos(\xi+\psi)\,C(\xi) + \sin(\xi+\psi)\,S(\xi)] \\ f_3(\xi) &= \sin\xi\,C(\xi) - \cos\xi\,S(\xi)\end{aligned}\right\} \quad (44)$$

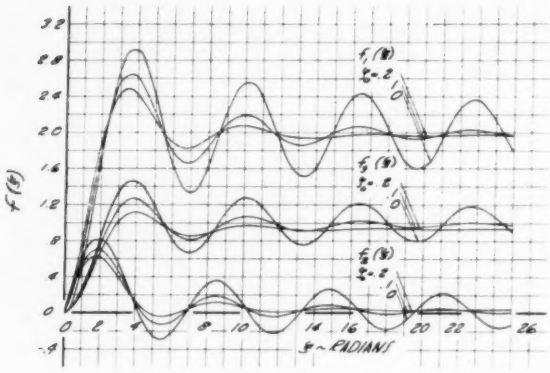

FIG. 3.

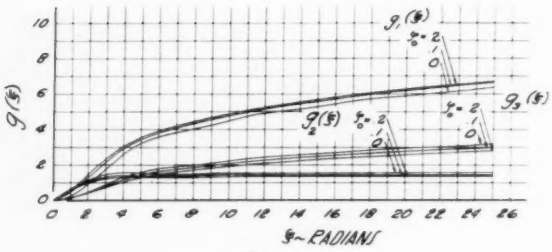

FIG. 4.

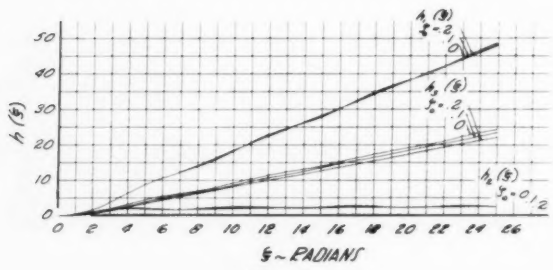

FIG. 5.

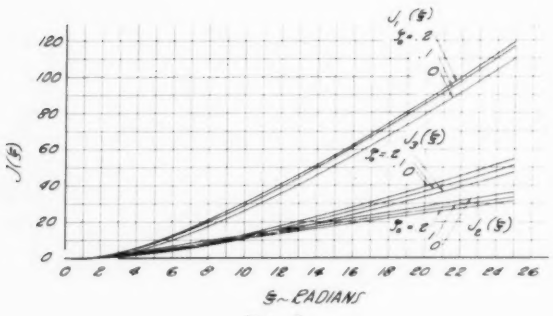

FIG. 6.

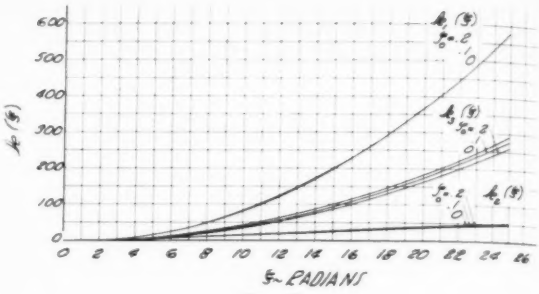

FIG. 7.

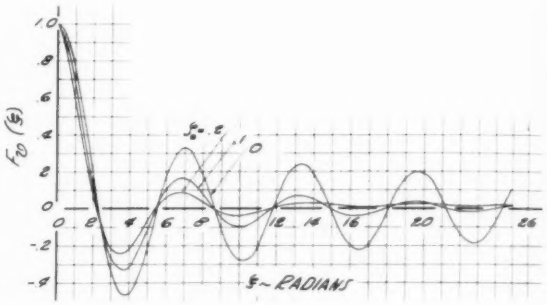

FIG. 8.

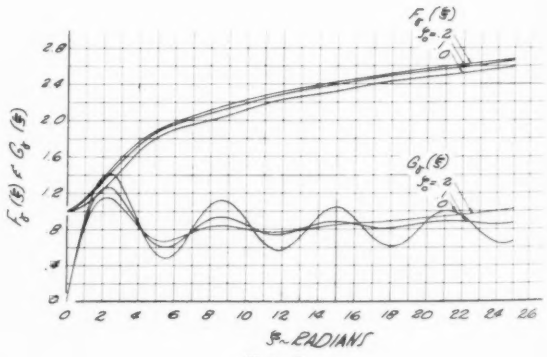

FIG. 9.

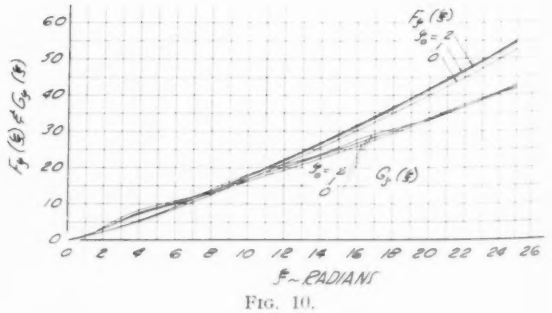

FIG. 10.

$$g_1(\xi) = \int_0^\xi \frac{f_1(\xi)}{\xi}\,d\xi \qquad g_2(\xi) = \int_0^\xi \frac{f_2(\xi)}{\xi}\,d\xi \qquad g_3(\xi) = \int_0^\xi \frac{f_3(\xi)}{\xi}\,d\xi$$

$$h_1(\xi) = \int_0^\xi f_1(\xi)\,d\xi \qquad h_2(\xi) = \int_0^\xi f_2(\xi)\,d\xi \qquad h_3(\xi) = \int_0^\xi f_3(\xi)\,d\xi$$

$$j_1(\xi) = \int_0^\xi g_1(\xi)\,d\xi \qquad j_2(\xi) = \int_0^\xi g_2(\xi)\,d\xi \qquad j_3(\xi) = \int_0^\xi g_3(\xi)\,d\xi$$

$$k_1(\xi) = \int_0^\xi h_1(\xi)\,d\xi \qquad k_2(\xi) = \int_0^\xi h_2(\xi)\,d\xi \qquad k_3(\xi) = \int_0^\xi h_3(\xi)\,d\xi$$

$$F\vartheta(\xi) = 1 - (1/2)f_1(\xi) \qquad F_\gamma(\xi) = 1 + (1/4)g_1(\xi) \qquad G_\gamma(\xi) = \xi - (1/2)h_1(\xi)$$

$$F_\xi(\xi) = \xi + (1/4)j_1(\xi) \qquad G_\xi(\xi) = \xi^2 - k_1(\xi) \qquad F_\Theta(\xi) = (1/2)f_1(\xi) + (1/4)g_1(\xi)$$

$$G_\Theta(\xi) = f_2(\xi) + (1/2)g_2(\xi) \qquad K_\Theta(\xi) = f_3(\xi) + (1/2)g_3(\xi)$$

These functions are plotted in Fig. 3–11 for $\zeta_0 = 0$, 0.10, and 0.20. Employing this notation, the solution is expressed in the following form.

Distance along flight path

$$x = \xi/\omega_0 \tag{45}$$

Velocity

$$V = U = \sqrt{2a\xi/\omega_0} \tag{46}$$

Angle of Attack

$$\vartheta = \vartheta_0 F_\alpha(\xi) + \frac{M'(\epsilon)}{a\omega_0} f_2(\xi) + \left[M(\delta)_0 - \frac{M_{q_0} Z(\delta)_0}{\omega_0^2}\right] f_3(\xi) + \frac{Z(\delta)_0}{\omega_0} f_2(\xi) \tag{47}$$

where $F_\alpha(\xi) = F_\vartheta(\xi) - (M_{q_0}/\omega_0) f_2(\xi)$

Flight path tangent measured from horizontal

$$\gamma = \Theta_1 - \vartheta_0 \Gamma_\alpha(\xi) + \frac{M'(\epsilon)}{a\omega_0} \Gamma_M(\xi) + \left[\frac{M(\delta)_0 - M_{q_0} Z(\delta)_0}{\omega_0^2}\right] \Gamma_0(\xi) - \frac{Z(\delta)_0}{\omega_0} \Gamma_M(\xi) + \frac{Z(\delta)_0}{\omega_0} \xi \tag{48}$$

where

$$\Gamma_\alpha(\xi) = F_\gamma(\xi) + \frac{Z_{w_0}}{\omega_0} G_\gamma(\xi) + \frac{M_{q_0}}{2\omega_0} g_2(\xi) - \frac{M_{q_0} Z_{w_0}}{\omega_0^2} h_2(\xi)$$

$$\Gamma_M(\xi) = \frac{1}{2} g_2(\xi) - \frac{Z_{w_0}}{\omega_0} h_2(\xi)$$

$$\Gamma_0(\xi) = \frac{1}{2} g_3(\xi) - \frac{Z_{w_0}}{\omega_0} h_3(\xi)$$

Distance normal to flight path (positive down)

$$\zeta = \frac{\vartheta_0}{\omega_0} H_\alpha(\xi) - \frac{M'(\epsilon)}{a\omega_0^2} H_M(\xi) - \frac{M(\delta)_0 - M_{q_0} Z(\delta)_0}{\omega_0^2} H_0(\xi) + \frac{Z(\delta)_0}{\omega_0^2}\left(\frac{\xi^2}{2} - H_M\right) \tag{49}$$

where

$$H_\alpha(\xi) = F_\xi(\xi) + \frac{Z_{w_0}}{2\omega_0} G_\xi(\xi) + \frac{M_{q_0}}{\omega_0} H_M(\xi)$$

$$H_M(\xi) = \frac{1}{2} j_2(\xi) - \frac{Z_{w_0}}{\omega_0} k_2(\xi)$$

$$H_0(\xi) = \frac{1}{2} j_3(\xi) - \frac{Z_{w_0}}{\omega_0} k_3(\xi)$$

Angle of missile centerline from horizontal

$$\Theta = \Theta_1 + \vartheta_0 \Theta_\alpha(\xi) + \frac{M'(\epsilon)}{\omega_0 a} \Theta_M(\xi) + \left[\frac{M(\delta)_0 - M_{q_0} Z(\delta)_0}{\omega_0^2}\right] \Theta_0(\xi) - \frac{Z(\delta)_0}{\omega_0} [\xi - \Theta_M(\xi)] \tag{50}$$

where

$$\Theta_\alpha(\xi) = F_\Theta(\xi) - (Z_{w_0}/\omega_0) G_\gamma(\xi) - (M_{q_0}/\omega_0) \Theta_M(\xi)$$

$$\Theta_M(\xi) = G_\Theta(\xi) - (Z_{w_0}/\omega_0) h_2(\xi)$$

$$\Theta_0(\xi) = K_\Theta(\xi) - (Z_{w_0}/\omega_0) h_3(\xi)$$

In Eqs. (47)–(50), it is noted that the quantities F_α, Γ_α, Γ_M, Γ_0, H_α, H_M, H_0, Θ_α, Θ_M, and Θ_0 are functions of the variable ξ and contain the two parameters M_{q_0} ω_0 and Z_{w_0}/ω_0 which depend on the configuration. The effects of launching angle and thrust misalignment are contained in the quantities, a, ϑ_0, and $M'(\epsilon)$. The effects of control surface deflection (or other aerodynamic moments and forces) are contained in $Z(\delta)_0$ and $M(\delta)_0$.

The trajectory may be computed in terms of horizontal and vertical distances (see Fig. 3) from the equations,

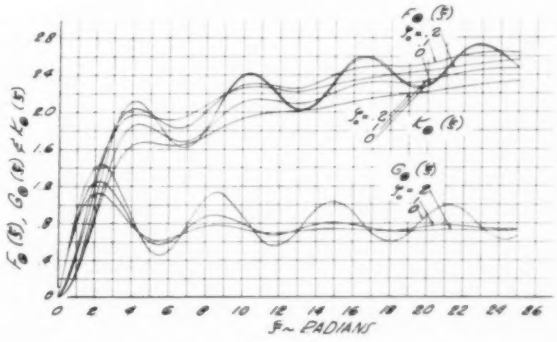

FIG. 11.

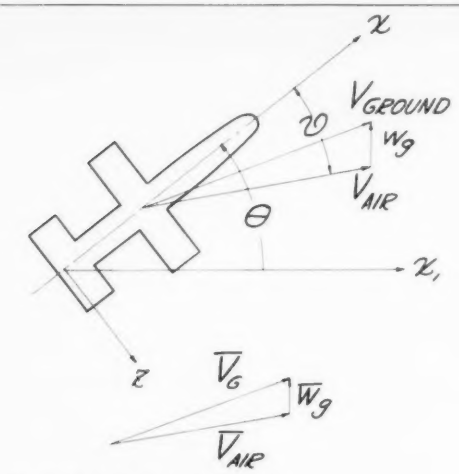

FIG. 12.

$$\left.\begin{aligned} h &= \frac{1}{\omega_0}\int_0^\xi \sin\gamma\,(x)\,dx \\ d &= \frac{1}{\omega_0}\int_0^\xi \cos\gamma\,(x)\,dx \end{aligned}\right\} \tag{51}$$

(V) Solution for Cross Wind

Let the cross component of the wind be w' and assume it to be constant. This corresponds to an initial angle of attack, $\vartheta = w_g/U$. Since the equation of motion is linear, the solution to the homogeneous equation with this initial condition will account for the wind effect, and this solution may be added to the solution for other disturbances.

$$\vartheta = \exp(-\zeta_0\xi)[C_1 J_{1/2}(\xi) + C_2 J_{-1/2}(\xi)] = y(\xi)\exp(-\zeta_0\xi) \tag{52}$$

Initial conditions

$$\vartheta_1 = [w_g/U(\xi_1)],\ q(\xi_1) = 0$$

if $\xi_1 = 0$, i.e., wind exists at launch

$$\vartheta_1 = \lim_{\xi\to 0}\,[w_g/U(\xi)]$$

The solution is then

$$\vartheta(\xi) = w_g\sqrt{\omega_0/2a\xi}\exp(-\zeta_0\xi)\cos\xi = [w_g/U(x)]\exp(-\eta_0 x)\cos(\omega_0 x) \tag{53}$$

With $\vartheta(\xi)$ determined, the trajectory can be computed. From Eq. (7), restricting attention to the effects of cross wind,

$$q = \dot\vartheta + (\vartheta/t) - z_{w_g} a t\,\vartheta$$

and integrating

$$\theta = \int_0^t q\,dt = \vartheta - \vartheta_0 + \int_0^\xi\left[\frac{\vartheta(x)}{2x} - \frac{Z_{w_g}\vartheta(x)}{\omega_0}\right]dx \tag{54}$$

Making use of Eq. (53) and integrating by parts

$$\left.\begin{aligned} \int_0^\xi \frac{\vartheta(x)}{2x}\,dx &= w_g\sqrt{\frac{\omega_0}{2a}}\left[-x^{-1/2}\exp(-\zeta_0 x)\cos x\,\Big|_0^\xi - \int_0^\xi \exp(-\zeta_0 x)\,x^{-1/2}(\zeta_0\cos x + \sin x)\,dx\right] \\ &= -\vartheta(\xi) + \vartheta_0 - w_g\sqrt{\omega_0/2a}\,[\zeta_0 C^-(\xi) + S^-(\xi)] \end{aligned}\right\} \tag{55}$$

where

$$C^-(\xi) = \int_0^\xi \exp(-\zeta_0 x)x^{-1/2}\cos x\,dx \tag{56}$$

$$S^-(\xi) = \int_0^\xi \exp(-\zeta_0 x)\,x^{-1/2}\sin x\,dx \tag{57}$$

Substituting in Eq. (54)

$$\theta = -w_g\sqrt{\omega_0/2a}\,[\zeta_0 + (Z_{w_0}/\omega_0)\,C^-(\xi) + S^-(\xi)] \tag{58}$$

Since the angle of attack ϑ is measured relative to the moving air mass, the trajectory angle $\gamma = \theta - \vartheta$ gives the direction of the velocity vector relative to the moving air mass. The trajectory direction relative to the original missile direction is then the direction of the resultant of the relative air velocity and the wind velocity (see Fig. 12). The distance along the trajectory is given by $x = \xi/\omega_0$, and the ground distance normal to the original direction of the missile axis is given by

$$\left.\begin{aligned} \zeta(\xi) &= -\int_0^\xi \sin(\theta - \vartheta)\,dx - \int_0^t w_g dt \\ &\doteq (w_g/\sqrt{2a\omega_0})\{C^-(\xi) + I_S^-(\xi) + [\zeta_0 + (Z_{w_0}/\omega_0)]I_c^-(\xi) - w_g\sqrt{2/\omega_0 a}\,\xi^{1/2}\} \end{aligned}\right\} \tag{59}$$

where

$$I_S^-(\xi) = \int_0^\xi S^-(x)\,dx \tag{60}$$

$$I_c^-(\xi) = \int_0^\xi C^-(x)\,dx \tag{61}$$

The functions $S^-(\xi)$, $C^-(\xi)$, $\theta(\xi)$, $\zeta(\xi)$, $I_c^-(\xi)$, and $I_S^-(\xi)$ are shown in Figs. 13–16.

(VI) Numerical Example

The method has been applied to a representative missile with the following characteristics:

U_{design} = 800 ft./sec.
ω_{design} = 10 rad./sec.

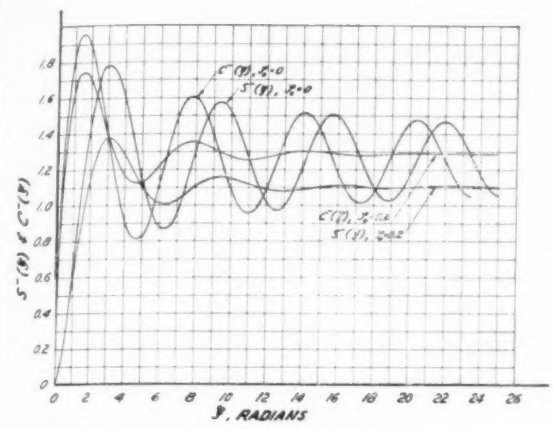

FIG. 13.

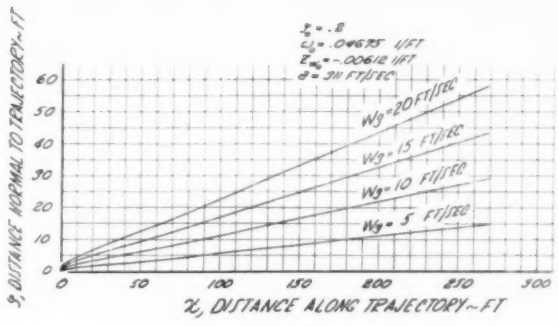
$\zeta_0 = .2$
$\omega_0 = .04675$ 1/FT
$Z_{w_0} = -.00612$ 1/FT
$a = 311$ FT/SEC
$W_g = 20$ FT/SEC
$W_g = 15$ FT/SEC
$W_g = 10$ FT/SEC
$W_g = 5$ FT/SEC
$\bar{s}$, DISTANCE NORMAL TO TRAJECTORY ~ FT
$\bar{x}$, DISTANCE ALONG TRAJECTORY ~ FT

FIG. 14.

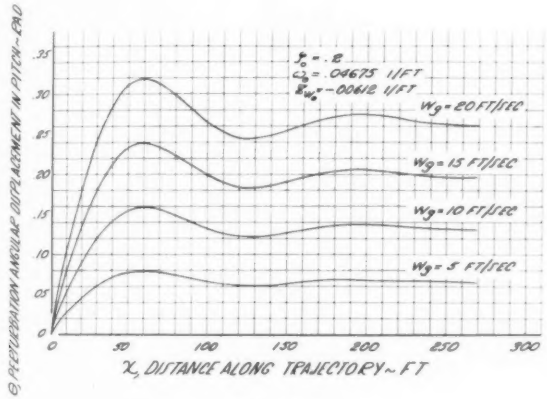
$\zeta_0 = .2$
$\omega_0 = .04675$ 1/FT
$Z_{w_0} = -.00612$ 1/FT
$W_g = 20$ FT/SEC
$W_g = 15$ FT/SEC
$W_g = 10$ FT/SEC
$W_g = 5$ FT/SEC
Θ, PERTURBATION ANGULAR DISPLACEMENT IN PITCH ~ RAD
$\bar{x}$, DISTANCE ALONG TRAJECTORY ~ FT

FIG. 15.

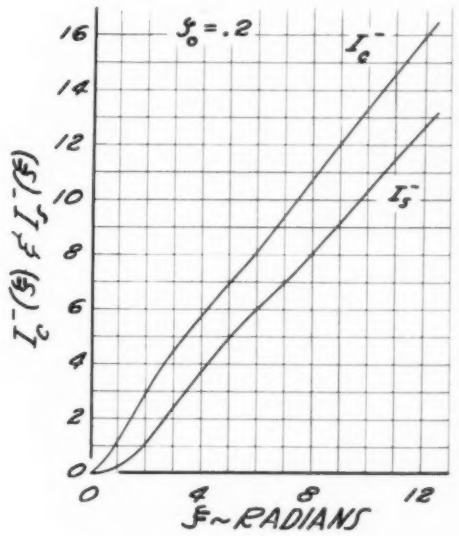

FIG. 16.

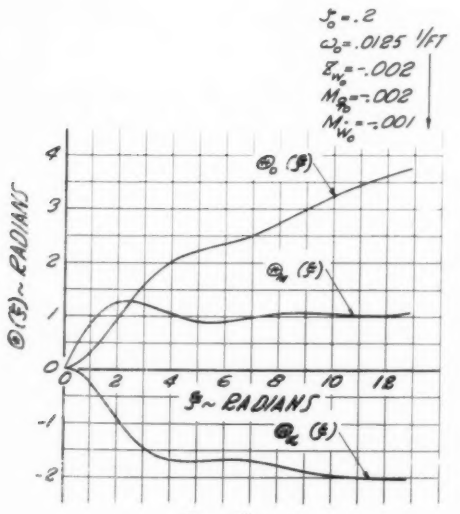

FIG. 17.

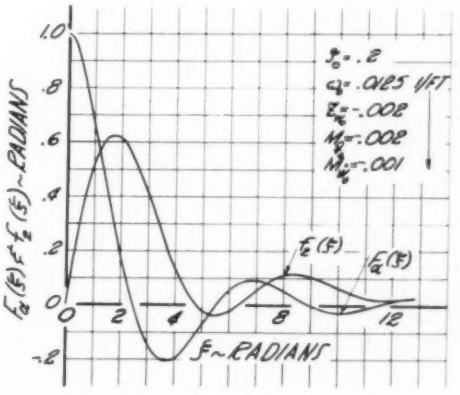

FIG. 18.

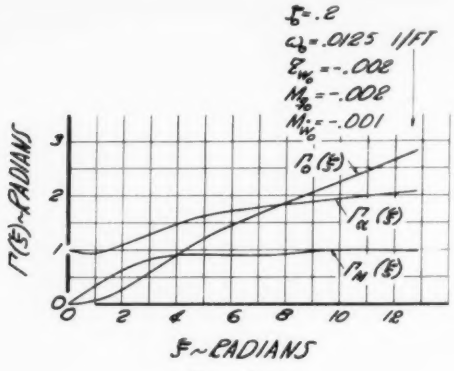

FIG. 19.

$$
\begin{aligned}
M_{\alpha_0} &= -0.002 \text{ ft.} \\
M_{\dot{w}_0} &= -0.001 \text{ ft.} \\
Z_{w_0} &= -0.002 \text{ ft.} \\
\omega_0 &= 0.0125 \text{ ft.} \\
\zeta_0 &= 0.20 \\
ml_1/I_y &= 0.23 \text{ ft.} \\
M_{q_0}/\omega_0 &= -0.16 \\
M'(\delta) &= 0 \\
Z_{w_0}/\omega_0 &= -0.16 \\
\frac{M_{q_0}Z(\delta)_0}{\omega_0^2} &= \frac{M_{q_0}g}{\omega_{\text{design}}^2} = -0.664 \times 10^{-3} \\
Z'(\delta) &= -g
\end{aligned}
$$

$$
\begin{aligned}
\frac{M'(\epsilon)}{a\omega_0^2} &= \frac{T'ml_1\epsilon}{I_y a\omega_0^2} = \frac{6000\epsilon}{a} \\
T' &= 10g
\end{aligned}
$$

Using these, and the values of the functions $f_1(\xi)$, $f_2(\xi)$, etc., from Figs. 3–11, the quantities F_α, Γ_α, etc., are computed and plotted in Figs. 17–19. Using these plots, the variation of angle of attack, ϑ, and angle of missile axis over the trajectory can be computed for any initial launching angle and thrust eccentricity. A typical trajectory is shown in Fig. 20.

(VII) Extension to Finite Launch Speed

The method outlined above can be extended to the case of launching with a finite velocity U_1. This velocity corresponds to the value of ξ_1.

$$\xi_1 = \omega_0 U_1^2/2a \tag{62}$$

The initial conditions to be prescribed are angle of attack and angular velocity at launch.

$$\left.\begin{aligned}\vartheta_1 &= \vartheta(\xi_1) \\ q_1 &= q(\xi_1)\end{aligned}\right\} \tag{63}$$

The corresponding initial value of $\dot{\vartheta}$ is obtained from Eq. 7.

$$\dot{\vartheta}_1 = q_1 - \left(\frac{a}{U_1} - Z_w'\right)\vartheta_1 + \frac{Z_1'}{U_1} \tag{64}$$

The complete solution for the angle of attack is then given by

$$\vartheta(\xi) = \exp(-\zeta_0\xi)[C_1 J_{1/2}(\xi) + C_2 J_{-1/2}(\xi)] + I(\xi,\xi_1) \tag{65}$$

where

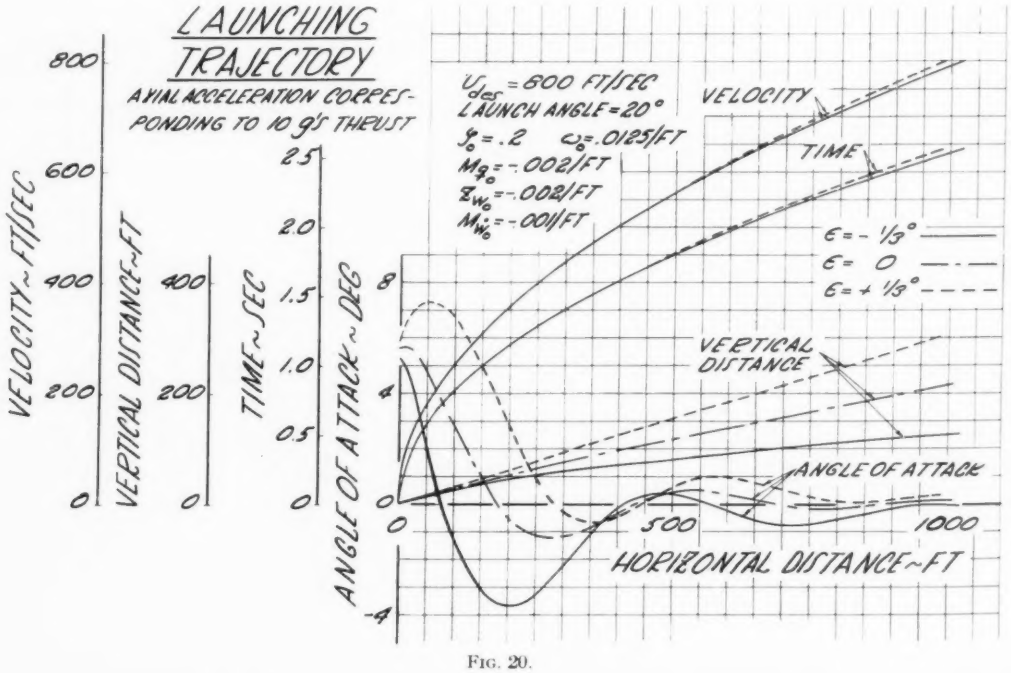

FIG. 20.

$$I(\xi,\xi_1) = \frac{\exp\ (-\zeta_0\xi)}{2a\omega_0\xi^{1/2}}\Bigg[\sin\ \xi\int_{\xi_1}^{\xi}\exp\ (\zeta_0 x)(\beta x^{-3/2} + \Lambda x^{-1/2} + \Omega x^{1/2})\cos x\,dx - \cos\xi\int_{\xi_1}^{\xi}\exp\ (\zeta_0 x)(\beta x^{-3/2} + \Lambda x^{-1/2} + \Omega x^{-1/2})\sin x\,dx\Bigg] \quad (66)$$

The particular integral, $I(\xi,\xi_1)$, satisfies zero initial conditions, and the constants C_1 and C_2 in Eq. (65) are evaluated to satisfy the specified initial conditions of Eqs. (63) and (64). This leads to the result

$$\vartheta(\xi) = (\xi_1/\xi)\exp\ [-\zeta_0(\xi - \xi_1)]\ [Q_1\sin\ (\xi - \xi_1) + \vartheta_1\cos\ (\xi - \xi_1)] + I(\xi,\xi_1) \quad (67)$$

where

$$Q_1 = \frac{q_1}{\omega_0 U_1} + \vartheta_1\left(\zeta_0 + \frac{Z_{w_0}}{\omega_0}\right) - \frac{Z(\delta)_0}{\omega_0} \quad (68)$$

and

$$I(\xi,\xi_1) = \vartheta_0\Bigg\{1 - \frac{f_1(\xi)}{2} + (1 + \zeta_0^2)\sqrt{\frac{\xi_1}{\xi}}\exp\ [-\zeta_0(\xi - \xi_1)][C(\xi_1)\sin\ (\xi + 2\psi) - S(\xi_1)\cos\ (\xi + 2\psi)] +$$

$$\left(\frac{Z_{w_0}}{\omega_0} + \frac{M_{\dot{w}_0}}{\omega_0}\right)f_2(\xi) - \left(\frac{Z_{w_0}}{\omega_0} + \frac{M_{\dot{w}_0}}{\omega_0}\right)\sqrt{1 + \zeta_0^2}\sqrt{\frac{\xi_1}{\xi}}\exp\ [-\zeta_0(\xi - \xi_1)]\ [C(\xi_1)\cos\ (\xi + \psi) + S(\xi_1)\sin\ (\xi + \psi)]\Bigg\} +$$

$$\sqrt{1 + \zeta_0^2}\sqrt{\frac{\xi_1}{\xi}}\exp\ [-\zeta_0(\xi - \xi_1)]\cos\ (\xi - \xi_1 + \psi) + \left[\frac{Z(\delta)_0}{\omega_0} + \frac{M'(\epsilon)}{\omega_0 a}\right]\Bigg\{f_2(\xi) - \sqrt{1 + \zeta_0^2}\sqrt{\frac{\xi_1}{\xi}}\exp\ [-\zeta_0(\xi - \xi_1)] \times$$

$$[C(\xi_1)\cos\ (\xi + \psi) + S(\xi_1)\sin\ (\xi + \psi)]\Bigg\} + \frac{M(\delta)_0 + Z(\delta)_0 M_{\dot{w}_0}}{\omega_0^2}\Bigg\{f_3(\xi) - \sqrt{\frac{\xi_1}{\xi}}\exp[-\zeta_0(\xi - \xi_1)][C(\xi_1)\sin\xi - S(\xi_1)\cos\xi]\Bigg\}$$

With ϑ determined, the missile axis angle and the flight path tangent can be determined as before.

References

[1] Durand, W. F.,[3] (Ed.), *Aerodynamics Theory*, Jones, B. Melvill, "Dynamics of the Airplane", Vol. V, Section N; Julius Springer, Berlin, 1935.

[2] Copson, E. T., *Introduction to the Theory of Functions of a Complex Variable;* Oxford University Press, London, 1935.

[3] Ince, E. L., *Ordinary Differential Equations;* Dover Publications, Inc., U.S.A.

An Analysis of the Performance of an Axial-Flow Compressor

(*Continued from page 746*)

[5] McCullough, G. B., and Gault, D. E., *Boundary-Layer and Stalling Characteristics of the NACA 64A006 Airfoil Section*, NACA TN 1923, 1949.

[6] Bursnall, W. J., and Loftin, L. K., *Experimental Investigation of Localized Regions of Laminar-Boundary-Layer Separation*, NACA TN 2338, April, 1951.

[7] Herrig, L. J., Emery, J. C., and Erwin, J. R., *Systematic Two-Dimensional Cascade Tests of NACA 65-Series Compressor Blades at Low Speeds*, NACA RM L51G31, September, 1951.

[8] Sawyer, W. T., *Experimental Investigation of a Stationary Cascade of Aerodynamic Profiles*, Mitteilungen aus dem Institut fur Aerodynamik NR. 17.

[9] Blight, F. G., and Howard, W., *Tests on Four Aerofoil Cascades: Part II, Boundary Layer Characteristics*, Aeronautical Research Laboratories (Australia) E 75, July, 1952.

[10] Maekawa, T., and Atsumi, S., *Transition Caused by the Laminar Flow Separation*, NACA TM 1352, September, 1952.

[11] Kuethe, A. K., and Schetzer, J. D., *Foundations of Aerodynamics;* John Wiley & Sons, Inc., New York, 1950.

[12] von Kármán, Th., and Von Mises, R., (Ed.), *Advances in Applied Mechanics*, Dryden, H. L. "Recent Advances in the Mechanics of Boundary Layer Flow"; Academic Press Inc., New York, 1948.

[13] Thwaites, B., *Approximate Calculations of the Laminar Boundary Layer*, Aero. Quart., Vol. I, Part III, November, 1949.

[14] Goldstein, A. W., and Mager, A., *Attainable Circulation of Airfoils in Cascade*, NACA TN 1941, September, 1949.

[15] Rannie, W. D., et al., *Theoretical and Experimental Investigations of Axial Flow Compressors*, Vol. 2, July, 1949. Published by the California Institute of Technology Mechanical Engineering Laboratory under Navy Contract N6-OR1-102 Task Order IV.

Readers' Forum

BRIEF REPORTS of investigations in the aeronautical sciences and discussions of papers published in the JOURNAL are presented in this special department. Entries must be restricted to a maximum of 1,300 words or the equivalent of one JOURNAL page including formulas and illustrations. Publication is completed as soon as possible after receipt of the material. The Editorial Committee does not hold itself responsible for the opinions expressed by the correspondents.

Contents

Vortex Structures in Pipe Flow ..... W. H. Webb and R. P. Harrington 792

On Inviscid Flow Near an Airfoil Leading Edge or an Ogive Tip at High Supersonic Mach Numbers ..... Abraham Kogan 794

On the Boundary-Layer Equations of a Very Slender Body of Revolution ..... S. I. Pai 795

Similarity-Rule Estimation Methods for Cones and Parabolic Noses ..... Richard D. Linnell and Jerry Z. Bailey 796

A Note on the Fatigue of Wings ..... A. O. Payne 797

Erratum—"On the Method of Averaging Stagnation Pressures" ..... Raymond L. Chuan 797

Transpiration Cooling Experiments in a Turbulent Boundary Layer at $M = 3$. ..... B. M. Leadon and C. J. Scott 798

The Decay of Turbulence Near the Critical Reynolds Number ..... A. F. Charwat 799

The Optimum Distribution of Lift in Certain Prismatic Regions at Supersonic Speed ..... William W. Willmarth 800

On the Supersonic Flow of a Viscous Fluid Past a Flat Plate ..... Stephen H. Maslen 801

On Thin-Ring Analysis ..... Bruno A. Boley 802

Approximative Determination of the Ceiling of Turbojet Engines ..... Karl L. Sanders 804

Vortex Structures in Pipe Flow*

W. H. Webb† and R. P. Harrington‡
Rensselaer Polytechnic Institute, Troy, N.Y.

March 3, 1956

QUALITATIVE photographic investigations of vortex structures occurring at transition are generally conducted for two distinct purposes: first, to explore the dynamical properties of artificially produced vortex systems in order to shed light on the characteristics of vortices which may be observed in future studies of natural transition, and, second, to concentrate exclusively on natural or nontrip-induced transition so that the uniqueness of occurrence of a prescribed vortex structure in such transition may be established.

The first course has been undertaken recently by Weske[1] at the University of Maryland, with the result that the motion of certain discrete vortices in shear flow has been revealed in some detail. Because of the nature of the apparatus used in his study, however, it was found difficult to follow through the complete cycle of transition from introduction of disturbance to complete turbulent flow. Therefore, as a first attempt at visualizing this process, a

* This research was supported by the United States Air Force through the Air Force Office of Scientific Research, ARDC.

Presented at the Research Conference on Transition and the Origin of Turbulence at the University of Maryland, December 1, 1955.

† Formerly, Research Assistant. Now, Aeronautical Engineer, Air Force Office of Scientific Research.

‡ Professor, Head of Department of Aeronautical Engineering.

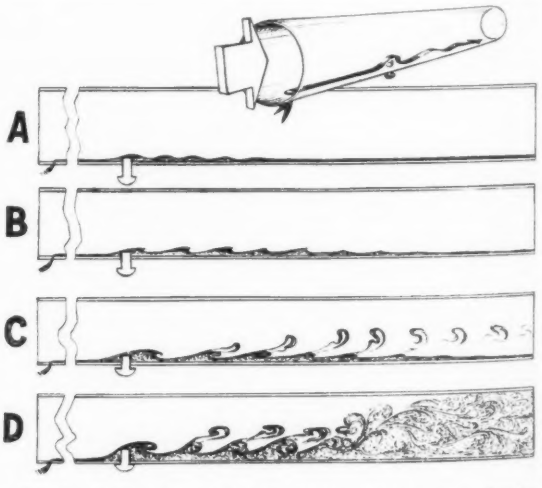

FIG. 1. Schematic of trip-induced transition pattern showing the effect of increasing disturbance height.

FIG. 2. Three-quarter view of typical trip-induced transition vortex structure. Flow in the pipe is from left to right.

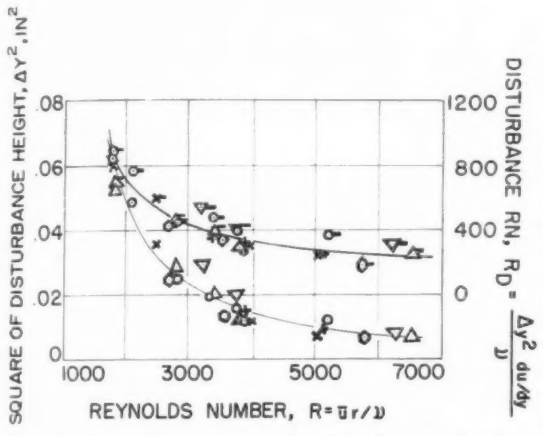

FIG. 3. Disturbance Reynolds Number (flagged points) and square of disturbance height for critical vortex production as a function of pipe Reynolds Number.

high laminar Reynolds Number pipe-flow apparatus was constructed at Rensselaer Polytechnic Institute. It consists principally of two large steel water tanks connected by a long straight 1¼ in. i.d. plastic pipe, flow being induced in the pipe by opening valves on the downstream tank. The maximum Reynolds Number obtainable, based on pipe radius and mean velocity, was about 10,000.

For visualization of the flow, dye was injected either through a rake inserted in the front of the entrance nozzle or through a thin slit in the pipe located some distance downstream of the inlet. The latter method provided a narrow band of dye on the bottom of the pipe which was suitable for visualizing wall-generated disturbances. A micrometer pitot tube connected to a bifluid manometer was used for measuring velocity profiles. Mean flow measurements were made by use of a sight glass on the upstream tank. It was found that laminar flow could be produced up to the maximum Reynolds Number obtainable if the water in the tanks was allowed to settle for a sufficient length of time before starting the flow.

To introduce a velocity perturbation normal to the mean parallel flow, many disturbance elements of widely varying shapes were used. Except for distortions in some cases, typical vortex sequences observed for all varieties of disturbances are shown in Figs. 1 and 2. The vortices are of the horseshoe type, as discussed by Theodorsen.[2]

No vortices were formed at Reynolds Numbers below a certain lower value. For a fixed Reynolds Number above this lower value, stages A through D of Fig. 1 show qualitatively the effect of increasing the height of the disturbance. (Stage D of this drawing corresponds to the flow situation which occurred in Fig. 2.) Small projections of the trip resulted only in the production of a wave-like disturbance which rapidly died out downstream. For slightly higher trip heights, the sharp crests of the waves folded over, and horseshoe vortices were expelled. The vortices were lifted in a diagonal direction to the center of the pipe at which point their circulation was immediately dissipated, the vortices therefore losing their identity and laminar flow prevailing throughout. If the disturbance height was only very slightly increased above that in stage C, the vortices disturbed the flow enough so that new larger disturbances were immediately created on the wall at the vortex ends. The shape of these secondary disturbances was not clearly defined; however, they were of such strength that, downstream of their occurrence, the flow was in a thoroughly mixed turbulent condition.

Following these qualitative studies, an attempt was made to measure the disturbance magnitude necessary to produce the last stage of flow described above for different Reynolds Numbers. A "disturbance Reynolds Number" R_D, as suggested by Theodorsen,[2] was used as a measure of the disturbance intensity. It is based on the square of the disturbance height and the local velocity gradient. Fig. 3 shows the results of this investigation.

To obtain these curves, a variable height trip was inserted into the flow at the wall. The trip was raised until, at a certain critical height Δy, it was observed that the horseshoe vortices were of sufficient strength to induce transition (last stage of Fig. 1). Fig. 3 shows the square of this height Δy, necessary to produce transition, as a function of pipe Reynolds Number. For each point, a wall velocity profile was measured slightly downstream of the trip before raising the trip, and the products of the slopes of these velocity curves at the wall and the disturbance heights squared are shown as the flagged points of Fig. 3.

Trips of three different diameters were used—namely, 3/16 in. and 1/8 in. machine screws and a 0.038 in. diameter wire. The octagonal points and the crosses represent data for the last two diameters, respectively. All other points are for the 3/16 in. trip. It is noted that the points for each diameter fall generally on the same curve. The difficulty in accurately measuring velocity profiles near the wall of the pipe is probably the cause for the small scatter observed in the curve for R_D.

As an attempt at establishing the uniqueness of a prescribed vortex system in the transition process, slow-motion photographs (1,000 frames/sec.) were taken of the turbulent burst which occurred naturally in the pipe at higher Reynolds Numbers. The burst was visualized by the smooth injection of a band of dye upstream of the viewing section. A typical sequence of events is shown in Fig. 4. The first picture represents the undisturbed laminar flow at $t = 0$. The next three show the development of the turbulent plug. The vortex-like motions which appear at the wall in these figures are not clearly defined, but it is hoped

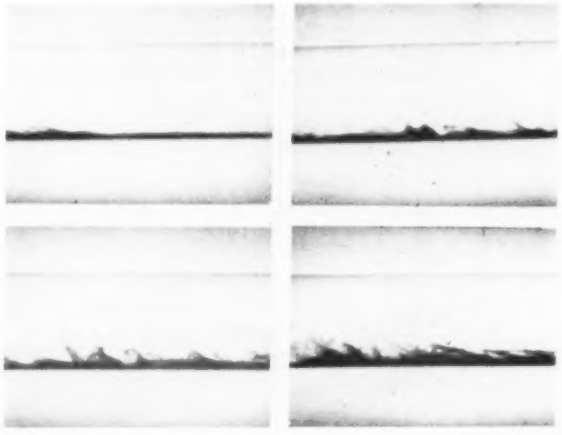

FIG. 4. Transition sequence without trip at Reynolds Number of 5,000. Flow is from right to left. Time t in sec. (*Upper left*) $t = 0$. (*Upper right*) $t = 0.3$. (*Lower left*) $t = 0.5$. (*Lower right*) $t = 0.7$.

that further photographic improvements will elucidate their basic structure and thereby enable a determination of the unique transition vortex configuration for pipe flow.

References

[1] Weske, J. R., and Plantholt, A. H., *Discrete Vortex Systems in the Transition Range of Fully Developed Flow in a Pipe*, Journal of the Aeronautical Sciences, Vol. 20, No. 10, pp. 717, 718, October, 1953.

[2] Theodorsen, T., *Mechanism of Turbulence*, Proceedings of the Second Midwestern Conference on Fluid Mechanics, 1952.

On Inviscid Flow Near an Airfoil Leading Edge or an Ogive Tip at High Supersonic Mach Numbers*

Abraham Kogan
Department of Aeronautical Engineering, The Technion, Haifa, Israel

March 23, 1956

Symbols

x, y = Cartesian coordinates
R, θ = polar coordinates
w = velocity, in units of limiting speed
u, v = components of w in x, y or R, θ directions
c = $\sqrt{[(\gamma - 1)/2]\,(1 - w^2)}$
Ψ = a Crocco stream function
S = entropy
γ = ratio of specific heats
c_v = specific heat at constant volume
M = free-stream Mach Number

* Part of this work was sponsored by ARDC, USAF Contract AF61(514)-870.

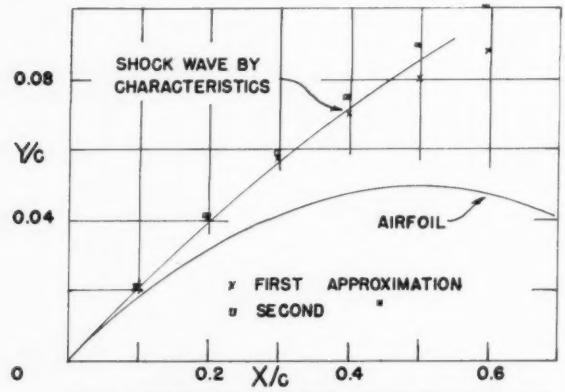

FIG. 1.— SHOCK PROFILE FOR BICONVEX PARABOLIC AIRFOIL T/C=0.10, M=∞, α=0°

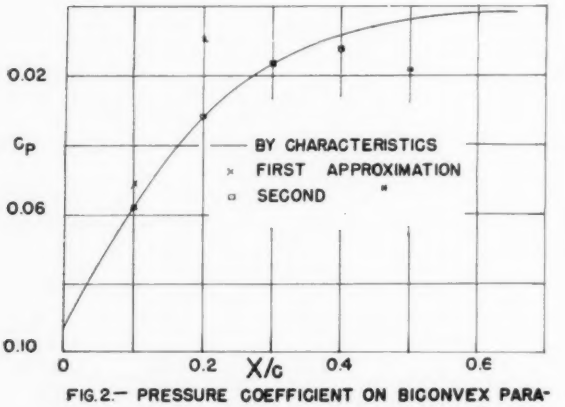

FIG. 2.— PRESSURE COEFFICIENT ON BICONVEX PARABOLIC AIRFOIL T/C=0.10, M=∞, α=0°

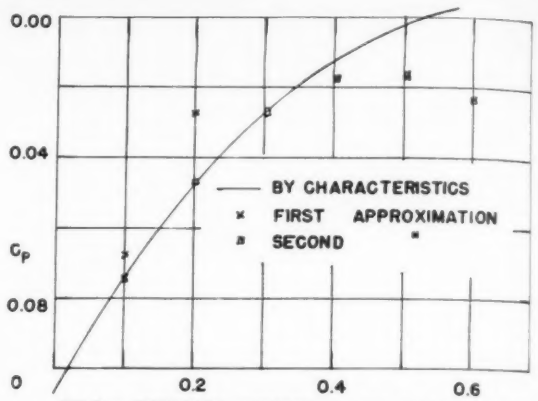

FIG. 3.— PRESSURE COEFFICIENT ON BICONVEX PARABOLIC AIRFOIL T/C=0.1, M=10, α=0°

(1) Two-Dimensional Flow Past an Airfoil

A convenient starting point for the study of high supersonic flow past airfoils is offered by the use of Crocco's stream function,[1] defined by

$$\Psi_y = u(1 - w)^{1/(\gamma-1)}; \qquad \Psi_x = -v(1 - w^2)^{1/(\gamma-1)} \quad (1)$$

since the flow equation

$$(c^2 - u^2)\Psi_{xx} - 2uv\Psi_{xy} + (c^2 - v^2)\Psi_{yy} = (1/2\gamma)\,(w^2 - c^2)\,(1 - w^2)^{(\gamma+1)/(\gamma-1)}\,(dS/c_v d\Psi) \quad (2)$$

satisfied by it is exact for rotational as well as for irrotational flows. The treatment of Eq. (2) is complicated by the fact that $dS/(c_v d\Psi)$ depends on the form of the shock wave which itself is an unknown of the problem. It can be attacked by successive approximations, taking the flow behind a plane shock wave as zero-order approximation. The shock-wave profile obtained in each step is used to determine the differential equation and the boundary conditions of the next one.

When the solution of the first-order problem is used to calculate, at the leading edge, the ratio of the curvatures of the shock wave and airfoil and the pressure gradient on the airfoil surface, results identical with those given by Cabannes[2] and Kraus[3] are obtained.

The second approximation has also been calculated by the above method. Figs. 1, 2, and 3 show a comparison of results thus obtained with those obtained by the method of characteristics[4] for flow about a 10 per cent thick parabolic biconvex airfoil placed symmetrically in a uniform stream at $M = 10$ and $M = \infty$.

(2) Rotationally Symmetric Flow Past an Ogive

Shen and Lin[5] investigated the flow behind an attached shock wave at the tip of an axisymmetrical body by perturbing the Taylor-Maccoll flow, using the usual form of the continuity, momentum, and energy equations. Their first-order-approximation velocity components, when expanded around the cone $\theta = \theta_0$, tangent to the ogive at the tip, contain terms in $\log(\theta - \theta_0)$ which cause complications. Because of these terms, they were unable to establish the validity of their first-order results when the ogive is convex. The initial pressure gradient at the ogive surface seemed to be infinite, although solutions by characteristics give no such indication. The logarithmic singularity also implies that an ogive of analytic profile would generate a shock wave of nonanalytic form.

Applying to the same problem his hypersonic small-disturbance theory, Van Dyke[6] found that the approximate expressions for the velocity perturbations contained a 1/2-power branch

point at $\theta = \theta_0$ but no logarithmic terms. Van Dyke conjectured that it is unlikely that a singularity could have disappeared as a result of his approximation which seems to retain the essential features of the exact solution, and he concluded that the singularity found by Shen and Lin arises from the asymptotic representation of the solution and probably does not exist physically.

This conclusion is borne out by the exact treatment of the problem based on the use of Crocco's stream function for axisymmetrical flow. The stream function, defined by

$$\left.\begin{aligned} \Psi_\theta &= uR^2 \sin\theta(1 - w^2)^{1/(\gamma-1)} \\ \Psi_R &= -vR \sin\theta\,(1 - w^2)^{1/(\gamma-1)} \end{aligned}\right\} \tag{3}$$

satisfies the equation

$$\begin{aligned}(c^2 - u^2)\Psi_{RR} - 2uv\Psi_{R\theta}/R + (c^2 - v^2)\Psi_{\theta\theta}/R^2 + \\ (2u^2v + v^3 - c^2u\cot\theta)\sin\theta(1 - w^2)^{1/(\gamma-1)} = \\ (1/2\gamma)R^2\sin^2\theta(w^2 - c^2)\,(1 - w^2)^{(\gamma+1)/(\gamma-1)}(dS/c_v d\Psi)\end{aligned} \tag{4}$$

With the flow past the cone $\theta = \theta_0$ as zero-order approximation and with suitable expansions for the shock-wave and ogive profile, successive approximations to Ψ can be evaluated from Eq. (4) and the appropriate boundary conditions. (Coordinate straining[7] is necessary for approximations after the first because of the singularity at the tip.)

The first-order solution for Ψ contains a 3/2-power branch point at $\theta = \theta_0$ and, therefore, a 1/2-power in the velocity components, but no logarithmic terms appear in the first-order velocity perturbations. This confirms the correctness of Van Dyke's approximation to this order. The tangency condition then serves to determine the ratio of the shock-wave and ogive curvatures. The same first-order formulas for stream function, pressure coefficient, and curvature ratio hold for both concave and convex ogives.

References

[1] Crocco, L., *Eine neue Stromfunktion fuer die Erforschung der Bewegung der Gase mit Rotation*, ZAMM, Vol. 17, pp. 1–7, February, 1937.

[2] Cabannes, H., *Determination de l'Onde de Choc Attachée lorsque la Vitesse aval à la Pointe est Subsonique*, Actes du Colloque International de Méchanique, Tome II, Poitiers, 1950.

[3] Kraus, S., *An Analysis of Supersonic Flow in the Region of the Leading Edge of Curved Airfoils*, NACA TN 2729, 1952.

[4] Eggers, A. F., Jr., Syverston, C. A., and Kraus, S., *A Study of Inviscid Flow about Airfoils at High Supersonic Speeds*, NACA TN 2579, 1951.

[5] Shen, S. F., and Lin, C. C., *On the Attached Curved Shock in Front of a Sharp-Nosed Axially Symmetrical Body Placed in a Uniform Stream*, NACA TN 2505, 1951.

[6] Van Dyke, M. D., *A Study of Hypersonic Small-Disturbance Theory*, NACA TN 3173, 1954.

[7] Lighthill, M. J., *A Technique for Rendering Approximate Solutions to Physical Problems Uniformly Valid*, Philos. Mag., Series 7, Vol. 40, pp. 1179–1202, December, 1949.

On the Boundary-Layer Equations of a Very Slender Body of Revolution*

S. I. Pai

Research Professor, Institute for Fluid Dynamics and Applied Mathematics, University of Maryland, College Park, Md.

April 6, 1956

For high-speed guided missiles, the study of hypersonic viscous flow over a body of revolution would be of great interest. At hypersonic speeds, the boundary-layer thickness is much larger than that at lower speed, and the proper radius of the body should be smaller than that for lower speed flight. As a result, the boundary-layer thickness may be of the same order of magnitude as the radius of the body of revolution. The boundary-layer equations are different from those for which the radius of the body is much larger than the thickness of the boundary layer. The well-known Mangler transformation[1] cannot be used in the present case. In this note, the author discusses the boundary-layer equations over a body of revolution of a very small radius and their transformation to an equivalent two-dimensional problem. Recently, Probstein and Elliott[2] used the same transformation to study this problem, but they did not notice that the fundamental equations can be transformed into *exactly the same* form of the two-dimensional equations, which is the essential point of this note.

The boundary-layer equations of a steady, axially symmetrical compressible fluid flow over a body of revolution whose radius is of the same order of magnitude as the thickness of the boundary layer are[3]

$$(\partial\rho uy/\partial x) + (\partial\rho vy/\partial y) = 0 \tag{1}$$

$$\begin{aligned}\rho[u(\partial u/\partial x) + v(\partial u/\partial y)] = \\ -(\partial p/\partial x) + (1/y)(\partial/\partial y)[\mu y(\partial u/\partial y)]\end{aligned} \tag{2}$$

$$\partial p/\partial y = 0 \tag{3}$$

$$\begin{aligned}\rho[u(\partial H/\partial x) + v(\partial H/\partial y)] = \\ u(\partial p/\partial x) + (1/y)(\partial/\partial y)[(\kappa y/C_p)(\partial H/\partial y)] + \mu[(\partial u/\partial y)]^2\end{aligned} \tag{4}$$

$$p = R\rho T \tag{5}$$

where x and y are, respectively, the distance along and perpendicular to the axis of revolution of the body. Here u and v are the x- and y-velocity components, respectively; ρ is the density, p the pressure, T the absolute temperature, μ the coefficient of viscosity, $H = C_pT$—the enthalpy, C_p the specific heat at constant pressure, and κ the coefficient of thermal conductivity.

Now we introduce the following transformations:[4]

$$\left.\begin{aligned} \bar{y} &= \int_{y_0}^{y} \frac{y}{L}\,dy, \qquad \bar{x} = \int_0^x \left(\frac{y_0}{L}\right)^2 dx, \qquad \bar{\psi} = \frac{\psi}{L} \\ \bar{p} &= p, \qquad \bar{\rho} = \rho, \qquad \bar{\mu} = \mu, \\ \bar{\kappa} &= \kappa, \qquad \bar{T} = T, \qquad \bar{H} = H \end{aligned}\right\} \tag{6}$$

where $y_0(x)$ is the radius of the body of revolution which is a function of x. ψ is the stream function which is defined by the following relations:

$$\partial\psi/\partial y = \rho uy, \qquad \partial\psi/\partial x = -\rho vy \tag{7}$$

L is a characteristic length, which may be arbitrarily chosen according to the convenience of the problem. We define the velocity components $\bar{u}$ and $\bar{v}$ in the $\bar{x}$, $\bar{y}$ plane as follows:

$$\partial\bar{\psi}/\partial\bar{y} = \bar{\rho}\bar{u}, \qquad \partial\bar{\psi}/\partial\,\bar{x} = -\bar{\rho}\bar{v} \tag{8}$$

Then

$$(\partial\bar{\rho}\bar{u}/\partial\bar{x}) + (\partial\bar{\rho}\bar{v}/\partial\bar{y}) = 0 \tag{8a}$$

From Eqs. (6), (7), and (8), it is easy to show that

$$u = \bar{u}, \qquad v = (y_0^2/yL)\bar{v} - (L/y)(d\bar{y}/dx)\bar{u} \tag{9}$$

Substituting Eqs. (6) and (9) into Eq. (2), we have

$$\begin{aligned}\bar{\rho}[\bar{u}(\partial\bar{u}/\partial\bar{x}) + \bar{v}(\partial\bar{u}/\partial\bar{y})] = \\ -(\partial\bar{p}/\partial\bar{x}) + (\partial/\partial\bar{y})[\mu^*(\partial u/\partial\bar{y})]\end{aligned} \tag{10}$$

where

$$\bar{\mu}^* = \mu[1 + (2\bar{y}L/y_0^2)] \tag{11}$$

Now we define a temperature function S such that

$$S = 1 - \{[H + (1/2)u^2]/[H_1 + (1/2)u_1^2]\} \tag{12}$$

where subscript 1 refers to values at some reference point—e.g. at $x = \infty$, $y = y_0 + \delta$, δ being the thickness of the boundary layer.

Substituting Eqs. (6), (9), and (12) into Eq. (4), we have

$$\bar{\rho}[\bar{u}(\partial S/\partial\bar{x}) + \bar{v}(\partial S/\partial\bar{y})] = (\partial/\partial\bar{y})[\bar{\mu}^*(\partial S/\partial\bar{y})] \tag{13}$$

where the assumption $P_r = 1$ has been used.

Our fundamental equations are then Eqs. (5), (8a), (10), and (13) for the variables $\bar{\rho}$, $\bar{u}$, $\bar{v}$, and S with given $y_0(\bar{x})$ and $p(\bar{x})$. These fundamental equations are identical with those of the two-dimensional case.[4] Hence the method of solution for the two-dimensional case may be used to solve this axially symmetrical problem; particularly if von Kármán's integral method is used, the viscosity μ (not $\bar{\mu}^*$) will remain in both the momentum in-

* This work was supported by the office of Scientific Research, ARDC, under Contract AF18(600)993.

tegral and the energy integral equations because

$$\bar{\mu}^*_{(y=0)} = \mu_{(y=0)} \tag{14}$$

The momentum and energy integral equations are identical to those given in reference 5.

References

[1] Mangler, W., *Zusammehang zwischen ebenen und rotation symmetrischen Greenzschicht in kompressiblen Fluessigkeiten*, ZAMM, Vol. 28, pp. 97–103, 1948.

[2] Probstein, R. F., and Elliott, D., *The Transverse Curvature Effect in Compressible Axially Symmetric Laminar Boundary-Layer Flow*, Journal of the Aeronautical Sciences, Vol. 23, No. 3, pp. 208–222, March, 1956.

[3] Pai, S. I., *Viscous Flow Theory, I—Laminar Flow*, Chap. VIII, D. Van Nostrand Company, Inc., New York, 1956.

[4] Mark, R. M., *Laminar Boundary Layers on Slender Bodies of Revolution in Axial Flow*, Mem. No. 21, Guggenheim Aeronautical Laboratory, California Institute of Technology, July 30, 1954.

[5] Pai, S. I., and Shen, S. F., *Hypersonic Viscous Flow over an Inclined Wedge with Heat Transfer*, 50 Jahre Grenzschichtforschung, ed. by H. Görtler and W. Tollmien, pp. 112–121, 1955.

Similarity-Rule Estimation Methods for Cones and Parabolic Noses

Richard D. Linnell* and Jerry Z. Bailey†

Convair, Fort Worth, A Division of General Dynamics Corporation

March 28, 1956

Introduction

For preliminary design estimates, simple prediction procedures giving moderate accuracy are needed. Analytical methods are needed for inclusion in electronic computer programs in order to determine a first estimate in iteration procedures. Graphical and analytical procedures are presented for obtaining characteristics of inviscid supersonic flow about cones and parabolic noses. Large-scale graphs can be constructed using the equations.

* Formerly, Project Aerodynamics Engineer, Convair. Now, Engineer, General Electric Company, Schenectady, N.Y.

† Technical Analyst.

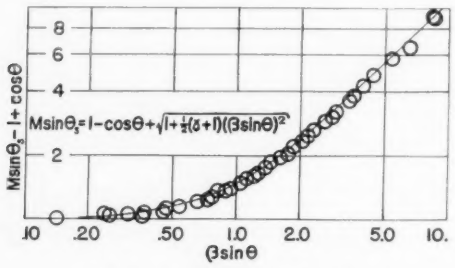

Fig. 1. Cone shock-wave angle.

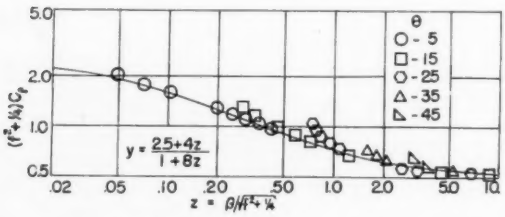

Fig. 2. Cone surface pressure coefficient.

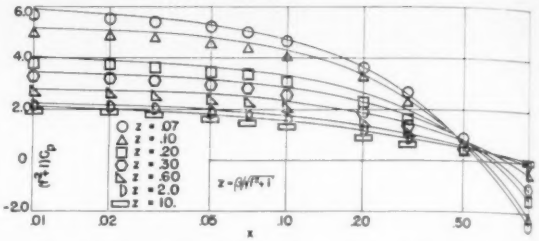

Fig. 3. Parabolic-nose pressure-coefficient distribution.

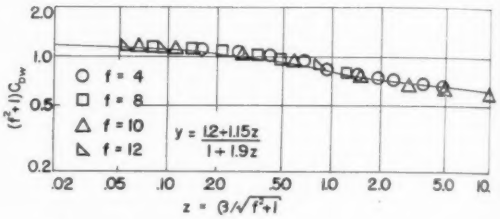

Fig. 4. Parabolic-nose wave-drag coefficient.

Cones

In electronic-computer solution of the Taylor-Maccoll equations by iteration, an analytical first estimate of the shock angle is needed. Reasoning based on the limiting values of the shock angle led to the equation

$$M \sin \theta_s - 1 + \cos \theta = G(\beta \sin \theta)$$

where θ_s is the shock angle, θ is the semiapex angle of the cone, $\beta = \sqrt{M^2 - 1}$, M is the free-stream Mach number, and G is a function of $\beta \sin \theta$. Points obtained by using θ_s values from the M.I.T. cone tables[1] have a scatter of about 5 per cent as shown in Fig. 1. The curve shown in Fig. 1 was obtained by selecting a function of $\beta \sin \theta$ to fit the points. The equation is

$$M \sin \theta_s = 1 - \cos \theta + \sqrt{1 + (1/2)(\gamma + 1)(\beta \sin \theta)^2} \tag{1}$$

The limiting value for a large $\beta \sin \theta$ corresponds to the result of hypersonic slender body theory.[2] The correlation was checked only for γ, the ratio of specific heats, equal to 1.4. Eq. (1) does not satisfy similarity rules, but the similarity concept was used in determining it.

The surface pressure coefficient and the wave-drag coefficient using base area are equal for cones. Similarity-rule correlations have been published[3] for these characteristics. The M.I.T. cone table was used to obtain the values of the pressure coefficient, C_p, shown in Fig. 2. The fineness ratio f is the axial length divided by the base diameter. It is related to the cone semiangle by $f = 1/(2 \tan \theta)$ and $\sqrt{f^2 + (1/4)} = 1/(2 \sin \theta)$. The correlation is within 10 per cent except for Mach Numbers very near shock detachment. The fitted curve in Fig. 2 is defined by

$$[f^2 + (1/4)]C_p = \left\{2.5 + 4[\beta/\sqrt{f^2 + (1/4)}]\right\} / \left\{1 + 8\,[\beta/\sqrt{f^2 + (1/4)}]\right\} \tag{2}$$

The equation is as accurate as any correlation line that could be drawn. It should be used for graphical procedures for consistency.

Parabolic Noses

Pressure distributions and wave-drag coefficients for ogival noses were presented in similarity form in reference 3. An exponential equation for the pressure distribution was given. Some pressure-coefficient distribution points for parabolic noses are shown in Fig. 3. These values were obtained by second-order theory[4] and hypersonic slender body theory.[2] A linear fraction was used to fit the points:

$$(f^2 + 1)C_p = (A + Bx)/(1 + Cx) \tag{3}$$

where x is the fraction of axial nose length and

$$\left.\begin{aligned} A &= [10 + 32(\beta/\sqrt{f^2+1})]/[1 + 16(\beta/\sqrt{f^2+1})] \\ B &= [-13 - 13(\beta/\sqrt{f^2+1})]/[1 + 7(\beta/\sqrt{f^2+1})] \\ C &= [1 + 16(\beta/\sqrt{f^2+1})]/[5 + 4(\beta/\sqrt{f^2+1})] \end{aligned}\right\} \quad (4)$$

The deviation of the equation is less than 5 per cent of the peak pressure coefficient at the apex of the parabolic nose. The computed points are within 5 per cent of the values for ogives determined by the method of characteristics in reference 3. This indicates that either the method of reference 3 or the above procedure can be used to make preliminary estimates for bodies of nearly ogival or parabolic shape. The algebraic function given here is simpler than the exponential function of reference 3.

The parabolic-nose wave-drag coefficient C_{Dw} is shown in Fig 4. The fitted curve is defined by the equation

$$(f^2+1)C_{Dw} = [1.2 + 1.15(\beta/\sqrt{f^2+1})]/[1 + 1.9(\beta/\sqrt{f^2+1})] \quad (5)$$

The accuracy of the equation as a correlation line is not as good as the small scatter of the computed points. The equation is about 10 per cent low when $\beta/\sqrt{f^2+1}$ is near 0.5. These results for parabolic noses check with the wave-drag results of reference 3 except for the two points it gives for $K = M/f$ equal 2 for ogives. Since the pressure distributions do correspond for K equal to 2, it appears that the present values are correct.

References

[1] Kopal, Z., *Tables of Supersonic Flow Around Cones*, Rept. No. 1, Computing Section, Center of Analysis, Dept. of Electrical Engineering, Massachusetts Institute of Technology, 1949.

[2] Eggers, A. J., Jr., and Savin, R. C., *Approximate Methods for Calculating the Flow about Nonlifting Bodies of Revolution at High Supersonic Airspeeds*, NACA TN 2579, December, 1951.

[3] Ehret, D. M., Rossow, V. J., and Stevens, V. I., *An Analysis of the Applicability of the Hypersonic Similarity Law to the Study of Flow about Bodies of Revolution at Zero Angle of Attack*, NACA TN 2250, December, 1950.

[4] Van Dyke, M. D., *Practical Calculation of Second-Order Supersonic Flow Past Nonlifting Bodies of Revolution*, NACA TN 2744, July, 1952.

A Note on the Fatigue of Wings

A. O. Payne*

Senior Scientific Officer, Aeronautical Research Laboratories, Department of Supply, Melbourne, Australia

April 6, 1956

Completed Project

A series of fatigue tests has recently been completed at the Aeronautical Research Laboratories on 90 P51-D Mustang mainplanes. The structure of this mainplane is regarded as being representative of a large class of riveted 24ST aluminum-alloy wings, and the project has provided comprehensive information on the fatigue characteristics of such a structure.

Tests showed that the effect on the fatigue characteristics of the varying service life experienced prior to test by some of the wings used was negligible. Consequently, all the test results have been pooled, and, further, since both port and starboard halves are practically identical, a half wing was taken as the unit specimen.

Tests were carried out at load ranges which covered all alternating load and mean-load combinations of practical interest. At least six specimens were tested at each load range so that the resulting data could be treated on a statistical basis.

The results obtained have led to the following general conclusions: (1) Several distinct types of failure occur, their relative frequencies of occurrence depending principally on the maximum load of the load cycle. (2) The rate of crack propagation is practically constant for a large part of the life. (3) Lines of constant life on the alternating load - mean load diagram are of the same general shape as those obtained for notched aluminum-alloy specimens. (4) In general, the fatigue life of the structures corresponds with that of a simple specimen possessing a stress concentrator having a theoretical stress-concentration factor of about 3. (5) The logarithmic normal distribution is a good approximation to the frequency distribution of fatigue life. (6) For a given value of preload, the relative increase in fatigue life is a function of the maximum load of the cycle only, and it progressively increases as the maximum load is decreased until failure occurs, finally, in the compression surface of the structure. (7) There is an optimum value of preload—namely 85 per cent ultimate failing load—which produces a maximum relative increase in life.

Current Projects

Further programs of tests on Mustang wings designed to investigate cumulative fatigue damage and methods of service life estimation are now in progress.

In one of these, the fatigue strength under actual service loads is being determined by subjecting the wings to a fatigue test designed to simulate the complete gust loading history experienced by a transport aircraft during normal operation.

The gust-velocity data being used have been based on counting accelerometer records obtained from a De Havilland Dove aircraft operating in Western Australia. For test purposes, these data are represented by a set of eleven positive and eleven negative loads, all of different magnitude and of appropriate relative frequency and applied to the specimen in a random manner by a random loading device which controls a hydraulic loading rig.

To date, one specimen of this program has been tested to destruction.

In a second program, the gust load spectrum is being replaced by three loads only, the loads being appropriately grouped around the maximum damage load and being applied according to a programed sequence and with relative frequencies such that they each contribute an equal amount of estimated damage.

In conjunction with the basic fatigue data already obtained from the completed "constant amplitude" project, the results of the current tests will enable various theories of cumulative damage to be explored for the various types of failure. In addition, it will be possible to assess the accuracy of current methods of life estimation.

Details of, and results from, both the completed and the current projects will be published in a comprehensive series of reports to be issued by the Aeronautical Research Laboratories.

* The author acknowledges the permission of the Chief Scientist, Department of Supply, Australia, to publish this note.

Erratum—"On the Method of Averaging Stagnation Pressures"[1]

Raymond L. Chuan

Research Associate, Engineering Center, University of Southern California, Los Angeles, Calif.

June 5, 1956

Equation (7) should be corrected to read

$$\bar{p}_s = e^{\int \rho u \log p_s \, dy / \int \rho u \, dy}$$

Reference

[1] Chuan, Raymond L., Journal of the Aeronautical Sciences Readers' Forum, Vol. 23, No. 4, pp. 378, 379, April, 1956.

Transpiration Cooling Experiments in a Turbulent Boundary Layer at $M = 3$*

B. M. Leadon and C. J. Scott†
Rosemount Aeronautical Laboratory, University of Minnesota, Minneapolis, Minn.
April 6, 1956

SUMMARY

Turbulent recovery factor and heat-transfer measurements have been made on a porous flat wall section at a nominal Mach Number of 3.0 and a Reynolds Number of approximately 4×10^6 using both air and helium as the transpired gas. Measured heat-transfer coefficients correlate well with the compressible theory of Rubesin[1] for air and qualitatively with simple film theory[2, 4] for either coolant, indicating that the heat transfer from a turbulent boundary layer can be reduced by transpiration cooling to well below that of the uncooled boundary layer at the same Reynolds Number.

INTRODUCTION

WHEN THE USUAL solid-wall boundary condition of zero normal velocity is replaced, for a porous wall, by one of finite normal velocities, it is to be expected that the properties of the viscous boundary layer associated with a convective flow over the wall will be affected. The distributions normal to the surface of such descriptive variables as velocity, temperature, and concentration of foreign gas may be modified strongly if gas is introduced which has markedly different kinetic and thermal properties from those of the free stream gas. Of practical interest are two possibilities: (1) the rate of heat transfer to the wall may be reduced to a significant extent by a small mass flow of transpired gas, and (2) the laminar stability of the boundary layer may be improved. Experiments on the first possibility for a turbulent boundary layer in a supersonic flow are reported herein.

Theories have been presented for statistically steady turbulent boundary-layer flow including the effect of finite normal velocity at the wall. Film theory[2] involves such crude assumptions that it may be accepted only qualitatively, but it displays the effect of mass diffusion in a simple manner whereas the more refined analytical estimates based upon mixing-length theory[1, 3] are available only for the case of air blowing into air.

APPARATUS, TECHNIQUE, RESULTS, AND DISCUSSION

A 7- by 1.5-in. porous flat plate constructed of sintered stainless-steel wire was set into the straight wall in the constant-pressure section of a 1.9- by 1.75-in. asymmetric supersonic channel with its leading edge located 7.5 in. from the throat. The boundary layer was known to be turbulent from previous experiments. The nozzle block, made of a fiberglass laminate having low thermal conductivity, was machined to contain a coolant stilling chamber. Thermocouples, 0.0031 in. diameter, were carefully installed in the porous surface (Fig. 1 shows Teflon plug, wires, and final welds) and suspended throughout the coolant stilling chamber at 1-in. intervals. Provision was made to heat the porous surface electrically and to preheat the inflowing gas.

* This research was sponsored by the Office of Scientific Research of the ARDC, USAF, under Contract AF 18 (600)-1226.

† The authors wish to acknowledge their indebtedness to Mikelis Geistauts for his work in the installation of the thermocouples.

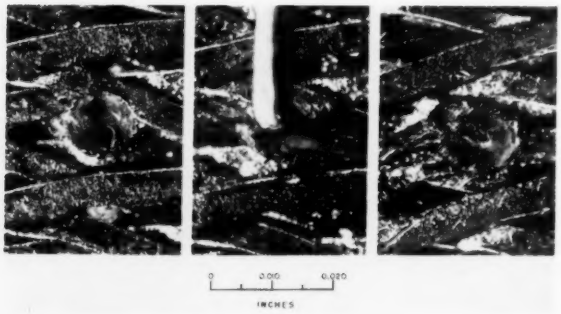

FIG. 1.

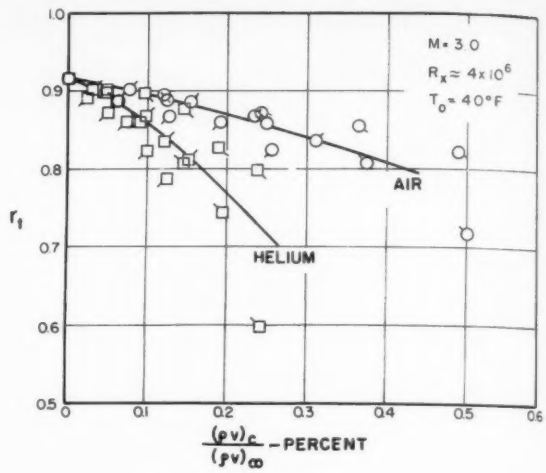

FIG. 2.

With zero electrical power input, the temperature of the transpired gas (referred to as the coolant although in these tests it was actually preheated) as measured at a point in the coolant stilling chamber was brought close to that of the wall as measured at the corresponding point on the wall, and at least three differences $T_w - T_c$ at each location for each coolant mass flow were plotted versus T_w/T_0 permitting interpolation for T_{aw} at $T_w = T_c$. The results for both air and helium are shown as recovery factor r_f versus coolant mass flux ratio $(\rho v)_c/(\rho v)_\infty$, the subscript ∞ referring to free-stream values (Fig. 2). Individual thermocouple pairs, indicated by flags on the symbols, show considerably less scatter than does the whole set. The faired curves represent average temperature recovery factors for air and helium at an average Reynolds Number of about 4×10^6.

If it is assumed that the temperature of the coolant on emergence equals that of the wall, the heat balance for the porous surface in a certain internal control volume can be written

$$(\rho v c_p)_c T_c + q_c = St(\rho u c_p)_\infty (T_w - T_{aw}) + (\rho v c_p)_c T_w + q_{rad} + q_{loss}$$

where the terms on the left give heat added by coolant convection and by electrical heating and the terms on the right give heat removed by outer boundary-layer convection, coolant convection, radiation, and extraneous heat loss, respectively. For several practical reasons, $T_c - T_w$ was minimized during the tests.[4] Normal emissivities were measured through the use of a total

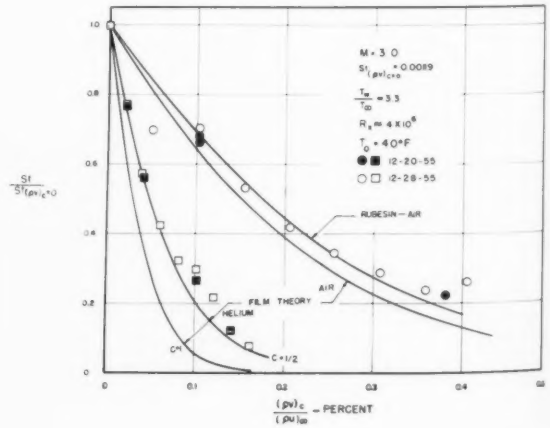

FIG. 3.

radiation pyrometer and found to be 0.44 for the porous surface and 0.94 for the opposing plastic nozzle.

Stanton numbers were computed from an average of five local values taken in the central 5-in. segment wherein there were only moderate variations of local surface temperature, porosity, and coolant flow distribution.

These are presented in Fig. 3 as relative to the zero blowing value. Runs on two different days, open and solid symbols, indicate repeatability. Comparison is made with Rubesin's estimate for air and with film theory[2] modified[4] to account for mass fraction concentrations of helium at the wall.

These heat-transfer measurements show that strong mass-transfer cooling effects in a turbulent boundary layer are possible at $M = 3.0$, $R_x = 4 \times 10^6$, and $T_w/T_\infty = 3.3$, even reducing heat transfer below laminar values at the higher blowing velocities. Noteworthy is the fact that the limit of relative coolant rates, air to helium, required to effect a given relative Stanton number reduction, as that reduction vanishes, is about 5, which is also the inverse ratio of their specific heats, but that this ratio appears to diminish with increased blowing.

These tests are preliminary to porous cone studies.

References

[1] Rubesin, Morris W., *An Analytical Estimation of the Effect of Transpiration Cooling on the Heat-Transfer and Skin-Friction Characteristics of a Compressible, Turbulent Boundary Layer*, NACA TN 3341, December, 1954.

[2] Mickley, H. S., Ross, R. C., Squyers, A. L., and Stewart, W. E., *Heat, Mass, and Momentum Transfer for Flow over a Flat Plate with Blowing or Suction*, NACA TN 3208, July, 1954.

[3] Dorrance, William H., and Dore, Frank J., *The Effect of Mass Transfer on the Compressible Turbulent Boundary-Layer Skin Friction and Heat Transfer*, Journal of the Aeronautical Sciences, Vol. 21, No. 6, pp. 404–410, June, 1954.

[4] Leadon, B. M., and Scott, C. J., *Measurement of Recovery Factors and Heat Transfer Coefficients with Transpiration Cooling in a Turbulent Boundary Layer at $M = 3.0$ Using Air and Helium as Coolants*, Univ. of Minnesota, Rosemount Aero. Lab. Rep. No. 126, 1956; and AFOSR TN 56-94 AD 82502, 1956.

The Decay of Turbulence Near the Critical Reynolds Number

A. F. Charwat*
University of California, Los Angeles

April 23, 1956

Measurements of the decay of turbulent axial velocity fluctuations close to the generating screens at low Reynolds Numbers are shown on Fig. 1. The data were collected at constant mean velocity and variable density. A 20 mesh per in., 0.0165-in. wire screen was used. The hot-wire anemometer (constant resistance type) was calibrated at each tunnel pressure (between 18 and 8 lbs. per sq.in. absolute). It was found to operate satisfactorily in conformance with predictions.

It is interesting to observe whether the decay of turbulence close to the critical Reynolds Number of the screen continues to fit the established behavior of isotropic turbulence behind screens at higher Reynolds Numbers.

The decay curves on Fig. 1 exhibit a noticeable irregularity near the origin. The evidence is that the level of fluctuations increases in that region. A similar occurrence, although over a much longer scale, was observed by Schubauer et al[1] in the case of some screens which they labeled "abnormal." These authors suggested that the abnormality was associated with large-scale irregularities in the screen; the present phenomenon may be similarly associated with the small-scale irregularity of the flow immediately downstream of the screen. One guess is that it is due to the instability of the jet-like structure of the flow.

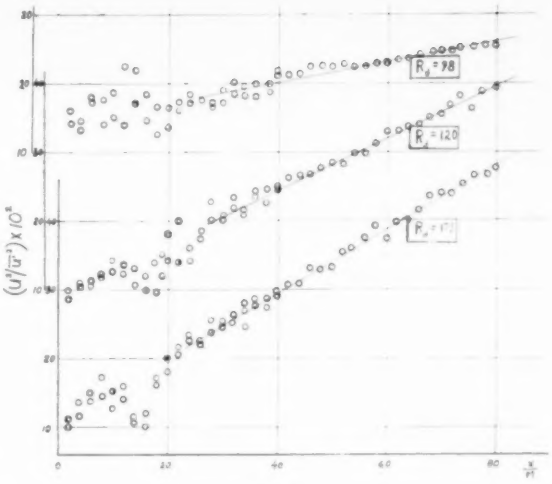

Fig. 1.

Beyond the initial mixing region, the decay of the turbulent energy seems to follow the linear law predicted for the "initial period" of isotropic turbulence[2]:

$$U_0^2/u'^2 = \alpha[(x/M) - (x/M)_0] \qquad (1)$$

However, this is not conclusive because the correlation between the data and Eq. (1) over the short range of initial decay is difficult to ascertain. The congruence of the slopes of this data with the slopes of known isotropic decay lines would provide a more sensitive test.

Batchelor and Townsend[2] suggested that the slope of the decay (as well as the initial magnitude) of the turbulent energy is related to the screen pressure loss as follows:

$$\alpha = \text{constant}/C_D \qquad (2)$$

To verify this, it is necessary to estimate the drag of the screens as a function of solidity and Reynolds Number. This has been done using data of references (1) and (3) at low Reynolds Numbers and of reference (4) at Reynolds Numbers above 1,000 (beyond which the screen pressure loss appears to be constant with increasing Reynolds Number). The Reynolds Number variation for screens of all solidities appears to be similar, within experimental accuracy, to that for a single cylinder.

Estimating the screen drag with correction for Reynolds Number, the constant of Eq. (2) is 105, 103, and 35 for Reynolds numbers 173, 120, and 98, respectively. Batchelor and Townsend suggested it should be 106 from their data. In addition, the data of reference 5 yields the following values:

Average value of decay constant: 109
Range of Reynolds Numbers: 1,600 to 5,000
Range of screen solidities: 30 to 55 per cent
Total number of tests: 24
Spread of slopes ref. to average: +69 per cent, −57 per cent
Spread of decay constants ref. to average: +29 per cent, −30 per cent

The scatter in the values of the decay constant is one half of the scatter in the slopes. This does indicate a basic correctness of Eq. (2). The average constant appears to be consistently between 100 and 110. The decay at the lowest Reynolds Number shown on Fig. 1 appears to be definitely outside the general model.

The physical picture of this was obtained by the use of a smoke tunnel. A grid of 3/16-in. rods at 50 per cent solidity was used for the purpose. It was observed that, above Reynolds Numbers of the order of 100, the von Kármán vortex patterns shed from the cylinders break down violently approximately five mesh lengths downstream of the grid. Below Reynolds Numbers of

* Assistant Professor of Engineering.

100, the clearly visible vortex sheets do not break down but proceed independently until they decay by viscosity. Reynolds Numbers of the order of 60 correspond to the lower limit of vortex shedding.

The conclusion of the present observation is that the lower limit of turbulent field, generated by the breakdown of vortexes shed off the grid, occurs around a wire Reynolds Number of 110 and that the decay of the turbulence closely approximates isotropic decay even at this lower limit. Below this limit, the field cannot at all be considered turbulent in the sense of random fluctuations.

References

[1] Schubauer, G. et al, *Aerodynamic Characteristics of Damping Screens*, NACA TN 2001, 1950.

[2] Batchelor, G., and Townsend, A., *Decay of Isotropic Turbulence in the Initial Period*, Proc. Roy. Soc. London (A), Vol. 193, p. 539, 1948.

[3] Eckert, B., and Pfluger, F., *The Resistance Coefficient of Commercial Round Wire Grids*, NACA TM 1003, 1942.

[4] Hoerner, S., *Pressure Losses Across Screens and Grids*, Air Force TR 6289, November, 1950.

[5] Davis, L., *Measurements of Turbulence Decay and Turbulent Spectra Behind Grids*, California Institute of Technology, Power Plant Labs. Report 3–17 (AMC contract W33-038-ac-4320) ATI 156500.

The Optimum Distribution of Lift in Certain Prismatic Regions at Supersonic Speed*

William W. Willmarth

Consultant, The RAND Corporation, Santa Monica, Calif., and Research Fellow, California Institute of Technology, Pasadena

April 12, 1956

Recently, Jones[1] has given criteria which identify the arrangements of lift, side force, and volume elements in a three-dimensional region that will have minimum drag when the total lift and volume are specified. These criteria are the following:

In superimposed forward and reversed flow, with a fixed lift distribution, the sum of the downwash velocities should be constant throughout the region

$$w_f + w_r = \text{const.} \tag{1}$$

the sum of the sidewash velocities should be zero in the region

$$v_f + v_r = 0 \tag{2}$$

and the streamwise gradient of the sum of the streamwise perturbation velocities should be constant in the region

$$\partial(u_f + u_r)/\partial x = \text{const.} \tag{3}$$

A class of simple examples that satisfy Jones' criteria can be obtained by placing end plates on flat plates of constant chord

* The results presented in this paper were obtained in the course of duties performed for The RAND Corporation.

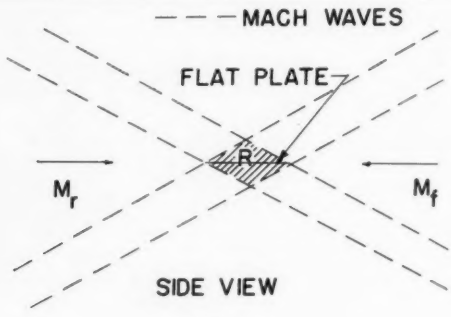

Fig. 1.

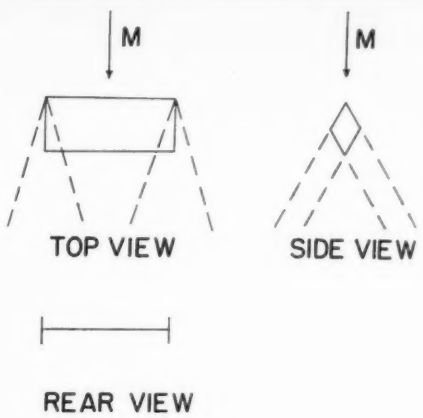

Fig. 2.

with supersonic edges. First consider a two-dimensional flat-plate wing with leading edge normal to the stream. As shown by the Ackeret theory, the wing produces a uniform lift distribution on the plan form. In reversed flow, the same uniform lift distribution will be reproduced if the angle of attack with respect to the air stream is the same. In addition, the Ackeret theory also gives a constant downwash velocity in that portion of the flow field bounded by the Mach waves from the leading and trailing edges. In superimposed forward and reversed flow, the regions bounded by the Mach waves from the leading and trailing edges have a prismatic region in common which extends to infinity in the spanwise direction and includes the wing. This region, R, is shown in Fig. 1. In the region R, the perturbation velocities in superimposed forward and reversed flow satisfy Jones' criteria [Eqs. (1), (2), and (3)]. Thus, the two-dimensional flat-plate wing produces a flow field which has minimum drag due to lift for a given lift distributed in the infinite prismatic region R.

A region of any length desired can be obtained when end plates are placed on the wing. If infinitely large end plates are placed parallel to the stream at two spanwise stations, the combined flow field will be unchanged. If these end plates are reduced in size until they have the diamond shape defined by the Mach waves from the leading edges in forward and reversed flow, the combined flow field in the region R will remain unchanged.

Thus, a uniform flat-plate wing, normal to the stream, of arbitrary span with end plates aligned with the stream and cut off along the forward and reversed flow Mach lines from the leading edge produces minimum drag due to lift for lift distributed in the prismatic region enclosed by the end plates (see Fig. 2). The drag is the Ackeret value

$$C_D = (\beta/4)C_L^2 \tag{4}$$

based on the plan-form area.

This result may be immediately extended to swept, flat wings with supersonic edges by the use of sweepback theory.[2] Consider a uniform flat wing, sweptback at an angle γ. In superimposed forward and reversed flow, the wing will again produce a prismatic region of disturbed flow common to the forward and reversed motions. In this case, the common region will not be bounded by Mach waves but by oblique planes which contain the leading edge and which are tangent to the Mach cones originating at the leading edge. If the lift distribution is the same in forward and reversed motion, the combined flow field in the disturbed region common to the forward and reversed flows will also have the properties given by Eqs. (1), (2), and (3).

Thus, Jones' criteria for minimum drag for a given total lift distributed in the infinite prismatic region above and below the wing are again satisfied. The value of the drag, obtained from sweepback theory, is

$$C_D = (\beta/4)C_L^2 \sqrt{1 - (\tan^2 \gamma/\beta^2)} \tag{5}$$

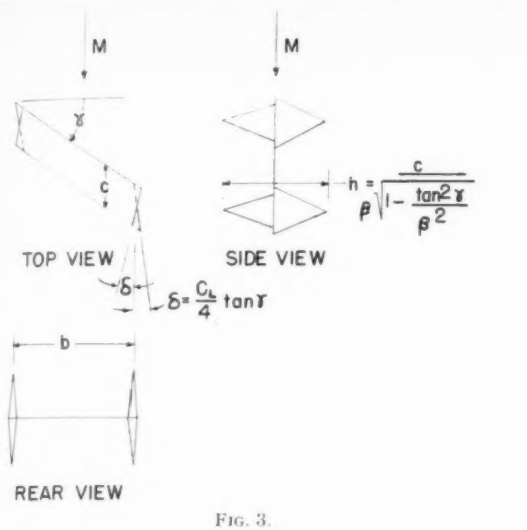

FIG. 3.

based on the plan-form area. The prismatic region above and below the wing need not be infinite if end plates are used. The necessary end plates are again diamond shaped and are aligned with the streamlines on the top and bottom of the wing. The diamond shape of the end plates is obtained by extending them until they intersect the oblique planes which are tangent to the Mach cones from the leading edge, and which contain the leading edge, in forward or reversed flow. End plates of this shape will completely isolate the prismatic region that they define. An illustration of a section of a swept wing with end plates is shown in Fig. 3. The end-plate dimensions are most easily obtained by considering the flow Mach Number normal to the leading edge.

It should be noticed that, in the case of the unswept wing, the necessary end-plate height becomes infinite as the Mach Number approaches one. For the swept wing, the end-plate height becomes infinite when the Mach Number normal to the leading edge approaches one. It seems desirable to base the drag and lift coefficients on one half the total wetted area. If this is done, one obtains

$$\left.\begin{aligned} C_D &= (\beta/4)C_L^2\left\{\sqrt{1-(\tan^2\gamma/\beta^2)}+(1/\beta AR)\right\} \\ C_L &= (4\alpha/\beta)\left\{1/\left[\sqrt{1-(\tan^2\gamma/\beta^2)}+(1/\beta AR)\right]\right\} \end{aligned}\right\} \quad (6)$$

for the drag and lift of a swept and unswept ($\gamma = 0$) wing with end plates of the shape specified above. The drag caused by the end-plate surfaces exterior to the prismatic region is not included in Eq. 6.

REFERENCES

[1] Jones, R. T., *Minimum Wave Drag for Arbitrary Arrangements of Wings and Bodies*, NACA TN 3530, February, 1956.

[2] Busemann, A., *Aerodynamischer Auftrieb bei Ueberschallgeschwindigkeit*, Proc. of 5th Volta Congress, pp. 328–360, 1935; also Luftfahrtforschung, Vol. 12, No. 6, pp. 210–220, 1935; also R.T.P. Translation No. 2844.

On the Supersonic Flow of a Viscous Fluid Past a Flat Plate

Stephen H. Maslen
Lewis Flight Propulsion Laboratory, NACA, Cleveland
April 23, 1956

IN REFERENCE 1, Kuo determines the second approximation to the supersonic viscous flow past a flat plate. Limiting the analysis to an insulated plate, Prandtl Number of unity, and a Chapman and Rubesin type of temperature-viscosity law, he performs a perturbation analysis. This is done in a distorted coordinate system using Lighthill's scheme.[2] The results are consistent with the assumptions and boundary conditions in all respects. Kuo states that these results are in contrast with those of reference 3 where no coordinate distortion is employed. It is the purpose of the present note to point out that the solution of reference 3 (which was intended only to produce information about the boundary layer) is also consistent and, in the boundary layer, agrees with Kuo's results.

In general, the procedure is as follows. The familiar boundary-layer solution in the absence of a pressure gradient is found. This determines an external flow field which, in turn, prescribes a perturbation pressure distribution. This latter determines a perturbation in the boundary layer and so on. The first two approximations to the inviscid field consist of purely outgoing waves, there being, as Kuo points out, no reflections from the shock to this order. Hence, to this order, the solution near the boundary layer is determined independently of the shock condition. However, if conditions near the shock are of interest, as in Kuo's Section (12), or if a higher approximation to the boundary layer is desired, then conditions at the shock become important. A very convenient method of solving this part of the problem is then the application of Lighthill's procedure.[2] If the analysis of the writer had been carried to higher order, some such procedure in the inviscid region would certainly have to be employed.

This brings us to the important point of difference between the analyses of Kuo and of the writer. In solving for the boundary-layer perturbations without a coordinate distortion, it is found in reference 3 that the first two approximations to the normal velocity at the outer edge of the boundary layer are (in the notation of reference 3)

$$0_{v(x,y)} \to b/2\sqrt{x}$$

$$1_{v(x,y)} \to (1/2x)\left[-\eta\beta^2K + bM^2K\right]$$

which lead, in Kuo's notation, to

$$v = (\epsilon v_0/\sqrt{x})\left[1 + (\beta y/2x) - (\epsilon v_0 M^2/\beta\sqrt{x})\right] \quad (1)$$

This is, to repeat, valid near the outer edge of the boundary layer and should not be considered to become infinite for large y. On the other hand, in the inviscid region outside the boundary layer, a modified simple-wave solution consisting only of outgoing waves applies. If, near the boundary layer, this is expanded for small $\beta y/x$, the same expression as that given in Eq. (1) is found. Hence, the apparently infinite (for large y) velocity indicated in Eq. (1) is only apparent, and the boundary-layer solution goes, to the order in question, smoothly into that for the inviscid region. If this same procedure is carried out with reference to the pressure, a similar behavior is found. In this connection it is found that the wall pressure is given to second order (in Kuo's notation) by

$$P = 1 + \frac{\gamma M^2 v_0\epsilon}{\beta\sqrt{x}}\left\{1 + \frac{v_0\epsilon}{\beta\sqrt{x}}\left[\frac{\gamma+1}{4}\frac{M^4}{\beta^2} - 1\right]\right\} \quad (2)$$

This result agrees exactly with Kuo's Eq. (10.3) to consistent orders. If it is plotted on his Fig. 1, the result is virtually indistinguishable from Kuo's theoretical curve over the entire range of the experimental data.

The basic difference between the analysis of Kuo and the writer is that, in contrast to the above, Kuo introduces a coordinate distortion into the boundary layer so that the behavior of the pressure and velocity at the edge of the boundary layer will not be as in Eq. (1) but, rather, that they will remain bounded as y becomes infinite. However, as there is no singularity of the flow at the boundary-layer edge, it is the opinion of the writer that this distortion (in the boundary layer) can in no way lead to new results. In any case, the inviscid solution, however obtained, is nonsingular near the plate and can be expanded in a Taylor series in $1/\sqrt{x}$, so that there is no difficulty about matching solutions.

In view of these remarks, it seems apparent that the results of the two analyses should agree to the order to which they have been carried. The results of reference 3 permit no comparison with Kuo's shock results since the inviscid solution, as constructed, is only valid near the boundary layer. However, a comparison of the wall pressure and skin friction for the two studies shows perfect agreement.

This leaves only consideration of the results near the leading edge—namely those given in Section (11) of reference 1. These results depend on knowing the variation of the pressure near the edge. Examination of Kuo's Eq. (10.3) indicates that, for various ranges of x, one has $P \propto 1$, $1/x$, or $1/\sqrt{x}$. However, the last two variations depend on [see Kuo's Eq. (3.1)] the perturbation pressure, $\epsilon p^{(1)}$, outweighing the zeroth approximations (unity). It is difficult to see any justification for this procedure and, hence, for the results given in Section (11).

An interesting result of these comparisons is that it is established that the results of Kuo can be made more generally valid and apply without regard for Prandtl Number, wall temperature condition, or temperature-viscosity law. That is, under these circumstances (which are those assumed in reference 3) the skin friction and wall pressure are given by

$$c_f \sqrt{Re_x} = 2\mu u_\eta + (2/\beta\sqrt{Re_x})\,[\sqrt{Re_x}(d\delta^*/dx)]^2 + O(\epsilon^2)$$

$$P = 1 + \frac{\gamma M^2}{\beta}\frac{d\delta^*}{dx}\left[1 + \frac{1}{\beta}\frac{d\delta^*}{dx}\left(\frac{\gamma+1}{4}\frac{M^4}{\beta^2} - 1\right)\right] + O(\epsilon^3)$$

where the displacement thickness, δ^*, and μu_η are found from their first approximations (the usual boundary-layer analysis).

Author's Reply

In commenting on my recent paper,[1] Dr. Maslen in his note brings up two points. The first is that his solution[3] is consistent and, in the boundary layer, agrees with mine. The second is that my results for the region near the leading edge, given in Section (11) of reference 1, are not justified. I would like to reply as follows:

(1) With respect to the first question, I feel that, since both of our solutions were derived from the standard mathematical procedure, there is no reason to doubt that they are consistent. As to whether they "agree" or not, this seems irrelevant. My view in this matter is that, in seeking approximate solutions of, say, the Navier-Stokes equations, different methods often lead to different solutions with different degrees of accuracy in different regions. A well-known classical example is the difference between the Prandtl-Glauert method of perturbation and Friedrichs' simple-wave solution in supersonic airfoil theory. If one's interest lies only in the pressure on the airfoil surface, then, for all practical purposes, the Prandtl-Glauert method is adequate. On the other hand, if one is not only interested in knowing the flow properties in the surface but also those such as the shock pattern, the flow field, etc., then the simple-wave solution is the better method to apply. In the present problem, the methods adopted by Maslen and me should be viewed in this same spirit. My results are valid for all y and may therefore be more useful for many purposes.

(2) Although my solution is uniformly valid for all y, it is, nevertheless, singular at the leading edge. The discussions in Section (11) of reference 1 were intended only to make this point clear. Since the solution is singular at the leading edge, somewhere in that neighborhood the approximation must break down. But Maslen's condition that the second term of my pressure formula should not exceed unity is certainly no criterion. In principle, my pressure formula consists of only two terms for all approximations and, hence, cannot be considered as an asymptotic expansion. To carry higher order approximations would only improve the accuracy of the argument ξ. For this quantity, there is, of course, a region of validity. But its range cannot be decided unless high-order solutions are investigated. This is the same difficulty that occurs in any perturbation theory; mine is no exception. For the moment, I would rely on experimental verification rather than arbitrary criteria.

References

[1] Kuo, Y. H., *Viscous Flow Along a Flat Plate Moving at High Supersonic Speeds*, Journal of the Aeronautical Sciences, Vol. 23, No. 2, pp. 125–136, February, 1956.

[2] Lighthill, M. J., *A Technique for Rendering Approximate Solutions to Physical Problems Uniformly Valid*, Philos. Mag., Vol. 40, pp. 1179–1201, December, 1949.

[3] Maslen, S. H., *Second Approximation to Laminar Compressible Boundary Layer on Flat Plate in Slip Flow*, NACA TN 2818, 1952.

On Thin-Ring Analysis

Bruno A. Boley*

Institute of Flight Structures, Columbia University, New York

April 23, 1956

Summary

A simple formula is presented which gives explicitly the bending moment at any point of a closed ring of arbitrary shape under arbitrary loadings in the plane of the ring. Simplifications for cases exhibiting symmetry and the calculation of the normal and shear forces are also discussed.

Introduction

It is customary in engineering practice to determine the bending moments in thin rings with the aid of the principle of least work (or of some equivalent principle involving energy considerations). To this end, the bending moment at any point in the ring is first expressed in terms of the indeterminate forces and bending moment existing at a given cross section, and the latter quantities are then found by minimization of the total strain energy. In the calculation of the strain energy U, it is assumed that, because of the thinness of the ring, the extensional and shearing deformations may be neglected and that the energy of bending, which alone need be considered, may be approximated by the equation

$$U = \int_0^S \frac{M^2}{2EI}\,ds \tag{1}$$

where s measures the distance along the median line of the ring, M is the bending moment, EI the bending rigidity in the plane of the ring, and S its perimeter.

For some simple loadings and geometries, the results of the above procedure are available in the literature; in a general case, however, it is necessary for the stress analyst to follow all the steps outlined above and to develop his solution from the very beginning. It would seem advantageous to have at one's disposal an explicit representation for the final bending moment at any point of the ring, which could be used for any loading or geometry; a formula answering this description is, in fact, easily derived from the procedure just described. To his surprise, however, the author has not been able to find it in the literature; it is therefore the purpose of this note to present and to discuss briefly this formula.

Formula for Bending Moments

Let, in the ring of Fig. 1, the unknown forces and moment at the point (x_0, y_0) be denoted by X_0, Y_0, (in the x and y directions, respectively) and N_0. Let the distance s be measured from this point. The bending moment at any point is then

$$M(s) = M_0(s) + N_0 + X_0(y_0 - y) - Y_0(x - x_0) \tag{2}$$

where $M_0(s)$ is the bending moment which would exist at any point s if the ring were open at $s = 0$; thus $M_0(0) = 0$. The conditions of minimum strain energy—namely,

* Associate Professor of Civil Engineering.

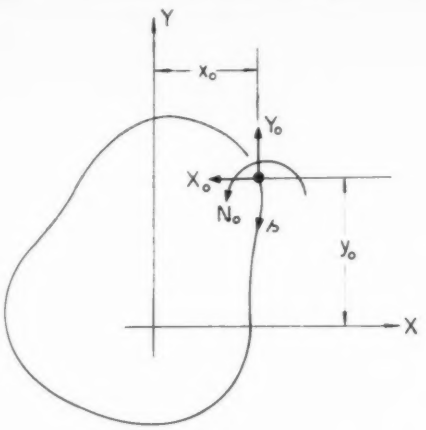

FIG. 1.

$$\partial U/\partial N_0 = \partial U/\partial X_0 = \partial U/\partial Y_0 = 0 \tag{3}$$

require that

$$\int_0^S \frac{M}{EI}\,ds = \int_0^S \frac{My}{EI}\,ds = \int_0^S \frac{Mx}{EI}\,ds \tag{3a}$$

The following well-known equations can then be written:

$$\left.\begin{aligned}
&(Y_0x_0 + X_0y_0 + N_0)S^* - X_0\int_0^S \frac{y}{EI}\,ds - \\
&\qquad Y_0\int_0^S \frac{x}{EI}\,ds = -\int_0^S \frac{M_0}{EI}\,ds \\
&(Y_0x_0 + X_0y_0 + N_0)\int_0^S \frac{y}{EI}\,ds - X_0I_x^* - \\
&\qquad Y_0I_{xy}^* = -\int_0^S \frac{M_0y}{EI}\,ds \\
&(Y_0x_0 + X_0y_0 + N_0)\int_0^S \frac{x}{EI}\,ds - X_0I_{xy}^* - \\
&\qquad Y_0I_y^* = -\int_0^S \frac{M_0x}{EI}\,ds
\end{aligned}\right\} \tag{3b}$$

with the following symbols:

$$S^* = \int_0^S \frac{ds}{EI}; \qquad I_x^* = \int_0^S \frac{y^2}{EI}\,ds;$$

$$I_{xy}^* = \int_0^S \frac{xy}{EI}\,ds; \qquad I_y^* = \int_0^S \frac{x^2}{EI}\,ds \tag{3c}$$

For simplicity, it will now be assumed that the origin of coordinates is taken in such a way that

$$\int_0^S \frac{x}{EI}\,ds = \int_0^S \frac{y}{EI}\,ds = 0 \tag{4}$$

Thus, for a ring of uniform cross section, the axes are centroidal. The quantities X_0, Y_0, and N_0 are then readily obtained from Eqs. (3b); substitution into Eq. (2) gives then the bending moment $M(s)$ explicitly in terms of $M_0(s)$ as follows:

$$M(s) = M_0(s) - \left[\left(\int_0^S \frac{M_0\,ds}{EI}\right)\Big/S^*\right] + \left[x\left(I_{xy}^*\int_0^S \frac{M_0y\,ds}{EI} - I_x^*\int_0^S \frac{M_0x\,ds}{EI}\right) + y\left(I_{xy}^*\int_0^S \frac{M_0x\,ds}{EI} - I_y^*\int_0^S \frac{M_0y\,ds}{EI}\right)\right]\Big/(I_x^*I_y^* - I_{xy}^{*2}) \tag{5}$$

SPECIAL CASES

The general formula just derived assumes simpler forms in the following special cases of practical interest.

(a) *Y-axis, say, an axis of symmetry; general loading*—Here $I_{xy}^* = 0$, and therefore

$$M = M_0 - \frac{1}{S^*}\int_0^S \frac{M_0\,ds}{EI} - \frac{x}{I_y^*}\int_0^S \frac{M_0x}{EI}\,ds - \frac{y}{I_x^*}\int_0^S \frac{M_0y}{EI}\,ds \tag{5a}$$

(b) *Y-axis, an axis of symmetry for both loading and structure*—Here

$$I_{xy}^* = \int_0^S \frac{M_0x}{EI}\,ds = 0$$

and therefore

$$M = M_0 - \frac{1}{S^*}\int_0^S \frac{M_0\,ds}{EI} - \frac{y}{I_x^*}\int_0^S \frac{M_0y}{EI}\,ds \tag{5b}$$

(c) *Y-axis, an axis of symmetry of the structure and of antisymmetry for the loading*—Here

$$I_{xy}^* = \int_0^S \frac{M_0}{EI}\,ds = \int_0^S \frac{M_0y}{EI}\,ds = 0$$

and therefore

$$M = M_0 - \frac{x}{I_y^*}\int_0^S \frac{M_0x}{EI}\,ds \tag{5c}$$

(d) Additional simplifications will of course be introduced in the case of beams with constant EI.

SHEAR AND NORMAL FORCES

A knowledge of the shear force $V(s)$ and the normal force $T(s)$ at any cross section is required, in addition to that of M, for the calculation of the stresses in the ring. These quantities are most easily obtained, when use is made of the above formulas, from the differential equations of equilibrium of an element of the ring. Denoting derivatives with respect to s by primes, one obtains then (see Fig. 2):

$$\left.\begin{aligned}
V' + (T/R) &= -p \\
T' - (V/R) &= -q \\
M' + V &= -qc
\end{aligned}\right\} \tag{6}$$

where $R = R(s)$ is the local radius of curvature of the median line and $c = c(s)$ is the distance from the median line to the place where the applied shear flow q is acting. The shear and normal forces are then, in terms of M, as follows:

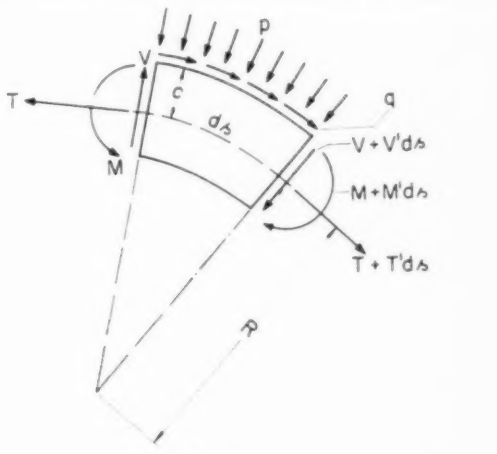

FIG. 2.

$$\left.\begin{aligned} V &= -M' - qc \\ T &= R[M'' + (qc)' - p] \end{aligned}\right\} \quad (6a)$$

In addition, the equations

$$\left.\begin{aligned} (RM'')' + (M'/R) &= -(qc/R) - [R(qc)']' - q + (Rp)' \\ (RV')' + (V/R) &= q - (Rp)' \\ (RT')' + (T/R) &= -p - (Rq)' \end{aligned}\right\} \quad (6b)$$

which follow from Eqs. (6), may occasionally be useful for a check on the calculations. Obvious simplifications arise if R is constant—i.e., for a circular ring. The first of Eqs. (6b) may also be used for the determination of M_0.

Approximative Determination of the Ceiling of Turbojet Engines

Karl L. Sanders
Design Engineer, IAME, Córdoba, Argentina
May 4, 1956

THE ADIABATIC ALTITUDE EQUATION proved to represent the turbojet ceiling due to suffocating with fairly good results.

After flame extinction, it may be roughly assumed that the conditions in the combustion chamber are only determined by the compression end state.

Evaluation of NACA TN 1357, *Effect of Combustor Inlet Conditions on Performance of an Annular Turbojet Combustor*, yielded a critical pressure range $p_{1\ crit.}$ of 0.8–1.0 atmosphere in the combustion chamber. Using these critical pressures in the equation for adiabatic altitude,

$$H_{ad.} = [x/(x-1)]RT_0[(p_1/p_0)^{(x-1)/x} - 1]$$

where

T_0 = atmospheric absolute temperature
p_0 = atmospheric pressure

the ceiling of the engine can be calculated with fairly good results. On the left side of Fig. 1, the adiabatic altitude $H_{ad.}$ is plotted vs. the static SL. compression ratio p_1/p_0 at maximum r.p.m. as given by the engine manufacturer. On the right side, $H_{ad.}$ for the critical compression ratios $p_{1\ crit.}/p_0$ is plotted vs. the critical altitude.

For other than maximum r.p.m., the $H_{ad.}$ values can easily be reduced using

$$H_{ad.\ r.p.m.} = H_{ad.\ max.\ r.p.m.}\ (\text{r.p.m.}/\text{max. r.p.m.})^2$$

Ceilings for some turbojet engines are indicated in the right side of the diagram showing quite good agreement.

The following influences have not been considered here: (1) combustion chamber type and fuel spray characteristics; (2) grade of fuel; (3) ram effect; and (4) compressor characteristics field.

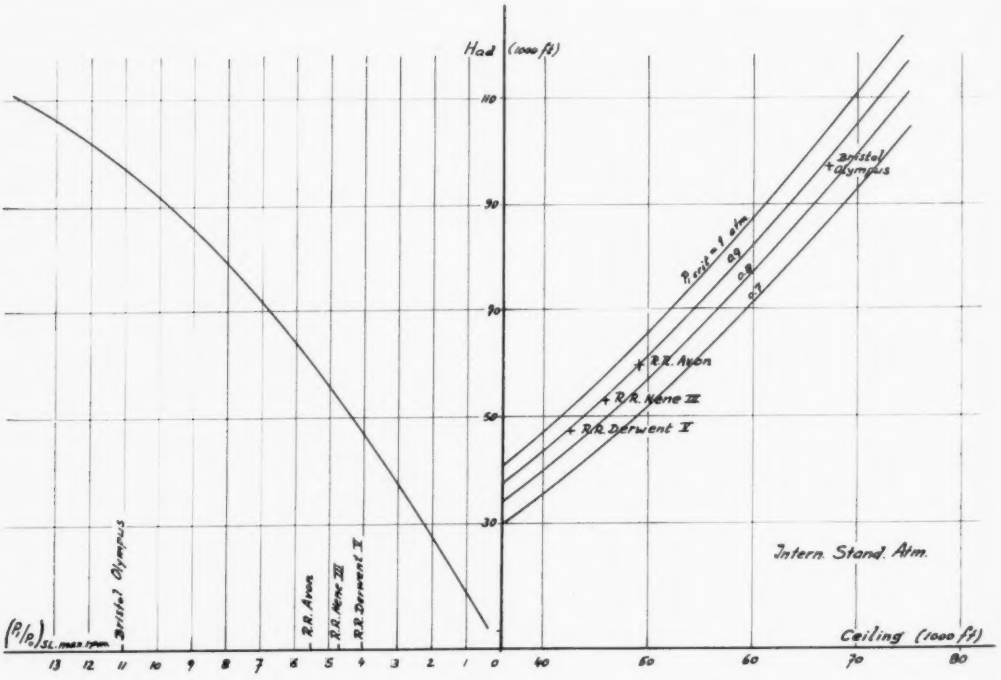

FIG. 1.